

# Infocommunications Journal

A PUBLICATION OF THE SCIENTIFIC ASSOCIATION FOR INFOCOMMUNICATIONS (HTE)

March 2021

Volume XIII

Number 1

ISSN 2061-2079

## MESSAGE FROM THE EDITOR-IN-CHIEF

Young researchers on radio communication advances, various machine learning applications, and traffic congestion in smart cities ..... *Pal Varga* 1

## SELECTED INVITED PAPERS

Improved Model for Indoor Propagation Loss in the 5G FR2 Frequency Band ..... *Árpád László Makara and László Csurgai-Horváth* 2

Exploring Embeddings for MIMO Channel Decoding on Quantum Annealers ..... *Ádám Marosits, Zsolt Tabi, Zsófia Kallus, Péter Vadera, István Gódor and Zoltán Zimborás* 11

Processing and Visualizing the Low Earth Orbit Radio Frequency Spectrum Measurement Results From the SMOG Satellite Project ..... *Donát Takács, Boldizsár Markotics and Levente Dudás* 18

Double-View Matching Network for Few-Shot Learning to Classify Covid-19 in X-ray images ..... *Gábor Szűcs and Marcell Németh* 26

Towards Machine Learning-based Anomaly Detection on Time-Series Data ..... *Daniel Vajda, Adrian Pekar, and Karoly Farkas* 36

Traffic congestion propagation identification method in smart cities ..... *Attila M. Nagy and Vilmos Simon* 45

## PAPERS FROM OPEN CALL

Joint Beacon Power and Beacon Rate Control Based on Game Theoretic Approach in Vehicular Ad Hoc Networks ..... *Hamid Garmani, Driss Ait Omar, Mohamed El Amrani, Mohamed Baslam and Mostafa Jourhmane* 58

Segmentation of MRI images to detect multiple sclerosis using non-parametric, non-uniform intensity normalization and support vector machine methods ..... *Mohammad Moghadasi and Gabor Fazekas* 68

## CALL FOR PAPERS / PARTICIPATION

CNSM 2021 / 17th International Conference on Network and Service Management  
CNSM 2021, Izmir, Turkey ..... 75

GLOBECOM 2021 / IEEE Global Communications Conference  
IEEE GLOBECOM, Madrid, Spain ..... 77

## ADDITIONAL

Guidelines for our Authors ..... 76

Technically Co-Sponsored by



**Editorial Board**

**Editor-in-Chief:** PÁL VARGA, Budapest University of Technology and Economics (BME), Hungary

**Associate Editor-in-Chief:** ROLLAND VIDA, Budapest University of Technology and Economics (BME), Hungary

**Associate Editor-in-Chief:** LÁSZLÓ BACSÁRDI, Budapest University of Technology and Economics (BME), Hungary

- |   |   |
|---|---|
| JAVIER ARACIL<br>Universidad Autónoma de Madrid, Spain                              | MAJA MATIJASEVIC<br>University of Zagreb, Croatia                               |
| LUIGI ATZORI<br>University of Cagliari, Italy                                       | VACLAV MATYAS<br>Masaryk University, Brno, Czech Republic                       |
| PÉTER BARANYI<br>Budapest University of Technology and Economics, Hungary           | OSCAR MAYORA<br>FBK, Trento, Italy  |
| JÓZSEF BÍRÓ<br>Budapest University of Technology and Economics, Hungary             | MIKLÓS MOLNÁR<br>University of Montpellier, France                              |
| STEFANO BREGNI<br>Politecnico di Milano, Italy                                      | SZILVIA NAGY<br>Széchenyi István University of Győr, Hungary                    |
| VESNA CRNOJEVIĆ-BENGIN<br>University of Novi Sad, Serbia                            | PÉTER ODRY<br>VTS Subotica, Serbia  |
| KÁROLY FARKAS<br>Budapest University of Technology and Economics, Hungary           | JAUELICE DE OLIVEIRA<br>Drexel University, USA                                  |
| VIKTORIA FODOR<br>Royal Technical University, Stockholm                             | MICHAL PIORO<br>Warsaw University of Technology, Poland                         |
| EROL GELENBE<br>Imperial College London, UK   | ROBERTO SARACCO<br>Trento Rise, Italy   |
| ISTVÁN GÓDOR<br>Ericsson Hungary Ltd., Budapest, Hungary                            | GHEORGHE SEBESTYÉN<br>Technical University Cluj-Napoca, Romania                 |
| CHRISTIAN GÜTL<br>Graz University of Technology, Austria                            | BURKHARD STILLER<br>University of Zürich, Switzerland                           |
| ANDRÁS HAJDU<br>University of Debrecen, Hungary                                     | CSABA A. SZABÓ<br>Budapest University of Technology and Economics, Hungary      |
| LAJOS HANZO<br>University of Southampton, UK  | GÉZA SZABÓ<br>Ericsson Hungary Ltd., Budapest, Hungary                          |
| THOMAS HEISTRACHER<br>Salzburg University of Applied Sciences, Austria              | LÁSZLÓ ZSOLT SZABÓ<br>Sapientia University, Tirgu Mures, Romania                |
| ATTILA HILT<br>Nokia Networks, Budapest, Hungary                                    | TAMÁS SZIRÁNYI<br>Institute for Computer Science and Control, Budapest, Hungary |
| JUKKA HUHTAMÄKI<br>Tampere University of Technology, Finland                        | JÁNOS SZTRIK<br>University of Debrecen, Hungary                                 |
| SÁNDOR IMRE<br>Budapest University of Technology and Economics, Hungary             | DAMLA TURGUT<br>University of Central Florida, USA                              |
| ANDRZEJ JAJSZCZYK<br>AGH University of Science and Technology, Krakow, Poland       | ESZTER UDVARY<br>Budapest University of Technology and Economics, Hungary       |
| FRANTISEK JAKAB<br>Technical University Kosice, Slovakia                            | SCOTT VALCOURT<br>University of New Hampshire, USA                              |
| GÁBOR JÁRÓ<br>Nokia Networks, Budapest, Hungary                                     | JÓZSEF VARGA<br>Nokia Bell Labs, Budapest, Hungary                              |
| MARTIN KLIMO<br>University of Zilina, Slovakia                                      | JINSONG WU<br>Bell Labs Shanghai, China   |
| DUSAN KOČUR<br>Technical University Kosice, Slovakia                                | KE XIONG<br>Beijing Jiaotong University, China                                  |
| ANDREY KOUCHERYAVY<br>St. Petersburg State University of Telecommunications, Russia | GERGELY ZÁRUBA<br>University of Texas at Arlington, USA                         |
| LEVENTE KOVÁCS<br>Óbuda University, Budapest, Hungary                               |   |

**Indexing information**

Infocommunications Journal is covered by Inspec, Compendex and Scopus.

**Infocommunications Journal is also included in the Thomson Reuters – Web of Science™ Core Collection, Emerging Sources Citation Index (ESCI)**

**Infocommunications Journal**

Technically co-sponsored by IEEE Communications Society and IEEE Hungary Section

**Supporters**

FERENC VÁGUJHELYI – president, Scientific Association for Infocommunications (HTE)

**Editorial Office** (Subscription and Advertisements):  
Scientific Association for Infocommunications  
H-1051 Budapest, Bajcsy-Zsilinszky str. 12, Room: 502  
Phone: +36 1 353 1027  
E-mail: info@hte.hu • Web: www.hte.hu

**Articles can be sent also to the following address:**  
Budapest University of Technology and Economics  
Department of Telecommunications and Media Informatics  
Phone: +36 1 463 4189, Fax: +36 1 463 3108  
E-mail: pvarga@tmit.bme.hu

**Subscription rates for foreign subscribers:** 4 issues 10.000 HUF + postage

Publisher: PÉTER NAGY

HU ISSN 2061-2079 • Layout: PLAZMA DS • Printed by: FOM Media

# Young researchers on radio communication advances, various machine learning applications, and traffic congestion in smart cities

Pal Varga

**T**HIS issue of the Infocommunications Journal raises our spirits by presenting the papers of young researchers as first authors. The first six papers are selected from the distinguished topics and awarded works of the Scientific Student Association of the Faculty of Electrical Engineering and Informatics, BME. The two papers that close the issue are submitted to our open call by young researchers, as well.

In their paper, Árpád László Makara and László Csurgai-Horváth analyze the wave propagation conditions for 5G FR2 bands regarding indoor cases, compare their measurements with the current models, and present an improved model for indoor propagation loss in real indoor scenarios. When calculating the average absolute error during a given measurement, it is found that it is nearly 70% smaller (by more than 80% in some cases) comparing it by the ITU model.

Ádám Marosits et. al. explore the embedding limits for MIMO channel decoding on quantum annealers. First, they showed that a linear QuAMax formulation can be employed together with Gray coding of 64-QAM to reduce the negative effect of bit errors during transmission. Besides, they have extended the range of embedding of MIMO ML decoding problems regarding both the modulation complexity and the transmitter number.

Donát Takács, Boldizsár Markotics, and Levente Dudás present their real-life measurement results on the SMOG satellite project. They briefly describe both the SMOG-P and ATL-1 PocketQube class satellites (they are 5x5x5cm and 5x5x10cm in size, respectively), and how they carried out LEO (Low Earth Orbit) radio frequency spectrum measurements with the help of these equipment. They analyzed and visualized the results, and present what sort and amount of radiated power is there, continuously heating the space and disturbing the communication system of LEO satellites.

Focusing on our everyday fears, Gábor Szűcs and Marcell Németh apply the few-shot hypothesis learning method to classify COVID-19 cases through X-ray images. Their method and results aim to help the work of those working in medicine and use merely a few images for the given problem. They compare various machine learning methods that they applied, and found that the so-called Double-View Matching Network (DVMN) reaches the best accuracy on a multi-view dataset at 1-shot, 2-shot, and 5-shot learning.

Following the machine learning thread in this issue, Daniel Vajda, Adrian Pekar, and Karoly Farkas present their new algorithm, Alter-Re2. It is an improved version of ReRe, the Long

Short-Term Memory-based algorithm, and they developed it to solve anomaly detection problems in time-series data with certain conditions that often arise in network infrastructure monitoring. Their evaluation found that Alter-Re2 can identify three times more anomalies on average when compared to ReRe on the same data.

In their paper, Attila M. Nagy and Vilmos Simon present their novel method for identifying traffic congestion propagation in smart cities. They compare the new SCPP (Spatial Congestion Propagation Patterns) algorithm with the STC (Spatio-Temporal Congestion) process, and found that SCPP is able to identify a much greater number of congestion propagation paths with better computational performance than STC.

Hamid Garmani et. al. aim to tackle the problem of joint beacon power and beacon rate in vehicular ad hoc networks (VANETs). They formulate cooperative and non-cooperative gaming approaches, where each vehicle in the VANET chooses the joint beaconing rate and beaconing power. They have performed the equilibrium analysis and proposed a three distributed algorithm for computing the equilibrium point. After extensive simulations they found that the Cooperative Bargaining Algorithm is a good choice, because it is fast and converges the equilibrium.

Finally, Mohammad Moghadasi and Gabor Fazekas propose a system that aims to reduce the effect of bias field on the MRI image using N3 (Nonparametric Non-uniform intensity Normalization) algorithm and pixels of MRI images clustered by k-means algorithm. Data dimensionality is reduced by Principal Component Analysis (PCA) algorithm, whereas the segmentation is done by the Support Vector Machine (SVM) algorithm. Their results show that the proposed system can diagnose multiple sclerosis with an average accuracy of 93.28%.



**Pal Varga** received his Ph.D. degree from the Budapest University of Technology and Economics, Hungary. He is currently an Associate Professor at the Budapest University of Technology and Economics and also the Director at AITIA International Inc. His main research interests include communication systems, Cyber-Physical Systems and Industrial Internet of Things, network traffic analysis, end-to-end QoS and SLA issues – for which he is keen to apply hardware acceleration and artificial intelligence, machine learning techniques as well.

Besides being a member of HTE, he is a senior member of IEEE, where he is active both in the IEEE ComSoc (Communication Society) and IEEE IES (Industrial Electronics Society) communities. He is Editorial Board member of the Sensors (MDPI) and Electronics (MDPI) journals, and the Editor-in-Chief of the Infocommunications Journal.

# Improved Model for Indoor Propagation Loss in the 5G FR2 Frequency Band

Árpád László Makara<sup>1</sup> and László Csurgai-Horváth<sup>2</sup>

**Abstract**—One of the latest developments today is the 5G, or 5th generation mobile network. In addition to a number of innovations, the new system also includes millimeter-wavelength frequency ranges denoted with FR2, that formerly not applied for these specific purposes. Proper management of the transmitter and receiver antenna beams is required for efficient communication in this frequency range. For future use, the simplest implementation way is electronically shaping the antenna beams by an algorithm to orient the antennas in the best possible direction. The prerequisites for these algorithms are appropriate propagation models, which are currently lacking, and those that publicly available are not accurate enough for practical use.

Due to its complexity, solving this task is expected to be feasible only with artificial intelligence based solutions that require large amounts of input data for training. This amount of data requires long-term measurement data, which is not a feasible solution considering the rate of development. There are two possible ways to solve this: creating more accurate propagation models or apply simulations. For the latter solutions, it may also be necessary to validate based on measurement results and models.

In this paper we provide an overview of the wave propagation conditions in the new FR2 frequency range in the case of indoor use, intending to create an accurate propagation model. We present the existing models in other fields of applications and the typical propagation conditions in these bands in view of the existing research in this area. By analyzing the measurements performed at the department, we point out the shortcomings of the previous models and the parameters to be taken into account. Then we present an improved model based on the ITU recommendation for indoor propagation.

**Index Terms**—5G, environmental coefficient, FR2 band, indoor propagation, path loss model

## I. INTRODUCTION

THE next generation of wireless networks is the 5th generation mobile network, for which some of the standards are still being developed today. The need to develop a new system is caused by the drastic increase in consumer demand [1], based on current trends. The number of devices on the network simultaneously is continuously growing, requiring a faster and higher capacity network creation.

With regard to the standardization processes, it is worth saying a few words about the bigger and more significant organizations. The 3GPP (3rd Generation Partnership Project) umbrella organization brings together the various

standardization processes of mobile communication. The ITU is the UN specialized agency whose task is international facilitating telecommunications cooperation. In this work, IMT-2020 (International Mobile Telecommunications-2020) standard was the guideline for specifications and standards [2].

### A. 5G system requirements

In 5G a number of new uses are planned, based on past trends [1]. With the new system for wireless connections in existing areas a drastic increase in speed would be achievable. Without wishing to be exhaustive, the main areas of application are: [2]:

- Support for real time video calls.
- High-speed data connection support (50 MB/s or higher).
- Serving high-speed users (up to 500 km/hr).
- IoT support (such as wireless operation of sensor networks).
- Ultra-reliable communications (URC).
- Massive machine type communications (mMTC).
- Enhanced mobile broadband (eMBB).

In fact, to meet user needs (existing and future) requirements for the 5G network [3], assumed increasing number of assets necessitated the designation of new frequency bands as listed in Table I:

TABLE I  
5G REQUIREMENTS

|                        |   |
|------------------------|---|
| User data speed        | Downlink: 100 Mbps - 1 Gbps<br>Uplink: 50 Mbps - 500Mbps  |
| Maximal data speed     | Downlink:20 Gbps; Uplink: 10 Gbps                         |
| Bandwidth              | 100 MHz – 1 GHz   |
| Mobility               | Up to 500 km/hr<br>Ultra-Reliable and Low Latency         |
| Delay                  | Communications: 0.5 ms<br>Enhanced Mobile BroadBand: 4 ms |
| Connections density    | 250.000 user/km <sup>2</sup>                              |
| Local traffic capacity | 15 Mbps/m <sup>2</sup>                                    |

The new frequency bands used previously only for satellite-to-Earth communications or in the access network of the mobile communications system. The characteristics of these new domains are different for mobile communication bands so far used, so their empirical description is particularly important for implementation.

### B. The frequency range examined

One of the many designated frequency bands is 38 GHz (and vicinity), which is the main subject of this paper. However, the statements made are similar to the other higher frequency ranges. The signal propagation in the investigated band has a different nature than the traditional lower frequencies. In

<sup>1</sup>Department of Broadband Infocommunications and Electromagnetic Theory, Budapest University of Technology and Economics, Hungary.

<sup>1</sup>(e-mail: makara.arpadlaszlo@edu.bme.hu)

<sup>2</sup>(e-mail: csurgai-horvath.laszlo@vik.bme.hu)

addition, it is no longer negligible that solid bodies also have significant attenuation effect [4]. Among other things, this is why we can talk about different indoors and outdoors models.

In such a high frequency range, the transmitter and receiver antenna beam orientations are particularly critical [5] for good reception conditions, in fact, for as long as a device is connected to the network. In many application areas the receiver moves relative to the transmitter while connected to the network. But even if both the transmitter and the receiver are in a constant, fixed position, a change can and will happen in the space between them. For all these reasons, it is essential that at least in the receiver, be able to control the antenna beam, thus provide better reception conditions [6]. However, the time required for control should be as short as possible, regardless of outdoor or indoor use, and no user can feel that there is significant fluctuation in the received signal level.

Summarizing all this, it becomes necessary to change the operational environment as quickly as possible by adaptive beamforming, in order to maximize the transmitter and receiver antenna directing at each other, over the entire range of operating time. The beamforming control must be such that the user does not take anything from it and the quality of service also meets the expectations.

The complexity of the task is predicted to require an adaptive beamformer solution based on artificial intelligence algorithms in the future application of higher frequency ranges. With all this, the goal is to ultimately produce a model with which the necessary beamforming algorithms will be trainable for future use.

### C. The structure of the paper

In Section 2, we present the frequency ranges of the 5G radio interface. Following this, in Section 3, we describe the various public propagation models, highlighting them separately the one that is best used for our purpose.

After all, we will briefly summarize how the department developed the competence required for the task in Section 4 and what tools are available to us to perform the measurements. Next, in Section 5, we analyze the completed measurements and compare these results with the relevant models and show what further steps are taken necessary for the end use. Finally, in Section 6, we present a new model designed to facilitate adaptive beamforming based on the experience shared in the previous chapters.

## II. 5G FREQUENCY BANDS AND THEIR CHARACTERISTICS

5G NR (Abbreviation for 5G New Radio) [8] stands for layer radio access technology (standard abbreviation: RAT) [9]. The 5G NR defines two frequency bands, and several within subbands:

- Frequency Range 1 (FR1): Bands below 6 GHz
- Frequency Range 2 (FR2): Between 24.25 and 52.5 GHz

There are also currently plans to expand the FR1 range to 410 MHz and 7125 MHz and that, in the case of FR2, bands up to 100 GHz should be established. How much bandwidth will

eventually be needed will be determined by the user needs.

In 2018, the n260 has already been allocated for use in the US (among other things) [10]. In the case of Hungary, during 2019 they were only allocated in FR1 bands for the operation of 5G [11]. The mobile service providers that have won these bands are already advertised as an available service.

This paper covers the frequency range of 38 GHz and surrounding in the FR2 band for a more thorough examination.

### A. Path loss in FR2 frequency bands

When using 5G, the radio waves will in most cases propagate in the air, respectively sometimes through walls, objects, but ultimately in a dominant path in open space. The relative dielectric constant of air is the function of frequency, temperature, pressure and humidity [12] (only the very first parameter has an actual influence). For outdoor use, this means that this frequency band is already highly exposed to the weather [14]. From a practical application point of view, the attenuation of the medium will change, which will be proportional to the distance [12].

Another significant factor besides attenuation is the occurrence of reflections (related to even the issue of transmission, but this is now secondary). The electromagnetic wave reflected at a certain percentage at the medium boundary. The degree of reflections is basically affected by material properties or the frequency, while the physical size of the reflecting object must be larger than the wavelength.

It is important to talk about interference on the topic of reflections. Interference occurs when two or more waves meet and their phases are different. We can speak of constructive or destructive interference, depending on whether the amplitude of the wave (signal) will be larger or smaller than it was originally. Where there is reflection, there is a high chance of interference that is greater it is likely to be destructive rather than constructive.

### B. Uses of the 38 GHz band to date

The department has former experience with this frequency band for Alphasat (Inmarsat-4A F4) [15] to communicate with a satellite and during these the main propagation characteristics were examined. A feature of this application is that the exact position of the satellite is always known, so the antennas are directed at each other without any particularly great obstacle in the path. The most important factor of the mode of use is the individual antennas orientation [5]. In terms of practical implementation, it is typically narrow in direction antennas with high gain are used.

In addition to satellite reception, the department has previously conducted a shorter research on 38 GHz band. In 2018 [7] we examined how behave electromagnetic waves at this frequency indoors, including in cases when antenna orientation to each other was not ensured. Measurements related to the project results were compared with ITU-R Recommendation P.1238 [16], during which it is concluded that the recommended model gives an acceptable result as long as antenna orientation towards each other is ensured.

### III. EXISTING PROPAGATION MODELS

The models can be divided into three large groups: indoor, outdoor and free space. In addition we can distinguish between empirical, deterministic, and semi-empirical models.

For empirical models a correlation based on a statistical approach can be given. Easily and are quick to use, in return they are not always the most accurate. In a deterministic case based on some preliminary model, the propagation in the given space is calculated to get the quantity sought.

For mobile communication networks, outdoor and indoor models are important, however, outdoor propagation models can also be used for a kind of control (but these are best for point-to-point connections in particular).

The number of models dedicated to this frequency band is very low in the literature. Due to the nature of the problem, deterministic modelling methods are accurate but require more computing capacity, while the ray-tracing methods can be used along affordable computational capacities [13].

From end use, it follows that we want to perform as few calculations as possible in order to get results as soon as possible. In this paper, we deal only with the examination of empirical models.

#### A. Free-space propagation

In the case of outdoor propagation, most models assume direct vision or other special circumstances. The attenuation per unit length thus calculated is typically lower as for indoor propagation models, but of a similar order of magnitude [17]. Hence an estimate can be used in indoor modelling (taking into account its limitations). The most common such relationship, which we simply refer to as outdoor attenuation hereinafter [21] takes the following form:

$$P_L = 20 \cdot \log_{10}(d) + 20 \cdot \log_{10}(f) + 92.45 \quad (1)$$

where  $d$  is the distance in kilometres,  $f$  is the frequency in GHz, and the result is given in decibels and describes the outdoor attenuation between isotropic antennas in vacuum. Once the medium in which the wave propagates is already air, additional attenuation occurs up. For low distances Fig. 1. depicts the path loss calculated with Equation (1).

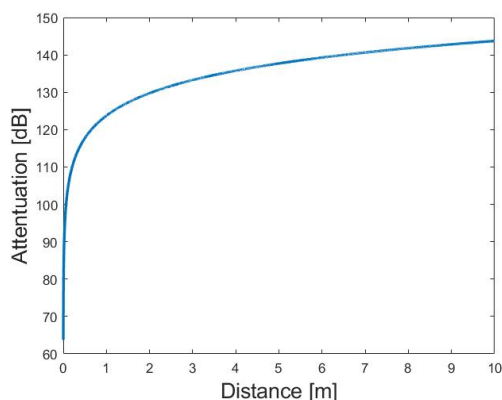


Fig. 1. Short-range free-space path loss in FR2 band at 38.72 GHz

#### B. Close-in free space reference distance path loss model

The Close-in free space reference distance path loss model [22] (hereinafter CI) is a reference model based on outdoor propagation and it is applied for comparison multiple indoor signal propagation results:

$$P_L^{(CI)} = FSPL(f, d_0) + 10 \cdot n \cdot \log_{10}\left(\frac{d}{d_0}\right) + X_\sigma^{CI} \quad (2)$$

where  $FSPL(f, d_0)$  is the outdoor attenuation at the reference distance ( $d_0$  is 1 meter) at the given frequency  $f$  measured in GHz,  $n$  is the path loss factor (PLE) and  $X_\sigma^{CI}$  is a zero-valued Gaussian random variable with  $\sigma$  standard deviation. The measured PLE [23] coefficients found in the literature are largely the same in the ITU model of indoor signal propagation with distance-based loss coefficients. A semi-outdoor, semi-indoor measurement can be found in the literature where the measured PLE is double of the ITU model, however, a high value for standard deviation was measured here [24].

#### C. Outdoor propagation models

Outdoor propagation models usually differentiate cases according to how they are built and whether the area is environmental or natural. In addition, one can count on individual models on topography, degree of incorporation, location of the transmitting antenna, climate characteristics and other similar factors. In a sense, the simplest such model is the ITU surface model [25]. Of interest for classification are models that are essentially outdoor, but are used in a somewhat enclosed built environment. In the literature can be found a measurement procedure (and, in fact, a result) that is a corridor open from one side were thus considered to be predominantly outdoor measurements [24].

One of the most common relationships describing outdoor propagation is the Okumura model [23], in the following form:

$$P_L = lf + A_{mu}(f, d) - G_{(hte)} - G_{(hre)} - G_{area} \quad (3)$$

where  $P_L$  is the attenuation,  $lf$  is the free-space attenuation,  $A_{mu}(f, d)$  is the relative median attenuation outdoors (as a function of frequency and distance),  $G_{(hte)}$  is the transmitter gain,  $G_{(hre)}$  is the receiver gain,  $G_{area}$  is the amplification of the environment. The model is actually breaks down the attenuation into two parts: into an outdoor component and factors that modify the environment, and to the amplifying of the environment (which can even be attenuation).

An improved version of the Okumura model is the Hata model [22], which distinguishes the outdoor locations depending on built-in rate.

The COST-Hata model [23], (a further development of the Hata model) takes the following form:

$$P_L = 46.3 + 33.9 \cdot \log_{10}(f) - 13.82 \cdot \log_{10}(h_B) - a(h_R, f) + (4.9 - 6.55 \cdot \log_{10}(h_B)) \cdot \log_{10}(d) + C_m \quad (4)$$

where  $P_L$  is the median loss/attenuation,  $f$  is the frequency in MHz,  $h_B$  is the transmitting antenna effective height in meters,  $d$  is the distance in km,  $h_R$  is the effective height of the (mobile) receiving antenna in meters,  $C_m$  is the constant offset in dB.

The model distinguishes through the parameter  $a(h_R, f)$  whether the propagation is urban or suburban.

D. Indoor propagation models

Indoor propagation models are the most important for this paper, as our primary goal is to create an improved model describing indoor propagation. The main feature is that the receiver area surrounded by walls, that represent significant attenuation for the passing wave. In addition, they are located at relatively short distances for some antennas, the air composition does not change for a significant part of the time (or up to negligible extent), but moving people and living things can occur [18]-[20]. In general it can be said that most models were originally for lower frequency bands made. In recent years, they extended for higher frequency bands (such as ITU indoor propagation model), upon different considerations [16], [24], but few models are available for such high frequency ranges (mainly empirical).

Starting from the COST-Hata model, the TYM model [23] was created, which is already indoor applicable, the results are consistent with the measurements can be obtained for the 38 GHz band. The COST-Hata model served as a basic idea for constructing the TYM model. The studied model takes into account the effects of temperature and humidity based on the signal propagation properties:

$$P_L = 96.7 - 0.562 \cdot S_{win} - 0.3666 \cdot f + 0.092 \cdot d - 0.187 \cdot h + 0.257 \cdot t \quad (5)$$

where  $P_L$  is the loss,  $S_{win}$  is the window size (at a given level the average window size, which is expressed by the surface of the window),  $f$  is the frequency,  $d$  is the distance (in meters),  $h$  is humidity and  $t$  is the temperature.

The biggest flaw of the model, in terms of practical use, is that of windows the average surface area on a mobile endpoint is not measurable or only impermissibly large at the cost of effort.

The ITU's empirical formula for indoor signal propagation is as follows [24]:

$$L_{total} = L(d_0) + N(f) \cdot \log_{10}(d/d_0) + L_f(n) \quad (6)$$

where  $L(d_0)$  is the basic transmission loss at a reference distance  $d_0 = 1$  m,  $N$  is the distance based loss factor, distance  $d$  in meters with a minimum value of 1 meter,  $L_f$  "floor" transit loss factor in dB and  $n$  is the number of floors crossed. Based on the measurement results presented in Section 5 and the literature, in simple, managed cases, the ITU model gives an acceptable result. If this is not the case above, we can experience a deviation of the order of 50 dB. There is a high degree of similarity between the ITU and CI models (Equations (6) and (2), respectively) as it can be seen at the formula level. The ITU model can actually be considered an averaged CI model, which was expanded with slabs intersected by the signal path.

Because of all this, the conclusion is that the initial model is hereinafter the ITU indoor propagation model, as it is the simplest and has only such parameters, which can be easily measured by a well-equipped receiver.

IV. THE MEASUREMENT SETUP

Under the frame of ESA's (European Space Agency) technology transfer program the Alphasat communication experiment's ground receiver system's elements were applied in a terrestrial, indoor propagation measurement system, designed for the Q-band. BME-HVT in collaboration with Totaltel Telecom Techniques Ltd. [7] developed the Q-band downconverter unit for the experiment.

The receiver for the indoor measurement setup is originated from the Alphasat ground receiver station of the department. The transmitter and receiver are made up of two directional horn antennas assembled on a motorized tripod with rotating platform. The 360° horizontal rotating capability allows scanning the entire horizontal plane and recording of the received signal power parameters for a specific location as shown in Fig. 2. The local clock frequency was generated by an external PLL synthesizer board [7], operating at 9.35 GHz. A frequency quadrupling in the receiver/transmitter site results the Q-band carrier signal. The intermediate frequency (IF) signal is an unmodulated sine wave at 1.32 GHz, therefore the exact transmit frequency is  $4 \cdot \text{CLK} + \text{IF} = 38.72$  GHz. The fixed transmitter and the rotated receiver configuration allow measuring both Non-Line of Sight (NLOS) and Line of Sight (LOS) scenarios.

With a systematic relocation of the receiver, a signal strength map of the room can be provided by the angular dependency of the signal to be measured. In order to measure and process the received signal a Software Defined Radio (SDR) platform is utilized. The SDR-based data collection and the platform-controlling software was developed by other colleagues at the department as it was published in [7]. The data collection took place in a GNU radio environment. The measurement data were generated by rotating the receiver every five degrees, which were processed with MATLAB. Measurements were made in a total of five different rooms, but due to lack of space, only one of them is presented in this article.



Fig. 2. Receiver on motorized platform with horn antenna and downconverter

The SDR acquires the measurement of incoming and downconverted L-band signal. After digitization the whole signal processing will be performed by the controlling computer using the GNU Radio software platform [7].

Improved Model for Indoor Propagation Loss in the 5G FR2 Frequency Band

There is a computer responsible for controlling and managing the SDR. This is an essential issue, because during the measurement human interaction is minimized as much as possible, since the millimeter wave frequency band is sensitive to humans in the measurement area, and this significantly influences the result. The signal reflections and interferences in this band can considerably modify the propagation environment.

V. MEASUREMENT RESULTS

Each measurement was performed in the BME V1 building. The affected parts of the building, respectively in the rooms we were locked out of the citizens of the university at the time of the measurement, so that the environment does not change in any way. Persons performing the measurements are always as far away from the antennas as possible.

One of the measurement sites was room 103 of the V1 building, which is on the first floor of the five-storey building and our measurements and methods are presented here with through this location. Fig. 3. shows the floor plan of the room. The measurement points are designated by each x/y format point, a TX is the transmitting antenna. At the top of the figure we indicate the windows and some furniture are also shown. The second measurement site was a classroom on the fifth floor of the building, and it has two sides with entirely plastic framed windows.

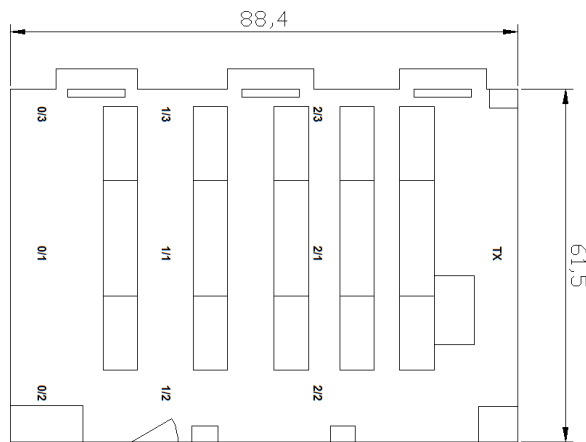


Fig. 3. Floor plan of room 103 in building V1 and the measurement points

Both the transmitter and receiver were located 1.5 meters high. On the moving platform, the receiver turned every 5 degrees, a positive detour direction, thus 73 measurement results were recorded at each position. The transmitter was always pointing toward the measured receiver location. As an example, Fig. 4. depicts a typical measurement where several reflections are observable besides the main lobe.

After analysing the results, the conclusions are the following:

- The received signal level is the function of distance, the angle of the antenna beams and the reflective surfaces around.
- At this frequency, the glass surfaces have a large angle of incidence they reflect.

- Even if the transmitter looks at the receiver, depending on the latter's direction there are usually two or three possible acceptable signal levels from reflected pathways.
- With a few degrees of rotation, the received signal level may decrease by 40-60 dB.
- The signal level (according to previous models) decrease by several dB on every few meters.

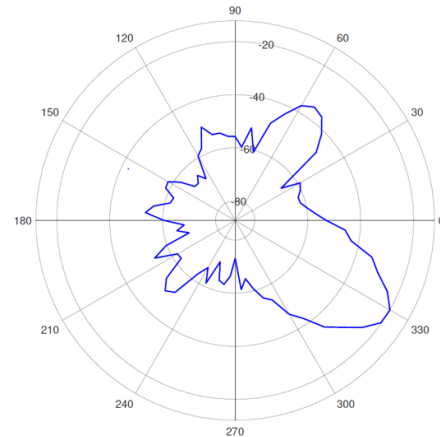


Fig. 4. A measurement result with high signal level reflected components

In Fig. 5. the measurement location is shown, where the transmitter is on the left side of the picture, while the receiver on the right side.



Fig. 5. Transmitter and receiver setups in the measurement location

Based on the results so far, it is appropriate to introduce a relative environment concept. By this is meant that the signal level that can be received at a given point depends on the distance and the reflection environment. For the latter, no matter how far there is a point from the transmitter, all that matters is the nature of the environment.

According to this the individual receiving points can be typified, which can be called relative environments, since ultimately, they specify the nature of the beamforming strategy required. The distance will only determine the maximum signal strength. With the concept thus created each acquisition point can be categorized as needed during the modelling.

VI. AN IMPROVED INDOOR PROPAGATION MODEL

To develop a new model, the main goal was to find the simplest solution that acceptably fits the measurement results and takes into account the physical factors influencing the spatial distribution. One of the possible alternatives the empirical expansion of the ITU indoor propagation model seemed to be the best choice. The following conditions can be formulated in advance:

- The measured values are considered correct, assuming only a small error.
- The main parameters should be the distance and the angle between the transmitter and receiver antenna directions.
- Work with as few parameters as possible.
- The parameters should be included in the simplest possible functional relationships.

On the basis of current measurement results and according to the literature [25], in NLoS situations (but more generally in all non-LoS cases) the attenuation behaves as if we were adding an additive term to the outdoor attenuation value. Of course, in reality, the process more complicated than this, however, in terms of empirical modelling, this approach is acceptable.

As a starting point, we used the ITU model for indoor propagation. The reason is that this model describes quite precisely the attenuation between the antennas directed at each other. The following model was found to be the most suitable for the previously stated goals in terms of use:

$$L_{total} = 63.76 + 20.3 \cdot \log_{10}(d) + F(x) + G(\alpha, \beta) + C \quad (7)$$

where  $d$  is the distance in meters,  $F$  is the relative environment as a function of attenuation and  $x$  is the relative environment in which it resides,  $G$  is the attenuation due to the directivity of the two antennas and constant  $C$  is the specification of the ITU recommendation constant.

The model formulated in this way leads to a regression calculation problem, where an algorithm using an iterative learning method can determine the coefficients.

The problem was solved by regression calculations. In doing so, LMS (Least-Mean-Square) error criterion was applied, using the instantaneous gradient method. Denote by  $F$  an error function whose global minimum we are looking for [26]-[27]:

$$\hat{F} = [t(k) - a(k)]^2 = e^2(k) \quad (8)$$

where  $k$  is the current iteration number,  $t$  is the target, i.e. the expected output, and  $a$  is the approximate value of the function in the given iteration. The error  $e$  is the difference between the expected and the calculated value. That is actually can be considered as supervised machine learning, where for specific input parameters the expected output is known. By the end of the process, the algorithm learns in the examined frequency band the coefficients of the empirical model. Using the stochastic gradient method (which converges the fastest to a minimum), the following result is obtained [27]:

$$\nabla \hat{F}(k) = \nabla e^2(k) \quad (9)$$

It can be deduced that in the case of LMS we get the

following form [26]:

$$\vec{W}(k + 1) = \vec{W}(k) + 2 \cdot \mu \cdot \vec{e}(k) \cdot \vec{p}(k) \quad (10)$$

where  $\vec{W}$  is the vector of the weights to be updated, constants of  $F$ ,  $G$ ,  $C$  members in Equation (7), and  $\vec{e}$  is the error vector, which in this case will be one-dimensional.  $\vec{p}$  is the input parameter vector, which in the model is a distance,  $\alpha$  is the localization, and  $\beta$  and constant  $l$  for the  $C$  term. The learning rate is less than 0.5 for this method in order to keep the method stable [26].

Here, in addition to the constants, we also have to talk about the function relationship with the input parameters. From the point of view of the implemented algorithm, it is important to mention the possibility of batch training. As the probability of occurrence of the parameters is equal, the run can be accelerated by combining the results of  $N$  iteration steps.

A. Parameter estimation

Another important factor in relation to each parameter is the type of functional relationship with the input parameters. Considering the angular relationship, we made an assumption that the transmitter is directed by an acceptable extent to the receiver, so the difference in angles is due to the fact that the receiver is not well oriented. Classic transmitting antennas (when the transmit antenna is wide-beam), this model is completely correct. In case the transmitter has some kind of MIMO layout (for which the 5G specification gives the possibility [2]) the problem goes beyond this simple model, so it cannot be used for it.

Considering the "classic" case, the main emphasis was on keeping the angle as small as possible close between the two antennas, the more accurate is the model, and yet the simplest functional relationship is existing for faster computation.

The conclusion is that we are looking for the connection in the form of  $D \cdot \sqrt{\beta}$  where  $D$  is the constant sought, closed by the angle  $\beta$  with the receiver, as they are typically root functions on those that are simple and have such properties.

Parameter  $C$  is to estimate the antenna beamwidth, also included in the ITU recommendation parameter and it can be refined, based on the measurement results.

B. The relative environmental coefficient

The relative environmental coefficient is the amount we introduced for how it could be to squeeze as much information about the environment into a constant and additionally it is possible to insert into the model and can be determined by measurement. We characterize the previously defined relative environment with a single coefficient at given moment and point. This constant will always be a function of the current direction of the transmitter.

The constant (denoted by  $RK$ ) can be approximated as the quotient of two integrals:

$$RK = \frac{\int_0^{2\pi} f(\phi, k) d\phi}{\int_0^{2\pi} g(\phi) d\phi} \quad (11)$$

where  $RK$  is the relative environmental coefficient,  $f(\phi, k)$  is

Improved Model for Indoor Propagation Loss in the 5G FR2 Frequency Band

the set of points above the level  $k$ , while  $g(\phi)$  are values for the entire range, as represented visually in Fig. 6. The result of the quotient is a number between 0 and 1.

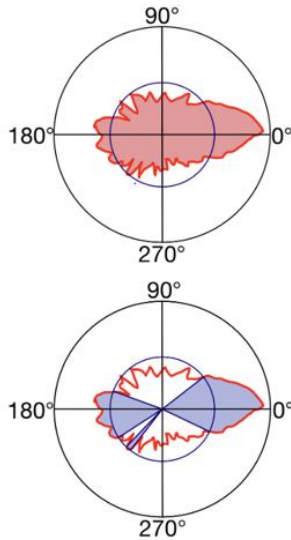


Fig. 6. Visual representation of Equation (11) for a general case. Top figure is the numerator, bottom figure is the denominator interpretation.

From a practical point of view, the choice of the coefficient  $k$  is critical. It can also be tied to a specific fixed signal level that expresses what is the minimum that it is necessary to achieve in order to measure, but it can also mean what the level is already important or confusing to us. To do this, we made the following consideration:

- If a dominant signal level exists, compute only those that are comparable to and even if there are several orders of magnitude smaller peaks, we neglect them.
- If there is no dominant signal level or there are several similar ones, avoid all of them into the calculation and all that is comparable to this.
- Unevenness of noise and error during measurement should not be included in the constant.

To solve this, a constant tied to the maximum signal level was obtained to best fit the problem. In terms of measurement, it is necessary to estimate the relative environmental coefficient from finite number of measurements. It is important that each measurement should always be made in a different direction, no two measurement locations should match, taking care to map the entire space as much as possible. Then let's get closer to integration with small  $d$  elements, which expresses that not at every point, but some (not necessarily equal) by closing small angles in each direction a measurements along a complete circle:

$$\widehat{RK} = \frac{\sum_{n=1}^N f(n, k) \cdot d\phi}{\sum_{n=1}^N g(n) \cdot d\phi} = \frac{\sum_{n=1}^N f(n, k)}{\sum_{n=1}^N g(n)} \approx \widehat{RK}_b = \frac{\sum_{n=1}^N t(n, k)}{\sum_{n=1}^N n} \quad (12)$$

where  $\widehat{RK}$  is the estimated coefficient and its approximated

value  $\widehat{RK}_b$  can be quickly calculated numerically,  $t(n, k)$  is a function above the corresponding signal level, which takes the following form (where  $t$  is a characteristic or indicator function,  $n$  is the measuring point):

$$t(n, k) = \begin{cases} 1, & \text{if } f(n) > k \\ 0, & \text{otherwise} \end{cases} \quad (13)$$

In determining the approximate value  $RK_n$  we used the assumption that a significant part of the calculated area will be above the specified  $k$  level, so we can simplify all of this in both the denominator and the numerator. According to experience, this is correct in practice and both solutions gives sufficiently accurate results.

Applying the numbers thus obtained to the room 103 of V1, we obtain Fig. 7. with which the model is perfectly functional and we get a result close to the measured value.

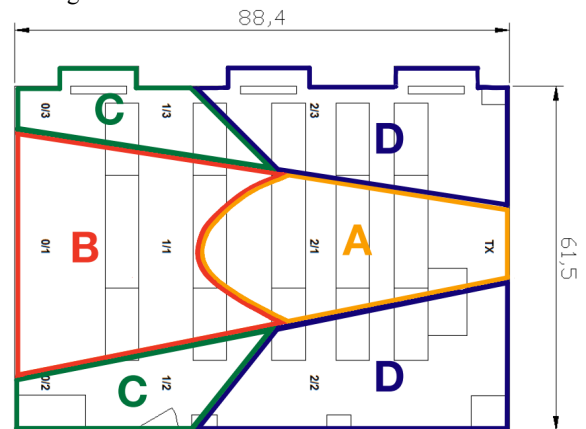


Fig. 7. Relative environmental coefficients in room 103, building V1

The model obtained by the procedure works well along the boundary conditions presented earlier. It can be used to calculate the maximum signal level that can be received at the individual points for known environment and the receiving antenna signal drop can be estimated resulted by the unalignment. On the other hand, with the estimated parameters required for the model is able to calculate the maximum value that belongs to the angle at which the beam of the transmitter and the receiver are directed to each other and are able to correct themselves based on this. The model is also functional in the inverse role of angles. As a result of the calculations, the new model takes the following form:

$$L_{total} = 63.76 + 20.3 \cdot \log_{10}(d) + 15 \cdot RK + 25 \cdot \sqrt{\beta} + C \quad (14)$$

where  $\beta=0$  radians is the direction in which the receiver is facing the transmitter directly with its beam and, by definition, may be  $\pi$  at most magnitude, its sign always being positive.  $C$  is the antenna beamwidth correction term.

Fig. 8. shows the difference expressed in [dB] between the measurement results and the individual models in room 103. For the ITU model, the deviation is between 0 and 40 dB (upper figure). For our model, the values are between -4.5 and 6 dB. Similar results were obtained for other measurements in different rooms.

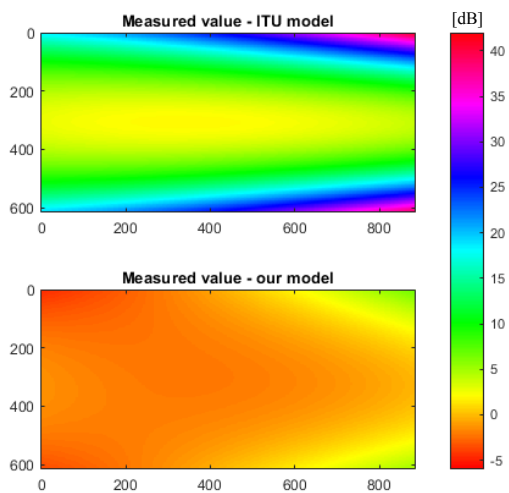


Fig. 8. The difference between the measured results and the values for both models in room 103, building V1

Thus, the average absolute error is calculated to be greatly reduced. The average absolute error during a given measurement is nearly 70% smaller (by more than 80% in some cases) comparing it by the ITU model.

The model created in this way is suitable to describe the propagation conditions of a real room. This way a large amount of data can be easily generated to train a machine learning algorithm to control the antenna beam direction, that is a desirable goal in 5G technology. However, the algorithm should be still improved since the initial model only describes simple, static problems. A future direction of this research is to implement these algorithms and prove their applicability in real environment.

VII. CONCLUSION

Possibilities and limitations of using higher frequencies in connection with 5G developments were known already before. Several reports can be found in the literature and measurement concluded that the antennas were directed at each other critical to a proper radio connection. However, the models available so far (which are relatively few) only describe cases where this condition is met. This is a main problem in the practical introduction of these higher (FR2) frequencies, since an unresolved issue on the FR2 bands is adaptive beamforming. In the course of this work, by processing the measurement results, we successfully prepared an angle-dependent model. This proves that a model for the frequencies in question can be created and based on this the beamforming control is feasible. The new model only includes parameters that by an average receiver can be measured. In addition, a more useful application option is that by using the model the results of Ray-Tracing procedures can be validated without measurements obtained. Artificial intelligence may already be sufficient for the resulting data set, which makes the problem much more solvable in real situations and makes the use of FR2 frequencies available to a wide range of users. As a further plan, it arises to refine the model and use the necessary one to create algorithms.

ACKNOWLEDGMENTS

The research reported in this paper and carried out at the Budapest University of Technology and Economics has been supported by the National Research Development and Innovation Fund based on the charter of bolster issued by the National Research Development and Innovation Office under the auspices of the Ministry for Innovation and Technology.

The authors also appreciate the support on SDR-based data collection system for Dr. Bálint Péter Horváth in the Digital and Optical Communications Systems Laboratory and the cooperation with Ericsson Hungary in this research field.

REFERENCES

- [1] R. E. Hattachi and J. Erfanian, "NGMN 5G White Paper," Final Deliverable, 5G Initiative Team, Feb. 2015.
- [2] ITU, "International Mobile Telecommunications-2020 (IMT-2020 Standard)," tech. rep., 2019.
- [3] T. Norp, "5G service requirements." <https://www.3gpp.org/news-events/3gpp-news/1831-sa1>, Accessed on 21.11.2020.
- [4] D. M. Pozar, "Microwave Engineering; Introduction to Microwave Systems." John Wiley & Sons, Inc., N.J., third ed., 2005.
- [5] ITU-R Recommendation V.431-8, "Nomenclature of the frequency and wavelength bands used in telecommunications." 08/2015.
- [6] T. S. Rappaport, S. Sun, R. Mayzus, H. Zhao, Y. Azar, K. Wang, G. N. Wong, J. K. S. Schulz, M. Samimi, and F. Guitierrez, "Millimeter Wave Mobile Communications for 5G cellular: It Will Work!," IEEE Access, vol. 1, 2013.
- [7] L. Csurgai-Horváth, B. Horváth, I. Rieger, J. Kertész, and B. Adjei-Frimpong, "Indoor Propagation Measurements for 5G Networks," 11th International Symposium on Communication Systems, Networks & Digital Signal Processing (CSNDSP), 2018. doi: 10.1109/CSNDSP.2018.8471761
- [8] Erik Dahlman, Stefan Parkvall, Johan Skold, "5G NR: The Next Generation Wireless Access Technology," Elsevier Ltd. 2018.
- [9] M. Säily et al., "5G Radio Access Network Architecture for Terrestrial Broadcast Services," in IEEE Transactions on Broadcasting, vol. 66, no. 2, pp. 404-415, June 2020, doi: 10.1109/TBC.2020.2985906.
- [10] Y. Wang, J. Li, L. Huang, Y. Jing, A. Georgakopoulos and P. Demestichas, "5G Mobile: Spectrum Broadening to Higher-Frequency Bands to Support High Data Rates," in IEEE Vehicular Technology Magazine, vol. 9, no. 3, pp. 39-46, Sept. 2014, doi: 10.1109/MVT.2014.2333694.
- [11] National Media and Infocommunications Authority (NMHH), "Documentation of the Auction Procedure Announced for Frequency Use Entitlements Related to Wireless Broadband Services Specially Supporting the Introduction of 5G," June, 2019.
- [12] F. W. Vook, E. Visotsky, T. A. Thomas and A. Ghosh, "Performance characteristics of 5G mmWave wireless-to-the-home," 2016 50th Asilomar Conference on Signals, Systems and Computers, Pacific Grove, CA, 2016, pp. 1181-1185, doi: 10.1109/ACSSC.2016.7869558.
- [13] F. Hossain, T. K. Geok, Tharek Abd Rahman, and M. N. Hindia, "Indoor Millimeter-Wave Propagation Prediction by measurement and Ray Tracing Simulation at 38 GHz," Symmetry, vol. 10, 2018.
- [14] H. Xu, T. S. Rappaport, R. J. Boyle, and J. H. Schaffner, "38-GHz Wide-Band Point to-Multipoint measurements Under Different Weather Conditions," IEEE COMMUNICATIONS LETTERS, vol. 4, p. 2, 2000.
- [15] G. Codispoti et al., "The propagation and telecom experiments of the Alphasat Aldo payload (TDP5 Q/V band experiment)," 6th European Conference on Antennas and Propagation (EuCAP), Prague, 2012, pp. 116-116, doi: 10.1109/EuCAP.2012.6206723.
- [16] ITU-R Recommendation P.1238-9, "Probability distributions relevant to radiowave propagation modelling," ITU, 2001.
- [17] H. T. Friis, "A Note on a Simple Transmission Formula," in Proceedings of the IRE, vol. 34, no. 5, pp. 254-256, May 1946, doi: 10.1109/JRPROC.1946.234568.

## Improved Model for Indoor Propagation Loss in the 5G FR2 Frequency Band

- [18] S. Sun, T. S. Rappaport, A. T. Timothy, G. Amitava, C. N. Huan, Z. I. Kovács, R. Ignacio, K. Ozge, and P. Andrzej, "Investigation of Prediction Accuracy, Sensitivity, and parameter Stability of Large-Scale Propagation Path loss Models for 5G Wireless Communications," *IEEE Transactions on Vehicular Technology*, vol. 65, pp. 1–18, May 2016.
- [19] S. Li, Y. Liu, L. Lin, X. Sun, S. Yang and D. Sun, "Millimeter-Wave Channel Simulation and Statistical Channel Model in the Cross-Corridor Environment at 28 GHz for 5G Wireless System," 2018 International Conference on Microwave and Millimeter Wave Technology (ICMMT), Chengdu, 2018, pp. 1-3, doi: 10.1109/ICMMT.2018.8563957.
- [20] Q. Faizan, M. H. S. Siddiqui, M. N. Hindia, and K. Dimiyati, "Propagation Channel Measurement at 38 GHz for 5G mm-wave communication Network," *IEEE 16th Student Conference on Research and Development (SCORED)*, 2018.
- [21] J. S. Seybold, "Introduction to RF propagation," Wiley, 2005.
- [22] T. S. Rappaport, "Wireless communications: principles and practice," Upper Saddle River, N.J.: Prentice Hall PTR, 2 ed., 2002.
- [23] Nossire, Z.; Gupta, N.; Almazaydeh, L.; Xiong, X. New Empirical Path Loss Model for 28 GHz and 38 GHz Millimeter Wave in Indoor Urban under Various Conditions. *Appl. Sci.* 2018, 8, 2122.
- [24] ITU-R Recommendation P.1238-10, "Propagation data and prediction methods for the planning of indoor radiocommunication systems and radio local area networks in the frequency range 300 MHz to 450 GHz," 2019.
- [25] T. S. Rappaport, E. Ben-Dor, J. N. Murdock, and Y. Qiao, "38 GHz and 60 GHz Angle-dependent Propagation for cellular & Peer-to-Peer Wireless Communications," *IEEE ICC 2012 - Wireless Communications Symposium*, 2012.
- [26] M. T. Hagan, H. B. Demuth, M. H. Beale, and O. D. Jesús, "Neural Network Design," M. Hagan, 2 ed. 2002.
- [27] K. P. Murphy, "Machine Learning: A Probabilistic Perspective," The MIT Press, 2012.



for 5G, and his first results in this field were presented on the EFOP-3.6.2 workshop in November, 2020.



**László Csurgai-Horváth** is employed as an Associate Professor at Budapest University of Technology and Economics (BME), Department of Broadband Infocommunications and Electromagnetic Theory. His current research interests are focused on indoor and outdoor propagation, measurements and modelling of the rain attenuation on terrestrial and satellite radio links, time series synthesis and cognitive spectrum management. He has been involved in several international projects such as SatNex, COST Action IC-0802 and QoS MOS. Recently, he has led some ESA-funded research projects relating to the Alphasat propagation and communications experiment and an ESA technology transfer demonstrator project for 5G indoor propagation measurements. Currently, he teaches space technology and channel modelling at BME in Budapest, Hungary.

# Exploring Embeddings for MIMO Channel Decoding on Quantum Annealers

Ádám Marosits<sup>1,2</sup>, Zsolt Tabi<sup>1,3</sup>, Zsófia Kallus<sup>1</sup>, Péter Vaderna<sup>1</sup>, István Gódor<sup>1</sup>, and Zoltán Zimborás<sup>4,2</sup>

**Abstract**—Quantum Annealing provides a heuristic method leveraging quantum mechanics for solving Quadratic Unconstrained Binary Optimization problems. Existing Quantum Annealing processing units are readily available via cloud platform access for a wide range of use cases. In particular, a novel device, the D-Wave Advantage has been recently released. In this paper, we study the applicability of Maximum Likelihood (ML) Channel Decoder problems for MIMO scenarios in centralized RAN. The main challenge for exact optimization of ML decoders with ever-increasing demand for higher data rates is the exponential increase of the solution space with problem sizes. Since current 5G solutions can only use approximate methodologies, Kim et al. [1] leveraged Quantum Annealing for large MIMO problems with phase shift keying and quadrature amplitude modulation scenarios. Here, we extend upon their work and present embedding limits for both more complex modulation and higher receiver / transmitter numbers using the Pegasus P16 topology of the D-Wave Advantage system.

**Index Terms**—Quantum Computing, Quantum Annealing, NP-hard optimization, Graph embedding, Telecommunication, Massive-MIMO

## I. INTRODUCTION

QUANTUM Computers use the unique information processing possibilities offered by quantum mechanics to solve complex problems [2], [3]. At the current level of technological maturity, universal large-scale Quantum Computers are still many years away. However, today's Noisy Intermediate-Scale Quantum (NISQ) devices already offer experimental platforms, and Quantum Annealers [4]–[6] play a prominent role, as they enable running optimization algorithms with few hundreds or even few thousands of qubits, although with considerable noise present in the system. In this paper, we study the embedding problem for topologies of state-of-the-art Quantum Annealers for the telecommunication problem of decoding wireless physical channel transmission by Large and Massive multiple input multiple output (MIMO) [7] antenna arrays.

Due to the ever-increasing demand for higher data rates, capacity and throughput, the application of MIMO antenna

arrays is indispensable to support multiple users near a wireless access point or base station at the same time [8]. As the number of antennas in MIMO setups increases, the complexity of encoding and decoding of signals requires an increasing computing power. [9]

The maximum likelihood (ML) MIMO decoding technique is – in theory – capable of high throughput, but is rarely used in practice as it requires exponential computing complexity in the number of antennas [10]. Kim et al. [1] examined the idea of quantum computation leveraged within the data center of a centralized radio access network (C-RAN) [11] in the hope of speeding up the computing and maintaining throughput by solving the decoding problem there. In such a solution, the ML decoding problem can be first formulated as a Quadratic Unconstrained Binary Optimization (QUBO) problem [12], [13], suitable for a QA processing unit. In the end, the results are mapped back to decoded bits.

Our goal was to extend upon the methodology in [1] and adapt it to set of modulation schemes most relevant for advanced telecommunication scenarios. The paper presents our extension of the known decoding problem to 64-QAM modulation by the maximum likelihood detection. Furthermore, we present a comparative analysis focusing on embedding efficiency using the topologies of both the D-Wave 2000Q Quantum Processing Unit (QPU) of 2000 qubits and the recently released D-Wave Advantage platform based on a 5000-qubit QPU [14].

In the next section, we give a brief overview of Quantum Annealing and the MIMO ML decoding and its formulation as a QUBO/Ising problem. In Sec. IV, we present our extension of this problem formulation for a higher-order modulation. Sec. V-A gives a description of the available D-Wave topologies and embedding methods, while in Sec. V-C the Theoretical limits of the mapping is explained and the largest embedded MIMO scenarios are presented. Finally, in Sec. VI we summarize our results and discuss further possibilities.

## II. THEORETICAL BACKGROUND

### A. Ising and QUBO models

In order to use the D-Wave Quantum Annealer, one needs to state the optimization problem as a standard QUBO or its equivalent Ising model. The Ising model describes physical systems of discrete spin variables, where each variable is either  $-1$  or  $1$ , i.e., the configuration space of dimension  $2^N$  is:

$$\Omega_N := \{-1, +1\}^{\times N} = \{(s_1, \dots, s_N) : s_k = \pm 1\}. \quad (1)$$

<sup>1</sup>Ericsson Research, Budapest, Hungary

<sup>2</sup>Budapest University of Technology and Economics, Budapest, Hungary

<sup>3</sup>Eötvös Loránd University, Budapest, Hungary

<sup>4</sup>Quantum Computing and Information Group, Wigner Research Centre for Physics, Budapest, Hungary

E-mail:{adam.marosits, zsolt.tabi, zsofia.kallus, peter.vaderna, istvan.godor}@ericsson.com; zimboras.zoltan@wigner.hu

The Ising spin glass model gives the energy function or Hamiltonian of a given spin configuration state  $\mathbf{s} \in \Omega_N$  of the system as follows:

$$H(\mathbf{s}) = -\frac{1}{2} \sum_{i,j=1}^N J_{ij} s_i s_j - \sum_{i=1}^N h_i s_i, \quad (2)$$

where  $h_i$  is the  $i$ th qubit's interaction with the external field (bias), and  $J_{ij}$  is the strength of the interaction between qubits  $i$  and  $j$  (coupling strength). If the system prefers the pair of spins to be aligned ( $s_i = s_j$ ) the interaction is called ferromagnetic coupling and, if the pair of spins to be anti-aligned ( $s_i = -s_j$ ) the interaction is called antiferromagnetic. To follow the notation of [1], we shall rewrite the optimization from Eq. 2 to the following form:

$$\begin{aligned} \hat{\mathbf{s}} &= \hat{s}_1, \dots, \hat{s}_N = \\ &= \arg \min_{\mathbf{s} \in \{(s_1, \dots, s_N)\}} \left( \frac{1}{2} \sum_{i,j=1}^N g_{ij} s_i s_j + \sum_{i=1}^N f_i s_i \right), \end{aligned} \quad (3)$$

where  $s_i \in \{-1, 1\}$  are the spin variables and  $f_i, g_{ij}$  contain the Ising model's coefficients corresponding to the biases and coupling strengths, respectively and  $\hat{\mathbf{s}}$  is a minimum energy Ising spin configuration vector.

Since the QUBO model has equivalent expressing power to the Ising model, we can easily convert back-and-forth between the two. The QUBO description of an optimization problem is stated as:

$$\hat{\mathbf{q}} = \hat{q}_1, \dots, \hat{q}_N = \arg \min_{\mathbf{q} \in \{(q_1, \dots, q_N)\}} \frac{1}{2} \sum_{i,j=1}^N Q_{ij} q_i q_j, \quad (4)$$

where  $q_i$  are binary decision variables,  $Q$  is a symmetric matrix of coefficients and  $\hat{\mathbf{q}}$  is the resulting bit string of the optimization.

Since  $q_i$  is binary, it has the property:  $q_i^2 = q_i$ , which can be very useful. With  $q_i = (s_i + 1)/2$ , one can convert between the two models effortlessly.

Finding the global minimum of a given Hamiltonian is an NP-hard task, i.e., for large problems it will take exponentially long time in the size of the problem to compute the exact solution on a classical computer.

Therefore, one often employs heuristic algorithms, such as Simulated Annealing (SA) [15] to produce approximate results for large problems in polynomial time.

### B. Quantum Annealing

QA is a heuristic method for finding a global minimum of an objective function using quantum mechanical evolution. QA is similar to Simulated Annealing in a sense that it randomly searches through the energy landscape of the optimization problem. However, unlike SA, QA does not use a temperature parameter to traverse the energy landscape, instead it slowly tunes the parameters of an Ising model Hamiltonian with transverse field that governs the quantum mechanical evolution of the system. The system starts from a superposition of all possible computational basis states with equal amplitudes,

all possible computational basis states with equal amplitudes, which is the ground state of the purely transverse field Hamiltonian. During the time-evolution the system approximately continues to be in the lowest energy state of the transverse-field Ising model with coupling strengths varying in time. As the coupling strength of the transverse field is approaching zero, the system evolves into the ground state of the original problem Ising Hamiltonian [16].

D-Wave's Quantum Annealer is a superconducting QPU that realizes the Ising spin system in a transverse field. Its qubits and couplers are individually controllable via digital-to-analog converters and have time-dependent control in order to implement the transverse-field Ising Hamiltonian [17]. The qubits of a D-Wave QPU are superconducting flux qubits, where the states are determined by whether the current is flowing clockwise or counterclockwise, or in the superposition of these. The interconnection between the qubits are called *couplers* and have less control circuits than the qubits. Their control represent the coupling strength ( $J_{ij}$  of Eq. 2). As the system is susceptible to noise (e.g., cross-talk, environment), the results produced by the QPU might not always represent the solution to the original problem. Furthermore, since the QPU is an analog device with limited precision, some problems might not be presentable at all. In the D-Wave QPU, the physical lattice of qubits and couplers has a limited connectivity and can be described special graph structures called *Chimera* and *Pegasus*. These architectures will be described in more detail in Sec. V-A.

## III. MIMO DECODING AS A QUBO PROBLEM

### A. Maximum Likelihood Detection for MIMO Decoding

In a multiple user MIMO (MU-MIMO) system there are multiple antennas that can simultaneously transmit to multiple recipients and vice-versa. The transmission goes through the channel matrix of  $N_t \times N_r$  in case of  $N_t$  transmit and  $N_r$  receive antennas. The receiver then has to decode the vector of complex receive symbols ( $\mathbf{y} \in \mathbb{C}^{N_r}$ ) to restore the originally transmitted bits. Such a MIMO system can be modelled as:  $\mathbf{y} = \mathbf{H}\mathbf{x} + \mathbf{n}$ , where the vector of complex transmit symbols  $\mathbf{x} \in \mathbb{C}^{N_t}$  is affected by the complex channel matrix  $\mathbf{H} \in \mathbb{C}^{N_r \times N_t}$  and the additive Gaussian white noise  $\mathbf{n} \in \mathbb{C}^{N_r}$ . In this text, we refer to such a system as a MIMO setup (or scenario) of  $N_t \times N_r$ .

Other than spatial multiplexing, digital modulation is also present in these communication scenarios. [18] This means that each symbol can represent multiple bits (dependent on the modulation scheme), where the bit-to-symbol mapping is usually given by the *constellation* ( $\mathcal{O}$ ).

The MIMO ML decoding [19] is a search in a space of  $|\mathcal{O}|^{N_t}$  for some symbol vector  $\hat{\mathbf{v}}$  that minimizes the symbol errors, with variable  $\mathbf{v}$  representing all the possible vector of transmitted symbols:

$$\hat{\mathbf{v}} = \arg \min_{\mathbf{v} \in \mathcal{O}^{N_t}} \|\mathbf{y} - \mathbf{H}\mathbf{v}\|^2. \quad (5)$$

The result is the decoded symbol vector  $\hat{\mathbf{v}}$ , which is mapped to the decoded bit-string  $\hat{\mathbf{b}}$  according to the used constellation.

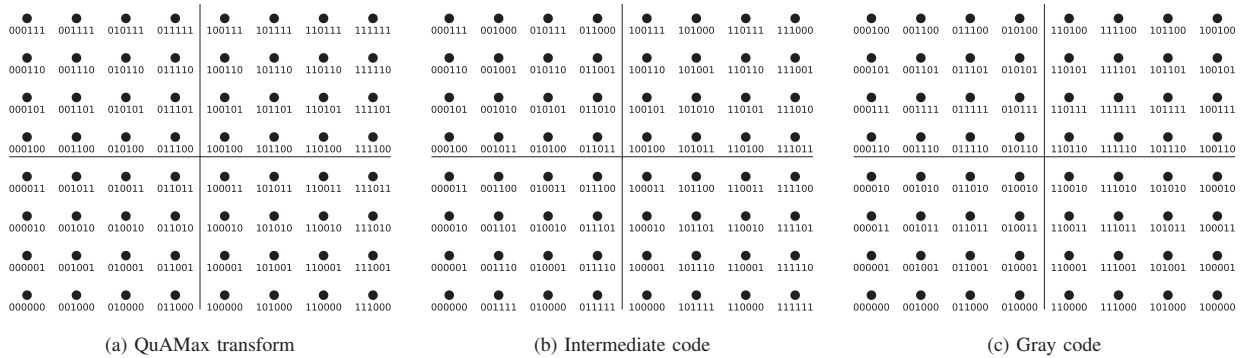


Fig. 1. The process of converting the *QuAMax* encoded bits to the original Gray-coded transmission with 64-QAM. The QuAMax constellation (1a) encodes non-Gray-coded bit-strings in order to retain linear QUBO translation, but the transmission is done using the Gray code constellation (1c), causing disparity. By using the Intermediate code’s (1b) constellation, we can easily convert back to the original sent data on the output of the minimization procedure (the QuAMax code).

The idea of ML decoding is to maximize throughput via minimizing the bit error rate, however, classical algorithms (such *Sphere Decoding* [20]) can hit a computational wall quickly as the complexity grows exponentially with the number of transmitters [21]. For this reason, practical (polynomial-time) MIMO decoding algorithms (like *Zero Forcing* [22]) often settle for sub-optimal solutions that are easier to obtain.

Kim et al. [1] show in their work how QA can speed up solution of ML MIMO decoding. We derive the explicit QUBO formulation for 64-QAM and present a study of embedding capacity of two currently available D-Wave QPUs of different size and topology. Through this experimental study, we uncover the limiting problem sizes that can be implemented on real-world Quantum Annealers for Massive-MIMO problems. In this study we also highlighted the efficiency of the embedding methods via length statistics of chains representing logical qubits – a crucial factor in annealing performance in non-fully connected Quantum Annealer topologies. For this we also use the non-trivial QUBO expansion of Eq. 5. Furthermore, we implement enhanced embedding algorithms to further improve the found limiting problem sizes of each scenarios. In this work we extend on the symmetric problem statement of [1], where  $N_t = N_r$  corresponding to the state-of-the-art commercially available Massive MIMO equipment [23].

However, the methodology can easily be applied to  $N_t \neq N_r$  scenarios. In these cases, the number of QUBO variables always equals to  $N_t$ , therefore the embedding of any  $N_t \times N_r$  MIMO ML decoding corresponds to the structure of  $N_t \times N_t$ .

**B. Overview of Ising Formulation of the ML MIMO Decoding**

In order to use a D-Wave QPU for solving MIMO ML decoding, we should formulate the QUBO formula of the optimization problem. Some basic modulation techniques are already investigated by Kim. et al. [1], these will be briefly described in the following subsections. Following that, we provide an extension of the ML to QUBO conversion (*QuAMax transform*) for the 64-QAM modulation.

In general, the QuAMax has a qubit requirement of  $N_t \log_2 M$  for a symmetric  $N_t \times N_r$  MIMO setup and a constellation of size  $M$ . One can arrive at the QUBO coefficients

by substituting the QuAMax-transformed  $v_i$  symbols to their respective equations with QUBO variables. The exact formulas to get the QUBO coefficients are described in [1].

1) *BPSK*: In the case of Binary Phase Shift Keying modulation, each symbol consists of one bit. There is a 180° phase-shifting between two possible states. The BPSK is the easiest modulation technique to convert into the QUBO form, since each symbol  $v_i \in \{-1, 1\}$  can be mapped to  $2q_i - 1$ , where  $q_i$  is the  $i$ th QUBO variable.

2) *QPSK*: The Quadrature Phase Shift Keying modulation transmits two bits as one symbol and the phase shifting between possible states is 90°. In case of QPSK, each symbol is a complex number number:  $v_i = v_i^I + jv_i^Q$ , and  $v_i \in \{\pm 1 \pm 1j\}$ , therefore we need 2 qubits to encode a single symbol:  $v_i = (2q_{2i-1} - 1) + j(2q_{2i} - 1)$ .

3) *16-QAM*: 16-QAM is a Quadrature Amplitude Modulation with  $|\mathcal{O}| = 16$ , that can transmit 4 bits per symbol. As both dimensions can have 4 possible values ( $v_i^I, v_i^Q \in \{\pm 1, \pm 3\}$ ), we need 2 qubits per dimension to describe each symbol. Since we want a linear transformation, the mapping:  $v_i = (4q_{4i-3} + 2q_{4i-2} - 3) + j(4q_{4i-1} + 2q_{4i} - 3)$  seems like a good choice.

However, since in wireless communication we often use Gray code<sup>1</sup> as a mean to avoid bit errors, we need to consider a mapping that takes this into account.

Nevertheless, as pointed out by Kim et al. [1], the mapping of a Gray-coded constellation to the QUBO form will always incorporate higher-order terms, that are not allowed in our Ising model. For this, following [1], we can retain a linear QuAMax transform with a non-Gray-coded bit encoding and use a post-processing technique to regain the original bits. We will elaborate on this technique in Sec. IV.

**IV. EXTENSION TO THE 64-QAM MODULATION**

Here we present the method for extension of the QUBO formulation of [1] to the 64-QAM case. 64-QAM is an amplitude modulation that can transmit 6 bits per symbol (Fig. 1a).

<sup>1</sup>Gray code is an encoding technique where each subsequent symbol is encoded by a bit pattern that only differs in one bit in order to make error correction more robust.

## Exploring Embeddings for MIMO Channel Decoding on Quantum Annealers

 TABLE I  
 QUBIT REQUIREMENTS OF DIFFERENT ML ENCODED MIMO CONFIGURATIONS.

| Config.   | BPKS | QPSK | 16-QAM | 64-QAM |
|-----------|------|------|--------|--------|
| 10 × 10   | 10   | 20   | 40     | 60     |
| 20 × 20   | 20   | 40   | 80     | 120    |
| 30 × 30   | 30   | 60   | 120    | 180    |
| 40 × 40   | 40   | 80   | 160    | 240    |
| 60 × 60   | 60   | 120  | 240    | 360    |
| 80 × 80   | 80   | 160  | 320    | 480    |
| 100 × 100 | 100  | 200  | 400    | 600    |
| 120 × 120 | 120  | 240  | 480    | 720    |
| 140 × 140 | 140  | 280  | 560    | 840    |
| 160 × 160 | 160  | 320  | 640    | 960    |
| 180 × 180 | 180  | 360  | 720    | 1080   |

Following [1], in order for the QUBO form to remain linear, we use Gray coding for the transmitted symbols and interpret the result according to the QuAMax transform constellation. The QA process solves for the QuAMax constellation which then needs to be mapped back to the Gray code to recover the original message.

In our extended formula, to accommodate both dimensions ( $v_i^I, v_i^Q \in \{\pm 1, \pm 3, \pm 5, \pm 7\}$ ), we need 6 qubits (3 per dimension) and so we chose the suitable linear transformation:

$$v_i = (8q_{6i-5} + 4q_{6i-4} + 2q_{6i-3} - 7) + j(8q_{6i-2} + 4q_{6i-1} + 2q_{6i} - 7). \quad (6)$$

From this, we get the conversion formulae to the Ising energy function values by expanding Eq. 5. The complete description is given in Ref. [24]. The constellations used to map of symbols from QuAMax to the Intermediate code and finally to Gray code is illustrated in Fig. 1.

## V. PROBLEM EMBEDDING ONTO D-WAVE QPUS

## A. D-Wave architectures

D-Wave currently has two types of publicly available QPUs. The older model is the D-Wave 2000Q, with up to 2048 physical qubits in a Chimera topology. The newer model is the D-Wave Advantage, with up to 5640 physical qubits in a Pegasus topology. The Chimera  $C_{16}$  topology has  $K_{4,4}$  graphs in a  $16 \times 16$  lattice for which the sub-graph is shown in Fig. 2a. The recently released D-Wave Advantage QPU has a Pegasus  $P_{16}$  topology, which is more connected than the  $C_{16}$  since it has degree 15 (each qubit is connected to 15 other qubits via couplers), while the older model has degree 6.

## B. Embedding methods

In the D-Wave programming model the linear and quadratic coefficients of the QUBO problem can be mapped to qubits and the connections of qubits, respectively. The direct mapping is rarely possible, since the QPU has a sparse graph topology, therefore we need to use embedding methods transforming

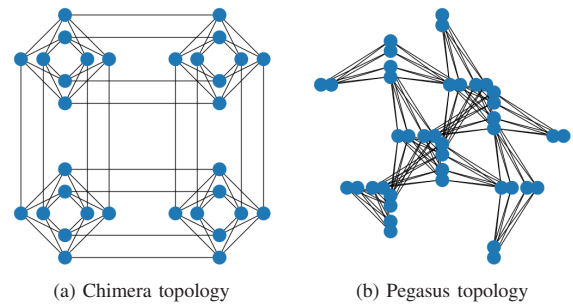


Fig. 2. Unit cells and their connections of currently available D-Wave hardware topology. The older QPU (D-Wave 2000Q) uses a less connected Chimera  $C_{16}$  architecture (2a) with degree 6, while the new Advantage System uses the denser Pegasus  $P_{16}$  architecture with degree of 15 (2b). Here, only  $C_2$  and a  $P_2$  graphs are depicted; the complete working graphs have around 2000 and 5000 qubits, respectively (some qubits are disabled due to manufacturing imperfection).

logical qubits to a chain of connected physical qubits [25]. The standard D-Wave MinorMiner (*MM*) embedding algorithm [26] works by searching loops in a set of logical qubits and interactions and mapping these qubits to the physical topology creating physical qubit chains (see Fig. 3).

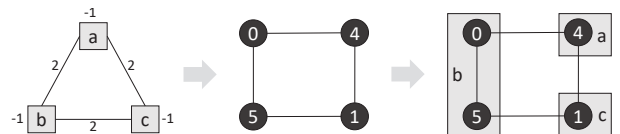


Fig. 3. The MinorMiner embedding method, source: [27]. A heuristic process which tries to find the best way to map source graph to the structure of the target graph. In case of D-Wave Quantum Annealers, we need to map QUBO problems (with up  $K_n$  structure) to either a Chimera graph or a Pegasus graph, both of which have limited connectivity.

The D-Wave open-source SDK [28] implements this algorithm for both Chimera and Pegasus architectures. Since embedding can have a direct effect on the quality of the solution of the annealing, finding close to optimal embedding is a crucial part of the problem solving. One measure of embedding quality is the chain lengths of physical qubits that represent a single logical QUBO variable. The shorter the chains, the closer the solution of the embedded problem to the original one, since current architectures are noisy and have imperfect qubits. Hence, in our experiments, we used improved embedding methods.

The Clique-Based MinorMiner (*CLMM*) and the Spring-Based MinorMiner (*SPMM*) embeddings, presented in [29], improve upon embeddings by providing heuristic initial chains to start the search from. We have experimented with these techniques to extend the maximal problem sizes that could be embedded into the hardware graph. SPMM uses a standard graph layout of the QUBO variables matched to the physical qubits on the same plane as initial chains, while CLMM constructs a native clique embedding with uniform chains as a starting point. Both algorithms pass the resulting initial chains to MM to find the final embedding.

C. MIMO ML decoding embedding onto the Chimera C-16 and Pegasus P-16 Architectures

To establish a baseline on what problem sizes map easily to the QPU, we used the native clique embedding for Chimera and Pegasus topologies [30] implemented in the D-Wave Ocean SDK. For the Chimera  $C_{16}$ , the largest native clique is  $K_{64}$ , while for the Pegasus  $P_{16}$ , that is  $K_{180}$ .

The QUBO equation of an  $N$ -QAM  $N_t \times N_r$  MIMO ML setup is (almost) equivalent to a  $K_{N_t \log_2 N}$  clique [1]. We summarize our results of the exact embedding requirements of the extended set of MIMO optimization problems showing the level of superiority of the  $P_{16}$  topology in Table I. For different ML encoded MIMO configurations (with native clique embedding) the green cells indicate feasible mapping to both QPU architectures, yellow cells are infeasible on  $C_{16}$  and red cells indicate non-feasibility on both the 2000Q and the Advantage system. Using the new, more connected architecture, the physical qubit requirement decreases significantly for each problem size, making possible the embedding of larger scenarios.

D. Enhanced embedding via heuristic algorithms

To extend the baseline limits, we now discuss the possibilities using D-Wave’s heuristic algorithm and its extensions. We were able to supersede the native clique embedding by using the CLMM algorithm. According to our results for extension of base MM for complete graphs, CLMM yields embeddings of larger MIMO setups with fewer physical qubit requirements in most of the problem sizes. We find SPMM method to be inferior in case of the clique embeddings. These limits exceed the ones published in [1] on the Chimera  $C_{16}$  architecture.

TABLE II  
UPPER LIMITS OF QUBO-FORM ML MIMO DECODING PROBLEMS MAPPING ONTO THE CHIMERA  $C_{16}$  AND PEGASUS  $P_{16}$  ARCHITECTURES.

| Arch     | Method | BPSK             | QPSK           | 16-QAM         | 64-QAM         |
|----------|--------|------------------|----------------|----------------|----------------|
| $C_{16}$ | CLIQUE | $64 \times 64$   | $32 \times 32$ | $16 \times 16$ | $10 \times 10$ |
|          | CLMM   | $65 \times 65$   | $33 \times 33$ | $16 \times 16$ | $11 \times 11$ |
| $P_{16}$ | CLIQUE | $180 \times 180$ | $90 \times 90$ | $45 \times 45$ | $30 \times 30$ |
|          | CLMM   | $182 \times 182$ | $91 \times 91$ | $45 \times 45$ | $30 \times 30$ |

Furthermore, using the new Pegasus  $P_{16}$  topology, we could more than double the number of users for each modulation and still embed the problem. This is of course, due to the new QPU architecture being larger (in qubit count) and more connected.

We highlighted the performance comparison of all embedding methods in case of the 64-QAM modulation in Fig. 4, testing all embeddable  $2^n \times 2^n$  MIMO scenarios. As mentioned earlier the CLMM algorithm had the best performance, with less number of physical qubit requirement for each problem size.

Table II summarizes the found theoretical and heuristic limits for the largest MIMO scenarios for each modulation comparing the baseline (native clique embedding) to the best-performing heuristic algorithm (CLMM).

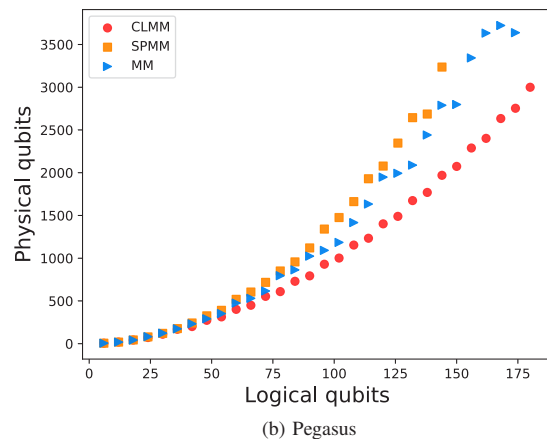
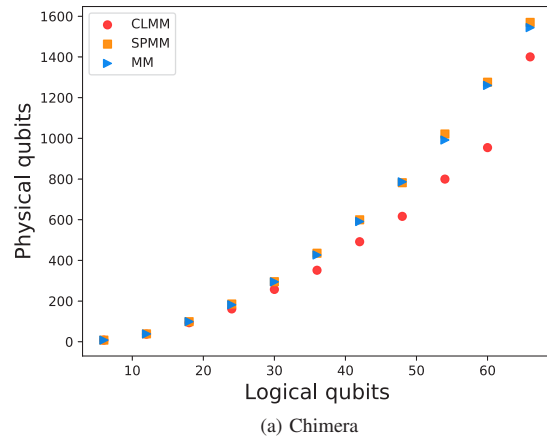


Fig. 4. Logical and physical qubits requirements of the embedding of the QUBO-formulated 64-QAM ML MIMO decoding problem with clique based minor miner for Chimera  $C_{16}$  (4a) and Pegasus  $P_{16}$  (4b) architectures. The number of logical qubits correspond to  $6N$ ,  $2 \leq N \leq N_{max}$ , where  $N$  is number of transmitters (and receivers) in the MIMO setup and  $N_{max}$  is the largest MIMO scenario that the given QPU can handle (11 and 30 for  $C_{16}$  and  $P_{16}$ , respectively).

VI. CONCLUSIONS AND OUTLOOK

In this paper, we presented the extension of the MIMO ML decoding as QUBO problem to the 64-QAM modulation scheme. By creating the required constellation diagrams, we showed that one can use a linear QuAMax formulation and still employ Gray code to reduce the number of bit errors during transmission.

Furthermore, we extended the range of embedding of MIMO ML decoding problems in both the dimension of modulation complexity and transmitter number. We used the Pegasus  $P_{16}$  architecture of the new D-Wave Advantage system to show the limits of each modulation scheme on a state-of-the-art QPU. Additionally, we explored heuristic embedding methods (such as MM, SPMM, CLMM) to further improve the range of MIMO setups that could benefit from quantum speedup. As a result, we were able to double the embeddable problem sizes compared to the earlier work.

Exploring Embeddings for MIMO Channel Decoding on Quantum Annealers

The currently available commercial Massive-MIMO solutions [23] have already reached the point of being able to decode transmissions beyond 64-QAM modulation in  $64 \times 64$ -MIMO setups. However, the potential advantage of QA lies in the problem sizes that are prohibitive for classical computers. Since the new Pegasus architecture shows promising scalability improvements regarding maximal problem size, we believe that future QPUs will stand as viable alternative to these classical solutions.

We believe that these result could further be improved by using manual embedding. We leave the study of this possibility to future work.

For next steps, we would like to study the performance of the D-Wave Advantage system on the ML decoding problems. Furthermore, since the 64-QAM case has never been tested before on any QPU, we see potential in testing it on both the D-Wave 2000Q and Advantage systems.

ACKNOWLEDGMENT

Zsolt Tabi and Zoltán Zimborás would like to thank the support of the Hungarian Quantum Technology National Excellence Program (Project No. 2017-1.2.1-NKP-2017-00001), and acknowledge also support from the Hungarian National Research, Development and Innovation Office (NKFIH) within the Quantum Information National Laboratory of Hungary and through Grants No. FK 135220, K124176, KH129601.

REFERENCES

[1] M. Kim, D. Venturilli, and K. Jamieson, "Leveraging quantum annealing for large MIMO processing in centralized radio access networks," in *Proceedings of the ACM Special Interest Group on Data Communication*, 2019, pp. 241–255.

[2] M. A. Nielsen and I. L. Chuang, *Quantum Computation and Quantum Information*. Cambridge University Press, 2000.

[3] S. E. Gaily and S. Imre, "Quantum optimization of resource distribution management for multi-task, multi-subtasks," *Infocommunications Journal*, vol. XI, no. 4, pp. 47–53, December 2019. doi: 10.36244/ICJ.2019.4.7

[4] T. Kadowaki and H. Nishimori, "Quantum annealing in the transverse Ising model," *Physical Review E*, vol. 58, no. 5, p. 5355, 1998. doi: 10.1103/PhysRevE.58.5355

[5] E. Farhi, J. Goldstone, and S. Gutmann, "Quantum adiabatic evolution algorithms versus simulated annealing," *preprint arxiv:quantph/0201031*, 2002.

[6] M. W. Johnson et al., "Quantum annealing with manufactured spins," *Nature*, vol. 473, no. 7346, pp. 194–198, 2011. doi: 10.1038/nature10012

[7] E. Dahlman, S. Parkvall, and J. Sköld, "Chapter 24 - new 5G radioaccess technology," in *4G LTE-Advanced Pro and The Road to 5G (Third Edition)*, 3rd ed., E. Dahlman, S. Parkvall, and J. Sköld, Eds. Academic Press, 2016, pp. 547–573. ISBN 978-0-12-804575-6

[8] G. Fodor, L. Pap, and M. Telek, "Recent advances in acquiring channel state information in cellular mimo systems," *Infocommunications Journal*, vol. XI, no. 3, pp. 2–12, September 2019. doi: 10.36244/ICJ.2019.3.2

[9] E. G. Larsson, O. Edfors, F. Tufvesson, and T. L. Marzetta, "Massive MIMO for next generation wireless systems," *IEEE communications magazine*, vol. 52, no. 2, pp. 186–195, 2014. doi: 10.1109/MCOM.2014.6736761

[10] B. Trotobas, A. Nafkha, and Y. Loüet, "A review to massive MIMO detection algorithms: Theory and implementation," in *Advanced Radio Frequency Antennas for Modern Communication and Medical Systems*. IntechOpen, 2020.

[11] K. Chen, "C-RAN: The road towards green RAN," China Mobile Research Institute, Beijing, China, China Mobile Research Institute, Tech. Rep., Oct 2011.

[12] A. Lucas, "Ising formulations of many NP problems," *Frontiers in Physics*, vol. 2, p. 5, 2014.

[13] F. Glover, G. Kochenberger, and Y. Du, "A tutorial on formulating and using QUBO models," *preprint arXiv:1811.11538*, 2018.

[14] K. Boothby, P. Bunyk, J. Raymond, and A. Roy, "Next-generation topology of D-Wave quantum processors," *arXiv preprint arXiv:2003.00133*, 2020.

[15] M. Pincus, "Letter to the editor monte carlo method for the approximate solution of certain types of constrained optimization problems," *Operations research*, vol. 18, no. 6, pp. 1225–1228, 1970. doi: 10.1287/opre.18.6.1225

[16] C. C. McGeoch, "Adiabatic quantum computation and quantum annealing: Theory and practice," *Synthesis Lectures on Quantum Computing*, vol. 5, no. 2, pp. 1–93, 2014.

[17] D-Wave, "Technical description of the D-Wave quantum processing unit, user manual," [https://docs.dwavesys.com/docs/latest/doc\\_qpu.html](https://docs.dwavesys.com/docs/latest/doc_qpu.html), 2021.

[18] P. Botsinis, S. X. Ng, and L. Hanzo, "Low-complexity iterative quantum multi-user detection in SDMA systems," in *2014 IEEE International Conference on Communications (ICC)*. IEEE, 2014. pp. 5592–5597 doi: 10.1109/ACCESS.2014.2322013.

[19] M. O. Damen, H. El Gamal, and G. Caire, "On maximum-likelihood detection and the search for the closest lattice point," *IEEE Transactions on information theory*, vol. 49, no. 10, pp. 2389–2402, 2003. doi: 10.1109/TIT.2003.817444

[20] A. Burg, M. Borgmann, M. Wenk, M. Zellweger, W. Fichtner, and H. Bolcskei, "VLSI implementation of MIMO detection using the sphere decoding algorithm," *IEEE Journal of solid-state circuits*, vol. 40, no. 7, pp. 1566–1577, 2005. doi: 10.1109/JSSC.2005.847505

[21] B. Hassibi and H. Vikalo, "On the sphere-decoding algorithm I. expected complexity," *IEEE transactions on signal processing*, vol. 53, no. 8, pp. 2806–2818, 2005. doi: 10.1109/TSP.2005.850352

[22] Q. H. Spencer, A. L. Swindlehurst, and M. Haardt, "Zero-forcing methods for downlink spatial multiplexing in multiuser MIMO channels," *IEEE transactions on signal processing*, vol. 52, no. 2, pp. 461–471, 2004. doi: 10.1109/TSP.2003.821107

[23] "Advanced antenna systems for 5G networks," Ericsson, Tech. Rep., November 2018. [Online]. Available: "https://www.ericsson.com/4a8a87/assets/local/reports-papers/white-papers/10201407\_wp\_advanced\_antenna\_system\_nov18\_181115.pdf"

[24] Z. Tabi et al., "Evaluation of quantum annealer performance for massive MIMO channel decoding problem," *to be published*, 2021.

[25] L. Lovász, "Graph minor theory," *Bulletin of the American Mathematical Society*, vol. 43, no. 1, pp. 75–86, 2006. doi: 10.1090/S0273-0979-05-01088-8

[26] J. Cai, W. G. Macready, and A. Roy, "A practical heuristic for finding graph minors," *arXiv preprint arXiv:1406.2741*, 2014.

[27] "Minor-embedding a problem onto the QPU," [https://docs.dwavesys.com/docs/latest/c\\_gs\\_7.html](https://docs.dwavesys.com/docs/latest/c_gs_7.html), accessed: 2020-01-30.

[28] "D-Wave ocean software documentation," <https://docs.ocean.dwavesys.com/en/stable/>, accessed: 2020-01-30.

[29] S. Zbinden, A. Bärttschi, H. Djidjev, and S. Eidenbenz, "Embedding algorithms for quantum annealers with chimera and pegasus connection topologies," in *International Conference on High Performance Computing*. Springer, 2020. pp. 187–206. doi: 10.1007/978-3-030-50743-5\_10

[30] T. Boothby, A. D. King, and A. Roy, "Fast clique minor generation in chimera qubit connectivity graphs," *Quantum Information Processing*, vol. 15, no. 1, pp. 495–508, 2016. doi: 10.1007/s11128-015-1150-6



**Ádám Marosits** received his BSc degree in electrical engineering from the Budapest University of Technology and Economics (BME), Budapest, Hungary, and he is currently a MSc student in electrical engineering. Ádám works as a student researcher at Ericsson Research. His research interests include optimization with quantum annealing, furthermore quantum communication and quantum random number generation.



**Zsolt I. Tabi** was born in Budapest, Hungary in 1990. He received the BSc and MSc degrees in computer science from Eötvös Loránd University, Budapest, Hungary in 2016 and 2018, respectively. He is currently pursuing the Ph.D. degree in computer science at Eötvös Loránd University.

From 2016 to 2020, he was a Developer on the MINI-LINK project with Ericsson Hungary. Since 2020 he is working with the Ericsson Research Team as part of the ETH Quantum Project. He is teaching programming languages at Eötvös Loránd University. His research interests include programming language design and adiabatic quantum computing.



**Zsófia Kallus**, PhD works as a master researcher at Ericsson Research, Traffic Analysis and Network Performance Laboratory in Hungary. She holds a PhD degree in Physics from the Doctoral School of Physics of Eötvös Loránd University, Budapest.

She studied open quantum systems and the structure and dynamics of large-scale real-world networks. She joined ER in 2014. Currently, she is focused on emerging quantum technologies, quantum computing applications and explainable machine learning solutions for optimization and automation of highperformance telecommunication systems. She is also interested in sustainability and urban sciences.



**Péter Vaderna** works as a master researcher at Ericsson Research, Traffic Analysis and Network Performance Laboratory in Budapest. He received his Ph.D. in physics from the Department of Physics of Complex Systems at Eötvös Loránd University, Budapest in 2008, in the area of traffic modeling in communication networks. Currently, he focuses on AI in network analytics, network management and network automation. His research interests also include emerging technologies that can potentially be involved

in various business areas of telecommunication such as quantum AI, camera based positional tracking and AR/VR.



**Dr. István Gódor** (M'01–SM'20) is a research leader at Ericsson Research, Traffic Analysis and Network Performance Laboratory of Ericsson Hungary. He is a senior member of IEEE and a member of public body of the Hungarian Academy of Sciences (MTA). He holds a Ph.D. from Budapest University of Technology and Economics. He was awarded the 2014 IEEE Communications Society Fred W. Ellersick Prize. His research interests include network design, traffic analysis and modeling, self-organizing networks, energy efficiency, collective sensing and industrial IoT & smart manufacturing.



**Zoltán Zimborás** is the head of the Quantum Computing and Information Group at the Wigner Research Centre for Physics (Budapest). He obtained his PhD at the Eötvös Loránd University in Budapest and worked later at ISI Torino, University College London, and Freie Universität Berlin before returning to Hungary. He is member of several editorial boards and is also a board member of QWorld, a nonprofit organization that aims to develop open-source software for quantum programming at all levels. His research interests include Quantum Computing, Quantum Control and Quantum Statistical Physics.

# Processing and Visualizing the Low Earth Orbit Radio Frequency Spectrum Measurement Results From the SMOG Satellite Project

Donát Takács, Boldizsár Markotics, and Levente Dudás

**Abstract**—On December 6, 2019, the second and third Hungarian satellites, SMOG-P and ATL-1 (both having been developed at the Budapest University of Technology and Economics) were launched. They both had a radio frequency spectrum analyzer on board, which was used to measure for the first time the strength of radio frequency signals radiated into space by terrestrial digital TV transmitters – that can be detected in orbit around the Earth. In this paper, we present how two- and three-dimensional radiosmog maps were created from raw data received from space. The goal of this paper is to demonstrate the process of creating these maps from the raw data collected; the analysis of the results visible in these maps is beyond the scope of the present discussion.

**Index Terms**—DVB-T Electromagnetic Pollution Map, Educational Student Satellite, PocketQube, Radiofrequency Smog, Spectrum Monitoring.

## I. INTRODUCTION

SMOG-P is a 1-PQ (PocketQube) class student satellite (5x5x5cm), ATL-1 is 2-PQ (5x5x10cm). SMOG-P was the first and smallest operational satellite in the world during its lifetime. First, the hardware used for the measurements is presented. Then a detailed description of the data processing follows, emphasizing the solutions provided for the unique challenges posed by the special circumstances of the measurements. These include filtering out the more reliable measurement data on a statistical basis and an inverse distance weighted interpolation of the filtered data. Finally several methods for visualizing the processed data are presented, including two-dimensional cartographic projections and a three-dimensional interactive web-application. <https://gnd.bme.hu>.

## II. HARDWARE

The SMOG-P and ATL-1 PocketQube class satellites contain the following sub-systems (SMOG-P is in Fig. 1. left before the integration): EPS – electrical power system including solar panels, maximal power point tracker circuits, battery charger & controller, limiter switches, step-down converters; OBC – on-board computer (micro-controller) with motion & magnetic sensor, real-time-clock and calendar and on-board memory; COM – communication and spectrum monitoring

Boldizsár Markotics, Donát Takács are BSc and MSc university students, respectively, at Budapest University of Technology and Economics (BME), Budapest, Hungary.

Levente Dudás PhD as supervisor is communicational and system engineer of SMOG student satellite project at the dept. of Broadband Infocommunications and Electromagnetic Theory, faculty of Electrical Engineering and Informatics, BME. (e-mail: [dudas.levente@vik.bme.hu](mailto:dudas.levente@vik.bme.hu))

DOI: 10.36244/ICJ.2021.1.3

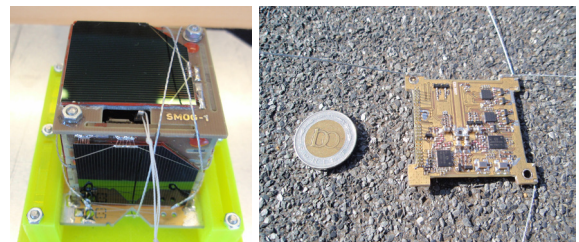


Fig. 1. The SMOG-P satellite before the integration in Glasgow (09-09-2019) - left; communication and spectrum monitoring sub-system - right

sub-system - Fig. 1 right: two independent UHF (ultra high frequency) transceiver and spectrum monitoring receiver based on Silabs<sup>1</sup> single-chip-radio type SI1060 and SI4464. The spectrum analyzer sub-system is a conventional heterodyne radio receiver with digital intermediate frequency: carrier 119–960 MHz; bandwidth 1.5–800 kHz; RSSI (received signal strength) range -10...-120 dBm.

## III. DATA PROCESSING

### A. Measurement data collected

A single spectrum measurement has the following data associated with it: a UTC (Universal Time Coordinated) timestamp with a resolution of one second ( $t$ , s); the latitude ( $\varphi$ , deg), longitude ( $\lambda$ , deg) and altitude ( $h$ , km) coordinates calculated from the TLE (two-lines element) records and the timestamp; the measurement frequency ( $f$ , Hz) and the result of the measurement itself (RSSI, dBm). Thus the entire spectrum measurement dataset can be formalized as an ordered set of tuples:

$$S = \{(t_i, \text{RSSI}_i, \varphi_i, \lambda_i, h_i, f_i)\}, \quad i = 1 \dots N, \quad (1)$$

where  $N = 19\,115\,754$  is the number of measurements performed during the two missions, namely between the 6th of December 2019 and 9th of October 2020.

### B. Aggregation regions

As explained in the previous section, there is no available orientation data for the spectrum measurements, so no single measurement result can be treated as reliable in itself: it is possible that at the time of any measurement, the antenna was

<sup>1</sup><https://silabs.com>

pointing away from the Earth. This means that we had to use a statistical approach; if a sufficient number of measurements are performed above a certain region, there must be at least a few that were performed with a correct orientation, since it is known from telemetry data that the satellites were constantly rotating. If these measurements can be selected, then the real intensity of the electromagnetic field in a certain frequency band can be estimated with a reasonable confidence. It is certain that the correct measurement at a given location is that with the highest RSSI value, so it can be selected in a straightforward way. However, determining reasonable regions from which the local maxima can be selected is not straightforward: this aggregation must be defined carefully.

As seen in Figure 2, the spatial distribution of the measurements is highly inhomogeneous, due to the location of the participating ground stations and the varying enthusiasm of amateur radio operators uploading their received data. The aggregation and interpolation methods were chosen in a way that they mitigate the negative effects this distribution as much as possible.

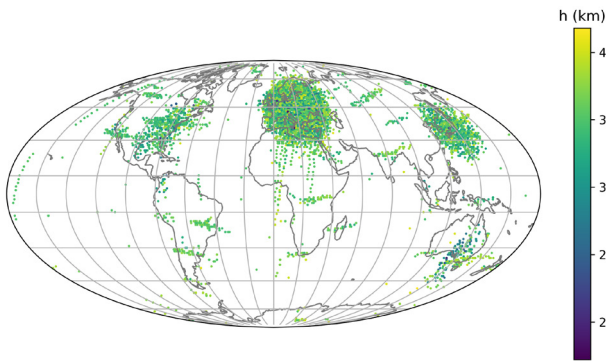


Fig. 2. The spatial distribution of the spectrum measurements performed by the satellites.

The spatial and frequency partitioning was performed by separating the set of measurements into equivalence classes. Two measurement points belong to the same spatial region if their coordinates  $(\varphi_i, \lambda_i)$  and  $(\varphi_j, \lambda_j)$  fulfill

$$\text{round}(\varphi_i/\tilde{\varphi}) = \text{round}(\varphi_j/\tilde{\varphi}), \text{ and} \quad (2)$$

$$\text{round}(\lambda_i/\tilde{\lambda}) = \text{round}(\lambda_j/\tilde{\lambda}), \quad (3)$$

where  $\tilde{\varphi}$  and  $\tilde{\lambda}$  are the latitudinal and longitudinal sizes of the regions, and round is the usual rounding function.

Similarly, an analogous partition of the measurement set regarding the frequency domain was performed. Since the goal is to create maps of the radio frequency transmissions for several frequency bands, simply selecting the largest measurement value in a spatial region is not a valid approach in itself. The frequency value of the measurement need to be taken into account as well. Similarly to the above, the size of a frequency region is  $\tilde{f}$ , and the corresponding equivalence relation is

$$\text{round}(f_i/\tilde{f}) = \text{round}(f_j/\tilde{f}). \quad (4)$$

If later we would like to calculate the average RSSI value in a frequency band larger than  $\tilde{f}$ , the corresponding measure-

ments result have to be averaged in a meaningful way, e.g. by calculating a root mean square value of the power ratios.

Equations (2)-(4) together define an equivalence relation on the set of measurements, which unambiguously partitions the measurements into distinct regions or classes. (It should be noted that this method does not yield equal-sized regions spatially due to the parametrization.) These regions will be used in a subsequent step, but first the effects of the varying altitude has to be taken into account.

### C. Reduction to mean spherical surface

As seen in Figure 3, the altitude of measurements varies in time due to the eccentricity of the orbits and the gradually decreasing apogee. It would be of interest to create radiosmog maps for different altitudes, however the measurements available were insufficient for this. Thus the RSSI values had to be reduced to a mean middle surface; this is a perfect sphere with a mean altitude of  $\bar{h} = 347$  km, indicated in Figure 3 with a horizontal line.

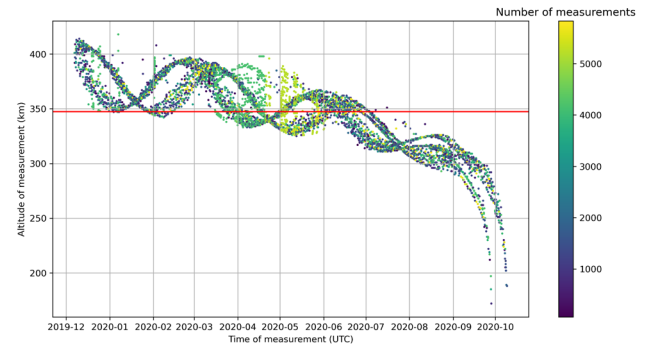


Fig. 3. The altitude and number of measurements performed by the two satellites over time.

The reduced  $RSSI'_i$  values are calculated based on the inverse square law of transmission power:

$$RSSI'_i = \rho \left( \pi (RSSI_i) \frac{h_i^2}{\bar{h}^2} \right) \quad (5)$$

with

$$\rho(P) = 10 \cdot \log_{10} P, \quad \pi(RSSI) = 10^{RSSI/10} \quad (6)$$

as the formulas for converting between RSSI and the corresponding power ratio values. This gives the  $S'$  set of measurements reduced to the mean surface:

$$S' = \{(t_i, RSSI'_i, \varphi_i, \lambda_i, f_i)\}, \quad i = 1 \dots N. \quad (7)$$

### D. Selecting the acceptable measurements

The relations (2)-(4) can be applied to  $S'$  yielding the reduced measurement values grouped into regions. From these regions we select the intensity measurement  $RSSI_i$  with the highest value, which is regarded as a valid measurement. The parameters  $\tilde{\lambda}$ ,  $\tilde{\varphi}$  and  $\tilde{f}$  are chosen in a way that we can be

reasonably confident that statistically enough measurements were performed in a region for it to contain a truly valid measurement. This yields a set of measurements that is significantly smaller in size than  $S$ , but the results contained are more probable to be valid:

$$\tilde{S} = \{(\text{RSSI}'_i, \varphi_i, \lambda_i, f_i)\}, \quad i = 1 \dots \tilde{N} \quad (8)$$

containing  $\tilde{N} = 5904$  aggregated measurement points using the parameters  $\tilde{\lambda} = \tilde{\varphi} = 5$  deg and  $\tilde{f} = 50$  MHz. The spatial distribution of the filtered measurement set is depicted in Figure 4.

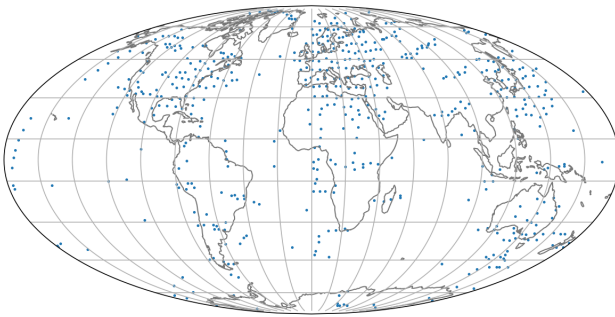


Fig. 4. The spatial distribution of the filtered measurement results on a Mollweide projection.

### E. Interpolation

Since we regard the measurements in  $\tilde{S}$  as valid, it is meaningful to interpolate them to get a sense of the electromagnetic field around the whole globe. The interpolation has to be performed over the mean spherical surface, so it has to take into account the two main features of the spherical geometry: its unboundedness (i.e. interpolation must be performed over the date line) and its curvature (i.e. the straight lines are the geodesics). To achieve this efficiently, we used a Python interface [1] to the established STRIPACK [2] and SSRFPACK [3] libraries used for performing calculations over triangular meshes. The mesh used was an icosahedral mesh (see Figure 5) of order 7 with the vertices and face centers as interpolation points.

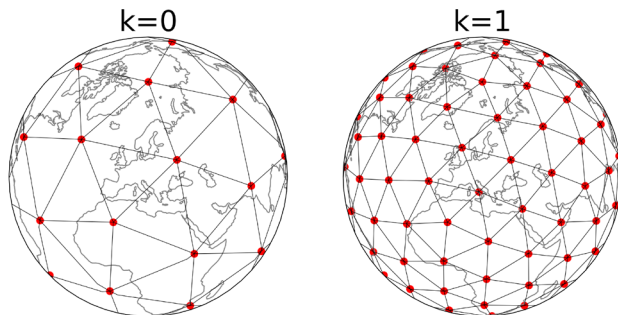


Fig. 5. The first two orders of refinement on the icosahedral mesh. The mesh used for the interpolation was of order  $k = 7$ , which is too dense to be illustrated on a global scale.

There several methods used for interpolating RSSI measurements, such as spline interpolation, distance weighting and kriging [4] [5]. We used inverse distance weighting (IDW) of the power ratio values for the interpolation based on several reasons: this method performed well in a similar task [4]; the main drawback of the IDW method, i.e. the difficulty of determining a proper exponent of the distance  $d$  to be used for the weights  $w$  does not exist here, since the wave propagation in space can be considered ideal, thus  $w \propto d^{-2}$ ; finally, of the three methods the IDW is the most tolerant to data points with measurement error, which can occur due to the nature of the dataset.

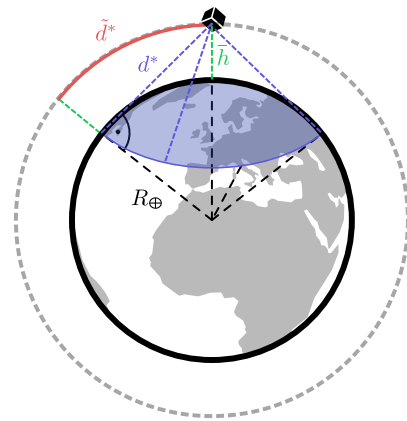


Fig. 6. A diagram illustrating the horizon of the satellite performing the measurements.

As illustrated in Figure 6, the points to be considered for the interpolation around a given satellite position are those that are above the areas on Earth visible from the satellite, i.e. within its horizon. This is simply due to the fact that radio transmitters below the horizon have no effect on the measurements performed at the given location, excluding atmospheric propagation effects. The two distances needed for performing an IDW interpolation using this method is the Euclidean distance to the horizon  $d^*$  and the corresponding geodesic distance  $\tilde{d}^*$  on the mean spherical surface, which can be calculated using elementary geometry:

$$d^* = \sqrt{(R_{\oplus} + \bar{h})^2 - R_{\oplus}^2}, \quad (9)$$

$$\tilde{d}^* = (R_{\oplus} + \bar{h}) \arcsin\left(\frac{d^*}{R_{\oplus} + \bar{h}}\right), \quad (10)$$

with  $R_{\oplus}$  denoting the mean radius of Earth. The interpolation function is thus:

$$\text{RSSI}(P_0) = \rho \left( \frac{\sum_i \pi (\overline{\text{RSSI}}_i) w(P_0, P_i)}{\sum_i w(P_0, P_i)} \right), \quad \text{if } \tilde{d}(P_0, P_i) < \tilde{d}^*, \quad (11)$$

with weights

$$w(P_0, P_i) = \frac{1}{d(P_0, P_i)^2}, \quad (12)$$

where  $d(P_i, P_j)$  denotes the Euclidean and  $\tilde{d}(P_i, P_j)$  the geodesic distance between the two points. The point  $P_0$  can be an arbitrary point on the mesh, while  $P_i$  is a measurement point.

#### IV. VISUALIZATION

With the filtered, reduced measurements in  $\tilde{S}$  and the interpolation defined by (11)-(12), several approaches for visualizing the resulting radiosmog maps were used. These include 2D map projections, and a 3D interactive web-application. There is no single best visualization of the data, all have their advantages and disadvantages. All of the results presented here show the power-averaged results over the frequency band from 119 MHz to 960 MHz.

##### A. Map projections

Two-dimensional map projections are used traditionally for geospatial datasets. The choice of the projection method is always a trade-off; here the Robinson projection method was used for easy interpretation of the results. All map projections were created using the open-source Python library Cartopy [6]. For these projections, a Plate Carree rectangular mesh had to be used, which is an additional interpolation on the icosahedral mesh points. The rectangular mesh was of order 6, which was chosen to be similar in resolution to that of the icosahedral mesh. Since the resolution of these meshes is sufficiently high, a linear interpolation on a local tangent planar surface was used. The two meshes are illustrated in Figure 7.

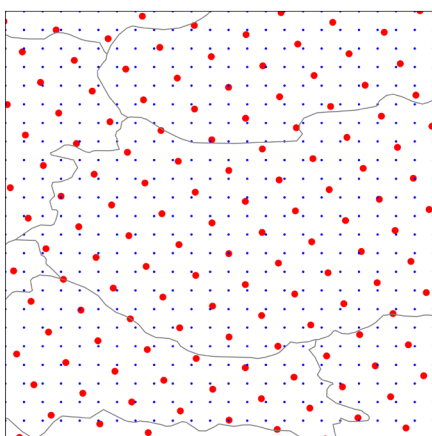


Fig. 7. A small section of the points in the two interpolation meshes (above Hungary for scale): icosahedral mesh of order 7 (red) and Plate Carree rectangular mesh of order 6 (blue).

1) *Voronoi-cell RSSI map:* If we would like to visualize the unaltered, but filtered measurement results (that is,  $\tilde{S}$ ), a Voronoi-cell based visualization can be used. This shows the spatial regions in which a measurement point is the nearest, and gives a sense of the distribution of values. This map is shown in Figure 8. It is clearly visible here that the intensity of received signals is higher over the more densely populated regions, as expected, but the distribution of the results is not continuous, which is not realistic.

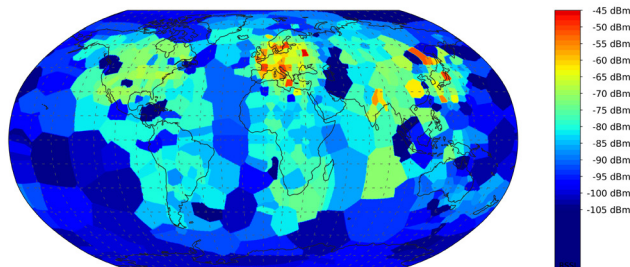


Fig. 8. The Voronoi cell map of the measurement results without interpolation.

2) *Interpolated, continuous distribution RSSI map:* Using the method described in subsection III-E, a continuously interpolated RSSI map can be created, which is shown in Figure 9. This interpolation takes into account the fact that the real distribution of the electromagnetic field is continuous.

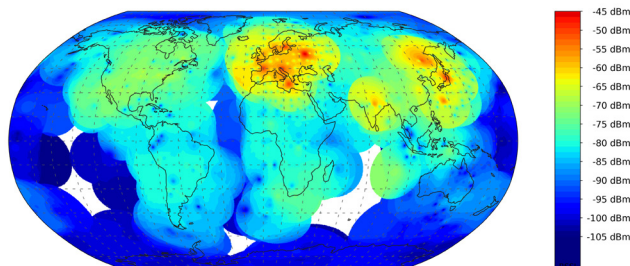


Fig. 9. The map created from IDW interpolated, filtered measurements results, using the Robinson-projection.

There several visible artifacts in this map. Due to the limiting nature of the horizon in the interpolating method, some areas (indicated in white) have no RSSI value associated: there is no valid measurement available within the horizon of these areas. In some other areas (e.g. above India), the border of the horizon-circles is sharply visible. Furthermore, in some other points (e.g. above South America) some outlier low values can be noticed. These indicate that the measurement result at those points, though treated as valid, is probably invalid: the IDW interpolation suggests that the nearby field is much stronger based on the surrounding measurement results.

3) *Gauss-smoothed RSSI map:* If we would like to get a qualitative sense of the entire global distribution, a smoothing of the power ratio values using a Gaussian kernel can be performed. This of course distorts the absolute value of the measurement results, thus this can only be used to estimate the overall shape and trends of the true spatial distribution of the

Processing and Visualizing the Low Earth Orbit Radio Frequency Spectrum Measurement Results From the SMOG Satellite Project

radio frequency pollution from Earth reaching the satellites. The smoothed, interpolated map is shown in Figure 10.

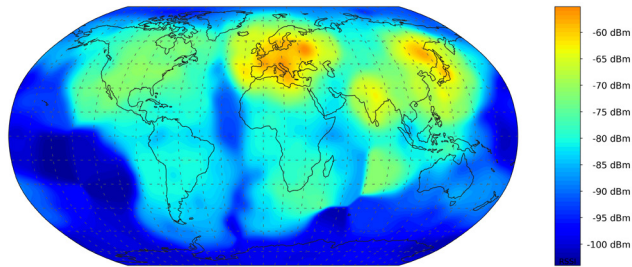


Fig. 10. The map of interpolated results of the measurement results with Gaussian smoothing.

B. Interactive 3D web-application

Further, the goal was to display the now filtered, interpolated data in an effective, visually appealing way.

This was achieved using a web application based on JavaScript technology. The WebGL-based library THREE.js was used for the display of the objects, because it is a lightweight and user friendly implementation of the WebGL technology.

The application can display the processed data set in various ways (discrete measurement points, continuous interpolated distribution, contour lines, etc.). The page is interactive, so the user can filter the results by frequency as well as is able to influence certain properties of the displayed objects, such as their movement or the used textures on them to achieve the required user experience.



Fig. 11. A screenshot of the 3D visualization web application.

The completed web application can be viewed by anyone at <https://gnd.bme.hu/mb/site/> at the time of this publication.

V. SPECTRUM MEASUREMENT RESULTS

In the previous sections we mainly focused on the spatial distribution and magnitude visualization of the measurement data. However, the measurements also span a significant frequency range, over which the measurement results highly vary based on the measurement locations. A few examples of these spectrum measurements are shown in this section. The timestamp and the RBW (Resolution Bandwidth) parameter of the spectrum measurements are also included in the figures.

Based on the TLE (two-lines element set - Keplerian data) and the timestamp of the measurement, the actual position of the satellite can be visualized with GPredict<sup>2</sup>. These maps are also presented for reference.

Due to their altitude (365 km LEO (Low Earth Orbit)), the satellites can only receive radio signals within a ca. 4000 km diameter horizon (per Figure 6) - yellow circle in maps, red line shows the trajectory of the satellite. The measured spectrum is corrected with the antenna factor of the spectrum measurement system (raw RSSI data downloaded from the satellite).

A. Pacific Ocean

Over the Pacific Ocean, the noise power level of the measurement system can be detected with 384 kHz resolution bandwidth (RBW). Inside this area, there is no TV watcher, this means: there is no DVB-T (Digital Video Broadcasting — Terrestrial) transmitter, hence there is no RF (Radio frequency) pollution: Fig. 12 - 13. In conclusion the spectrum measurement system is working.

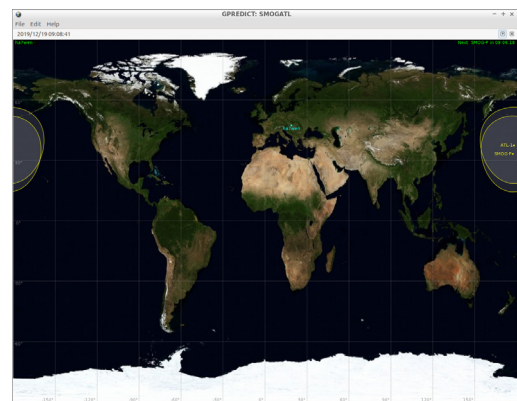


Fig. 12. Satellites over Pacific Ocean.

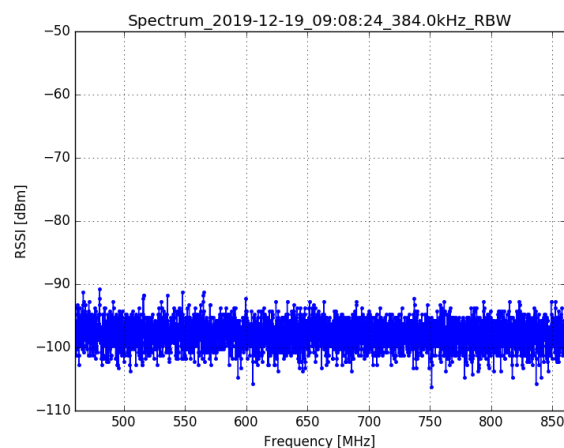


Fig. 13. Measured spectrum over Pacific Ocean on 2019. 12. 19. with 384 kHz RBW.

<sup>2</sup><http://gpredict.oz9aec.net/>

*B. Europe*

Over Europe, -60 ... -80 dBm signal level of DVB-T transmitters and between 790 and 820 MHz with -70 dBm power level 5G mobile system can be measured: Fig. 14 - 15. The whole lower DVB-T sub-band is continuously filled with signal of TV transmitters. The signal levels of 5G and DVB-T can be measured with almost the same signal level.

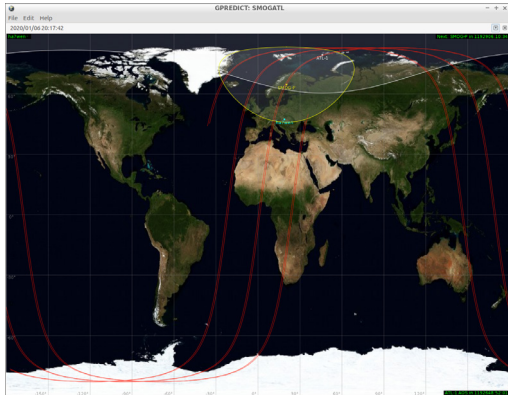


Fig. 14. Satellites over Europe.

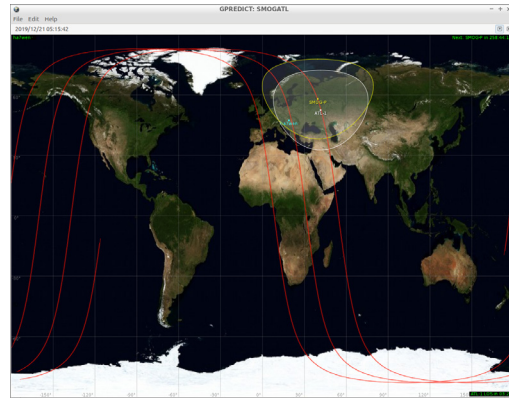


Fig. 16. Satellites over Eur-Asia.

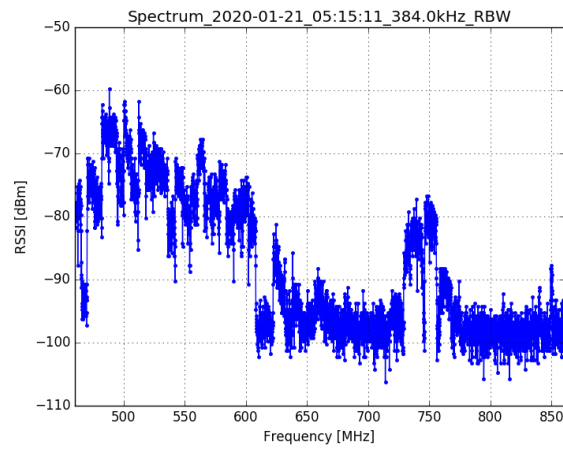


Fig. 17. Measured spectrum over Eur-Asia on 2020. 01. 21. with 384 kHz RBW.

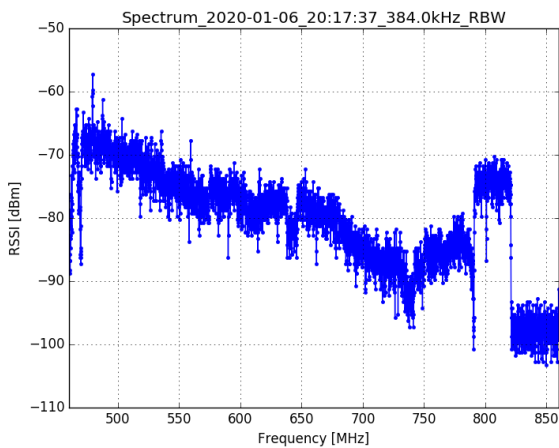


Fig. 15. Measured spectrum over Europe on 2020. 01. 06. with 384 kHz RBW.

*C. Europe-Asia*

Between Europe and Asia, only DVB-T transmitters can be measured: Fig. 16 - 17, there is no 5G signal.

*D. North-America*

Over America, high-power-level of DVB-T band pollution can be measured: Fig. 18 - 19, 480-610, 625-675, 725-775 MHz sub-bands are filled up with TV signals, GSM band communication is visible over 850 MHz.

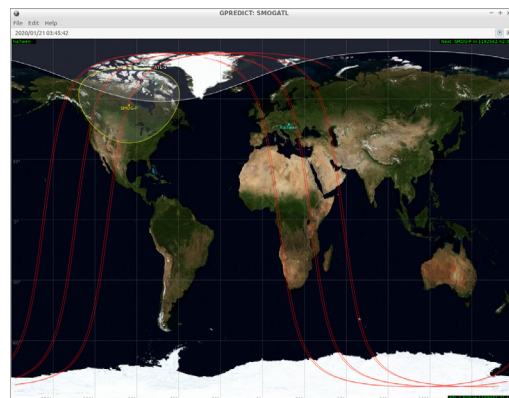


Fig. 18. Satellites over North-America.

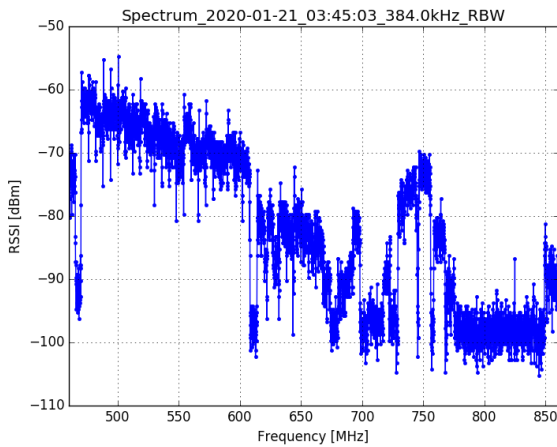


Fig. 19. Measured spectrum over North-America on 2020. 01. 21. with 384 kHz RBW.

E. Central-America

Over Central-America, there is lower power level of DVB-T band pollution detected, because of the longer range between the satellite and the DVB-T transmitters and the low-elevation radiation angle of the TV transmitters: Fig. 20 - 21 - the TV transmitters radiate its RF signal to lower elevation angle ranges toward to the TV watcher (on the Earth surface).

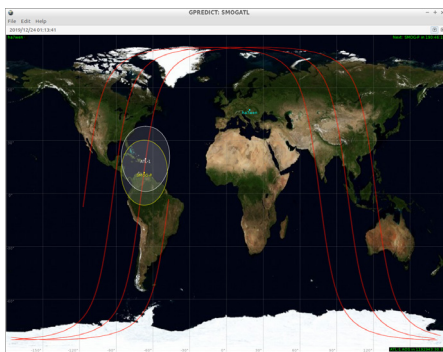


Fig. 20. Satellites over Central-America.

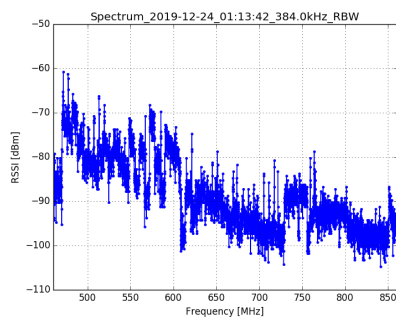


Fig. 21. Measured spectrum over Central-America on 2019. 12. 24. with 384 kHz RBW.

F. Arctic and European RF pollution comparison

Arctic and over Europe measured spectrum can be seen in Fig. 22 with the same scale: blue - European region, grey - Arctic. The differences between only the noise power and the RF pollution level caused by TV transmitters is highly visible.

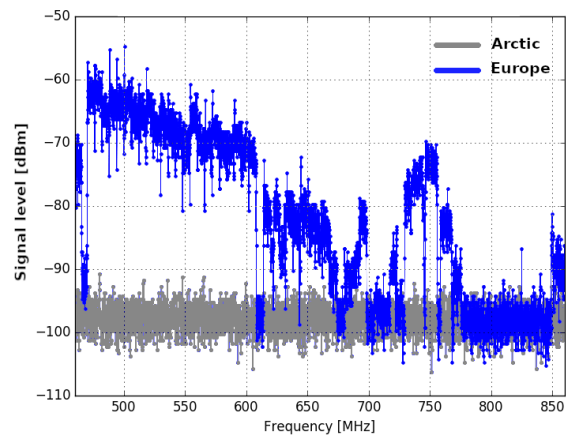


Fig. 22. Spectrum comparison between the Arctic and Europe.

SMOG-P and ATL-1 mainly focused on the DVB-T band, but measured not only DVB-T: radiated RF signal of 5G and GSM band mobile phone system can be identified on the spectrum figures.

VI. CONCLUSION

According to the presented measurement results and its visualization, the level of electromagnetic pollution caused by human beings on the digital video broadcasting terrestrial (DVB-T) frequency band had been measured: there is a huge amount of radiated power on low-Earth-orbit (LEO), that heats the space and disturbs the communication system of LEO satellites.

ACKNOWLEDGMENTS

The authors would like to thank the engineers that have worked on the SMOG-P and ATL-1 satellites, having made this analysis possible through their efforts and technical expertise. We are especially thankful for Dr. András Gschwint for his overarching vision and for bringing us together for this work, as well as Emil Viktor Hödl for his patient answers and continuous support.

Author contributions

D.T.: implementation of filtering, idea for and implementation of interpolation method, mean surface reduction and map projections, manuscript text and figures; B.M.: idea for frequency selection, concept and implementation of 3D visualization, manuscript text; L.D.: spectrum analyzer hardware, spectrum measurement figures and interpretations, idea for filtering approach, manuscript text. All authors have read and agreed to the published version of the manuscript.

REFERENCES

[1] L. Moresi and B. Mather, "Stripy: A Python module for (constrained) triangulation in Cartesian coordinates and on a sphere." *Journal of Open Source Software*, vol. 4, no. 38, p. 1410, Jun. 2019. [Online]. Available: <http://joss.theoj.org/papers/10.21105/joss.01410>

[2] R. J. Renka, "Algorithm 772: STRIPACK: Delaunay triangulation and Voronoi diagram on the surface of a sphere," *ACM Transactions on Mathematical Software*, vol. 23, no. 3, pp. 416–434, Sep. 1997. [Online]. Available: [doi: 10.1145/275323.275329](https://doi.org/10.1145/275323.275329)

[3] —, "Algorithm 773: SSRFPACK: interpolation of scattered data on the surface of a sphere with a surface under tension," *ACM Transactions on Mathematical Software*, vol. 23, no. 3, pp. 435–442, Sep. 1997. [Online]. Available: [doi: 10.1145/275323.275330](https://doi.org/10.1145/275323.275330)

[4] M. A. Azpurua and K. D. Ramos, "A COMPARISON OF SPATIAL INTERPOLATION METHODS FOR ESTIMATION OF AVERAGE ELECTROMAGNETIC FIELD MAGNITUDE," *Progress In Electromagnetics Research M*, vol. 14, pp. 135–145, 2010. [Online]. Available: <http://www.jpier.org/PIERM/pier.php?paper=10083103>

[5] B. Li, Y. Wang, H. Lee, A. Dempster, and C. Rizos, "Method for yielding a database of location fingerprints in WLAN," *IEE Proceedings - Communications*, vol. 152, no. 5, p. 580, 2005. [Online]. Available: [https://digital-library.theiet.org/content/journals/10.1049/ip-com\\_20050078](https://digital-library.theiet.org/content/journals/10.1049/ip-com_20050078)

[6] M. Office, *Cartopy: a cartographic python library with a matplotlib interface*, Exeter, Devon, 2010. [Online]. Available: <https://scitools.org.uk/cartopy>



**Donát Takács** has received the BSc degree in mechatronical engineering at the Budapest University of Technology and Economics (BME) in 2020. He is currently pursuing the MSc in mechanical engineering modelling at BME, with a major in solid mechanics and a minor in fluid mechanics.

His research interests include general mathematical and computational modelling of various engineering phenomena, new methods in finite element analysis (such as isogeometric analysis) and failure prediction

of composite materials. He is a founding member, and currently the president of the BME Cosmos Society.



**Boldizsár Markotics** has ongoing BSc studies at the Budapest University of Technology and Economics (BME) as an electrical engineer in the field of High Frequency System Techniques.

Currently working on a project in Radar Research Group regarding the Doppler effect. His interests include various radar technologies, programming languages, the theory of electromagnetic fields and lately web development. He is currently the vice president of the BME Cosmos Society.



**Levente Dudás** has received the MSc degree in 2007 in electrical engineering, PhD in 2018 – Radar and Satellite Applications of Radio and Antenna Systems – at the Budapest University of Technology and Economics (BME). He is currently senior lecturer at the Department of Broadband Infocommunications and Electromagnetic Theory at BME, working as electrical engineer in Microwave Remote Sensing Laboratory, president of Radio Club of BME.

His research interests include microwave remote sensing (RADAR): active and passive radar; CubeSat and PocketQube type satellite development; analog RF hardware and antenna design; automated and remote controlled satellite control station development; Software Defined Radio based signal processing for satellite and radar applications.

# Double-View Matching Network for Few-Shot Learning to Classify Covid-19 in X-ray images

Gábor Szűcs<sup>1</sup> and Marcell Németh<sup>2</sup>

**Abstract** — The research topic presented in this paper belongs to small training data problem in machine learning (especially in deep learning), it intends to help the work of those working in medicine by analyzing pathological X-ray recordings, using only very few images. This scenario is a particularly hot issue nowadays: how could a new disease for which only limited data are available be diagnosed using features of previous diseases? In this problem, so-called few-shot learning, the difficulty of the classification task is to learn the unique feature characteristics associated with the classes. Although there are solutions, but if the images come from different views, they will not handle these views well. We proposed an improved method, so-called Double-View Matching Network (DVMN based on the deep neural network), which solves the few-shot learning problem as well as the different views of the pathological recordings in the images. The main contribution of this is the convolutional neural network for feature extraction and handling the multi-view in image representation. Our method was tested in the classification of images showing unknown COVID-19 symptoms in an environment designed for learning a few samples, with prior meta-learning on images of other diseases only. The results show that DVMN reaches better accuracy on multi-view dataset than simple Matching Network without multi-view handling.

**Index Terms** — COVID-19, convolutional neural network, deep learning, feature extraction, few-shot learning, image classification, image representation, machine learning, multi-view

## I. INTRODUCTION

A necessary, but not sufficient condition for the effective use of machine learning (especially deep learning) methods is the availability of large amounts of training data. This condition cannot be satisfied in many applications (e.g., in image classification [15], especially in medical images [12]), in most cases due to a lack of available knowledge or excessive costs of expertise [23]. The research topic presented in this paper belongs to this problem type that is often lacking in such data, it intends to help the work of those working in medicine by analyzing pathological recordings, using only very few images. This scenario is a particularly hot issue nowadays: how could a new disease for which only limited data are available be diagnosed using features of previous diseases? (If the number of labeled data is small, but the huge amount of unlabeled data is available, then this can lead to active learning [14], but in this paper, we consider that there is no unlabeled data at all.)

<sup>1</sup> Department of Telecommunications and Media Informatics, Budapest University of Technology and Economics (BME), Budapest, Hungary (e-mail: szucs@tmit.bme.hu)

<sup>2</sup> M. Németh is a student in BME Balatonfüred Student Research Group (e-mail: marcell.nemeth@edu.bme.hu)

In the case of learning from a small amount of labeled data, so-called “few-shot learning” (FSL), there are only a few samples from each class, so the difficulty of the classification task is to learn the unique feature characteristics associated with the classes as quickly and accurately as possible. In the few-shot learning literature *A-way-B-shot* means that we use  $B$  samples from  $A$  different classes for learning, so the training set has a total of  $I = A \cdot B$  samples. This type of meta-learning in image recognition area requires knowledge transfer of high-level characteristics of training images similar to the target images. Although there are methods that can solve the problem, but if the images come from different views [17][24], they will not handle these views well. In this paper, we proposed an improved method, so-called Double-View Matching Network, which solves the few-shot learning problem as well as the different views of the pathological recordings in the images.

The next section discusses the theory of few-shot type machine learning in hypothesis space and its limits in Hilbert spaces. Then the paper presents the advanced methods, particularly the Matching Network (with a special focus on the attention mechanism and neural network architecture) for few-shot learning. For improvement and handling more views in the images, we suggested Double-View Matching Network, which is capable of recognizing multi-view recordings. The suggested method was tested in the classification of images showing unknown COVID-19 symptoms in an environment designed for learning a few samples, with prior meta-learning on images of other diseases only. The results of the new method are detailed at the end of the paper.

## II. FEW-SHOT HYPOTHESIS LEARNING

### A. Hypothesis Learning

Most few-shot learning tasks can be traced back to supervised learning problems, with only a few labeled samples from each class available to the classifier [4] (at unsupervised case, e.g., the graph clustering can be used [28]). The most common applications are image recognition, emotion recognition, object classification and multimedia analysis.

The general task of the problem is to parameterize a classifier  $h$  using only a very small number of samples that predicts label  $y_i$  for each input  $x_i$ . When a machine learner is trained on a large amount of training data, several models can be created at the end of the learning that are able to produce output from the input samples. However, with only a few data, a much larger number of such models can be “fitted” to the input-output pairs due to the wide variety of options (fewer constraints). These

models can be considered as hypothesis, that is, a function that produces the output from the input; and the aim is to find the best solution in this hypothesis space, as we present in the following based on a tutorial [10].

There is a function  $f: X \rightarrow Y$ , which can be quantified by the so-called empirical error:

$$R_{emp}[f] = \frac{1}{N} \sum_{i=1}^N L(f(x_i), y_i) \quad (1)$$

Thus, with the previous notations, we can formalize the problem of learning in an  $X$  input and  $Y$  output space, where  $D$  is an unknown distribution in an  $X \times Y$  space and  $F$  is the hypothesis space for the functions

$$f : X \rightarrow Y \quad (2)$$

and  $S = (x_1, y_1), \dots, (x_N, y_N)$  samples from  $D$ . Based on these, the goal is to find a hypothesis  $f \in F$  for which the real error is minimal:

$$R[f] = \mathbb{E}_D[L(f(x), y)] \quad (3)$$

The main disadvantage of the above relation is that it is not possible to minimize it clearly since we do not know the distribution  $D$ . However, it is possible to find an estimation by taking advantage of the fact that in most cases, the real error of the hypotheses takes on values significantly similar to the empirical error. The difference between the two errors is influenced by the flexibility of the used model (i.e., how many degrees of freedom it has). The disadvantage of a large number of degrees of freedom is that the hypothesis space is accompanied by a tendency to overfit the model, as we can fit innumerable functions to the desired distribution. Based on this idea, the so-called uniform convergence bounds can be defined, for all hypotheses  $f$  in a given hypothesis space, it is true that [10]:

$$R[f] \leq R_{emp}[f] + \varepsilon \quad (4)$$

where  $\varepsilon$  is the generalization error.

Despite the uniform convergence bounds defined by (4), there may be some training sets for which the model produces poor results, so the probability of the good results can be written with the following inequality for a given distribution  $D$ :

$$\mathbb{P}[R[f] - R_{emp}[f] \leq \varepsilon \mid \forall f \in F] \geq 1 - \delta \quad (5)$$

The main difficulty of finding a solution to this problem is that in the absence of accurate knowledge of  $D$ , the above relation must exist for all possible distributions of  $D$  in  $X \times Y$  space (i.e., not just for a given distribution of  $D$ ). However, inequality (5) should also be satisfied with a probability of  $1 - \delta$  simultaneously for all hypotheses, thus for each function  $f$  we can write this formula within all possible distributions of  $D$ , so that we get the following:

$$\mathbb{P}[R[f] - R_{emp}[f] \leq \varepsilon] \geq 1 - \delta \quad \forall f \in F \quad (6)$$

The latter inequality expresses that for any given  $f \in F$ , except for the  $\delta$  proportion of samples sampled “unlucky”,

equation (4) will be true. Inequality (6) is easier to accomplish because it is easier to achieve the same success rate in the whole set than the same rate within each subset. In contrast, the inequality (5) has the advantage that we can tell from sampling whether a given set of the training set is “lucky” or “unlucky”. If it is “lucky”, the inequality will be true for all hypotheses at once, i.e., we have achieved our goal. Based on this, it is advisable to write equation (5) in the following formula:

$$\mathbb{P} \left[ \sup_{f \in F} [R[f] - R_{emp}[f]] \leq \varepsilon \right] \geq 1 - \delta \quad (7)$$

The distinction between (7) and (6) is essential for what we want to use the bounds in the future; in the case of the FSL learning problem, the most important is the error of the hypothesis  $f^*$  for which the empirical error is minimal, which depends significantly on the choice of the training set.

The error of the model is influenced by the number of samples in the available training set  $S$  and the hypothesis space  $F$ . Starting from this statement, error minimization can be approached from several sides to reduce estimation inaccuracy using prior knowledge [26]. The possible approaches are the number of samples (a larger training set could help, but in FSL, only very few samples are available), and the algorithm for finding optimal parameters. The last method approaches the part of the model, which is responsible for defining and narrowing the hypothesis space. In this case, the use of a priori knowledge is aimed at reducing the complexity of the hypothesis space, excluding several potential hypotheses in advance.

### B. Hilbert-space methods

Minimizing only empirical error is not sufficient, as this type of approach can lead to overfitting. To avoid this, it is necessary to narrow hypothesis  $F$  with certain limits. To solve this, starting from equation (4), we can introduce a penalty term,  $\Omega[f]$ , which quantifies the complexity of each hypothesis and minimizes the following error instead of the method presented in equation (1) [10]:

$$R_{reg}[f] = R_{emp}[f] + \Omega[f] \quad (8)$$

where  $\Omega[f]$  is the regularization term, and  $R_{reg}$  is the regularized error. The learning problem should therefore focus on three components: the loss function  $L$ , the regularization term  $\Omega$  and hypothesis space  $F$ .

In constructing the hypothesis space  $F$ , the natural expectation is that  $F$  is a linear function space in which for any  $f \in F$  and  $\lambda$ , the product  $\lambda \cdot f$  is also in  $F$ , and for any  $f_1, f_2 \in F$  it is true that  $f_1 + f_2 \in F$ .

In addition, the structure of  $F$  should be related to the regularization term  $\Omega$  in some way. This property is defined by an  $\Omega[f] = \|f\|^2$  norms. For the new norm, the linear mappings taken with  $\lambda$  should also be satisfied and in order to obtain as a scalar product, let  $\|f\| = \langle f, f \rangle^{1/2}$ . These types of spaces are called Hilbert space, and the great advantage of this is that Frigyes Riesz's theory can be applied to the present problem because in Hilbert spaces, the Riesz representation theorem is

## Double-View Matching Network for Few-Shot Learning to Classify Covid-19 in X-ray images

true [6], as a result of which for any  $x \in X$  there exists a representation  $k_x$ , for which it is true that:

$$f(x) = \langle k_x, f \rangle \quad \forall f \in F \quad (9)$$

We do not know  $k_x$  in equation (9), but we know for sure that it exists. A key element of the idea is that it creates a connection between the abstract structure of  $F$  and the elements in it, and we can use its representation instead of any  $x$ . If we rewrite the complete regularized error problem as follows

$$\hat{f} = \arg \min_{f \in F} \left[ \frac{1}{N} \sum_{i=1}^N L(\langle k_{x_i}, f \rangle, y_i) + \langle f, f \rangle \right] \quad (10)$$

then it can be seen that  $f$  appears only in the form  $F$  with scalar products of other functions. It follows that if we know the scalar product and  $k_x$ , we will apply equation (9) with  $k_x$  to some  $x' \in X$ :  $k_{x'}(x) = \langle k_x, k_{x'} \rangle = k_x(x')$ . From the context, it can be seen that the inner products of the different  $k_{x'}$  tell us what form each vector takes, and leaving the unnecessary elements, it can be seen that the quality of the algorithm is determined by the internal products called kernels:

$$k(x, x') = \langle k_x, k_{x'} \rangle \quad (11)$$

The only condition for kernels is that they should be symmetric as well as satisfying the following expression:

$$\sum_{i=1}^n \sum_{j=1}^n c_i c_j k(x_i, x_j) \geq 0, \quad (12)$$

where  $c_i, c_j$  are real coefficients, and they should result in  $\langle \sum_{i=1}^n c_i k_{x_i}, \sum_{j=1}^n c_j k_{x_j} \rangle \geq 0$ .

Summarizing the above, the learning problem has been traced back to the proper definition of an  $L$  loss function and  $k$  kernels. Looking at equation (10), it can be seen that  $\hat{f}$  will be derived from the representatives of the training data  $k_{x_1} \dots k_{x_N}$ , since the error term depends only on the internal product of  $f$  with different  $k$ , while the regularization term will affect all its dimensions. If  $f$  has a component that is orthogonal to the subspace spanned by  $k_{x_1} \dots k_{x_N}$ , then the error term will not be affected, but the regularization term will be. It follows that the optimal  $f$  will entirely be in the subspace spanned by the representatives:

$$\hat{f}(x) = b + \sum_{i=1}^N \alpha_i k(x_i, x) \quad (13)$$

where  $\alpha_1 \dots \alpha_N$  are real coefficients and  $b$  is the offset (bias). Substituting formula (13) into (10), it can be observed that the task of the learning algorithm has been simplified to calculating the offset and the coefficients (the interpretation of these coefficients is the learnt knowledge after the learning).

### III. MATCHING NETWORK ARCHITECTURE

#### A. Matching Network for few-shot learning

Several methods have been developed to solve the FSL problem: Prototypical Network [20], Attentive Recurrent Comparators [18], Simple Neural Attentive Learner (SNAIL)

[13], Memory-Augmented Neural Network (MANN) [2], ModelAgnostic Meta-Learning [3], Relation Network [21] and Siamese networks [9][16]. Based on the sources in the FSL literature, analyzing the results and considering further potential improvements, we chose one of the best methods, Matching Network [25], as the basis of our research. This solution adapts many techniques, including deep parameterized networks and metric learning [7] using feature vectors and deep neural networks with memory.

The essential idea of the Matching Network classifiers is to combine two learning phases: metric learning and the ‘‘lazy-learner’’ k-NN (k Nearest Neighbor) method. Metric learning is realized in the Hilbert-type spaces detailed in the previous section, while the k-NN-type classification takes place in the last phase during comparing feature vectors.

In the first phase, neural networks can be used. The main task of this phase is to learn a distance metric, a metric space in which the representations of samples from different classes are separated from each other as much as possible. Thus, the task of the applied neural networks is to parameterize a metric with such properties, i.e., an optimal hypothesis function to calculate the coefficients based on what is described in the previous section.

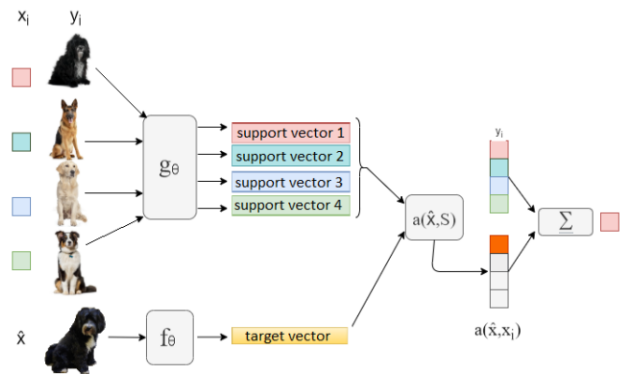


Figure 1. Matching Network architecture

The training set of the few-shot learner is called support set. The applied method in Matching Network defines a classifier ( $S \rightarrow C_S(\cdot)$  mapping) for each support set sampled from the training set, and then combines the stored mappings to make the best use of the available knowledge. Thus, Matching Network type classifiers are able to categorize unknown classes with high efficiency without changing the networks.

In the following, we define the task description in more detail. Let  $S$  be a support set containing  $n$  sample-label pairs:  $S = \{(x_i, y_i)\}_{i=1}^n$ . As shown in Figure 1, the operation of the model was illustrated by recognizing dog breeds. The sample-label pairs (label means class label) of the support set are given as input to a classifier  $C_S(\hat{x})$ , which defines a probability distribution for a given sample  $\hat{x}$  based on the class label  $\hat{y}$ . This mapping can be written as follows:  $S \rightarrow C_S(\hat{x}) = P(\hat{y} | \hat{x}, S)$ , where the function  $P$  is parameterized by neural networks. This construction allows us to use the model parameterized during learning to classify all elements of an  $S'$  support set containing unseen patterns. The class prediction of each sample can be

described as follows:

$$P(\hat{y} | \hat{x}, S) = \sum_{i=1}^n a(\hat{x}, x_i) y_i \quad (14)$$

where  $x_i, y_i$  are the samples, and their associated labels from the  $S = \{(x_i, y_i)\}_{i=1}^n$  support set, and  $a(\cdot, \cdot)$  is the kernel (also known as attention kernel or attention mechanism). It is worth noting that the above relation produces the output (label) of the samples of the new classes as a linear combination of the sample labels in the support set.

Appropriate selection of the model components that make up the attention kernel is key to the effectiveness of the model. In its most basic form, the kernel can be written using the softmax function applied to cosine distances as follows:

$$a(\hat{x}, x_i) = \frac{e^{c(f(\hat{x}), g(x_i))}}{\sum_{j=1}^n e^{c(f(\hat{x}), g(x_j))}} \quad (15)$$

where function  $c$  describes the cosine similarity, functions  $f$  and  $g$  are the neural networks responsible for constructing the feature vector formed from  $x_i$  and  $x$  ( $f$  and  $g$  preferably have the same architecture).

### B. Multiple views challenge in images

In the first phase of the Matching Network, the appropriate feature vectors are essential. In our task, images of pathological chest X-rays were available; and we used a deep neural network (Convolutional Neural Network – CNN) detailed later to generate the characteristic vectors of the X-rays. The largest challenge in the image data set was that two types of recording perspectives - frontal and profile (side) recording - were stored for each disease type in the data set, but only one of them (frontal or profile) was available at each patient. In order to handle more views in the method, we developed an extended (improvement) version of the Matching Network, the so-called Double-View Matching Network. The next section presents this proposed method.

## IV. DOUBLE-VIEW MATCHING NETWORK

### A. Convolutional Neural Network for Feature Extraction

At image recognition topic, there is a frequent case that samples come from different perspectives. In the investigated dataset of medical images (in our case chest X-ray images), this was also true, the dataset contained two views. Our research focused on how recordings from the same class but from different perspectives can be used effectively. Our proposed method, the so-called Double-View Matching Network (DVMN for short) answers the question. In this section, we present the DVMN in two parts; firstly, the architecture and the details of the Convolutional Neural Network for feature extraction, then the solution of the combination of more views.

Proper selection of neural networks generating mappings from image into a common feature space (i.e., the feature extraction), is a key component of the accuracy. The publication of Matching Network [25], which is considered as the basic paper of our research, shared only small information about the neural network architecture for feature extraction that VGG

[19] and Inception [22] networks can be used. However, these network architectures are not dedicated to medical images. Thus, we deviated from this approach and used our own structure, which is shown in Table 1, where each Convolution row consists of a convolution layer, then a batch normalization, and ReLu.

Images sampled from the set of training data serve as input to the convolutional network that produces the mapping. During the learning, an extra FC (fully connected) layer was added after the last layers of the CNN network to generate the output vectors. The CNN was used to the two networks,  $f$  and  $g$  having the same architecture (Figure 1.).

| Operation layer | # filters | Size of filter | Stride value | Padding value | Size of output |
|-----------------|-----------|----------------|--------------|---------------|----------------|
| Convolution     | 64        | 3x3x64         | 1x1          | 1x1           | 460x460x64     |
| MaxPooling      | 1         | 2x2            | 2x2          | 0             | 230x230x64     |
| Convolution     | 64        | 3x3x64         | 1x1          | 1x1           | 230x230x64     |
| MaxPooling      | 1         | 2x2            | 2x2          | 0             | 115x115x64     |
| Convolution     | 64        | 3x3x64         | 1x1          | 1x1           | 115x115x64     |
| MaxPooling      | 1         | 2x2            | 2x2          | 0             | 57x57x64       |
| Convolution     | 64        | 3x3x64         | 1x1          | 1x1           | 57x57x64       |
| MaxPooling      | 1         | 2x2            | 2x2          | 0             | 28x28x64       |

Table 1. CNN network architecture

It is important to note that the mapping of each  $x_i$  per support set is independent of other samples. If the mapping of a sample  $x_i$  and  $x_j$  is close to each other in the parameter space, it is worthwhile to change the parameters of the model in order to refine the feature vectors, taking into account the mappings of other samples. Based on this idea, a component containing memory, the context embedding layer, was added to the network, similar to the original paper of Matching Network [25]. A bidirectional LSTM layer was used to embed each  $x_i$  sample, which stores the other feature mappings of the  $x_i$  sample support set:

$$f(\hat{x}, S) = LSTM(f'(\hat{x}), g(S), K) \quad (17)$$

where  $f'(\hat{x})$  denotes the characteristics generated by CNN that serve as input to the LSTM,  $g(S)$  is the mapping of the given support set by  $g$ , and  $K$  is the number of “time steps” of the LSTM. This allows the attention mechanism to utilize only certain elements of the support set that add meaningful value to the mappings.

Context embedding of the classifier's  $f$  network based on equation (17) assuming a previous step  $k$ :

$$\hat{h}_k, c_k = LSTM(f'(\hat{x}), [h_{k-1}, r_{k-1}], c_{k-1}) \quad (18)$$

$$h_k = \hat{h}_k + f'(\hat{x}) \quad (19)$$

$$r_k = \sum_{j=1}^{|\mathcal{S}|} a(h_{k-1}, g(x_j)) g(x_j) \quad (20)$$

$$a(h_{k-1}, g(x_j)) = \frac{e^{h_{k-1}^T g(x_j)}}{\sum_{j=1}^{|\mathcal{S}|} e^{h_{k-1}^T g(x_j)}}, \quad (21)$$

where  $x$  is the input,  $h$  is the output (cell after the output gate) and  $c$  is the memory cell. Furthermore, it is a function of the

Double-View Matching Network for Few-Shot Learning to Classify Covid-19 in X-ray images

attention mechanism with softmax activation. Context embedding of the classifier's  $g$  (target image) network:

$$g(x_i, S) = \vec{h}_i + \vec{h}_l + g'(x_i) \quad (22)$$

B. Handling the views

Our idea was to separate the different perspectives in some way in order to find a better model. In designing our solution with more views, the most important task was the optimal use of the feature vectors (hereafter vectors) of the images taken from each view. In DVMN, we suggested that the vectors of each perspective should be constructed by different CNN networks with separate parameters instead of a common one [5][27]. Behind this idea was that during training iterations, due to the small number of samples, tuning the model parameters to the appropriate "direction" is key, and recordings from different perspectives can easily miscalibrate weight settings. In addition, the mappings generated by the two separate networks need to be aggregated before classification [8], as the Matching Network would learn the difference between views instead of similarities among images from the same class, so our solution was based on the basic idea of working with a union of views.

Continuing the previous thoughts, let  $S_{L1}$  be a labeled image set that contains only the images in the first view and whose images we want to use to teach a metric space. To generate feature vectors from the images, we used a self-made CNN, because it is more flexible to learn new types of images than a pretrained deep neural network. By separating the last FC layers of CNN, the remained network generates a feature vector of  $n$  elements for each input image, denoting this feature extraction mesh as a function of  $f$ :  $v_{L1} = f_{CNN1}(x)$ . For all images in the tagged image set  $S_{L1}$ , the set of feature vectors generated in this way is denoted by  $V_{L1}$ :

$$V_{L1} = \{v_{L1} | v_{L1} = f_{CNN1}(x), x \in S_{L1}\} \quad (23)$$

The Matching Network generates a new vector from each entered feature vector that already describes the image in the new vector space, denoting this new vector by  $v'_{L1}$ , so that we can write that  $v'_{L1} = f_{MN1}(v_{L1})$ . The set of new vectors thus obtained is denoted by  $V'_{L1}$ :

$$V'_{L1} = \{v'_{L1} | v'_{L1} = f_{MN1}(v_{L1})\} \quad (24)$$

For an unknown class set (by unknown, we mean the set of classes belonging to the previous image set  $S_{L1}$  and the set of classes of the unknown set are disjoint sets, i.e., their intersection is an empty set, but the new set has some class labeled images) we want to use the learned new vector space, where the image set also consists only of images from the first view. With the previously learned CNN and MN models, vectors can be generated for all images (without the labels of the unknown image set), so we denote the set of new vectors obtained for the unknown image set by  $V'_{U1}$ , which will be:

$$V'_{U1} = \{v'_{U1} | v'_{U1} = f_{MN1}(f_{CNN1}(x)), x \in S_{U1}\} \quad (25)$$

If we select the vectors with the class label from the elements of  $V'_{U1}$  into the support set (this is the training set of the few-shot learner), we will be able to classify each of the other vectors with unknown class labels by predicting the class label whose the support vector is closest to the vector to be classified.

Using the notations used in the previous paragraphs in an analogous way to the second view:

$$V_{L2} = \{v_{L2} | v_{L2} = f_{CNN2}(x), x \in S_{L2}\} \quad (26)$$

$$V'_{L2} = \{v'_{L2} | v'_{L2} = f_{MN2}(v_{L2})\} \quad (27)$$

$$V'_{U2} = \{v'_{U2} | v'_{U2} = f_{MN2}(f_{CNN2}(x)), x \in S_{U2}\} \quad (28)$$

This mathematical framework of handling multi-view data is our contribution in this paper. In B-shot learning the images of each view are fed to the two CNNs, they will output two  $m$  long vectors. Let  $n_1$  and  $n_2$  be the number of samples in the first and in the second view, respectively in a given class. If the image dataset is ideal (that is  $n_1 = n_2 = n$ ), the input data table will have a dimension  $n \times 2m$  at the case of the concatenation of vectors belonging to two views. In a real environment, expecting an ideal dataset would be an unrealistic requirement, so the following options are available at this point:

- If at least one image is available from both views, but the number of images in a view is larger, the images already used can be re-input as the replacement for the missing images (in order to get the same number in each view). This method can easily lead to overfitting due to the repetition of samples.
- In order to get the same number in each view the other solution is the selection the minimum number among different views. In this case, a sample  $\min(n_1, n_2)$  is used from both views, so the size of the input data table will be  $\min(n_1, n_2) \times 2m$  at the case of concatenation. The negative result of this solution is the artificial reduction of the number and the expected decrease in accuracy based on the measurements.
- Instead of the concatenation of the vectors, we can get the union of the set of vectors. There is a requirement for the number of samples per view, the only condition is that  $k_1 + k_2 \geq B$  (in B-shot learning). This solution with the union of views eliminates the imbalanced problem, thus our method works with this, and the dimension of the data table will be  $(n_1 + n_2) \times m$ .

C. DVMN on multiple views

During the DVMN method, we trained two CNNs based on the idea of a union of sets of vectors. Let  $V_{L1}$  and  $V_{L2}$  be sets of characteristic vectors analogous to equation (23) and (26). The solution presented below builds the model to take advantage of the union of views. Consider the union of feature vectors:

$$V_L = V_{L1} \cup V_{L2} \quad (29)$$

This complete set is given to the Matching Network (MN) to perform the vector space teaching required for a few-shot classification. The set of new vectors of  $(n_1 + n_2) \times m$  thus obtained is denoted by  $V'_L$ :

$$V'_L = \{v'_L | v'_L = f_{MN}(v_L), v_L \in V_L\} \quad (30)$$

For using the learned new vector space for an unknown image set, the previously learned CNN1 and CNN2 (depending on whether the unknown image is in the first or second view) and MN can be applied to generate vectors for all images, so we denote the set of new vectors obtained for the unknown image

set by  $V'_U$ , which will be:

$$V'_U = \left\{ v'_U \middle| \begin{array}{l} v'_U = f_{MN}(f_{CNN1}(x)), x \in S_{U1} \\ v'_U = f_{MN}(f_{CNN2}(x)), x \in S_{U2} \end{array} \right\} \quad (31)$$

The depicting part of the support set of the Double-View Matching Network architecture, which makes efficient use of multiple views and can handle the problem of unbalanced classes, is shown in Figure 2.

As a concluding point of the section, although the present implementation (described above) uses only two types of views due to the characteristics of the data set (and the architecture of the model), it would be able to take advantage of more different perspectives instead of two.

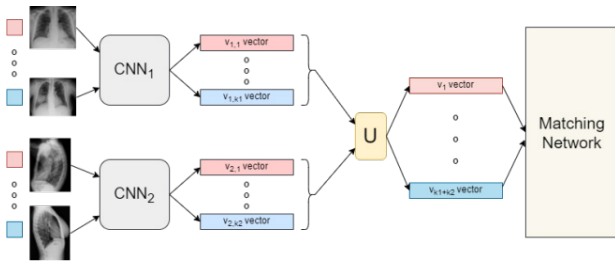


Figure 2. Mapping the Double-View Matching Network support vector

D. Training setup

So far, the operation of the Matching Network has been presented, which uses a set of support as an input of an  $S \rightarrow C(x)$  classifier. In the method, using set-by-set sampling, a mapping in the form  $P_\theta(y|\hat{x}, S)$  is obtained, in which  $\theta$  denotes the parameters of the model.

In learning, in each iteration/epoch in which the gradients are calculated, and the model parameters are updated, we first sample a class set  $C$  from a set  $F$  (all classes) that contains a subset of all classes. Next, using  $C$ , we select the elements of the support set  $S$ , along with a  $S_B$  batch that contains some instances of the classes of the  $C$  set.

The model parameters are then parameterized in such a way that the error of the class predictions given to the samples in  $S_B$  is minimized when trained on  $S$ :

$$\theta = \arg \max_{\theta} E_{C \sim F} \left[ E_{S \sim C, S_B \sim C} \left[ \sum_{(x,y) \in S_B} \log P_\theta(y|x, S) \right] \right] \quad (32)$$

Sampling batches through different iterations helps to avoid overfitting by providing the model with inputs of combinations of available images that it has not yet encountered in a given order of occurrence. This type of approach is particularly advantageous in context embedding, as identical sequences of repetitive images may in themselves lead to overfitting due to their repetitive (non-random) order through iterations. On the other hand, if we vary not only the images but also the order of their context learning, then the context embedding layer can perform different parameter tunings due to the changing environment.

V. EXPERIMENTAL RESULTS

A. Dataset

We investigated a real problem for testing the Double-View Matching Network method in the recognition and classification of viral diseases using pathological chest X-rays, for which only a very limited number of training samples are available. It is easy to imagine the potential of such a solution, which can detect new, almost unknown diseases without the use of extensive data collection and expertise (oracle), even at the beginning of an outbreak like COVID-19.

A publicly available COVID-19 data set [1] was used to design the experimental environment, which was expanded with chest X-rays of other diseases. It is important to note that the recordings are not assignable to humans, are completely anonymized, and do not contain any patient-specific information in their metadata. As we mentioned before, two types of recording perspectives for each disease in the data set are available - frontal and profile (side) recording. The well-known multi-view solutions [11] cannot be used because only one view was recorded at each patient.

The complete data set contains 758 records of a total of 19 disease classes. After data cleaning (removal of erroneous, watermarked, etc. recordings), 680 recordings from 15 classes were added to the final data set. Another special circumstance is that image collections from different sources have different resolutions, with the smallest reaching only 150x150 and the largest reaching up to 2500x2500 pixels. Regarding the classes of the data set, it shows an unequal number of samples for each perspective:

- Completely unbalanced (only images from one perspective can be found in the samples) classes include the following diseases: ecoli, ards, sars.
- Balanced (same number of images from both views): influenza, mycoplasma, bacterial, chlamydomphila, COVID-19.
- For the other classes, there are recordings from both perspectives, but not in equal numbers: klebsiella, legionella, lipoid, pneumocystis, pneumonia, streptococcus, varicella.

The abnormalities of the lung caused by the COVID-19 virus are well recognized in the images in Figure 3 as a good example. Left side: symptoms are recognizable from “denser” lung areas, right side: “denser” areas are depicted on a heat map.

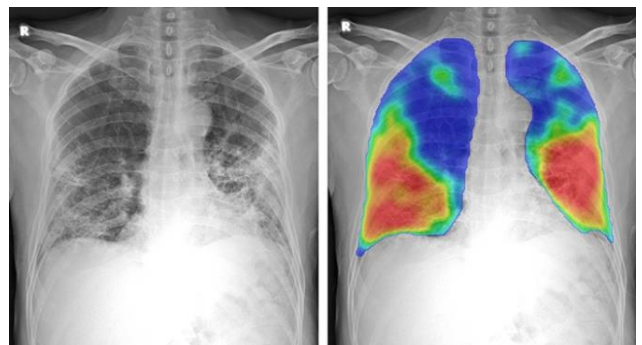


Figure 3. Chest X-ray showing COVID-19 symptoms.

B. Baseline classifier

Before measuring the performance of the proposed method, a baseline solution with k-NN (k-Nearest Neighbor) classifier was developed as a baseline. Measurement results were obtained by comparing and classifying 1-NN (nearest neighbor) characteristic vectors for averaging over 5 random test sets, as shown in the Table 2.

| Number of train and test classes | accuracy      |
|----------------------------------|---------------|
| 4 train – 2 test                 | 0.6980        |
| 4 train – 4 test                 | 0.6499        |
| 6 train – 2 test                 | 0.6563        |
| 6 train – 4 test                 | 0.6499        |
| 8 train – 2 test                 | 0.6199        |
| 8 train – 4 test                 | 0.5567        |
| <b>Average</b>                   | <b>0.6384</b> |

Table 2. Results of the k-NN classifier

The data in the table show the following trends: as the number of known classes increases, the accuracy decreases, and the accuracy of the model also decreases by estimating more and more classes within the same class number group.

C. Test scenarios

After the implementation of DVMN classifier, it was necessary to create a comprehensive plan. Three testing scenarios have been developed that are suitable for testing different types of tasks:

- i. New world scenario: it measures the ability to classify new classes after learning (e. g., the recognition of new diseases).
  1. phase: learning distance metrics based on set  $S_B$ , where there are  $N_C$  classes in set  $S_B$ .
  2. phase: selection of a support set (disjoint from set  $S_B$ ) by selecting one (or a few) images per class from  $M$  new classes for the classifier.
  3. phase: prediction for unknown images belonging to one of the  $M$  new classes.
- ii. Standard scenario: after learning, measures the ability to classify in learned classes on new samples (i.e., on a disjoint test set).
  1. phase is the same as in the first scenario (i/1).
  2. phase: select support set from set  $S_B$ .
  3. phase: prediction for unknown images belonging to one of the  $N_C$  known classes.
- iii. Hybrid scenario: after learning, measures the ability to classify in learned and new classes (i.e., the test set includes both known and unknown classes).
  1. phase is the same as in the first scenario (i/1).
  2. phase: selection of support set by selecting one (or a few) images from class  $K$  (known and unknown) for each class.
  3. phase: prediction for unknown images belonging to one of the  $K$  classes.

The results of each test plan are presented below, where the tables show the accuracy values (i.e., the ratio of the correct decision to the total classification decision). 1/2/5-shot learning was tested using 1/2/5 samples per class, and the notation in the

header of the rows is as follows: C <training classes> / C <test classes> / S <samples per class> / E <number of the epochs>.

The results in Table 3 were measured on the data set described earlier with the baseline classifier (i.e., there was no double-view feature as with DVMN), where the images include recordings from multiple perspectives. As a baseline, we were interested in the results of three scenarios simulating different test circumstances. The measured values in the table clearly show that even the baseline classifier is able to classify with relatively good accuracy in the “Standard” scenario; the results of the “New World” scenario provided an encouraging starting point for recognizing unknown diseases as the main goal of the research, using already known diseases.

| Number of train, test classes, shots and epochs | New World scenario | Standard scenario | Hybrid scenario |
|---|--------------------|-------------------|-----------------|
| C4/C2/S2/E1                                     | 0.920              | 0.939             | 0.766           |
| C4/C2/S2/E5                                     | 0.924              | 0.896             | 0.846           |
| C4/C2/S2/E10                                    | 0.898              | 0.904             | 0.825           |
| C4/C4/S2/E1                                     | 0.620              | 0.759             | 0.800           |
| C4/C4/S2/E5                                     | 0.760              | 0.892             | 0.823           |
| C4/C4/S2/E10                                    | 0.742              | 0.890             | 0.805           |
| C6/C2/S2/E1                                     | 0.779              | 0.939             | 0.750           |
| C6/C2/S2/E5                                     | 0.800              | 0.888             | 0.776           |
| C6/C2/S2/E10                                    | 0.793              | 0.898             | 0.770           |
| C6/C4/S2/E1                                     | 0.759              | 0.779             | 0.699           |
| C6/C4/S2/E5                                     | 0.648              | 0.836             | 0.693           |
| C6/C4/S2/E10                                    | 0.708              | 0.858             | 0.673           |
| C8/C2/S2/E1                                     | 0.960              | 0.940             | 0.600           |
| C8/C2/S2/E5                                     | 0.884              | 0.868             | 0.726           |
| C8/C2/S2/E10                                    | 0.872              | 0.870             | 0.713           |
| C8/C4/S2/E1                                     | 0.680              | 0.800             | 0.766           |
| C8/C4/S2/E5                                     | 0.720              | 0.880             | 0.746           |
| C8/C4/S2/E10                                    | 0.690              | 0.818             | 0.726           |
| <b>Average</b>                                  | <b>0.7808</b>      | <b>0.8696</b>     | <b>0.7501</b>   |

Table 3. Accuracy results of test scenarios

In the Table 3, the three numerical values below each other belong to a common measurement in such a way that the accuracy values after 1, 5, and 10 epochs were measured. In most cases, after the 5<sup>th</sup> epoch, the training reached the accuracy value after that the system could no longer learn. In order to avoid overfitting, we used the results after the 5<sup>th</sup> epoch; and the test results presented in the rest of the paper also include learnings up to the first 5 epochs.

D. Classification of unknown diseases, like COVID-19

In the following, the measurements of the “New World” scenario, which simulates the recognition of new diseases, is the topic that gives the main objective of our research. The tables compare the classifiers:

- MN (Matching Network) for only first, and for only second view (and average accuracy of them),
- k-NN classifier for only first, and for only second view (and average accuracy of them),
- DVMN as our proposed method
- k-NN classifier for two views

- MN (Matching Network) for all data (without distinguishing views)
- k-NN classifier for all data (without distinguishing views)

Looking at the results in Table 4, it can be seen that the DVMN method performs best with an average accuracy of 81.2%, even when using a single sample for the one-shot-learning task.

| # train, test class, shots | Average of 2 different views |                | Double view   |             | Without distinguishing views |        |
|----------------------------|------------------------------|----------------|---------------|-------------|------------------------------|--------|
|                            | Ave. of 2 MN                 | Ave. of 2 k-NN | DVMN          | 2-view k-NN | MN                           | k-NN   |
| accuracies                 |                              |                |               |             |                              |        |
| C4/C2/S1                   | <b>0.8566</b>                | 0.6560         | 0.7766        | 0.6200      | 0.8380                       | 0.5833 |
| C4/C4/S1                   | <b>0.8683</b>                | 0.6333         | 0.8333        | 0.6366      | 0.7640                       | 0.6500 |
| C6/C2/S1                   | 0.8149                       | 0.5933         | <b>0.8200</b> | 0.6600      | 0.7940                       | 0.6499 |
| C6/C4/S1                   | 0.7599                       | 0.5426         | <b>0.7600</b> | 0.5666      | 0.7240                       | 0.5400 |
| C8/C2/S1                   | 0.7450                       | 0.6205         | 0.8333        | 0.6000      | <b>0.8740</b>                | 0.5600 |
| C8/C4/S1                   | 0.7900                       | 0.6220         | <b>0.8466</b> | 0.5200      | 0.7700                       | 0.6199 |
| <b>Average</b>             | 0.8057                       | 0.6112         | <b>0.8116</b> | 0.6005      | 0.7940                       | 0.6005 |
| F <sub>1</sub> scores      | Ave. of 2 MN                 | Ave. of 2 k-NN | DVMN          | 2-view k-NN | MN                           | k-NN   |
| C4/C2/S1                   | <b>0.795</b>                 | 0.574          | 0.762         | 0.510       | 0.751                        | 0.480  |
| C4/C4/S1                   | 0.743                        | 0.570          | <b>0.795</b>  | 0.593       | 0.746                        | 0.546  |
| C6/C2/S1                   | 0.704                        | 0.524          | <b>0.776</b>  | 0.604       | 0.717                        | 0.587  |
| C6/C4/S1                   | 0.701                        | 0.492          | <b>0.724</b>  | 0.530       | 0.709                        | 0.519  |
| C8/C2/S1                   | 0.725                        | 0.586          | 0.797         | 0.549       | <b>0.800</b>                 | 0.556  |
| C8/C4/S1                   | 0.745                        | 0.577          | <b>0.810</b>  | 0.507       | 0.766                        | 0.532  |
| <b>Average</b>             | 0.736                        | 0.554          | <b>0.777</b>  | 0.549       | 0.748                        | 0.537  |

Table 4. Accuracies and F<sub>1</sub> scores of 1-shot learning at New World scenario

| # train, test class, shots | Average of 2 different views |                | Double view   |             | Without distinguishing views |        |
|----------------------------|------------------------------|----------------|---------------|-------------|------------------------------|--------|
|                            | Ave. of 2 MN                 | Ave. of 2 k-NN | DVMN          | 2-view k-NN | MN                           | k-NN   |
| accuracies                 |                              |                |               |             |                              |        |
| C4/C2/S2                   | 0.9000                       | 0.6828         | 0.8633        | 0.6300      | <b>0.924</b>                 | 0.6980 |
| C4/C4/S2                   | <b>0.9000</b>                | 0.6616         | 0.8434        | 0.5833      | 0.760                        | 0.6499 |
| C6/C2/S2                   | 0.8459                       | 0.6425         | <b>0.8566</b> | 0.6166      | 0.800                        | 0.6563 |
| C6/C4/S2                   | 0.7680                       | 0.6649         | <b>0.7966</b> | 0.6500      | 0.678                        | 0.6499 |
| C8/C2/S2                   | 0.7739                       | 0.6636         | <b>0.9133</b> | 0.5333      | 0.884                        | 0.6199 |
| C8/C4/S2                   | 0.7340                       | 0.6499         | <b>0.8666</b> | 0.5833      | 0.720                        | 0.5567 |
| <b>Average</b>             | 0.8203                       | 0.6608         | <b>0.8566</b> | 0.5994      | 0.7943                       | 0.6384 |
| F <sub>1</sub> scores      | Ave. of 2 MN                 | Ave. of 2 k-NN | DVMN          | 2-view k-NN | MN                           | k-NN   |
| C4/C2/S2                   | <b>0.836</b>                 | 0.561          | 0.810         | 0.547       | 0.826                        | 0.570  |
| C4/C4/S2                   | <b>0.792</b>                 | 0.526          | 0.772         | 0.515       | 0.731                        | 0.535  |
| C6/C2/S2                   | 0.771                        | 0.576          | <b>0.791</b>  | 0.536       | 0.754                        | 0.514  |
| C6/C4/S2                   | 0.707                        | 0.511          | <b>0.745</b>  | 0.510       | 0.667                        | 0.556  |
| C8/C2/S2                   | 0.735                        | 0.595          | <b>0.843</b>  | 0.479       | 0.814                        | 0.547  |
| C8/C4/S2                   | 0.684                        | 0.540          | <b>0.786</b>  | 0.524       | 0.659                        | 0.486  |
| <b>Average</b>             | 0.754                        | 0.552          | <b>0.791</b>  | 0.519       | 0.742                        | 0.535  |

Table 5. Accuracies and F<sub>1</sub> scores of 2-shot learning at New World scenario

It can be read from Table 5 that in the case of increasing the number of samples, in the vast majority of test cases, the

DVMN method achieves the best classification performance with an average accuracy of 85.7% in 2-shot learning.

At 5-shot learning, significantly fewer samples are available from the second view than from the first, so a comparison of the results would not have been statistically possible. Although fewer test cases were available compared to the previous two measurements (Tables 4 and 5), the results of Table 6 showed that the performance of the DVMN classifier is the best in this case as well, with an average accuracy of 85.4%.

| # train, test class, shots | First view       |                    | Double view   |             | Without distinguishing views |        |
|----------------------------|------------------|--------------------|---------------|-------------|------------------------------|--------|
|                            | first view of MN | first view of k-NN | DVMN          | 2-view k-NN | MN                           | k-NN   |
| accuracies                 |                  |                    |               |             |                              |        |
| C4/C2/S5                   | 0.8180           | 0.6333             | <b>0.8433</b> | 0.6400      | 0.7780                       | 0.6100 |
| C4/C4/S5                   | 0.7580           | 0.5800             | 0.7960        | 0.5200      | <b>0.8159</b>                | 0.6400 |
| C6/C2/S5                   | 0.8320           | 0.6599             | <b>0.924</b>  | 0.4400      | 0.8539                       | 0.6333 |
| <b>Average</b>             | 0.8026           | 0.6244             | <b>0.8544</b> | 0.533       | 0.8159                       | 0.6277 |
| F <sub>1</sub> scores      | first view of MN | first view of k-NN | DVMN          | 2-view k-NN | MN                           | k-NN   |
| C4/C2/S5                   | 0.746            | 0.529              | <b>0.770</b>  | 0.568       | 0.710                        | 0.535  |
| C4/C4/S5                   | 0.697            | 0.520              | 0.706         | 0.475       | <b>0.764</b>                 | 0.510  |
| C6/C2/S5                   | 0.763            | 0.547              | <b>0.836</b>  | 0.437       | 0.776                        | 0.493  |
| <b>Average</b>             | 0.735            | 0.532              | <b>0.771</b>  | 0.493       | 0.750                        | 0.513  |

Table 6. Accuracies and F<sub>1</sub> scores of 5-shot learning at New World scenario

VI. CONCLUSION

The few-shot learning problem presented in this paper intends to help the work of those working in medicine by analyzing pathological X-ray recordings, using only very few images. Although there are solutions, if the images come from different views, they will not handle these views well. We proposed an improved method, the so-called Double-View Matching Network (DVMN based on the deep neural network), which solves the few-shot learning problem as well as the different views of the pathological recordings in the images. The main contribution of this paper is the convolutional neural network for feature extraction and handling the multi-view in image representation. Our method was tested in the classification of images showing unknown COVID-19 symptoms in an environment designed for learning a few samples, with prior meta-learning on images of other diseases only. We compared the results with k-NN classifiers, with different variants of the Matching Network method (one variant for only one view and another without distinguishing views). The results show that DVMN reaches the best accuracy on multi-view dataset (better than Matching Network as well) at 1-shot, 2-shot, and 5-shot learning.

ACKNOWLEDGMENT

The research has been supported by the European Union, co-financed by the European Social Fund (EFOP-3.6.2-16-2017-00013, Thematic Fundamental Research Collaborations Grounding Innovation in Informatics and Info-communications).

Double-View Matching Network for Few-Shot Learning to Classify Covid-19 in X-ray images

REFERENCES

[1] Cohen, J. P., Morrison, P., Dao, L., Roth, K., Duong, T. Q. and Ghassemi, M. (2020). COVID-19 Image Data Collection: Prospective Predictions Are the Future, arXiv:2006.11988, <https://github.com/ieee8023/covid-chestxray-dataset>

[2] Collier, M., & Beel, J. (2019). Memory-Augmented Neural Networks for Machine Translation. arXiv preprint arXiv:1909.08314.

[3] Finn, C., Abbeel, P., & Levine, S. (2017). Model-agnostic meta-learning for fast adaptation of deep networks. In Proceedings of the 34th International Conference on Machine Learning (ICML 2017), Volume 70 (pp. 1126-1135). doi: 10.5555/3305381.3305498

[4] Garcia, V., & Bruna, J. (2017). Few-shot learning with graph neural networks. arXiv preprint arXiv:1711.04043.

[5] Geras, K. J., Wolfson, S., Shen, Y., Wu, N., Kim, S., Kim, E., ... & Cho, K. (2017). High-resolution breast cancer screening with multi-view deep convolutional neural networks. arXiv preprint arXiv:1703.07047.

[6] Goodrich, R. K. (1970). A Riesz representation theorem. Proceedings of the American Mathematical Society, 24(3), 629-636. doi: 10.1090/S0002-9939-1963-0145334-0

[7] Jain, P. (2018). Metric Learning Tutorial. [https://parajain.github.io/metric\\_learning\\_tutorial/](https://parajain.github.io/metric_learning_tutorial/)

[8] Kan M, Shan S. and Chen X., (2016). Multi-view Deep Network for Cross-View Classification, Proceedings of the IEEE Conference on Computer Vision and Pattern Recognition (CVPR), Las Vegas, NV, pp. 4847-4855, doi: 10.1109/CVPR.2016.524

[9] Koch, G., Zemel, R., & Salakhutdinov, R. (2015). Siamese neural networks for one-shot image recognition. In ICML deep learning workshop (Vol. 2).

[10] Kondor, R. (2003). A Short Introduction to Hilbert Space Methods in Machine Learning. Tutorial at Columbia University.

[11] Li, Y., Yang, M., & Zhang, Z. (2018). A survey of multi-view representation learning. IEEE transactions on knowledge and data engineering, vol. 31, no. 10, pp. 1863-1883, doi: 10.1109/TKDE.2018.2872063

[12] Metzen, J. H., Kröger, T., Schenk, A., Zidowitz, S., Peitgen, H. O., & Jiang, X. (2009). Matching of anatomical tree structures for registration of medical images. Image and Vision Computing, Volume 27, Issue 7, pp. 923-933. doi: 10.1016/j.imavis.2008.04.002

[13] Mishra, N., Rohaninejad, M., Chen, X., & Abbeel, P. (2017). Meta-learning with temporal convolutions. arXiv preprint arXiv:1707.03141, v3.

[14] Papp, D., & Szűcs, G. (2017). Balanced active learning method for image classification. Acta Cybernetica, 23(2), 645-658. doi: 10.14232/actacyb.23.2.2017.13

[15] Papp, D., & Szűcs, G. (2018). Double probability model for open set problem at image classification. Informatica, 29(2), 353-369. doi: 10.15388/Informatica.2018.171

[16] Ramachandra, B., Jones, M.J., & Vatsvai, R. (2020). Learning a distance function with a Siamese network to localize anomalies in videos. 2020 IEEE Winter Conference on Applications of Computer Vision (WACV), 2587-2596.

[17] Seeland, M., & Mäder, P. (2021). Multi-view classification with convolutional neural networks. Plos ONE, 16(1), e0245230. doi: 10.1371/journal.pone.0245230

[18] Shyam, P., Gupta, S., & Dukkipati, A. (2017). Attentive recurrent comparators. In Proceedings of the 34th International Conference on Machine Learning - Volume 70 pp. 3173-3181. doi: 10.5555/3305890.3306009

[19] Simonyan, K., & Zisserman, A. (2014). Very deep convolutional networks for large-scale image recognition. arXiv preprint arXiv:1409.1556.

[20] Snell, J., Swersky, K., & Zemel, R. (2017). Prototypical networks for few-shot learning. In Advances in neural information processing systems, pp. 4077-4087. doi: 10.5555/3294996.3295163

[21] Sung, F., Yang, Y., Zhang, L., Xiang, T., Torr, P. H., & Hospedales, T. M. (2018). Learning to compare: Relation network for few-shot learning. In Proceedings of the IEEE conference on computer vision and pattern recognition (pp. 1199-1208).

[22] Szegedy, C., Liu, W., Jia, Y., Sermanet, P., Reed, S., Anguelov, D., ... & Rabinovich, A. (2015). Going deeper with convolutions. In Proceedings of the IEEE Conference on Computer Vision and Pattern Recognition (CVPR) pp. 1-9. doi: 10.1109/CVPR.2015.7298594

[23] Szűcs, G., & Henk, Z. (2015). Active clustering based classification for cost effective prediction in few labeled data problem. Academy of Economic Studies. Economy Informatics, vol. 15, no. 1/2015, pp. 5-13.

[24] Szűcs, G., Papp, D., & Lovas, D. (2014). Viewpoints combined classification method in image-based plant identification task. In Working Notes for CLEF 2014 Conference, vol. 1180, pp. 763-770.

[25] Vinyals, O., Blundell, C., Lillicrap, T., & Wierstra, D. (2016). Matching networks for one-shot learning. Advances in neural information processing systems, 29, 3630-3638. doi: 10.5555/3157382.3157504

[26] Wang, Y., Yao, Q., Kwok, J. T., & Ni, L. M. (2020). Generalizing from a few examples: A survey on few-shot learning. ACM Computing Surveys (CSUR), 53(3), 1-34. doi: 10.1145/3386252

[27] Zhao, A., Balakrishnan, G., Durand, F., Guttag, J. V., & Dalca, A. V. (2019). Data augmentation using learned transformations for one-shot medical image segmentation. In Proceedings of the IEEE Conference on Computer Vision and Pattern Recognition (CVPR) pp. 8543-8553. doi: 10.1109/CVPR.2019.00874

[28] Ziko, I., Dolz, J., Granger, E., & Ayed, I. B. (2020). Laplacian regularized few-shot learning. Proceedings of the 37th International Conference on Machine Learning, PMLR 119, pp. 11660-11670.



**Gábor Szűcs** has received MSc in electrical engineering and PhD in computer science from the Budapest University of Technology and Economics (BME) in 1994 and in 2002, respectively. He is an at Department of Telecommunications and Media Informatics of BME. His research areas are data science, artificial intelligence, deep learning, content-based image retrieval, multimedia mining. The number of his publications is more than 100. He is the president of the Artificial Intelligence Section of HTE (Scientific Association for Infocommunications), he is the leader of the research group DCLAB (Data Science and Content Technologies). He has earned János Bolyai Research Scholarship of the Hungarian Academy of Science some years ago.



**Marcell Németh** was born in Budapest, Hungary in 1997. He is a MSc student at the Budapest University of Technology and Economics, Faculty of Electrical Engineering and Informatics as computer engineering. His research activities are data science, data series analytics, image recognition and machine learning. He took second place in the Students' Scientific Conference 2020 at Budapest University of Technology and Economics.

# Towards Machine Learning-based Anomaly Detection on Time-Series Data

Daniel Vajda, Adrian Pekar, and Karoly Farkas

**Abstract**—The complexity of network infrastructures is exponentially growing. Real-time monitoring of these infrastructures is essential to secure their reliable operation. The concept of telemetry has been introduced in recent years to foster this process by streaming time-series data that contain feature-rich information concerning the state of network components. In this paper, we focus on a particular application of telemetry — anomaly detection on time-series data. We rigorously examined state-of-the-art anomaly detection methods. Upon close inspection of the methods, we observed that none of them suits our requirements as they typically face several limitations when applied on time-series data. This paper presents Alter-Re<sup>2</sup>, an improved version of ReRe, a state-of-the-art Long Short-Term Memory-based machine learning algorithm. Throughout a systematic examination, we demonstrate that by introducing the concepts of ageing and sliding window, the major limitations of ReRe can be overcome. We assessed the efficacy of Alter-Re<sup>2</sup> using ten different datasets and achieved promising results. Alter-Re<sup>2</sup> performs three times better on average when compared to ReRe.

**Index Terms**—anomaly detection, LSTM, neural network, time-series data, Alter-Re<sup>2</sup>.

## I. INTRODUCTION

**N**OWADAYS, infrastructure monitoring, including networks, systems, and services, is more critical than ever before. It is essential for several reasons, such as alerting partial or total system malfunction, outage prevention based on predictive identification of such situations, performance tracking, and, last but not least, security detection of system penetration.

However, with the exponential increase in the number of interconnected devices and traffic volume, it has become far from obvious how to achieve timely, reliable, and sound infrastructure monitoring. It requires understanding the details of system processes and recognize how they influence each other or the whole infrastructure. The concept of network telemetry has been introduced to streamline this goal. It allows automated, fast, and simultaneous collection of a wide variety of time-series data from a large number of devices. However, processing massive data volumes is challenging, especially in terms of timeliness and scalability.

Machine learning techniques can process, understand, and classify problematic infrastructure behaviours, even in massive data volumes. Despite recent advances in machine learning, their application to anomaly detection remains poorly understood and investigated in the network telemetry domain. This

paper attempts to shed new light on anomaly detection on time-series telemetry data.

Anomaly detection is a critical component of network and services management as it can provide valuable insights into the operation of the network and its components. Broadly speaking, measurement data are created by a generating process. If this generating process behaves unusually due to the system's abnormal behaviour or the entity that impacts the generating process, it produces anomalies. The manifestation of anomalous behaviour can be identified by examining the generated time-series data.

Our survey of anomaly detection on time-series data yielded ReRe [1], a Long Short-Term Memory (LSTM) [2] based machine learning algorithm, as one of the most promising state-of-the-art approaches. ReRe is claimed to achieve high accuracy in detecting abnormal behaviour while minimizing false positives and re-trainings. However, our evaluation revealed several limitations when ReRe was applied on time-series data. Thus, we introduce Alter-Re<sup>2</sup>, an enhanced version of ReRe which extends the original algorithm with two additional features to improve its efficacy. The first feature ensures that the collected data ages out; thus, its weight decreases as time passes, allowing faster adaption to short-term history and more precise anomaly detection. The second feature serves the purpose of a sliding window that reduces the anomaly detector's resource demands.

The evaluation of our approach with ten different time-series datasets has shown promising results. Alter-Re<sup>2</sup> achieved approximately three times higher but never worse anomaly detection accuracy as opposed to ReRe. Not only could we eliminate issues obstructing real-time use, but we also enhanced sensitivity to detect anomalies with smaller amplitude and length. That said, we argue the strong applicability of Alter-Re<sup>2</sup> in real-world scenarios.

The rest of this paper is organized as follows. In Section II, we discuss related works in the field of anomaly detection on time series, especially network telemetry-related data. Section III describes two state-of-the-art time-series anomaly detection algorithms — RePAD [3] and ReRe [1]. In Section IV, we present Alter-Re<sup>2</sup>, our approach to address the identified limitations. In Section V, we present experiments to examine Alter-Re<sup>2</sup> performance when compared to ReRe. Finally, Section VI draws conclusions while also discussing further research implications and work directions.

## II. RELATED WORK

Despite the recent proliferation of telemetry in networking, there is only a handful of research in the topic of anomaly

<sup>1</sup>The authors are with the Department of Networked Systems and Services, Budapest University of Technology and Economics, Budapest, Hungary. Karoly Farkas is also with NETvisor Ltd., Budapest, Hungary.

E-mail: vajdadaniellaszlo@edu.bme.hu, {apekar, farkask}@hit.bme.hu

detection. Putina *et al.* [4] at Cisco developed a streaming telemetry-based anomaly detection engine for BGP anomalies. However, it uses a legacy clustering algorithm called DenStream [5] that has limited performance.

Other works with limited applicability to anomalies and computer networks include [6], [7]. Ye *et al.* [6] use a statistical approach to detect zero-day attacks and malicious intent. The paper claims that machine learning techniques miss the bigger picture of network behaviour. Kaiafas *et al.* [7] use multiple unsupervised machine learning algorithms in an ensemble to identify fraudulent private exchange phone calls, yet their approach only works on off-line data.

More generic real-time anomaly detection approaches are AnomalyDetectionTs (ADT) and AnomalyDetectionVec (ADV) developed by Twitter [8]. ADT works on time-series data, while ADV is designed for vectors without timestamp information. These algorithms employ statistical-based approaches, therefore require massive data points. This results in poor applicability to streaming time-series data.

In spite of the limited number of directly applicable research in the area of network traffic anomaly detection, the trend of using machine learning solutions for time-series analysis is emerging. Syal *et al.* [9] propose an SVM (Support Vector Machine) [10] based supervised learning method to detect abnormally slow network transfers in real time, focusing on TCP flows. Pilinszki-Nagy *et al.* [11] analyze and investigate a special type of artificial neural network called HTM (Hierarchical Temporal Memory) [12] to model and predict sequential data, including time series. They use off-line, unsupervised learning to train the HTM model. Unfortunately, they discuss only the prediction part of anomaly detection and do not deal with the decision logic to indicate anomalous data.

A few recent works have proposed and investigated the applicability of deep learning, especially LSTM [2] and AutoEncoder [13] based methods for anomaly detection on time-series data. Zhou *et al.* [14] propose an off-line, variational LSTM learning model based on reconstructed feature representation to detect anomaly on industrial big data. Lazaris *et al.* [15] aim to predict fine-grained network traffic using an LSTM model in the domain of SDN (Software-Defined Networking). Soheil *et al.* [16] investigate aspects of network traffic forecasting using real-world data streams and two machine learning models, namely LSTM and SARIMA (Sequential Auto-Regressive Integrated Moving Average) [17], in a supervised manner. Unfortunately, they focus only on traffic prediction and do not deal with the anomaly detection logic. Gjorgiev *et al.* [18] propose several off-line deep learning architectures based on variational AutoEncoders [19] for detecting cyber-attacks on water distribution system. They calculate the Mahalanobis distance [20] instead of the traditional mean square error in the objective function to get better performance. RE-ADTS [21] is an unsupervised anomaly detection approach using a deep AutoEncoder model that can be applied either to batch or real-time anomaly detection. It seems to perform evenly well on time-series datasets from various domains. STAD [22] is a dynamic on-line data mining technique; an automated framework to detect cellular network anomalies. It uses a combination of machine learning methods, such as OC-SVM

(One-class SVM) [23], SVR (Support Vector Regression) [24], and LSTM. Similarly, Said Elsayed *et al.* [25] propose a hyper approach based on LSTM AutoEncoder and OC-SVM to detect anomalies based attacks in SDN environments. However, it is not clear how this method can be applied in real time. LSTM-FUZZY [26] is a system to detect and mitigate different attacks in SDN environments. In this system, LSTM is used for network traffic forecasting since fuzzy logic is applied for anomaly detection.

The Greenhouse [27] algorithm fits our design goals best, combining state-of-the-art machine learning and data management methods for anomaly prediction over immense volumes of time-series data. The algorithm must be trained on normal data but does not require labeled anomalies, which technique is referred to as ‘zero-positive’ or semi-supervised learning. Greenhouse uses a look-back, predict-forward approach to detect anomalies. It employs an LSTM model to first predict new values based on old ones, then compares the prediction to the actual data point. RePAD [3] is an improvement of Greenhouse that eliminates the need for normal training data. ReRe [1] is an upgrade of RePAD that aims to mitigate false positive detections. As ReRe appeared to be the most suitable approach for our work, we base our approach for streaming telemetry anomaly detection on it. A detailed description of RePAD and ReRe is provided in Section III.

In summary, there is only a handful of existing works aimed at anomaly detection in streaming telemetry data. Generic real-time anomaly detectors, however, have gone through a major improvement in the last decade. Despite recent advances, they still face several challenges. For example, anomaly detection in an unsupervised manner is limited, while other approaches need domain knowledge to set critical parameters or cannot adapt to changing behaviours.

### III. BACKGROUND AND MOTIVATION

#### A. RePAD

RePAD [3] developed by Lee *et al.* is a cutting-edge LSTM-based algorithm designed for time-series anomaly detection. The authors claim that RePAD can detect anomalies proactively in real time, without domain knowledge.

RePAD uses short-term historical data points to predict the upcoming value; then, it compares this prediction with the real value to determine if an anomaly is likely to happen in the near future. RePAD can adjust detection thresholds dynamically, making it well-suited to tolerate minor pattern changes as well. Its fast convergence (i.e., it can detect anomalies soon after start) and unsupervised training (i.e., it does not require a labelled dataset) set it apart from previous approaches.

A key part of RePAD is the LSTM model used for data prediction. LSTMs are a type of recurrent artificial neural networks (RNNs). LSTMs form layers of neurons. One neuron can have many input and output connections. We assign weights to these connections that impact the propagation of information through the network. Training consists of multiple forward and backward passes (one round is called an ‘epoch’) during which these weights and other parameters are tuned to reflect certain patterns. Essentially, if an LSTM model has

a complicated structure or the training data is large, training time increases significantly, limiting real-time use. That is why the LSTM model used in RePAD has only one hidden layer with ten hidden units. Additionally, a fast learning speed is guaranteed by a learning rate of 0.15. The number of epochs is a key factor in determining the precision and speed of a neural network model. RePAD employs Early Stopping [28] to choose the number of epochs dynamically, which aims to prevent overfitting and underfitting. A detailed discussion of LSTMs is out of the scope of this work. For a better comprehension of the topic, we refer the reader to [2], [29], [30].

RePAD is based on a so-called ‘look back, predict forward’ approach. It takes the previous  $b$  data points ( $b$  is the look-back parameter) and uses them to predict the next  $f$  data points ( $f$  is the predict-forward parameter). RePAD uses  $f = 1$ . The operation of RePAD is presented in Algorithm 1 ( $M$ ,  $M'$  denote the LSTM models). The algorithm uses four equations:

$$AARE_t = \frac{1}{t - b + 1} \cdot \sum_{y=b}^t \frac{|v_y - \hat{v}_y|}{v_y} \quad (1)$$

where

- $AARE_x$  = Average Absolute Relative Error at timestep  $x$ ;
- $t$  = current timestep, starts from  $t = 0$ ;
- $b$  = look-back parameter;
- $v_x$  = data point at timestep  $x$ ;
- $\hat{v}_x$  = predicted data point for timestep  $x$ .

AARE is a well-known measure for determining the accuracy of prediction. A low AARE value indicates that the forecast value is close to the observed value [3].

$$\mu_{AARE,t} = \frac{1}{t - b + 1} \cdot \sum_{y=b}^t AARE_y \quad (2)$$

where

- $\mu_{AARE,x}$  = the average of  $AARE_y$  values at timestep  $x$ .

$$\sigma_{AARE,t} = \sqrt{\frac{\sum_{y=b}^t (AARE_y - \mu_{AARE,t})^2}{t - b + 1}} \quad (3)$$

where

- $\sigma_{AARE,x}$  = the standard deviation of  $AARE_y$  values at timestep  $x$ .

$$thd_t = \mu_{AARE,t} + 3 \cdot \sigma_{AARE,t} \quad (4)$$

where

- $thd_x$  = threshold value at timestep  $x$ .

As seen above in Equation (4), the  $thd_x$  values are determined using the Three-Sigma Rule [31], which is commonly used for anomaly detection threshold calculation.

From Algorithm 1, it is evident that RePAD requires only a short preparation for anomaly detection. However, a major flaw of this approach is the relatively high number of false positives it yields. Lee *et al.* strive to overcome this shortcoming by ReRe, a refinement of the RePAD algorithm.

---

### Algorithm 1 RePAD

---

```

1: t = 0
2: while (t++) do
3:   Collect data point  $v_t$ 
4:   if t < b - 1 then
5:     ▷ Step 1: collect  $b - 1$  points passively
6:   else if t == b - 1 then
7:     ▷ Step 2: first training and prediction
8:     Train the LSTM model  $M$  using the first  $b$  data
9:     points:  $v_0, \dots, v_t = v_{b-1}$ 
10:    Predict the next data point  $\hat{v}_{t+1} = \hat{v}_b$  using  $M$ 
11:   else if b - 1 < t < 2b - 1 then
12:     ▷ Step 3: preparing for detection
13:     Calculate  $AARE_t$  using Equation (1)
14:     Train the LSTM model  $M$  using the previous  $b$ 
15:     data points:  $v_{t-b+1}, \dots, v_t$ 
16:     Predict the next data point  $\hat{v}_{t+1}$  using  $M$ 
17:   else if t ≥ 2b - 1 then
18:     ▷ Step 4: anomaly detection
19:     Calculate  $AARE_t$  using Equation (1)
20:     Calculate  $thd_t$  using Equations (2), (3) and (4)
21:     if  $AARE_t \leq thd_t$  then
22:       ▷  $v_t$  is similar to previous points, NO
23:       ANOMALY
24:     Predict the next data point  $\hat{v}_{t+1}$  using  $M$ 
25:   else
26:     ▷ Pattern change or anomaly
27:     Train the LSTM model  $M'$  using the previous
28:      $b$  data points
29:     Predict the current point  $\hat{v}_t$  again using  $M'$ 
30:     Recalculate  $AARE_t$  using Equation (1)
31:     if  $AARE_t > thd_t$  then
32:       Signal an ANOMALY
33:       Discard  $M'$  and use  $M$  to predict the next
34:       data point  $\hat{v}_{t+1}$ 
35:     else
36:       Signal a PATTERN CHANGE
37:       Replace  $M$  with  $M'$  to predict new points
38:       accurately
39:     Use  $M$  to predict the next data point  $\hat{v}_{t+1}$ 

```

---

### B. ReRe

ReRe employs two LSTM models that provide two levels of detection sensitivity. They are deployed in two detectors:

*Detector 1:* operates the same way as RePAD described in Section III-A. It first acquires  $t$  and  $v_t$  values and then produces one of the three output signals, namely ‘normal,’ ‘pattern change,’ and ‘anomaly.’ Fundamentally, it stores and calculates  $AARE_t$  and  $thd_t$  using RePAD methods and Equations (1) to (4). When it detects a pattern change, it retrains its own LSTM model,  $M_1$  that is used for data value prediction.

*Detector 2:* uses the same algorithm structure as RePAD while also acquiring  $t$  and  $v_t$  in the same way. However, the input values for  $AARE_t$  and  $thd_t$  are calculated variously. Specifically, Detector 2 uses its own  $M_2$  LSTM model to predict the values.  $M_2$  is structurally identical to  $M_1$ , but it

produces various predictions as it uses a different equation for calculating the  $thd_t$  threshold. Indeed, Detector 2 uses only  $AARE_x$  for this calculation, where  $v_x$  is considered ‘normal’ (no ‘pattern change’ or ‘anomaly’) by itself. Broadly speaking, this difference results in giving ReRe the capability to suppress anomalies detected by Detector 1 (RePAD). Finally, an anomaly or pattern change is only detected and signalled if both detectors return the same detection for a given timestep.

### C. Limitations

The current implementation of ReRe stores all the computed values and derived information since the beginning of its operation. Consequently, there is no upper bound on the memory requirements of ReRe. Moreover, the performance of ReRe significantly depends on the setting of the look-back parameter  $b$ , which has been pointed out and also discussed by the authors of RePAD / ReRe in their recent study [32]. Additionally, ReRe can only detect anomalies when both detectors have an  $AARE_t$  value higher than  $thd_t$ , and both detectors indicate no pattern change. That means, typically,  $AARE_y$  values are lower than  $thd_y$ .

In both RePAD and ReRe, the  $AARE_t$  and  $thd_t$  values are computed using Equation (1) and Equation (4). Both values include a sum whose starting value is fixed (i.e., timestep  $y = b$ ) and ends at the current timestep ( $y = t$ ). All terms in these sums have an equal weight of 1, which means that all terms have an equal priority in determining current  $AARE_t$  and  $thd_t$  values. As a result, the speed of anomaly detection is adversely impacted.

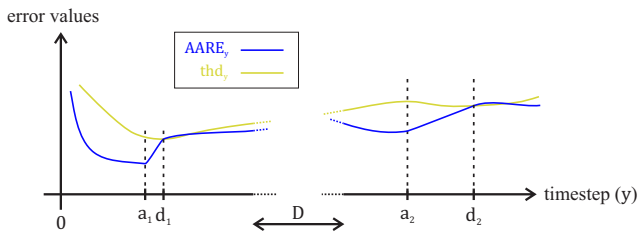


Fig. 1: The slope of AARE depends on the current timestep.

This issue is illustrated in Figure 1 on the left side of the graph. At timestep  $a_1$ , there is an anomaly in the dataset.  $AARE_y$  values start to rise rapidly as new absolute relative error terms are high, and there are only a few error terms to be averaged. At timestep  $d_1$ , the  $AARE_y$  curve crosses the  $thd_y$  curve and an anomaly is detected. However, when a considerable time has passed ( $D$  is at least a few thousand timesteps), a high count of terms in  $AARE_t$  calculation is to be averaged. Consequently, when an anomaly occurs at timestep  $a_2$ , the  $AARE_y$  curve starts to rise slowly, as averages increase slower with more terms (the impact of one new high term is proportionally less). As the starting timestep for the average is always  $y = b$ , the steepness of the slope decreases as  $y$  increases. That is why the anomaly at  $a_2$  is only detected at  $d_2$ .

Consider the algorithm runs in a real-world production environment, uninterrupted. Due to the flaw mentioned above,

it becomes very likely that some anomalies are unnoticed past a certain timestep. Indeed, in such a scenario, the  $AARE_y$  curve may never reach the  $thd_y$  curve since it normalises before normal data points arrive. These limitations of ReRe have motivated us to introduce our enhancements.

## IV. ALTER-RE<sup>2</sup>

Streaming network telemetry anomaly detection is not obvious. While there has been some attempts to detect anomalies on time-series data, as described above, they fall short when applied in a real-world production environment. To fill this important gap in the field, we enhanced ReRe, a real-time anomaly detection algorithm that is, to the best of our knowledge, a cutting-edge technique. Alter-RE<sup>2</sup>, our attempt towards machine learning-based anomaly detection on time-series data, comprises two enhancements — ageing and sliding window. In what follows, we describe these enhancements.

### A. Ageing

We designed ageing so that it places greater emphasis on a few previous data points instead of averaging them with the same weight. Our ultimate goal was to decrease the weight of a given data point as time elapses. We achieve this by introducing an extra ageing coefficient  $C_y$  in Equation (1), which yields the following formula:

$$AARE_{t,ageing} = \frac{1}{t-b+1} \cdot \sum_{y=b}^t C_y \cdot \frac{|v_y - \hat{v}_y|}{v_y} \quad (5)$$

The  $C_y$  coefficient is calculated using the following equation:

$$C_y = \left( \frac{y-W}{t-W} \right)^{AP} \quad (6)$$

where

- $y$  = timestep running variable in the sum;
- $W$  = starting timestep of the window (see details in Section IV-B);
- $AP$  = age power;
- $C_y$  = ageing coefficient.

### B. Sliding Window

ReRe stores all data from the point in time they were generated. We mitigate the consequence of this issue by storing only the previous value of the average error terms and the number of data points it was calculated from. This recursive method is formally expressed as follows:

$$AARE_t = \frac{1}{t-b+1} \cdot \left( AARE_{t-1} \cdot (t-b) + \frac{|v_t - \hat{v}_t|}{v_t} \right) \quad (7)$$

To calculate the threshold value  $thd_t$ , we need to determine the standard deviation of the  $AARE_y$  values. However,  $\sigma_{AARE,t}$  cannot be expressed only using values from the previous timestep  $t-1$  and the number of timesteps due to the

changing  $\mu_{AARE,y}$  values in every timestep. Therefore, every  $AARE_y$  value must be stored from the beginning.

We avoid storing every data point by implementing a sliding window with only one parameter — WINDOW\_SIZE or simply  $WS$ . The starting timestep  $W$  is calculated via the following formula:

$$\begin{cases} W = t - WS + 1 & \text{if } t - WS + 1 > b \\ W = b & \text{if } t - WS + 1 \leq b \end{cases} \quad (8)$$

where

$W$  = beginning timestep of the window.

As a result, the data points before the beginning of the window are discarded. The equations known from ReRe (see Section III) are modified according to the following formulas:

$$AARE_t = \frac{1}{t - W + 1} \cdot \sum_{y=W}^t C_y \cdot \frac{|v_y - \hat{v}_y|}{v_y} \quad (9)$$

$$\mu_{AARE,t} = \frac{1}{t - W + 1} \cdot \sum_{y=W}^t AARE_y \quad (10)$$

$$\sigma_{AARE,t} = \sqrt{\frac{\sum_{y=W}^t (AARE_y - \mu_{AARE,t})^2}{t - W + 1}} \quad (11)$$

$$thd_t = \mu_{AARE,t} + 3 \cdot \sigma_{AARE,t} \quad (12)$$

### C. Effects of the Enhancements

The effects of ageing and sliding window can perhaps be best comprehended via Figure 2. The impact of ageing becomes evident, as the age power variable ( $AP$ ) in Equation (6) determines the pace of ageing, i.e., the extent to which previous data points should impact the operation of ageing. If  $AP = 1$ , there is linear ageing. Negative numbers are not recommended, as they result in inverse ageing.

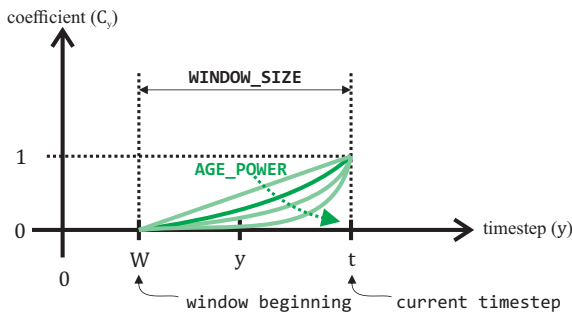


Fig. 2: The operational principles of ageing and sliding window.

Obviously,  $AP$  becomes an additional hyperparameter of the algorithm. Equation (6) always produces a number between 0 and 1 for  $C_y$  if  $y \in [W, t]$ . This way, the last few data points will remain approximately the same, while the ones closer to the start will be scaled down. Ageing gives the algorithm the capability to address slow or no reaction to

certain anomalies (see Section III-C) since new high error terms influence  $AARE_y$  values more than older smaller ones.

The implemented sliding window has a significant benefit, as shown in Figure 2. The values of  $thd_y$  are calculated using  $AARE_y$  values only from within the window. Therefore, the detection threshold adjusts faster and more precisely, and high  $AARE_y$  values from a few thousand past timesteps do not distort the performance until the very end of the operation.

Figure 2 also demonstrates the dependence between ageing and sliding window. Equation (6) produces values of 0 at the beginning of the window (timestep  $W$ ) and produces values of 1 at the current timestep  $t$ . If ageing is deactivated, all values of  $C_y$  are set to 1. On the other hand, if the sliding window is disabled, the window size parameter  $WS$  is set to one more than the current timestep  $t$ . This way, Equation (8) always chooses the timestep  $b$  as the beginning of the window because the first predicted value is produced then. In this case, ageing is implemented on the whole previous dataset, i.e., from  $b$  to the current timestep  $t$ . The disabled sliding window and disabled ageing effects are visualized in Figure 3.

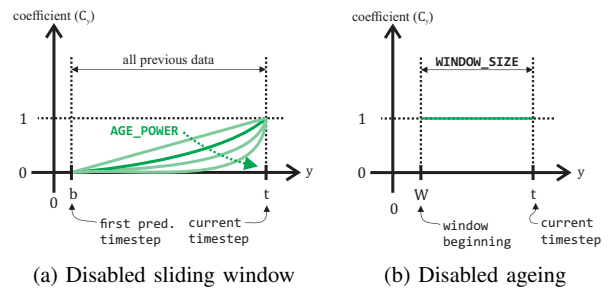


Fig. 3: Effects of disabled sliding window and ageing.

## V. RESULTS

The introduced enhancements in the previous section serve the purpose of real-time anomaly detection on time-series data. In what follows, we assess the performance of Alter- $Re^2$  when compared to ReRe.

### A. Preliminaries

To date, there is no publicly available implementation (i.e. source code) of the RePAD and ReRe algorithms. Therefore, we have implemented them in Python. However, it is worth mentioning that our way of implementing LSTM, including the functions used for training/testing, might differ from the method implemented by Lee *et al.* This speaks to the continuous research challenge of reproducibility.

Initially, we configured ReRe with the parameters used in [1]. Specifically, we defined one hidden LSTM layer and set the number of its neurons to 10. However, such a configuration has been shown to be insufficient, as the neural network model made unreasonable predictions likely due to the inability to learn data patterns with enough complexity at the beginning. After rigorous experimentation with various configuration settings and manual hyperparameter optimization, we observed that 30 neurons in the one hidden layer with 30 epochs

Towards Machine Learning-based Anomaly Detection on Time-Series Data

yielded the best results. On the one hand, increasing these numbers further significantly increased the training time. On the other hand, decreasing these values degraded the prediction performance.

We also conducted experiments to determine the look-back parameter ( $b$ ). Lee *et al.* used a relatively low parameter, i.e.,  $b = 3$ . Interestingly, in our assessment, such a value of  $b$  could not produce satisfying results. Upon experimenting with the effect of all parameters on the overall performance, we concluded that setting  $b$  to 30 resulted in the best performance. A higher or lower number has occasionally manifested in a constant offset between the original and predicted data points. The predict-forward parameter  $f$  was set to a constant value of 1, as discussed in Section III-A (ReRe predicts only the next datapoint  $\hat{v}_{t+1}$ ).

Our finding regarding the WINDOW\_SIZE ( $WS$ ) parameter is that a too-small value results in an unstable operation since the number of data points are low to learn long-term dependencies. The upper bound on  $WS$  is the storage capacity allocated for the algorithm. CPU and time constraints might also have to be considered as the volume of data points impacts the computational complexity and timeliness. Eventually, we deduced experimentally that the setting of  $WS$  to 1000 was optimal with the datasets we performed our tests on.

Last, we also observed that the most promising results could be obtained by setting the AGE\_POWER ( $AP$ ) parameter to 2. This ends up in a quadratic ageing equation. If  $AP$  is significantly lower, old data points have a strong influence on the current  $AARE_t$  value, which is undesirable. On the contrary, if  $AP$  is too high, only the last data points affect the performance, resulting in unstable operation. In our experiments, we eventually set  $AP$  to 2. Table I summarizes the parameter settings we have used in our experiments.

TABLE I: Summary of the used parameter settings.

| Parameter | ReRe | Alter-Re <sup>2</sup> |
|-----------|------|-----------------------|
| neurons   | 30   | 30                    |
| epochs    | 30   | 30                    |
| $b$       | 30   | 30                    |
| $WS$      | -    | 1000                  |
| $AP$      | -    | 2.0                   |

B. ReRe vs. Alter-Re<sup>2</sup>

Our experiments have used the Numenta Anomaly Benchmark (NAB) [33] datasets. NAB is destined for evaluating streaming and real-time applications of anomaly detection algorithms. The datasets comprise real-world and artificial data containing human-labelled anomalous behaviour periods. The majority of the data is real-world from various sources such as AWS server metrics, Twitter volume, advertisement clicking metrics, and traffic data. Data are ordered, timestamped, and single-valued metrics. The timestamps of the anomaly labels are provided as a separate file.

We examined the efficacy of Alter-Re<sup>2</sup> compared to ReRe using various datasets (see Table II for details on the used NAB datasets containing anomalies related to CPU utilization, request latency, and request count, among others). In

this work, we detail the observations achieved with the ‘ec2\_cpu\_utilization\_ac20cd’ dataset, which contains CPU utilization percentages collected from AWS servers using the CloudWatch monitoring tool [34].

Figures 4 and 5 depict the detection results achieved by ReRe and Alter-Re<sup>2</sup>, respectively. The figures have the same layout. They consist of three graphs that show the details of algorithm operation. The top graphs show the original data points ( $v_y$ ) with green, and the LSTM-predicted data points ( $\hat{v}_y$ ) using red. The original and predicted values have been scaled down to the  $[0, 1]$  interval (a requirement of LSTM). In the middle graph, we plot the absolute average relative error ( $AARE_y$ ) using blue and the thresholds ( $thd_y$ ) with yellow. The bottom figures display detections made by ReRe. Furthermore, anomaly detection is drawn with purple, while the pattern changes have a turquoise colour. The configuration of WINDOW\_SIZE ( $WS$ ) and AGE\_POWER ( $AP$ ) parameters used in our experiment are shown in the figure captions. In the captions, we also indicate the timesteps of the anomaly labels.

From Figures 4 and 5, we find that the first anomaly is detected by both algorithms (see the bottom graphs). When the  $AARE$  curve in the middle graph rises above the  $thd$  curve, the algorithms determine that an anomaly has occurred. At around timestep 600, the original data rises again. Both ReRe and Alter-Re<sup>2</sup> signal a pattern change as a result and retrain the LSTM models accordingly.

However, the shortcoming of ReRe comes to the surface soon. As shown in the middle graph of Figure 4, after detecting the first anomaly,  $thd$  values rise significantly as they are calculated using the average and standard deviation of  $AARE$  values. Additionally, as the second anomaly comes at timestep 3576, many data points have already been collected, and the issue (the slope of the  $AARE$  curve is much lower) arises. In consequence, ReRe fails to detect the anomaly.

Alter-Re<sup>2</sup>, on the other hand, reliably detects the second anomaly, as shown in Figure 5. The  $thd$  curve is being ‘reset’ between timesteps 1500 and 2500 caused by the sliding window. This leads to increased detection accuracy. The slope of the  $AARE$  curve increases significantly due to the implemented ageing. Note that because of the limited range of the plots that can be expressed, there is a trade-off in these figures between the visibility of the individual points and the expression of pattern changes/anomalies.

C. Discussion

The above-discussed experiment had also been performed using nine other NAB datasets. The used datasets contain anomalies related to CPU utilization, request latency, and request count, among others.

The properties of these datasets are highlighted in Table II. We have used the same parameter settings, collected in Table I, in all of the experiments. Interestingly, these LSTM based methods provide, on each occasion, slightly deviating predictions even in the case of running the same test with the same settings on the same dataset. This deviation can be explained by the inherent randomness in the LSTM

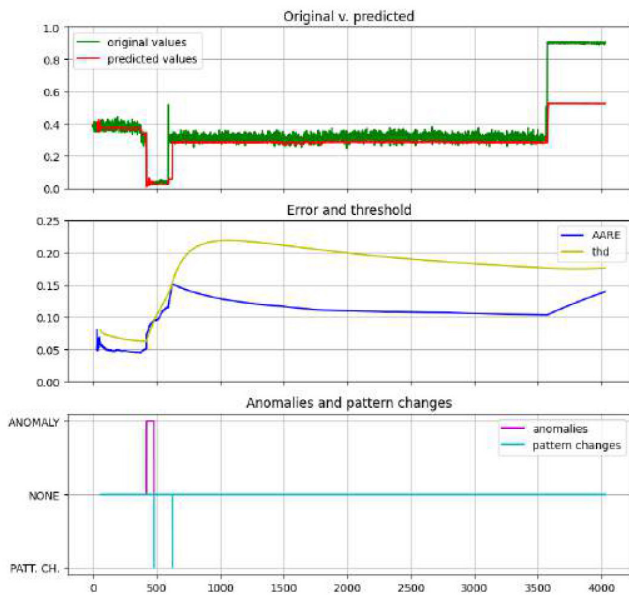


Fig. 4: ReRe output for ec2\_cpu\_utilization\_ac20cd.csv (no ageing, no window). Labeled anomalies at timesteps 421, 3576.

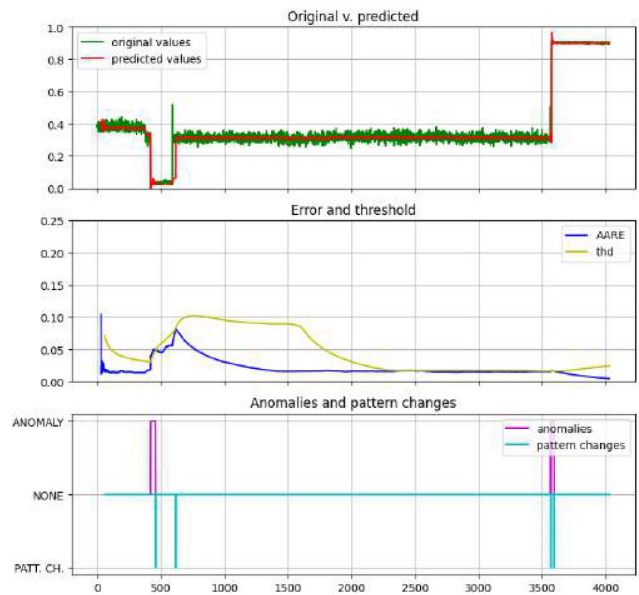


Fig. 5: Alter-Re<sup>2</sup> output for ec2\_cpu\_utilization\_ac20cd.csv (AP: 2, WS: 1000). Labeled anomalies at timesteps 421, 3576.

model’s implementation, resulting in different initial weights and parameters. Unfortunately, we were unable to compare our implementation with the original one because there was no publicly available source code of the ReRe algorithm at the date of carrying out this work. However, the apparent difference of prediction visible in Figures 4 and 5 is not due to this phenomenon. Instead, it results from the difference in the timesteps where the algorithms triggered an LSTM retrain. To recap, this happens when ReRe or Alter-Re<sup>2</sup> detects a pattern change. From this point on, they use their new LSTM model that, in this case, are trained on slightly different data resulting in slightly different predictions. Nonetheless, reducing the offset between predicted and original values constitutes a high priority task on our list of future work.

The results of the ten experiments mentioned above are presented in Table III. For the traditional performance metrics, like Precision, Recall and F-score, to be calculated, the elements of the confusion matrix have to be populated. These are the True Positives (TP), False Positives (FP), True Negatives (TN) and False Negatives (FN). Other special metrics, e.g., LSTM retrain ratio, can also provide valuable pivots in performance evaluation. We selected the metrics to be used in this work and implemented their calculation techniques according to the study of Lee *et al.* [32].

Mapping the ground truth anomalies to the detected ones relies on anomaly windows around the timesteps of the ground truth labels. The only parameter  $K$  determines the size of this anomaly window. If the timestep for a ground truth anomaly is denoted by  $y_{GT}$ , the anomaly window starts at  $y_{GT} - K$  and ends at  $y_{GT} + K$ . We set  $K = 7$ , as per the recommendations in [35] for minute-based time series.

Anomaly signals have also been processed. More specifically, all detections longer than one timestep are remapped to

the timestep they started at. After creating anomaly windows and remapping signals, the algorithm calculates the confusion matrix elements in the following way. All signals outside the anomaly window are considered as false positive. Only the first signal inside each window is regarded as a true positive. All others inside the same window are discarded. If no signals are present in the whole window, the number of false negatives is incremented by one. True negatives are the remaining number of timesteps to ensure the length of the dataset is equal to the sum of the elements in the confusion matrix.

The values of the selected performance metrics of our experiments using the ten datasets listed in Table II are summarized in Table III. In total, using the evaluation method detailed above, Alter-Re<sup>2</sup> was able to identify seven anomalies, while ReRe detects only one correctly. Simultaneously, the number of false positives (not depicted in the table) also increased by introducing Alter-Re<sup>2</sup>. Upon closer examination of the experiment results, we found that this phenomenon comes from the oscillations in the anomaly signals (i.e., an alternation between signal and no signal) just outside the anomaly window and rarely from really false detections. Comparing the number of true negatives (not depicted in the table) between the two algorithms has little significance, as values differ only by fractions of percentages. On the other hand, false negatives (not depicted in the table) are reduced when contrasting Alter-Re<sup>2</sup> with ReRe.

In Table III, we have also depicted the traditional metrics generally used for performance analysis. Precision is the number of correctly identified anomalies divided by the number of all anomaly signals. It is a meaningful metric for anomaly detection, and Alter-Re<sup>2</sup> outperforms ReRe almost all the time, as shown in the table (the ‘nan’ value means that division by zero would be required to calculate the metric). The next

TABLE II: Datasets used for evaluation.

| No. | Dataset                                | First record time   | Last record time    | No. of data points | No. of anomalies | Sampling rate |
|-----|--|---------------------|---------------------|--------------------|------------------|---------------|
| 01  | ec2_cpu_utilization_5f5533.csv         | 2014-02-14 14:27:00 | 2014-02-28 14:22:00 | 4032               | 2                | 5 min         |
| 02  | ec2_cpu_utilization_825cc2.csv         | 2014-04-10 00:04:00 | 2014-04-24 00:09:00 | 4032               | 2                | 5 min         |
| 03  | ec2_cpu_utilization_ac20cd.csv         | 2014-04-02 14:29:00 | 2014-04-16 14:49:00 | 4032               | 2                | 5 min         |
| 04  | ec2_network_in_257a54.csv              | 2014-04-10 00:04:00 | 2014-04-24 00:09:00 | 4032               | 1                | 5 min         |
| 05  | ec2_request_latency_system_failure.csv | 2014-03-07 03:41:00 | 2014-03-21 03:41:00 | 4032               | 3                | 5 min         |
| 06  | elb_request_count_8c0756.csv           | 2014-04-10 00:04:00 | 2014-04-24 00:39:00 | 4032               | 2                | 5 min         |
| 07  | grok_asg_anomaly.csv                   | 2014-01-16 00:00:00 | 2014-02-01 01:00:00 | 4621               | 3                | 5 min         |
| 08  | iio_us-east-1_j-a2eb1cd9_NetworkIn.csv | 2013-10-09 16:25:00 | 2013-10-13 23:55:00 | 1243               | 2                | 5 min         |
| 09  | rds_cpu_utilization_cc0c53.csv         | 2014-02-14 14:30:00 | 2014-02-28 14:30:00 | 4032               | 2                | 5 min         |
| 10  | rds_cpu_utilization_e47b3b.csv         | 2014-04-10 00:02:00 | 2014-04-23 23:57:00 | 4032               | 2                | 5 min         |

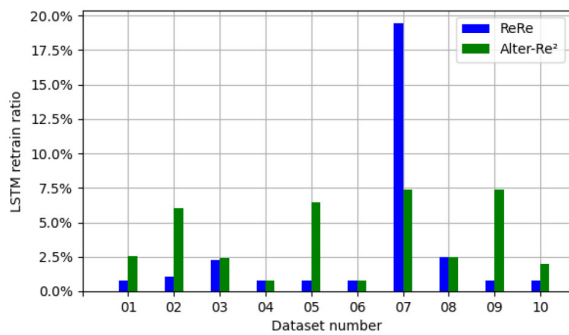


Fig. 6: LSTM retrain ratio.

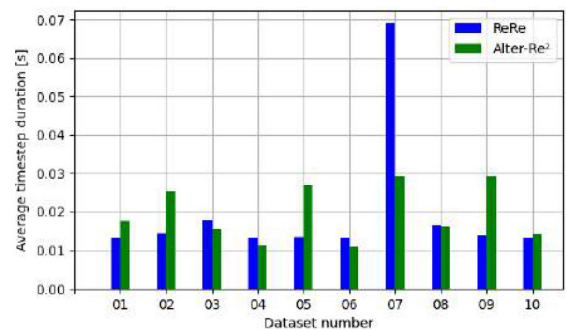


Fig. 7: Average timestep duration.

depicted metric is Recall, which denotes the ratio of the number of true positives to the number of all ground truth labels. This is also an essential indicator in anomaly detection, and Alter-Re<sup>2</sup> overperforms ReRe by also this regard in most cases. Finally, we depicted the F-score, which is the harmonic mean of Precision and Recall. When available, Alter-Re<sup>2</sup> is superior to ReRe considering this metric, as well.

We believe that a more appropriate setting of the anomaly window (instead of  $K = 7$ ) can eliminate the above-mentioned phenomenon of indicating detection signals outside this window as false positives. Nonetheless, our experiment results confirm the significance and superiority of our Alter-Re<sup>2</sup> algorithm over ReRe since the performance metrics used in the comparison were calculated in the same way. In order to empirically compare the number of anomalies detected by ReRe and Alter-Re<sup>2</sup>, we manually adjusted the number of true positives (we increased the number of true positives by the number of signals just outside of the given anomaly window, that were clearly resulted from the given ground truth anomaly). We found that even so, ReRe detected only three anomalies compared to the ten ones identified by Alter-Re<sup>2</sup>, resulting in a more than three-fold increase.

The other special metrics we have also used in our evaluations were: a) LSTM retrain ratio (the number of timesteps with an LSTM retrain divided by the total number of timesteps); b) Average timestep duration (total time divided by the number of timesteps); and c) Preparation period (number of timesteps after which ReRe or Alter-Re<sup>2</sup> can detect anomalies). As depicted in Figure 6, the LSTM retrain ratio increased significantly in the case of Alter-Re<sup>2</sup> in

most of the experiments. This is due to the larger number of signals (anomalies and pattern changes) raised by the algorithm. Considering the Average timestep duration, the two algorithms show similar performance in most of the experiments as depicted in Figure 7. Finally, the Preparation period was the same for both algorithms on all datasets, as it depends solely on the  $b$  parameter. In our experiments, it was  $2b - 1 = 2 \cdot 30 - 1 = 59$ . This can be interpreted as both algorithms can detect anomalies soon, 59 timesteps after being turned on.

Nevertheless, there are some limitations of LSTM based approaches. The predictive power of LSTM networks is relatively low at the beginning. Essentially, LSTM was designed to learn long term dependencies, *i.e.*, it remembers the information for long periods. A well-performing LSTM on very long sequences of non-stationary data commensurate with an increase in required network capacity and training. In response, if a pattern change is detected in our approach, the LSTM is re-trained using the previous  $b$  data points. However, in extreme scenarios where anomalies are relatively frequent, the LSTM network might constantly have low predicting power.

Transfer learning appears suitable to address this limitation. Broadly speaking, in transfer learning, a model developed for a task is reused as the starting point for a model in the next task. By applying this logic in LSTM time series, the weights obtained from the first task could be used in the next task [36]. Consequently, in cases where anomalies are frequent, the low predictive performance of LSTM could presumably be overcome. However, further research is needed to study the applicability of transfer learning (and other

TABLE III: Evaluation results (traditional metrics; R: ReRe, A: Alter-Re<sup>2</sup>).

| Dataset no. | No. of detected anomalies |   | Precision  |               | Recall |               | F-score |               |
|-------------|---------------------------|---|------------|---------------|--------|---------------|---------|---------------|
|             | R                         | A | R          | A             | R      | A             | R       | A             |
| 1           | 0                         | 1 | nan        | <b>0.3333</b> | 0.0    | <b>0.5</b>    | nan     | 0.4           |
| 2           | 0                         | 1 | 0.0        | <b>0.3333</b> | 0.0    | <b>0.5</b>    | nan     | 0.4           |
| 3           | 1                         | 2 | <b>1.0</b> | 0.6667        | 0.5    | <b>1.0</b>    | 0.6667  | <b>0.8</b>    |
| 4           | 0                         | 0 | nan        | nan           | 0.0    | 0.0           | nan     | nan           |
| 5           | 0                         | 1 | nan        | <b>0.3333</b> | 0.0    | <b>0.3333</b> | nan     | <b>0.3333</b> |
| 6           | 0                         | 0 | nan        | nan           | 0.0    | 0.0           | nan     | nan           |
| 7           | 0                         | 1 | 0.0        | <b>0.2</b>    | 0.0    | <b>0.3333</b> | nan     | <b>0.25</b>   |
| 8           | 0                         | 0 | nan        | nan           | 0.0    | 0.0           | nan     | nan           |
| 9           | 0                         | 1 | nan        | <b>0.3333</b> | 0.0    | <b>0.5</b>    | nan     | <b>0.4</b>    |
| 10          | 0                         | 0 | nan        | 0.0           | 0.0    | 0.0           | nan     | nan           |

advanced approaches, such as online learning) in time-series anomaly detection.

Furthermore, another question yet to be examined is the efficiency of *AARE*. When an outlier value is detected in our prototype implementation, its error is included in the calculation. This can result in a significant increase of *AARE*, implying that anomalies might remain undetected for the period when *AARE* is high. Undoubtedly, further study is needed to assess the practicability of *AARE* in anomaly detection accuracy. A naive solution of this challenge considered in future work could be excluding the extreme values causing anomalies from the *AARE* calculation and focus only on the values considered normal instead.

VI. CONCLUSIONS

Real-time anomaly detection in time-series data is an emerging area with approaches mostly based on neural networks, while there is a noticeable increase in the use of LSTMs. Despite recent advances in anomaly detection, classifying abnormal behaviour in time-series data is still challenging.

In this paper, we introduced Alter-Re<sup>2</sup>, an enhancement of the cutting-edge ReRe algorithm. Specifically, we discuss our sliding window and ageing techniques. The former is aimed at limiting memory and CPU overheads. The latter serves the purpose of ageing the data points that are used for calculating error terms. Ageing addresses the issue of slow anomaly detection times. Furthermore, it is also destined to observe abnormal behaviour that is unpredicted by prior works.

We rigorously evaluated Alter-Re<sup>2</sup> and observed promising results. Our approach achieved significantly better performance when compared to ReRe. Specifically, it can detect three times more anomalies. Furthermore, Alter-Re<sup>2</sup> can detect such anomalies too that ReRe falls short.

As future work, we plan to evaluate the applicability and usefulness of several other concepts, such as offset compensation, adaptive threshold sigma-coefficient, automatic setting of some hyperparameters, introducing real-time normalization, adapting the algorithm to support multivariate data, and incorporate them into our algorithm. We also plan to study the applicability of transfer learning in time series anomaly detection.

As time-series data streams are now an integral part of almost every field of technology, real-time anomaly detection on these data is a vital tool that deserves more attention.

We believe that our contribution is valuable in facilitating the development of relevant techniques, yet we argue our approach has immediate real-world applicability.

ACKNOWLEDGMENT

The research reported in this paper and carried out at the BME has been supported by the NRDI Fund based on the charter of bolster issued by the NRDI Office under the auspices of the Ministry for Innovation and Technology.

REFERENCES

- [1] M.-C. Lee, J.-C. Lin, and E. G. Gran, "ReRe: A Lightweight Real-Time Ready-to-Go Anomaly Detection Approach for Time Series," in *2020 IEEE 44th Annual Computers, Software, and Applications Conference (COMPSAC)*, 2020, pp. 322–327.
- [2] S. Hochreiter and J. Schmidhuber, "Long Short-Term Memory," *Neural Computation*, vol. 9, no. 8, pp. 1735–1780, 1997.
- [3] M.-C. Lee, J.-C. Lin, and E. G. Gran, "RePAD: Real-Time Proactive Anomaly Detection for Time Series," in *Proceedings of the Advanced Information Networking and Applications*, L. Barolli, F. Amato, F. Moscato, T. Enokido, and M. Takizawa, Eds., Cham: Springer International Publishing, 2020, pp. 1291–1302.
- [4] A. Putina et al., "Telemetry-Based Stream-Learning of BGP Anomalies," in *Proceedings of the 2018 Workshop on Big Data Analytics and Machine Learning for Data Communication Networks*, ser. Big-DAMA '18, Budapest, Hungary: Association for Computing Machinery, 2018, pp. 15–20.
- [5] F. Cao, M. Estert, W. Qian, and A. Zhou, "Density-Based Clustering over an Evolving Data Stream with Noise," in *Proceedings of the 2006 SIAM International Conference on Data Mining*, pp. 328–339.
- [6] N. Ye, D. Montgomery, K. Mills, and M. Carson, "Multivariate metrics of normal and anomalous network behaviors," in *Proceedings of the 2019 IFIP/IEEE Symposium on Integrated Network and Service Management (IM)*, IEEE, 2019, pp. 55–58.
- [7] G. Kaiafas et al., "An Experimental Analysis of Fraud Detection Methods in Enterprise Telecommunication Data using Unsupervised Outlier Ensembles," in *Proceedings of the 2019 IFIP/IEEE Symposium on Integrated Network and Service Management (IM)*, IEEE, 2019, pp. 37–42.
- [8] Twitter. (). "Twitter/anomalydetection [online code repository]," [Online]. Available: <https://github.com/twitter/AnomalyDetection>. Accessed: 2021-01-13.
- [9] A. Syal, A. Lazar, J. Kim, A. Sim, and K. Wu, "Automatic Detection of Network Traffic Anomalies and Changes," in *Proceedings of the ACM Workshop on Systems and Network Telemetry and Analytics*, ser. SNTA '19, Phoenix, AZ, USA: Association for Computing Machinery, 2019, pp. 3–10.
- [10] C. Cortes and V. N. Vapnik, "Support-vector networks," *Machine Learning*, vol. 20, no. 3, pp. 273–297, 1995.
- [11] C. Pilinszki-Nagy and B. Gyires-Tóth, "Performance Analysis of Sparse Matrix Representation in Hierarchical Temporal Memory for Sequence Modeling," *Infocommunications Journal*, vol. 12, no. 2, pp. 41–49, 2020.

Towards Machine Learning-based Anomaly Detection on Time-Series Data

[12] J. Hawkins, S. Ahmad, S. Purdy, and A. Lavin, "Biological and Machine Intelligence (BAMI)," Initial online release 0.4, 2016.

[13] M. A. Kramer, "Nonlinear principal component analysis using autoassociative neural networks," *AICHE Journal*, vol. 37, no. 2, pp. 233–243, 1991.

[14] X. Zhou, Y. Hu, W. Liang, J. Ma, and Q. Jin, "Variational LSTM Enhanced Anomaly Detection for Industrial Big Data," *IEEE Transactions on Industrial Informatics*, vol. 17, no. 5, pp. 3469–3477, 2021.

[15] A. Lazaris and V. K. Prasanna, "An LSTM framework for modeling network traffic," in *Proceedings of the 2019 IFIP/IEEE Symposium on Integrated Network and Service Management (IM)*, IEEE, 2019, pp. 19–24.

[16] J. Soheil et al., "On the Practicality of Learning Models for Network Telemetry," *Proceedings of Network Traffic Measurement and Analysis Conference*.

[17] G. Box and G. Jenkins, *Time Series Analysis: Forecasting and Controls rev.* Oakland California: Holden-Day, 1976.

[18] L. Gjorgiev and S. Gievska, "Time Series Anomaly Detection with Variational Autoencoder Using Mahalanobis Distance," in *Proceedings of the ICT Innovations 2020. Machine Learning and Applications*, V. Dimitrova and I. Dimitrovski, Eds., Cham: Springer International Publishing, 2020, pp. 42–55.

[19] P. Diederik and M. Welling, *Auto-Encoding Variational Bayes*, 2013. arXiv:1312.6114.

[20] G. McLachlan, "Mahalanobis distance," *Resonance*, vol. 4, no. 6, pp. 20–26, 1999.

[21] T. Amarbayasgalan, V. H. Pham, N. Theera-Umpon, and K. H. Ryu, "Unsupervised Anomaly Detection Approach for Time-Series in Multi-Domains Using Deep Reconstruction Error," *Symmetry*, vol. 12, no. 8, 2020.

[22] A. Dridi, C. Boucetta, S. E. Hammami, H. Afifi, and H. Mounjla, "STAD: Spatio-Temporal Anomaly Detection Mechanism for Mobile Network Management," *IEEE Transactions on Network and Service Management*, vol. 18, no. 1, pp. 894–906, 2021.

[23] B. Schölkopf, R. C. Williamson, A. J. Smola, J. Shawe-Taylor, and J. C. Platt, "Support Vector Method for Novelty Detection," *Advances in Neural Information Processing Systems*, pp. 582–588, 2000.

[24] H. Drucker, C. C. Burges, L. Kaufman, A. J. Smola, and V. N. Vapnik, "Support Vector Regression Machines," in *Proceedings of the Advances in Neural Information Processing Systems*, ser. NIPS 1996, vol. 4, MIT Press, 1997, pp. 155–161.

[25] M. Said Elsayed, N.-A. Le-Khac, S. Dev, and A. D. Jurcut, "Network Anomaly Detection Using LSTM Based Autoencoder," in *Proceedings of the 16th ACM Symposium on QoS and Security for Wireless and Mobile Networks*, ser. Q2SWinet '20, Alicante, Spain: Association for Computing Machinery, 2020, pp. 37–45.

[26] M. P. Novaes, L. F. Carvalho, J. Lloret, and M. L. Proença, "Long Short-Term Memory and Fuzzy Logic for Anomaly Detection and Mitigation in Software-Defined Network Environment," *IEEE Access*, vol. 8, pp. 83 765–83 781, 2020.

[27] T. J. Lee, J. Gottschlich, N. Tatbul, E. Metcalf, and S. Zdonik, *Greenhouse: A Zero-Positive Machine Learning System for Time-Series Anomaly Detection*, 2018. arXiv:1801.03168 [cs.AI].

[28] DeepLearning4j. (). "What is early stopping?" [Online]. Available: <https://deeplearning4j.konduit.ai/tuning-and-training/early-stopping>. Accessed: 2021-01-13.

[29] K. Gurney, *An introduction to neural networks*. CRC press, 1997.

[30] A. Sherstinsky, "Fundamentals of Recurrent Neural Network (RNN) and Long Short-Term Memory (LSTM) network," *Physica D: Nonlinear Phenomena*, vol. 404, p. 132 306, 2020.

[31] J. Hochenbaum, O. S. Vallis, and A. Kejariwal, *Automatic Anomaly Detection in the Cloud Via Statistical Learning*, 2017. arXiv:1704.07706 [cs.LG].

[32] M.-C. Lee, J.-C. Lin, and E. G. Gran, *How Far Should We Look Back to Achieve Effective Real-Time Time-Series Anomaly Detection?* 2021. arXiv:2102.06560 [cs.LG].

[33] A. Lavin and S. Ahmad, "Evaluating Real-Time Anomaly Detection Algorithms – The Numenta Anomaly Benchmark," in *Proceedings of the IEEE 14th International Conference on Machine Learning and Applications (ICMLA)*, 2015, pp. 38–44.

[34] I. Numenta. (). "NAB: Numenta Anomaly Benchmark [Online code repository]." [Online]. Available: <https://github.com/numenta/NAB>. Accessed: 2021-01-13.

[35] H. Ren et al., "Time-series anomaly detection service at microsoft," in *Proceedings of the 25th ACM SIGKDD International Conference on Knowledge Discovery & Data Mining*, ser. KDD '19, Anchorage, AK, USA: Association for Computing Machinery, 2019, pp. 3009–3017.

[36] F. Karim, S. Majumdar, H. Darabi, and S. Chen, "LSTM Fully Convolutional Networks for Time Series Classification," *IEEE Access*, vol. 6, pp. 1662–1669, 2018.



**Daniel Vajda** received his B.Sc. degree in electrical engineering at the Budapest University of Technology and Economics, Hungary, in 2021. Currently, he is an M.Sc. student with the same university. He is a research fellow at NETvisor Ltd. His research interests include network and service management, network telemetry, machine learning, and big data analytics.



**Adrian Pekar** received the Ph.D. degree in computer science from the Technical University of Košice, Slovakia, in 2014. Currently, he is an Assistant Professor with the Department of Networked Systems and Services, Budapest University of Technology and Economics, Hungary. Prior to this, he held research, teaching, and engineering positions in New Zealand and Slovakia. His research interests include network traffic classification and management, traffic measurement data reduction and visualisation, and stream processing.



**Karoly Farkas** did his habilitation in 2017 at the Budapest University of Technology and Economics (BME), received his Ph.D. degree in Computer Science in 2007 from ETH Zurich, and his M.Sc. degree in Computer Science in 1998 from BME. Currently he is working in parallel as an associate professor at BME, and as the head of R&D at NETvisor Ltd. His research interests cover, among others, the field of infocommunication networks, IoT, Industry 4.0 and AI. He has published more than 100 scientific papers, given a plenty of regular and invited talks and acted as organizer or TPC member of numerous scientific conferences. Currently he acts as board member of the Hungarian Scientific Association for Infocommunications (HTE). He is the coordinator of the local Cisco Networking Academy and was the founding initiator of the Cisco IPv6 Training Laboratory and the NetSkills Challenge student competition at BME. Between 2012-2015 Dr. Farkas has been awarded the Bolyai Janos Research Fellowship of the Hungarian Academy of Sciences

# Traffic congestion propagation identification method in smart cities

Attila M. Nagy, and Vilmos Simon

**Abstract**—Managing the frequent traffic congestion (traffic jams) of the road networks of large cities is a major challenge for municipal traffic management organizations. In order to manage these situations, it is crucial to understand the processes that lead to congestion and propagation, because the occurrence of a traffic jam does not merely paralyze one street or road, but could spill over onto the whole vicinity (even an entire neighborhood). Solutions can be found in professional literature, but they either oversimplify the problem, or fail to provide a scalable solution.

In this article, we describe a new method that not only provides an accurate road network model, but is also a scalable solution for identifying the direction of traffic congestion propagation.

Our method was subjected to a detailed performance analysis, which was based on real road network data. According to testing, our method outperforms the ones that have been used to date.

**Index Terms**—congestion propagation, frequent propagation trees, traffic study, city planning

## I. INTRODUCTION

One of the major problems of traffic in big cities around the world is the phenomenon of traffic congestion (traffic jams) on the road network. Traffic jams have a serious effect not only on the lives of drivers, but also on every city inhabitant. Traffic jams increase not only energy and fuel consumption [1], but also harmful emissions [2]. According to a laboratory testing [3], congestion-related emissions cause increased cases of allergies and exacerbate existing conditions among people who are sensitive to it. Additionally, other research [4] shows that traffic jams raise the risk of heart attack. That is why attention needs to be paid to avoiding traffic jams and possibly eliminating them, because in addition to significant economic costs [5], they are also harmful to the health of city inhabitants (which can also be expressed as a financial costs for health insurers).

Intelligent city management systems can provide a solution to these problems, or at least substantially reduce the negative effects on the daily life of city dwellers. It is the task of these systems to continually monitor the traffic and to provide information on the basis of the collected data, as well as to manage the automated allocation of resources [6], for example, opening new lanes or closing them, adapting traffic lights to current traffic conditions [7] or assisting route planning applications with accurate forecasts.

Attila M. Nagy is with the Department of Networked Systems and Services, Faculty of Electrical Engineering and Informatics, Budapest University of Technology and Economics, Hungary, e-mail: anagy@hit.bme.hu.

Vilmos Simon is with the Department of Networked Systems and Services, Faculty of Electrical Engineering and Informatics, Budapest University of Technology and Economics, Hungary, e-mail: svilmos@hit.bme.hu.

In the first generation of the intelligent traffic management systems, the utilized data sources were different type of presence sensors in fixed positions, which were able to detect the presence of nearby vehicles. Initially, inductive loop detectors were the most popular, but nowadays, a wide variety of sensors became available such as traffic cameras, laser radar sensors or microwave radar sensors [8], [6]. Recently, the advent of GPS equipped smartphones and vehicles has given rise to a relatively new type of data source that could supplement presence type sensors to gather more detailed information or to get data about the roads, which have not been covered with presence sensors yet. In addition to existing data sources, the emerging Vehicle to Everything (V2X) communication technologies [9], [10] will become a vital data source in the future that can improve the performance of intelligent traffic management systems. The V2X defines messaging protocols to communicate between cars and the infrastructure. The V2X protocols are already integrated into the newest vehicles, but the number of equipped vehicles is still low; thus, the role of V2X will be more significant in future applications.

When a traffic jam starts to develop on a segment of the road network, it often also affects the surrounding road segments of the network. These effects are complicated - they always depend on current environmental factors (time of day, weather, holidays, etc.) but if we examine properly chosen time periods, we can collect useful information. The information gathered could make the operation of intelligent city management systems more efficient and provide new data to city planners and managers.

There are several studies exploring the propagation of the effects of developing traffic jams, which face a number of significant challenges. The first is that the road networks of large cities form an extensive and complex system in which the study of the traffic jam propagation is difficult to scale. Several studies have developed alternative models for solving the problem, but these oversimplify the road network, and so the output of their methods are imprecise. The second challenge is that it is not enough to detect a traffic jam, it is also important be able to identify the relationships between the road segments.

In this article, we would like to present a new method we have developed, which takes into account the spatial and temporal relationships:

- 1) is able to identify the appearance of congestion propagation across the entire road network in a scalable way,
- 2) is able to identify frequently occurring traffic jam propagation within these (the importance of which will be explained later).

The output of the process can be used by city traffic management system operators to map the source and propagation of frequently occurring traffic jams, and identify bottlenecks of the road network, which can be used in city traffic network planning and real-time interventions (if they have an Intelligent Transportation System (ITS) system). The output can be useful for route planning methods and can be used to refine forecasts of traffic prediction methods as well.

The remainder of this article contains the following chapters. Section II summarizes what research has been done in this field to date. In Section III, we introduce a new definition for traffic jams that, unlike the definition used in previous research, does not require manual parameter setting. We then introduce our developed congestion propagation detection method in Section IV and we perform a detailed performance analysis in Section V. We end the article with a short conclusion in the Section VI.

## II. RELATED RESEARCH

### A. Congestion occurrence

To be able to reliably identify a traffic jam occurrence from traffic data, you first need to define exactly what a traffic jam is. Traffic jam definitions are not uniform in the literature [11], and they often depend to a large extent on empirically set parameters.

Methods found in the literature, which are used to explore the propagation of traffic jams or predict traffic congestions rely almost exclusively on the speed data to determine the size of a traffic jam. In addition, we have also found other definitions from related researches that use other types of data. The definitions can be separated into three main categories:

- speed-based methods,
- travel time-based methods,
- volume-based methods.

The speed-based methods can be separated to threshold-based and ratio-based subcategories. In the case of threshold-based methods [12], [13], [14], the researchers manually, in advance, determine the possible traffic states (typically 4-5 traffic classes) and their associated boundaries. Then the measured speed data is categorized into the defined traffic classes. As an extension, the authors of [15] defined the boundaries between traffic classes as fuzzy and also incorporated other coefficients such as traffic volume.

The ratio-based methods [16], [17], [18], [19], [20], [13], [21] do not determine velocity limits but numbers in a ratio. They compare the current measured speeds with the previously measured average or *free-flow* speeds. The *free-flow* is the speed at which the vehicle drivers would be able to travel if unimpeded by other vehicles [22]. In the literature, we have found two ways to determine the *free-flow* speed. The Speed Reduction Index (SRI) definition [23], [24] uses the 85th percentile of the off-peak speed, while the Speed Performance Index (SPI) definition [24] applies the maximum permissible road speed.

If the ratio of current speed to the average (*free-flow*) speed is lower than the pre-determined ratio, then the current measured speed is considered a traffic jam situation, that is,

based on the velocities measured in the area, they determine that a traffic jam has occurred. Some methods [16], [13], [24] define more than one traffic class. In these cases, different ratios are established for every traffic class.

The travel time-based methods use probe vehicle data to determine the congestion level of the examined road segments. The Travel rate method [25] calculates the ratio of the current segment travel time and the segment length to quantify the congestion level. The Delay rate [26], [25] and Delay ratio [26], [25] methods are the extensions of the Travel rate method where the measured travel rate is compared with a predefined acceptable travel rate value. The Relative Congestion Index (RCI) definition [27] relies on the ratio of the current measured travel time and the *free-flow* travel time. The *free-flow* travel time can be calculated with the ratio of the road segment length and *free-flow*.

The volume-based methods examine the traffic volume that denotes the number of passing vehicles in predefined time frames. A well-known volume-based method is the Volume to Capacity (V/C) ratio definition [28] that compares the measured volume with the maximum number of vehicles that a segment can handle within its capacity. The V/C ratio is often used together with the Level of Service (LOS) [29] where the measured V/C ratio values are classified in 6 traffic classes.

Using the criteria of a good congestion measure from article [11], the majority of these methods' weak point is that they only take one data type into consideration, and except for some definitions [24], [28], do not describe the state of the traffic appropriately because the occurrence of the traffic jam always depends on the properties of the road segment as well. For example, the number of lanes, the speed limits for a given segment of road, the number of vehicles passing through, or the road segment's capacity all affect whether or not a traffic jam has occurred.

Another problem that appears is if the method uses manually set values or values that rely on previously measured data. Unfortunately, several cases occur where an explanation is missing as to why a threshold value or a ratio is used, seemingly depending on the subjective decision of the authors.

### B. Congestion propagation

As opposed to the occurrence of a traffic jam, the definition of the propagation of a traffic jam is mostly uniform in the professional literature. A road segment can be in one of two states: congested (1) or free flowing vehicle movement (0). Traffic jam propagates between neighboring road segments *A* and *B*, if at time *t* road segment *A* is congested and *B* isn't, but at time *t* + 1 segment *B* is congested too.

The *Propagation Probability Graph* (PPG) [20] method models the road network as a directed graph. It relies on a historical database to decide on the probability of traffic jam propagation between two neighboring road segments. It states that the propagation of the traffic jam has a Markov property. In this context, this means that the likelihood of a traffic jam propagating between road segments *A* and *B* is independent of what traffic propagation probabilities have been measured before road segment *A*. The PPG method uses this property

to assign probabilities to each traffic jam propagation path. It then only pays attention to whichever possibility is greater than a predetermined value  $\gamma$ . PPG does not take into account those situations where other road segments than  $A$  also flow into road segment  $B$ , and therefore in these cases the results can be imprecise.

The *Congestion Prediction Model with ConvLSTM* (CPM-CONVLSTM) [30] method also models the road network with a directed graph. It collects propagation patterns from the road network, but unfortunately does not specify how it does this. It places a square grid over the road network, and then maps the propagation. Thus, the propagations can be described by directed edges between the points of the square grid. The CPM-CONVLSTM method, like PPG, also focuses on predicting traffic jam propagations. Using the square grid model, they train a Convolutional Long Short Term Memory (CONVLSTM) network [31]. A major disadvantage of this method is that the square grid-based model oversimplifies the road network, and this simplification makes the modeling inaccurate. For example, if a busy highway and another nearby unfrequented road are in the same cell they cannot be distinguished despite the fact that they have completely different traffic demand.

The *Cascading Patterns in Scale-Free Network* (CP-SFN) [32] method also models the road networks as a directed graph. This method's purpose is to find propagation graphs in a graph of the road network. These propagation graphs will be subgraphs of the road network graph. It considered two components to determine propagation paths: Individual Transmission Likelihood (ITL) and Environmental Intensity Inference (EMT). The ITL determines the probability of traffic jam propagation between two road segments. The monotonic exponential model used in social networks [33] was used to model propagation. The EMT component collects environmental information for the study, which is then used to weigh the output of the ITL. The EMT takes into account the Point of Interest (POI) that are close to the road segments and what weather conditions have been measured in the studied areas. The search for propagation patterns is carried out by the authors of the article using their own approximation procedure, since the Network Inference problem used in the article is an NP-hard problem [34]. The disadvantage of this method is that the original monotonic exponential model applied by CP-SFN operates on scale-free [35] graphs, while the road networks form a scale-rich [35] graph.

The aim of the *Spatio-Temporal Outlier* (STO) [36] method is to find frequent traffic jam propagation trees in the road network. The authors of the article did not study the road network as a graph, but divided the road network into regions using the Connected Components Labeling (CCL) process [37]. Relationships between regions were determined based on vehicle trajectories. The STO method identifies congestion as an outlier, and therefore when examining propagations it follows the propagation of outliers. It constructs congestion propagation graphs from the propagations using a recursive approach. The disadvantage of the STO method is that the regional division oversimplifies the road network. To overcome this problem, the authors of [38] implemented an extension of

STO in which they already use the directed graph of the road network instead of regions. The other disadvantage of the STO method is that due to the search for recursive propagation trees its complexity is  $O(N^{T-1})$ , where  $T$  is the length of the studied period in time intervals and  $N$  is the number of congestion phenomena in the period of time  $T$ .

The *Spatio-Temporal Congestion* (STC) [39] process develops the STO method further. Instead of using regions it models the road network as a directed graph of road segments. Congestion propagations are described by a directed graph of the road segments involved in the propagation that form a directed tree. It uses a new approach to search for congestion propagations, which examines the congestion trees backwards in time, so that the complexity of the procedure is only  $O(TN^2)$ , where  $T$  is the length of the examined period in time intervals and  $N$  is the number of traffic jam phenomena during period  $T$ . It then filters out frequent congestion propagation trees from the collected propagation trees using the Apriori algorithm [40]. A congestion propagation tree counts as frequent if its occurrence is above an  $\epsilon$  threshold in the studied time interval, so its frequency is greater than a predefined threshold value. Within a frequent congestion propagation tree, a propagation path is a directed path that connects the root of the tree to any leaf.

Although STC is significantly faster than the STO method, the  $O(TN^2)$  complexity remains too high for modeling a city with an extensive road network. The other problem is that the Apriori algorithm has exponential complexity  $O(2^M)$ , where  $M$  is the number of congestion propagation found.

The *Spatio-Temporal Congestion Subgraph* (STCS) [41] method is a further development of the STC in which the FP-Growth algorithm [42] is used instead of the Apriori algorithm. Because the complexity of the FP-Growth algorithm is lower than that of the Apriori algorithm, its use made the search for frequent congestion propagation trees quicker, but STCS uses STC found propagation trees, which has  $O(TN^2)$  complexity.

After reviewing the literature, it can be seen that the problem is actively studied by many researchers and they have presented several methods to solve the problem of finding frequent congestion propagation trees.

The problem with these solutions is that either the models of the road network are overly simplified (for example, with a square grid), or the method's complexity is so high that in a real environment it is not able to search effectively or find every propagation in a sprawling city. They can not be used this way in real time, but even if the speed of the algorithms is not critical, they still require a lot of processing, which can be costly.

In the following chapters we introduce our newly developed method that solves the search for traffic jam propagation trees, in a way that:

- 1) describes the road network as a directed graph in the greatest detail possible,
- 2) while the algorithmic complexity is only linear, and therefore surpasses the existing solutions.

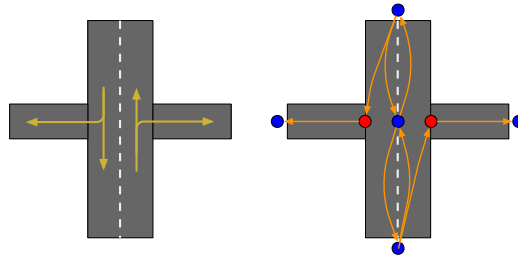


Fig. 1: Example for modeling a common intersection.

### III. FLOW-SPEED RATIO-BASED CONGESTION DEFINITION

In Section II-A we have seen that there is currently no uniform traffic jam definition that does not use manually preset values. In this section, before introducing the Spatial Congestion Propagation Patterns (SCPP) algorithm, we thought it necessary to introduce a new traffic jam definition that does not require manual setting of thresholds or ratios, but does so automatically. Using our definition, it is easier and more reliable to generate input data for the Spatial Congestion Propagation Patterns (SCPP) algorithm.

In a real environment, the correct interpretation of a traffic jam always depends on the current road segment. Each road segment has a capacity value that determines how many vehicles can pass through that road segment per hour. The capacity is the theoretical upper limit of the number of vehicles that the measured hourly vehicle number never exceeds. If a higher load is imposed on a road segment it will mean that as the number of vehicles increases, their speed will begin to decrease. This will cause an increase in the ratio of traffic flow (volume) and speed until it finally reaches a critical value above which the traffic phenomenon can be considered a traffic jam. The critical flow-speed rate can be determined by the ratio of the capacity and the upper speed limit of the road segment.

Let  $\mathcal{N}(\mathcal{I}, \mathcal{R})$  be a directed graph representing a city's road network, where  $\mathcal{I} = \{I_1, I_2, \dots, I_{|\mathcal{I}|}\}$  is the set of intersections and  $\mathcal{R} = \{R_1, R_2, \dots, R_{|\mathcal{R}|}\}$  the set of road segments. Since the road network model uses directed edges, the bidirectional road segments will be represented with two directed edges. It is not uncommon to see that vehicles can turn only in specific directions in complex intersections. To model these intersections, additional intermediate nodes (intersections) have to be added. On Figure 1, we show an example for modeling a common intersection. The blue dots denote the intersections as the nodes of the graph, while the orange arrows are the directed edges. The red dots depict the intermediate nodes. These intermediate nodes help to model the allowed turning directions properly.

Using the recommendation of the Highway Capacity Manual 2016 (HCM2016) [43] and considering the current speed limit, the theoretical capacity of a segment of  $R_r$  (Free-way (FW)) road is described in Equation 1, where  $S_{R_r, limit}$  is the maximum allowed speed in mph for road segment  $R_r$ , while the  $Lanes$  is the number of lanes on the road segment  $R_r$ . This equation is only valid for freeways, whereas equations for multi-lane highways, signalized highways and other road types can be found in HCM2016 [43]. It is worth mentioning

that the spread of autonomous vehicle will change the capacity formula in the future because the throughput of road segments will be increased due to better resource utilization [44], [45], [46].

Let  $\mathcal{F}_{R_r} = \{F_1, F_2, \dots, F_T\}$  be the time series of vehicle numbers (volume), where  $R_r$  is the edge of the road network graph  $\mathcal{N}(\mathcal{I}, \mathcal{R})$ , where the data was measured,  $T$  is the length of the time series, and  $F_t \in \mathbb{R}^+$  ( $t = 1, 2, \dots, T$ ). The vehicle speed time series is given by  $\mathcal{S}_{R_r} = \{S_1, S_2, \dots, S_T\}$ , where  $R_r$  is the edge of the road network graph  $\mathcal{N}(\mathcal{I}, \mathcal{R})$ , where the data was measured,  $T$  is the length of the time series, and  $S_t \in \mathbb{R}^+$  ( $t = 1, 2, \dots, T$ ).

Using time series  $\mathcal{F}_{R_r}$  and  $\mathcal{S}_{R_r}$ , the road segment's  $\mathcal{FSR}_{R_r} = \{FSR_{R_r,1}, FSR_{R_r,2}, \dots, FSR_{R_r,T}\}$  flow-speed rate time series can also be calculated. The instantaneous rate  $FSR_t$  of a road segment  $R_r$  can be determined using the following formula:

$$FSR_t = \frac{F_t}{S_t} \quad t = 1, 2, \dots, T \quad FSR_t \in \mathbb{R}^+. \quad (2)$$

The critical flow-speed rate value for the road segment  $R_r$ :

$$FSR_{R_r, critical} = \frac{CP(S_{R_r, limit})}{S_{R_r, limit}}, \quad (3)$$

where  $CP(S_{R_r, limit})$  is the capacity of the road segment and  $S_{R_r, limit}$  is the speed limit of the road segment in mph. Critical flow-speed rate  $FSR_{R_r, critical}$  is a predetermined constant value that does not vary with time.

Using the instantaneous and critical flow-speed rate, the current level of the traffic jam  $\mathcal{C}_{R_r} = \{C_1, C_2, \dots, C_T\}$  can be determined, where

$$C_t = \frac{FSR_t}{FSR_{R_r, critical}} \quad t = 1, 2, \dots, T \quad C_t \in \mathbb{R}^+. \quad (4)$$

**Definition 1.** At time  $t$  a traffic jam will occur on the road segment  $R_r$  of the road network  $\mathcal{N}(\mathcal{I}, \mathcal{R})$ , if  $C_t \geq 1$  ( $C_t \in \mathcal{C}_{R_r}$ ) so  $FSR_t \geq FSR_{R_r, critical}$ .

Figure 2 shows an example of a flow-speed rate-based congestion definition. Data shown in the figure were obtained from the Caltrans Performance Measurement System (PEMS) [47]. The first and second rows of the figure show vehicle number and speed data. The third row contains the momentary congestion levels. The dashed red line is the critical flow-speed rate of congestion. Times above the line can be considered a traffic jam. It is worth noting that in all periods where the speed has declined significantly, the congestion level is above the critical value.

$$CP(S_{R_r,limit}) = \min(2200 + 10(S_{R_r,limit} - 50), 2400) \times Lanes, \tag{1}$$

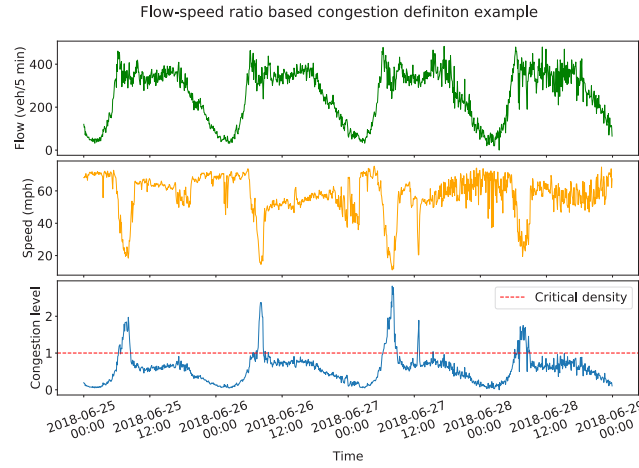


Fig. 2: Example for flow-speed ratio based congestion

This means that the flow-speed ratio-based method identifies traffic jams at the same time intervals as the speed-based methods. This is an important result, because while most of the methods from the literature require manually adjusting the parameters for each segment of the road, the parameters of the flow-speed ratio-based method are set automatically and an adaptive manner for each segment of the road.

In the case of propagation examining methods, it is often enough to know if the traffic jam had occurred, the actual level is not important (how much it is below or above the threshold). The momentary level of the congestion  $C_{R_r}$  can be converted to a  $\hat{C}_{R_r} = \{\hat{C}_1, \hat{C}_2, \dots, \hat{C}_T\}$  time series, where  $R_r$  is a road segment in the road network graph  $\mathcal{N}(\mathcal{I}, \mathcal{R})$ ,  $T$  is the length of the time series, and  $\hat{C}_t \in \{0, 1\}$ .

The  $\mathcal{Z} : C_{R_r} \rightarrow \hat{C}_{R_r}$  transformation can be used, where  $\forall C_t$  can be converted to  $\hat{C}_t$  as:

$$\hat{C}_t = \begin{cases} 1 & , \text{if } C_t \geq 1 \\ 0 & , \text{if } C_t < 1. \end{cases} \tag{5}$$

We wanted to validate the correctness of our definition, so we compared the binary output with other definitions from the literature. In our investigations, the SRI and SPI methods were implemented, and the used dataset was collected from the PEMS. The SRI required the precalculation of free-flow speed parameter, which were set to the 85th percentile of the off-peak speed. The SPI's max speed parameter was set to upper speed limit. In the examined dataset, the result of the Flow-speed ratio method differed from the SPI's output by only 2.8%, while 2.9% was the difference in the case of SRI. It is a minimal difference that means the Flow-speed ratio method gives appropriate output.

We have also checked the seven criteria of a good congestion measure from [11], and we have seen that the flow-speed ratio-based method satisfies all the listed criteria. The great advantage of the flow-speed ratio-based method is that it does not require the manual tuning of parameters for each

segment of the road, and utilizes two data types for the calculation of the congestion level. Thanks to the used capacity function, our method adapts to the parameters of the given road segment. Using flow and speed data together could also be a disadvantage because the flow-speed ratio-based congestion definition cannot be used if only the flow, the speed, or the travel time data is available alone.

#### IV. SPATIAL CONGESTION PROPAGATION PATTERNS (SCPP) ALGORITHM

In this chapter, we will explain the operation of the Spatial Congestion Propagation Patterns (SCPP) algorithm in detail. The SCPP algorithm is able to solve the problem of searching for frequent congestion propagation paths with linear complexity while describing the road network in as much detail as possible using a directed graph. The presented algorithm is a brand new algorithm, and we did not use parts from other algorithms in the literature. We would like to highlight that the presented algorithm supports arbitrary congestion definition, which can produce binary congestion information (signalling if congestion occurred or not). It means that the SCPP algorithm can also be used when the Flow-speed ratio-based congestion definition is not applicable.

First we define the necessary concepts, followed by the pseudo-codes and an explanation of the two main components of the algorithm in the order the processes are run:

- 1) Propagation Tree (PT) method: From the measured traffic data, it determines how many times the congestion propagated between road segments, and creates a describing graph based on the propagations, in which the nodes are the road segments and the edges are the propagations between the road segments.
- 2) Frequent Propagations (FP) method: Using the output of the Propagation Tree (PT) method and a certain threshold value, it searches for the most frequent traffic jam propagation patterns in the road network.

## Traffic congestion propagation identification method in smart cities

To run the SCPP algorithm, you need three input parameters: data matrix  $\overline{\mathcal{C}}_{\mathcal{N}}$ , edge-adjacency matrix  $\overline{\mathcal{A}}_{\mathcal{N}}$ , and a  $\epsilon$  threshold value.

$\overline{\mathcal{C}}_{\mathcal{N}}$  is a  $|\mathcal{R}| \times T$  matrix containing the traffic jam observations of road segments  $\mathcal{R}$  within road network  $\mathcal{N}(\mathcal{I}, \mathcal{R})$  for a period of time  $T$ . Every field in the matrix has a value of 0 or 1 ( $\overline{\mathcal{C}}_{R_r, t} \in \{0, 1\}$ , if  $R_r \in \mathcal{R}$ ), where 1 means there is a traffic jam and 0 is a state of free-flow.

The matrix  $\overline{\mathcal{A}}_{\mathcal{N}}$  is the  $|\mathcal{R}| \times |\mathcal{R}|$  sized edge-adjacency matrix of directed graph  $\mathcal{N}(\mathcal{I}, \mathcal{R})$ , which can be determined from the adjacency matrix of the line graph of the graph  $\mathcal{N}(\mathcal{I}, \mathcal{R})$ .  $\overline{\mathcal{A}}_{R_u, R_v} = 1$  if two road segments are adjacent to each other, otherwise  $\overline{\mathcal{A}}_{R_u, R_v} = 0$  ( $R_u, R_v \in \mathcal{R}$ ).

Here  $\epsilon$  is the threshold value that determines the minimum frequency. It is worthwhile to determine its value based on the length of the examined time period  $T$ , but it also depends on what qualifies as a frequent traffic jam in the environment, so designers can set it themselves depending on the traffic control and optimization goals.

Before beginning the presentation of methods PT and FP, we need to define what exactly ‘‘congestion occurrence’’ and ‘‘congestion propagation’’ are.

**Definition 2.** Let  $R_v$  ( $R_v \in \mathcal{R}$ ) be any segment of the road network  $\mathcal{N}(\mathcal{I}, \mathcal{R})$ . Let  $\overline{\mathcal{A}}_{\mathcal{N}}$  be the  $|\mathcal{R}| \times |\mathcal{R}|$  edge-adjacency matrix of the road network  $\mathcal{N}(\mathcal{I}, \mathcal{R})$ . **Congestion occurrence** is observed on the segment  $R_v$  at time  $t + 1$ , if  $R_v$  was not congested at time  $t$  ( $\overline{\mathcal{C}}_{R_v, t} = 0$ ) but is by the time  $t + 1$  ( $\overline{\mathcal{C}}_{R_v, t+1} = 1$ ). In addition, none of the neighbors of road segment  $R_v$  were congested at time  $t$ , so for  $\forall R_u$  it is true that  $\overline{\mathcal{C}}_{R_u, t} = 0$  if  $R_u \in \mathcal{R}$  and  $\overline{\mathcal{A}}_{R_u, R_v} = 1$ .

**Definition 3.** Let  $R_u$  and  $R_v$  ( $R_u \neq R_v$ ;  $R_u, R_v \in \mathcal{R}$ ) be the two road segments of road network  $\mathcal{N}(\mathcal{I}, \mathcal{R})$ . Let  $\overline{\mathcal{A}}_{\mathcal{N}}$  be the  $|\mathcal{R}| \times |\mathcal{R}|$  edge-adjacency matrix of road network  $\mathcal{N}(\mathcal{I}, \mathcal{R})$ . **Congestion propagation** is observed between  $R_u$  and  $R_v$  at time  $t + 1$ , if  $R_u$  was congested at time  $t$  ( $\overline{\mathcal{C}}_{R_u, t} = 1$ ) while  $R_v$  was not ( $\overline{\mathcal{C}}_{R_v, t} = 0$ ), but by time  $t + 1$  it is ( $\overline{\mathcal{C}}_{R_v, t+1} = 1$ ).  $R_u$  and  $R_v$  are adjacent to each other ( $\overline{\mathcal{A}}_{R_u, R_v} = 1$ ).

#### A. Propagation Tree (PT) method

The Propagation Tree (PT) method uses data matrix  $\overline{\mathcal{C}}_{\mathcal{N}}$  and the edge-adjacency matrix  $\overline{\mathcal{A}}_{\mathcal{N}}$  as input to generate a directed tree describing the propagation path  $\mathcal{P}(\mathcal{V}, \mathcal{L})$ , which contains all the congestion propagation paths according to Definition 3 observed within the data matrix. Propagation paths are directed paths within a propagation tree that connect the root of the tree to any leaf.

$\mathcal{V} = \{V_0, V_1, V_2, \dots, V_{|\mathcal{V}|}\}$  is the set of vertices of the tree in which any vertex  $V_v = \{R_x \rightarrow \dots \rightarrow R_y\}$  contains an observed unique propagation path. For example, let  $V_1 = \{R_1 \rightarrow R_2\}$  be an observed propagation path. There is a directed edge from  $V_1$  to  $V_v$ , if  $V_v = \{R_1 \rightarrow R_2 \rightarrow R_r\}$ , so that road segment  $R_r$  is adjacent to the road segment  $R_2$  according to the edge-adjacency matrix  $\overline{\mathcal{A}}_{\mathcal{N}}$  and propagation path  $V_v$  is observable in data matrix  $\overline{\mathcal{C}}_{\mathcal{N}}$ .

The root of the directed tree describing propagation paths

$\mathcal{P}(\mathcal{V}, \mathcal{L})$  will be vertex  $V_0 = \{-1\}$ , which does not contain a valid propagation path. Edge  $L_l$  exists between  $V_0$  and any vertex  $V_v = \{R_r\}$  if a traffic jam occurrence according to Definition 2 or a traffic jam propagation according to Definition 3 has been observed on road segment  $R_r \in \mathcal{R}$ . In addition, each edge  $L_l$  records a *freq* value that describes the frequency of propagation. Everytime when a propagation is detected between  $V_u$  and  $V_v$ , *freq* value of  $L_l$  is increased by one ( $L_l$  is the directed edge from  $V_u$  to  $V_v$ ).

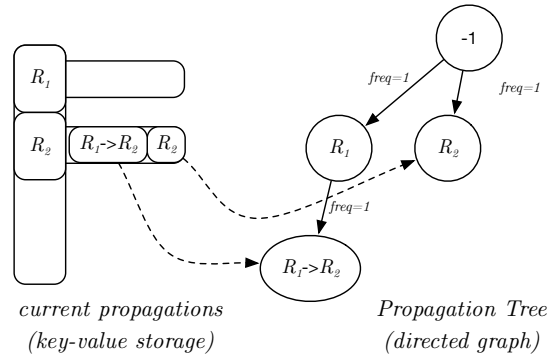


Fig. 3: Example of the relationship between *current\_propagations* and *tree* variables.

The steps of the Propagation Tree (PT) method are as follows. In the first step, we query the dimensions of the input data matrix, from which we determine the number of road segments (variable  $R$ ) and the length of the examined period (variable  $T$ ) (line 1). We then initialize the variables that store the results (lines 3-5). The *tree* stores the propagation paths observed so far in a directed graph. In addition to the *tree*, an important variable is *current\_propagations*, which records which propagation paths are currently active. The variable is a key-value storage in which the keys are the identifiers of each road segment and the values are the propagation paths in which the road segment in the key is the last road segment of the propagation path. This way, if the traffic jam propagates from the road segment in the key it is possible to follow which propagation paths need to be further developed. Figure 3 is an example of the relationship between the *current\_propagations* and *tree* variables when an  $R_1 \rightarrow R_2$  propagation happens.

PT starts processing the matrix *data\_mx* forward in time (lines 7-38). The *c\_state* variable stores the state at the current time (line 9), while the *p\_state* variable contains the previous state. The *where* method gives us the identifiers of the road segments on which the traffic jam phenomenon was observed by returning the array indices where the value is 1.

In the first loop, the previous state (*p\_state*) will still be empty, so we simply copy the value of the current state (lines 10-14) to the *tree* and *current\_propagations* variables using the *add\_propagations* method (Algorithm 2) and then go to the second loop immediately.

Starting from the second loop, we iterate over the road segments that are congested in their current state (lines 15-

27). If the congested road segment ( $c\_road$ ) was not present in the previous state, it is worth investigating, because this is when important state change occurs (lines 17-26). We then extract the adjacent road segments ( $source\_roads$ ) preceding the examined road segment from the edge-adjacency matrix  $adj\_mx$  and see if we find them in the previous state (lines 18-19).

If none are found, it means that we have detected a congestion occurrence on the examined road segment (lines 20-22). Propagations that occur within the loop are stored in the  $propagations$  key-value variable (line 15), where the key is the source of the propagation and the value is the road segment to which the traffic jam has propagated. In the case of a new propagation, the source of the propagation is the  $-1$  identifier (line 21).

Otherwise, the congestion has not occurred on the examined road segment, but on one of the neighboring road segment (lines 22-25). Because it cannot be ruled out that several congested neighbors are affecting it simultaneously, all possible cases must be added to the  $propagations$  variable.

Once we have traversed all the road segments from  $c\_state$ , we add the propagations registered in  $propagations$  to the  $tree$  and  $current\_propagations$  variables using the  $add\_propagation$  method (lines 28-30).

We then go through the road segments that were congested in the previous state and see which of them are still congested in the current state (lines 32-36). If the traffic jam on a road segment has ended, the propagation pointers of the road segment are removed from  $current\_propagations$ .

Since we have to study all road segments where a congestion phenomenon has occurred within all time intervals, the step number of the PT method is  $O(T|\mathcal{R}|)$ , where  $T$  is the length of the examined period in time intervals and  $|\mathcal{R}|$  the number of road segments, which is the upper estimate for the number of traffic jams that have occurred.

Another important part of the PT method is the  $add\_propagation$  submethod. Its function is to maintain the tree describing the propagation ( $tree$ ) and the currently tracked traffic jams ( $current\_propagations$ ). When these variables need to be updated,  $add\_propagation$  receives these two variables as input parameters and modifies their internal state.

As the first step,  $add\_propagation$  checks to see if the source of the propagation ( $from\_road$ ) obtained as a parameter is the same as node  $-1$ . If so, the propagation is added to the tree as a congestion occurrence (lines 1-10). In this case, it adds the target road segments to the tree variable if they do not exist yet (lines 3-6) and then increments the associated frequency  $freq$  counter by one (line 7). It then registers the node in the  $current\_propagations$  variable as a one-element propagation path identifier (line 8).

If the traffic jam has not occurred on that segment of road, it should be added to the tree as a propagation (lines 10-30). We have to iterate over all the cases where the source of the propagation was previously active. These are contained in  $current\_propagations[from\_road]$  (line 11). Since the traffic jam can propagate from one road segment to several road segments at the same time, we have to go through these as well (lines 12).

**Input:**  $data\_mx$ : data matrix  $\bar{\bar{C}}_{\mathcal{N}}$ ;  
 $adj\_mx$ : edge-adjacency matrix  $\bar{\bar{A}}_{\mathcal{N}}$

**Output:** Directed graph describing the propagations  $\mathcal{P}(\mathcal{V}, \mathcal{L})$

```

1  $R, T = data\_mx.shape$ 
2
3  $current\_propagations = empty$ 
4  $tree = DirectedGraph()$ 
5  $tree.add\_node(-1, route\_id = -1)$ 
6
7  $p\_state = None$ 
8 for  $t = 1$  to  $T$  do
9    $c\_state = where(data\_mx[:, t] == 1)$ 
10  if  $p\_state$  is  $None$  then
11     $add\_propagation(p\_state, c\_state, state$ 
12     $current\_propagations, tree)$ 
13     $continue$ 
14  end
15   $propagations = empty$ 
16  for  $c\_road$  in  $c\_state$  do
17    if  $c\_road$  not in  $p\_state$  then
18       $pred\_roads = where(adj\_mx[:,$ 
19       $, c\_road] == 1)$ 
20       $source\_roads =$ 
21       $intersect(pred\_roads, p\_state)$ 
22      if  $len(source\_roads) < 1$  then
23         $propagations[-1].append(c\_road)$ 
24      else
25        for  $s\_road$  in  $source\_roads$  do
26           $propagations[s\_road].append(c\_road)$ 
27        end
28      end
29    end
30  end
31  for  $from\_road, to\_roads$  in  $propagations$  do
32     $add\_propagation(from\_road, to\_roads,$ 
33     $current\_propagations, tree)$ 
34  end
35  for  $c\_road$  in  $p\_state$  do
36    if  $c\_road$  not in  $c\_state$  then
37       $current\_propagations[c\_road] = []$ 
38    end
39  end
40   $p\_state = c\_state$ 
41 end

```

**Algorithm 1:** The pseudo code of the PT method

We generate a pointer for the propagation path, which has occurred from the concatenation of the previous propagation path identifier and the congested road segment (line 13). If the propagation path identifier has not yet been included, we add it to the tree as a new node (lines 14-16), then increase the frequency counter (line 17) and register the propagation path identifier in the  $current\_propagations$  variable to the  $to\_road$  road segment (line 18).

Traffic congestion propagation identification method in smart cities

**Input:** *from\_road*: source of the propagation;  
*to\_roads*: target of propagation,  
*current\_propagations*: currently congested road segments, *tree*: tree describing the propagations

**Output:** void

```

1 if from_road == -1 then
2   for to_road in to_roads do
3     if to_road not in tree then
4       tree.add_node(to_road, route_id =
5         to_road)
6       tree.add_edge(-1, to_road, freq = 0)
7     end
8     tree.edges[-1, to_road]['freq'] += 1
9     current_propagations[to_road] = [to_road]
10  end
11 else
12   for c_prop in current_propagations[from_road] do
13     for to_road in to_roads do
14       prop_pointer = c_prop + ' ' + to_road
15       if prop_pointer not in tree then
16         tree.add_node(prop_pointer,
17           route_id = to_road)
18         tree.add_edge(c_prop,
19           prop_pointer, freq = 0)
20       end
21       tree.edges[c_prop, prop_pointer]['freq'] +=
22         1
23       current_propagations[to_road]
24       .append(prop_pointer)
25       if to_road not in tree then
26         tree.add_node(to_road, route_id =
27           to_road)
28         tree.add_edge(-1, to_road, freq = 0)
29       end
30       tree.edges[-1, to_road]['freq'] += 1
31       if to_road not in
32         current_propagations[to_road] then
33         current_propagations[to_road]
34         .append(to_road)
35       end
36     end
37   end
38 end

```

**Algorithm 2:** The pseudo code for *add\_propagations* submethod

It may be that part of a propagation path occurs more frequently than the entire propagation path itself, e.g., from the propagation  $R_1 \rightarrow R_2 \rightarrow R_3$ , the propagation  $R_2 \rightarrow R_3$  occurs more frequently. This may be due to the fact that a traffic jam has already occurred in  $R_2$  or that  $R_2$  is connected with another road segment  $R_4$  from which the congestion often propagates as part of an  $R_4 \rightarrow R_2 \rightarrow R_3$  propagation. To record these as well, we add the variable *to\_road* to the graph describing the propagations (*tree*) as a congestion occurrence and also register this in the variable *current\_propagations* to the road segment *to\_road* (lines 21-28).

**B. Frequent Propagations (FP) method**

**Input:** *tree*: graph describing propagations  $\mathcal{P}(\mathcal{V}, \mathcal{L})$ ,  
*eps*:  $\epsilon$  frequency threshold

**Output:** *subtrees*: frequent propagation graphs

```

1 tree_cp = tree.copy()
2 removable_edges = []
3 for edge in tree_cp.edges do
4   if edge.freq < eps then
5     removable_edges.append(edge)
6   end
7 end
8 tree_cp.remove_edges_from(removable_edges)
9
10 isolated = get_isolated_nodes(tree_cp)
11 tree_cp.remove_nodes_from(isolated)
12
13 if not tree_cp.has_node(-1) then
14   return []
15 end
16 propagation_sources = tree_cp.successors('-1')
17 sub_trees = []
18 for propagation_source in propagation_sources do
19   sub_tree =
20     bfs_tree(tree_cp, propagation_source)
21   if sub_tree is not None then
22     sub_trees.append(sub_tree)
23   end
24 end

```

**Algorithm 3:** Pseudo code for the FP method

The task of the FP method is to find the frequent propagations based on the descriptive tree  $\mathcal{P}(\mathcal{V}, \mathcal{L})$  constructed by the PT method and a  $\epsilon$  threshold ( $\epsilon \in \mathbb{N}^+$ ). To do this, the FP method iterate over the edges of the graph  $\mathcal{P}(\mathcal{V}, \mathcal{L})$  and deletes all edges whose frequency *freq* value is less than the threshold value. This will result in the originale breaking into several subgraphs that now only contain edges that satisfy the condition.

It is worth noting that the graph  $\mathcal{P}(\mathcal{V}, \mathcal{L})$  only needs to be calculated once, and after that any number of  $\epsilon$  thresholds can be tested on it. This is a faster approach to the problem than if the propagation graph had to be rebuilt for each  $\epsilon$  threshold.

The first step of the algorithm is to copy the original tree (line 1). This is necessary because the graph describing the propagation does not have to be recalculated for each new *eps*.

We then iterate over the edges of the copied tree and collect those with a *freq* value less than *eps* (lines 2-7). The edges collected in the *removable\_edges* variable are then deleted from the *tree\_cp* tree (line 8).

After the step, there may be vertices in the graph that have no edges connected to them. Using the *get\_isolated\_nodes* method, we collect these and then delete them from the graph as well (lines 10-11).

If there is no node  $-1$  in the graph after that, it means that no edge met the condition, so we return with an empty array (lines 13-15).

In the last step, we go through the direct descendants of node  $-1$ , which are the starting road segments of the propagations (lines 16-23). Starting from each starting road segment (*propagation\_source*), we perform a breadth-first search with the *bfs\_tree* method. In this, we traverse the subtree (*sub\_tree*) and add it to the list of subtrees *sub\_tree*, but only if the traversed subtree is not empty.

The number of steps of the FP method can be estimated by the cardinality of the edge sets ( $|\mathcal{L}|$ ) of the graph  $\mathcal{P}(\mathcal{V}, \mathcal{L})$ . To delete edges that do not meet the  $\epsilon$  threshold  $|\mathcal{L}|$  number of steps are required. The maximum number of steps of the breadth-first search even in the worst case can be estimated with the value of  $|\mathcal{L}|$ . Thus the FP method's number of steps will be  $O(2^{|\mathcal{L}|}) \rightarrow O(|\mathcal{L}|)$ . This also means that the number of steps of the entire SCPP algorithm is  $O(T|\mathcal{R}| + |\mathcal{L}|)$ .

V. EVALUATION OF THE SCPP ALGORITHM

The performance of the SCPP algorithm was compared with the performance of the STC algorithm, because of all the methods described in the professional literature, only this one uses a quadratic number of steps.

In addition, the algorithm's author made the implementation of the method [48], and the test data set they used open source, so we could reproduce their results and compare them with the results of our own algorithm.

We were forced to modify the implementation of the STC algorithm at one point because we noticed that there was a theoretical error in the original implementation: The STCTree method of the algorithm [39] examines whether the traffic jam currently being examined may be a source of a previous propagation in a nested loop (line 20 of STCTree). However, when specifying the *if* condition, it does not take into account whether the previous propagation had already existed at the time of the occurrence of the currently examined traffic jam. Thus, it also included propagations in the comparison that did not actually exist.

In the first step of our study, we compared the output of the modified implementation of STC with the output of our own solution (Section V-A). Our goal was to examine the differences in the outputs of the two algorithms. We then wondered whether SCPP, which in theory is faster, would actually find frequent propagations sooner than STC, considering the changing input parameters (Section V-B).

In our performance analysis, we examined how much the average execution times depend on:

- the length of the examined time period,
- the size of the road network,
- the value of the threshold value.

The dataset [49] used in the evaluation for each test was the same and identical to that used in [39]. This is a real dataset recorded between June 17, 2013 and July 14, 2013 in Melbourne. The provided dataset contained only the required binary congestion data. Thus, we could not execute the Flow-speed ratio congestion definition on the dataset, but we could use it as an input for SCPP because it supports binary congestion data. The examined road network contains 586 road segments, from which data were collected every 5 minutes on

average, and in total 7,657 times. Each test case was run at least 10 times to be sure that a temporary slow-down of the test system does not affect the results' correctness. During the evaluations, we used the average value of these executions' result.

A. Testing of the congestion propagation path identification

To be able to compare the outputs of the SCPP and STC algorithms, we need to better understand how the STC works. The STC algorithm uses the Apriori algorithm to discover frequent propagation paths (subtrees). The Apriori algorithm was basically invented to search for association rules (frequent coincidences) in a large database. A good example of this is understanding people's shopping habits, where the question is what products are purchased together by customers. With each purchase, the store saves what was in a customer's basket at the time of payment. On the database built from these baskets, we can execute the Apriori algorithm, which looks for products that were purchased together frequently. A product list will be common if the items in it are listed together at least  $\epsilon$  times. This, in the context of a congestion study, means that a congestion path is considered to be frequent if the road segments within in the path have been congested together at least  $\epsilon$  times.

It is important to note that STC and SCPP interpret the meaning of  $\epsilon$  differently. While SCPP simply considers this value as a frequency ( $\epsilon_{SCPP} \in \mathbb{R}^+$ ), the STC algorithm uses the Apriori algorithm to filter out frequent propagation, in which  $\epsilon$  as a ratio to the total number of propagations found ( $\epsilon_{STC} \in (0, 1)$ ) where the size of the set of propagations found is denoted by  $M$ . To make the results comparable, we first ran the STC procedure with the  $\epsilon_{STC}$  values that are being examined. Based on this, a propagation is considered frequent if it has occurred at least  $\epsilon_{STC} \times M$  times, so  $\epsilon_{SCPP}$  can be calculated as  $\epsilon_{SCPP} = \epsilon_{STC} \times M$ . The SCPP algorithm was run with the  $\epsilon_{SCPP}$  value derived from the STC algorithm, so the efficiency of the two methods can be compared.

To make the notation system simple in the following, when we refer to  $\epsilon$ , we mean  $\epsilon_{STC}$ .

To compare SCPP and STC, propagation paths were generated from the output propagation trees of both algorithms as shown in Figure 4 to include partial propagation paths in the comparison.

We then examined whether the propagation paths of one algorithm could be found among the propagation paths of the other algorithm. Performance-efficiency studies were run at different settings.

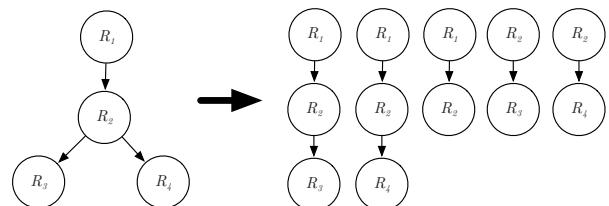


Fig. 4: Example of generating propagation paths.

Traffic congestion propagation identification method in smart cities

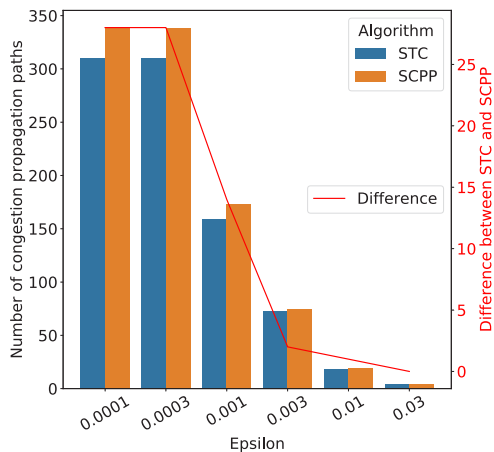


Fig. 5: Comparison of the number of traffic jam propagation paths found.

In all cases examined, it was true that the output of the SCPP included the output of the STC, but that STC did not include all the propagation paths of the SCPP. All of these were cases where the propagation path already consisted of at least 2 road segments and then propagated to a third road segment as the traffic jam on segment 2 disappeared. These cases were all successfully identified by the SCPP, while the STC was unable to do so. To compare the cardinality of the outputs, Figure 5 was prepared, where the number of propagation paths found was also displayed as a function of  $\epsilon$ . At high  $\epsilon$  values, the difference in the number of propagation paths found can be small, even 0. However, as we move toward the smaller  $\epsilon$  values, the number of propagation paths not found by the STC begins to increase. In some cases, SCPP found up to 8.28% more, and on average 5.84% more, propagations than STC. This is because, in the case of less frequent propagations, the aforementioned situation when the STC is unable to identify the propagation path occurs more.

B. Study of computational performance

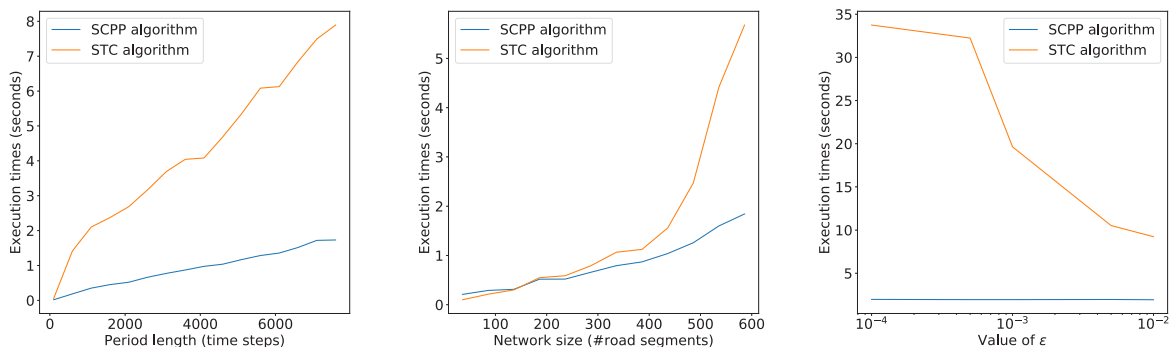
We started our measurements by changing the size of the studied time period. In these tests, we looked at how increasing

the length of the studied time period ( $T$  parameter) changes the average execution time of the algorithms. Tests were started off with  $T = 100$  and then increased step by step up to  $T = 7657$ . It can be seen on Figure 6a that with the increase of  $T$ , the average execution time of STC and SCPP both increase, but the STC is much steeper. The reason for this is that the STC's complexity is  $O(TN^2)$ , while that of the SCPP is only  $O(TN)$ , where  $T$  is the length of the examined time period in time intervals and  $N$  is the number of traffic jam phenomena that occurred during the period  $T$ . At maximum  $T$ , the STC execution time was 7.499 seconds, while the SCPP completed the task in 1.164 seconds. This means that SCPP solved the task 763% faster. Looking at all the studied cases, the SCPP performed calculations 483% faster on average.

We then looked at how increasing the number of road segments affect average execution times. First  $|\mathcal{R}| = 36$  road segments were examined, then we increased the number of road segments by 50 every time up to  $|\mathcal{R}| = 586$ . The length of the studied time period was  $T = 7657$  for all test cases. The results are shown in Figure 6b. It is clear that initially there is not much difference in the execution times of the two algorithms, but then the execution time of the STC starts to increase quadratically. The reason for this is that with the addition of new road segments, the number of traffic phenomena to be tested increases, of which the STC's complexity depends quadratically. Meanwhile, the runtime of the SCPP increases almost linearly. In the cases studied, SCPP was 146% faster on average, but at  $|\mathcal{R}| = 586$ , the difference was 308%.

We were also curious about how much the size of the  $\epsilon$  threshold value affects the average execution times. During the tests  $|\mathcal{R}| = 586$  road segments and  $T = 7657$  time periods were used and only the value of  $\epsilon$  was changed.

The result of the study is shown in Figure 6c, where the scaling of the x-axis is logarithmic. It can be seen that as the value of  $\epsilon$  decreases, the average running time of the STC increases exponentially. This is because the Apriori algorithm has  $O(2^M)$  exponential complexity, where  $M$  is the number of total propagations found. As we decrease  $\epsilon$ 's value, the number of propagations that meet the frequency condition increase.



(a) The performance of the algorithms as a function of the studied time period (b) The performance of the algorithms as a function of the number of road segments examined (c) The performance of the algorithms as a function of  $\epsilon$

Fig. 6: Results of the performance study

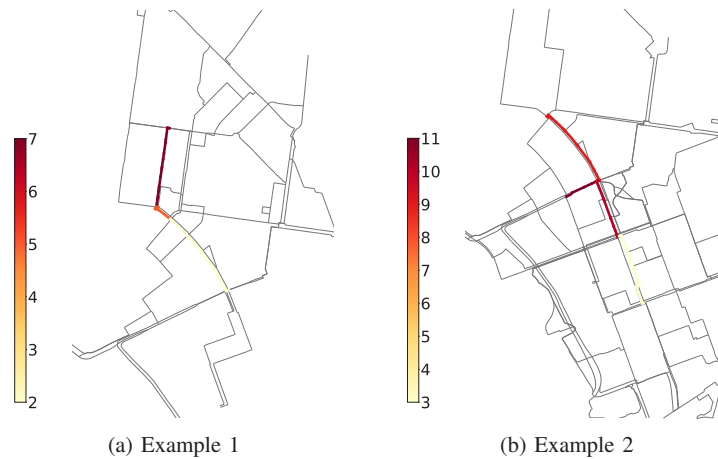


Fig. 7: Visualizing the frequent propagations in Melbourne

In contrast, the average run time of the SCPP algorithm remained nearly constant, independent of  $\epsilon$ 's change. This is explained by the fact that within the SCPP algorithm, the step number of the Frequent Congestions (FC) method is  $O(|\mathcal{L}|)$ , which does not correlate with  $\epsilon$ .

This resulted in the fact that in the studied cases the SCPP ran on average 10.79 times faster, while in the case of the lowest  $\epsilon$  value examined the execution time was 17.13 faster.

C. Visualization of results

The SCPP algorithm not only provides the frequent propagation paths with greater accuracy and more quickly, unlike previous methods it also provides the quantification of propagation phenomena.

This is an extra piece of information when visualizing frequent propagations, so we can weight the frequency of propagation with appropriate coloring. The map used for visualization was downloaded from OpenStreetMap and the measurement points were mapped onto it. The propagation paths between the measurement points were determined by the Dijkstra algorithm running on the road network, which was weighted by the length of the road segments.

Figure 7 shows two different examples from the city of Melbourne. In the lower left corner of each example, there is a color scale showing the hues associated with the frequencies. With the visualization of SCPP, the propagation paths have become well identifiable, which in several cases branch out. In figure 7a spike-shaped propagations can be observed at two separate points. This is because in some cases, the GPS coordinates of the measurement points are not accurate, which distorts the output.

Visualization of traffic jams is important because urban traffic management authorities can discover correlations that can help them plan long-term urban transport (traffic light settings, public transport routes) and even shorter-term intervention.

VI. CONCLUSION

Managing the frequent congestion in the traffic networks of large cities is a serious challenge for municipal traffic

managing organizations. In order to handle these situations, it is crucial to understand the processes that lead to congestion and propagation.

In this article, we introduce a new method capable of using city traffic data to find frequent traffic jam propagations. We introduce the steps of the method in detail and then we compare the output to the accepted and the widely cited solutions of the professional literature. In addition to introducing the method, we also lay out a new definition for "traffic jam" that, unlike previous solutions, does not rely on manually setting parameters, and instead is able to define traffic jam levels on the basis of the size of the road segment.

During our evaluation we look at how the performance of our method depends on the input parameters and real datasets. The results of our testing clearly show that SCPP carries out its task significantly faster and more precisely than the other solution, while also adding frequency information to the output, further aiding the refinement of the road network analysis and the visualization of propagations.

In the future, we would like to extend SCPP to use continuous congestion data instead of binary congestion data, as it can further improve the performance of the algorithm.

REFERENCES

- [1] N. Zhong, J. Cao, and Y. Wang, "Traffic congestion, ambient air pollution, and health: Evidence from driving restrictions in Beijing," *Journal of the Association of Environmental and Resource Economists*, vol. 4, no. 3, pp. 821–856, 2017, doi: 10.1086/692115.
- [2] M. Rosenlund, F. Forastiere, M. Stafoggia, D. Porta, M. Perucci, A. Ranzi, F. Nussio, and C. A. Perucci, "Comparison of regression models with land-use and emissions data to predict the spatial distribution of traffic-related air pollution in Rome," *Journal of Exposure Science and Environmental Epidemiology*, vol. 18, no. 2, pp. 192–199, 2008, doi: 10.1038/sj.jes.7500571.
- [3] O. K. Kurt, J. Zhang, and K. E. Pinkerton, "Pulmonary health effects of air pollution," *Current opinion in pulmonary medicine*, vol. 22, no. 2, p. 138, 2016, doi: 10.1097/MCP.0000000000000248.
- [4] K. Chen, A. Schneider, J. Cyrus, K. Wolf, C. Meisinger, M. Heier, W. von Scheidt, B. Kuch, M. Pitz, A. Peters et al., "Hourly exposure to ultrafine particle metrics and the onset of myocardial infarction in Augsburg, Germany," *Environmental Health Perspectives*, vol. 128, no. 1, p. 017003, 2020, doi: 10.1289/EHP5478.

Traffic congestion propagation identification method in smart cities

[5] X. Tian, H. Dai, Y. Geng, J. Wilson, R. Wu, Y. Xie, and H. Hao, "Economic impacts from pm2.5 pollution-related health effects in china's road transport sector: A provincial-level analysis," *Environment international*, vol. 115, pp. 220–229, 2018, doi: 10.1016/j.envint.2018.03.030.

[6] L. Zhu, F. R. Yu, Y. Wang, B. Ning, and T. Tang, "Big data analytics in intelligent transportation systems: A survey," *IEEE Transactions on Intelligent Transportation Systems*, vol. 20, no. 1, pp. 383–398, 2018, DOI: 10.1109/TITS.2018.2815678.

[7] J. Li, Y. Zhang, and Y. Chen, "A self-adaptive traffic light control system based on speed of vehicles," in *2016 IEEE International Conference on Software Quality, Reliability and Security Companion (QRS-C)*. IEEE, 2016, pp. 382–388, doi: 10.1109/QRS-C.2016.58.

[8] L. A. Klein, M. K. Mills, and D. R. Gibson, "Traffic detector handbook: 3rd ed. — volume II." Federal Highway Administration, Tech. Rep. Publi. No. FHWA-HRT-06-139, October 2006.

[9] Z. MacHardy, A. Khan, K. Obana, and S. Iwashina, "V2x access technologies: Regulation, research, and remaining challenges," *IEEE Communications Surveys & Tutorials*, vol. 20, no. 3, pp. 1858–1877, 2018, doi: 10.1109/COMST.2018.2808444.

[10] A. Paranjothi, M. S. Khan, and S. Zeadally, "A survey on congestion detection and control in connected vehicles," *Ad Hoc Networks*, vol. 108, p. 102277, 2020, doi: 10.1016/j.adhoc.2020.102277.

[11] T. Afrin and N. Yodo, "A survey of road traffic congestion measures towards a sustainable and resilient transportation system," *Sustainability*, vol. 12, no. 11, p. 4660, 2020, doi: 10.3390/su12114660.

[12] S. Wang, X. Zhang, J. Cao, L. He, L. Stenneth, P. S. Yu, Z. Li, and Z. Huang, "Computing urban traffic congestions by incorporating sparse gps probe data and social media data," *ACM Transactions on Information Systems (TOIS)*, vol. 35, no. 4, p. 40, 2017, doi: 10.1145/3057281.

[13] S. Wang, F. Li, L. Stenneth, and S. Y. Philip, "Enhancing traffic congestion estimation with social media by coupled hidden markov model," in *Joint European Conference on Machine Learning and Knowledge Discovery in Databases*. Springer, 2016, pp. 247–264, doi: 10.1007/978-3-319-46227-1\_16.

[14] Y. Yang, Y. Xu, J. Han, E. Wang, W. Chen, and L. Yue, "Efficient traffic congestion estimation using multiple spatio-temporal properties," *Neurocomputing*, vol. 267, pp. 344–353, 2017, doi: 10.1016/j.neucom.2017.06.017.

[15] X. Kong, Z. Xu, G. Shen, J. Wang, Q. Yang, and B. Zhang, "Urban traffic congestion estimation and prediction based on floating car trajectory data," *Future Generation Computer Systems*, vol. 61, pp. 97–107, 2016, doi: 10.1016/j.future.2015.11.013.

[16] S. Yang, "On feature selection for traffic congestion prediction," *Transportation Research Part C: Emerging Technologies*, vol. 26, pp. 160–169, 2013, doi: 10.1016/j.trc.2012.08.005.

[17] M. Fouladgar, M. Parchami, R. Elmasri, and A. Ghaderi, "Scalable deep traffic flow neural networks for urban traffic congestion prediction," in *2017 International Joint Conference on Neural Networks (IJCNN)*. IEEE, 2017, pp. 2251–2258, doi: 10.1109/IJCNN.2017.7966128.

[18] M. Chen, X. Yu, and Y. Liu, "Penn: Deep convolutional networks for short-term traffic congestion prediction," *IEEE Transactions on Intelligent Transportation Systems*, vol. 19, no. 11, pp. 3550–3559, 2018, doi: 10.1109/TITS.2018.2835523.

[19] Y. Wang, J. Cao, W. Li, and T. Gu, "Mining traffic congestion correlation between road segments on gps trajectories," in *2016 IEEE International Conference on Smart Computing (SMARTCOMP)*. IEEE, 2016, pp. 1–8, doi: 10.1109/SMARTCOMP.2016.7501704.

[20] H. Xiong, A. Vahedian, X. Zhou, Y. Li, and J. Luo, "Predicting traffic congestion propagation patterns: A propagation graph approach," in *IWCTS@ SIGSPATIAL*, 2018, pp. 60–69, doi: 10.1145/3283207.3283213.

[21] M. Bai, Y. Lin, M. Ma, P. Wang, and L. Duan, "Prepct: Traffic congestion prediction in smart cities with relative position congestion tensor," *Neurocomputing*, 2020, doi: 10.1016/j.neucom.2020.08.075.

[22] N. H. Gartner, C. J. Messer, and A. Rathi, "Traffic flow theory—a state-of-the-art report: revised monograph on traffic flow theory," *FHWA, U.S. Department of Transportation*, 2002.

[23] A. M. Rao and K. R. Rao, "Measuring urban traffic congestion—a review," *International Journal for Traffic & Transport Engineering*, vol. 2, no. 4, 2012, doi: 10.7708/IJTTE.2012.2(4).01

[24] F. He, X. Yan, Y. Liu, and L. Ma, "A traffic congestion assessment method for urban road networks based on speed performance index," *Procedia engineering*, vol. 137, pp. 425–433, 2016, doi: 10.1016/j.proeng.2016.01.277.

[25] D. Ter Huurne and J. Andersen, "A quantitative measure of congestion in stellenbosch using probe data," in *Proc. of the 1st Int. Conf. on the use of Mobile Informations and Communication Technology (ICT) in Africa UMICT*. STIAS Conference Centre, 9–10 Dec 2014, Stellenbosch, South Africa.

[26] M. Aftabuzzaman, "Measuring traffic congestion—a critical review," in *30th Australasian Transport Research Forum*, 2007, pp. 1–16.

[27] C. Wan, Z. Yang, D. Zhang, X. Yan, and S. Fan, "Resilience in transportation systems: a systematic review and future directions," *Transport reviews*, vol. 38, no. 4, pp. 479–498, 2018, doi: 10.1080/01441647.2017.1383532.

[28] J. Tang and H. R. Heinimann, "A resilience-oriented approach for quantitatively assessing recurrent spatial-temporal congestion on urban roads," *PLoS one*, vol. 13, no. 1, p. e0190616, 2018, doi: 10.1371/journal.pone.0190616.

[29] *Highway Capacity Manual 6th Edition: A Guide for Multimodal Mobility Analysis*. TRB, 2016.

[30] X. Di, Y. Xiao, C. Zhu, Y. Deng, Q. Zhao, and W. Rao, "Traffic congestion prediction by spatiotemporal propagation patterns," in *2019 20th IEEE International Conference on Mobile Data Management (MDM)*. IEEE, 2019, pp. 298–303, doi: 10.1145/3283207.3283213.

[31] S. Xingjian, Z. Chen, H. Wang, D.-Y. Yeung, W.-K. Wong, and W.-c. Woo, "Convolutional lstm network: A machine learning approach for precipitation nowcasting," in *Advances in neural information processing systems*, 2015, pp. 802–810.

[32] Y. Liang, Z. Jiang, and Y. Zheng, "Inferring traffic cascading patterns," in *Proceedings of the 25th ACM SIGSPATIAL International Conference on Advances in Geographic Information Systems*. ACM, 2017, p. 2, doi: 10.1145/3139958.3139960.

[33] A.-L. Barabasi, "The origin of bursts and heavy tails in human dynamics," *Nature*, vol. 435, no. 7039, p. 207, 2005, doi: 10.1038/nature03459.

[34] M. G. Rodriguez and B. Schölkopf, "Submodular inference of diffusion networks from multiple trees," *arXiv preprint arXiv:1205.1671*, 2012.

[35] R. Albert and A.-L. Barabási, "Statistical mechanics of complex networks," *Reviews of modern physics*, vol. 74, no. 1, p. 47, 2002, doi: 10.1103/RevModPhys.74.47.

[36] W. Liu, Y. Zheng, S. Chawla, J. Yuan, and X. Xing, "Discovering spatiotemporal causal interactions in traffic data streams," in *Proceedings of the 17th ACM SIGKDD international conference on Knowledge discovery and data mining*. ACM, 2011, pp. 1010–1018, doi: 10.1145/2020408.2020571.

[37] L. Di Stefano and A. Bulgarelli, "A simple and efficient connected components labeling algorithm," in *Proceedings 10th International Conference on Image Analysis and Processing*. IEEE, 1999, pp. 322–327, doi: 10.1109/ICIAP.1999.797615.

[38] B. Hossain, K. A. Adnan, M. F. Rabbi, and M. E. Ali, "Modelling road traffic congestion from trajectories," in *Proceedings of the 3rd International Conference on Data Science and Information Technology*, 2020, pp. 117–122, doi: 10.1145/3414274.3414491.

[39] H. Nguyen, W. Liu, and F. Chen, "Discovering congestion propagation patterns in spatio-temporal traffic data," *IEEE Transactions on Big Data*, vol. 3, no. 2, pp. 169–180, 2016, doi: 10.1109/TBDATA.2016.2587669.

[40] R. Agrawal, R. Srikant et al., "Fast algorithms for mining association rules," in *Proc. 20th int. conf. very large data bases, VLDB*, vol. 1215, 1994, pp. 487–499,

[41] Z. Chen, Y. Yang, L. Huang, E. Wang, and D. Li, "Discovering urban traffic congestion propagation patterns with taxi trajectory data," *IEEE Access*, vol. 6, pp. 69 481–69 491, 2018, doi: 10.1109/ACCESS.2018.2881039.

[42] J. Han, J. Pei, and Y. Yin, "Mining frequent patterns without candidate generation," in *ACM sigmod record*, vol. 29, no. 2. ACM, 2000, pp. 1–12, doi: 10.1145/335191.335372.

- [43] L. A. Elefteriadou, "New trb publication: The highway capacity manual: A guide for multimodal mobility analysis," *TR News*, no. 306, 2016.
- [44] B. Friedrich, "The effect of autonomous vehicles on traffic," in *Autonomous Driving*. Springer, 2016, pp. 317–334, doi: 10.1007/978-3-662-48847-8\_16.
- [45] Q. Lu, T. Tettamanti, D. Hörcher, and I. Varga, "The impact of autonomous vehicles on urban traffic network capacity: an experimental analysis by microscopic traffic simulation," *Transportation Letters*, vol. 12, no. 8, pp. 540–549, 2020, doi: 10.1080/19427867.2019.1662561.
- [46] A. Ghiasi, "Connected autonomous vehicles: Capacity analysis, trajectory optimization, and speed harmonization," Ph.D. dissertation, University of South Florida, 2018.
- [47] "Caltrans pems," 2020, [Online; accessed 17-March-2020]. [Online]. Available: <http://pems.dot.ca.gov/>
- [48] H. Nguyen, "congestionpropagation," <https://github.com/nguyend/congestionpropagation>, 2021, [Online; accessed 22-March-2021].
- [49] —, "Melbourne congestion dataset," <https://github.com/nguyend/congestionpropagation/tree/master/matdata>, 2021, [Online; accessed 22-March-2021].



series data mining and analysis, traffic prediction, traffic congestion data analysis, automatic traffic incident detection.

**Attila M. Nagy** received the B.S. and M.S. degrees in computer engineering from the Budapest University of Technology and Economics (BME), Budapest, in 2016. From 2016-2020, he was PhD student in computer engineering from the Budapest University of Technology and Economics (BME), Budapest. Since 2020 he is a Research Assistant in MEDIANETS laboratory at Department of Networked Systems and Services, BME. His research interests include time



interests include machine learning and data analytics for smart cities and intelligent transportation management systems.

He published 50+ papers in international journals and conferences, and acts as a reviewer or organizer for numerous scientific conferences. He serves currently as the Corporate liaison vice president for the Connected and Automated Mobility Cluster of Zala.

**Vilmos Simon** received his PhD from the Budapest University of Technology and Economics (BME) in 2009. Currently he is an Associate Professor at the Department of Networked Systems and Services, Head of the Multimedia Networks and Services Laboratory and Deputy Head of Department of Networked Systems and Services.

He has done research on mobility management and energy efficiency in mobile cellular systems and self-organized mobile networks, recently his research

# Joint Beacon Power and Beacon Rate Control Based on Game Theoretic Approach in Vehicular Ad Hoc Networks

Hamid Garmani, Driss Ait Omar, Mohamed El Amrani, Mohamed Baslam, and Mostafa Jourhmane

**Abstract—** In vehicular ad hoc networks (VANETs), each vehicle broadcasts its information periodically in its beacons to create awareness for surrounding vehicles aware of their presence. But, the wireless channel is congested by the increase beacons number, packet collision lost a lot of beacons. This paper tackles the problem of joint beaconing power and a beaconing rate in VANETs. A joint utility-based beacon power and beacon rate game are formulated as a non-cooperative game and a cooperative game. A three distributed and iterative algorithm (Nash Seeking Algorithm, Best Response Algorithm, Cooperative Bargaining Algorithm) for computing the desired equilibrium is introduced, where the optimal values of each vehicle beaconing power and beaconing rate are simultaneously updated at the same step. Extensive simulations show the convergence of a proposed algorithm to the equilibrium and give some insights on how the game parameters may vary the game outcome. It is demonstrated that the Cooperative Bargaining Algorithm is a fast algorithm that converges the equilibrium.

**Index Terms—** Beacon rate, Beacon power, Non-cooperative game, Cooperative game, VANETs, Game theory, Nash equilibrium, Nash bargaining solution.

## I. INTRODUCTION

VANETs is a new paradigm of wireless communications that aim to exploit the recent advances in wireless devices technology to enable intelligent inter-vehicle communication. The appearance of VANETs has been becoming an interesting field for the traffic research community during the last decades. VANETs provides a new trend for Intelligent Transportation Systems such as public transport management [1], and improve security in transportation to reduce the number of disasters. Various types of safety have been designed for VANETs, including emergency alert, accident notification, curve alert, file-sharing, internet, and advertisements.

This paragraph of the first footnote will contain the date on which you submitted your paper for review.

Authors are with the Information Processing and Decision Support Laboratory, Faculty of Sciences and Technics, University Sultan Moulay Slimane, Beni Mellal, Morocco (e-mails: garmani.hamid@gmail.com, aitomard@gmail.com, med.el.amran@gmail.com, baslam.med@gmail.com, jourhman@hotmail.com).

Enhance security is achieved by Basic Safety Messages (BSMs) exchanged between vehicles in VANETs, the BSMs are called beacons. Vehicles periodically broadcast beacons within the network to inform other vehicles of their situation (vehicle nodes position, speed, and direction information). On the other hand, beacons or safety messages are broadcasted in case of emergencies, such as collisions, accidents, and road surface collapse. In dense vehicular networks, a high number of beacons get lost, and congestion in the channel load result because of the growth in beaconing rates, and thus, degrades vehicles' awareness and the accuracy of the safety of vehicles. Channel congestion is a critical factor that leads to delayed or failed messages delivery. With higher vehicle density, it is not clear if the channel capacity will be sufficient to support the data load generated by beacons. Therefore, the development of effective congestion control strategies for VANETs is of utmost importance and has been an area of intense research interest in recent years.

The modelization of analytical models to study the behavior of the vehicle in VANETs is a challenge that gets an increasing interest of researchers. Several models have been proposed to analyze the VANET performance to suggest suitable solutions to VANETs. Congestion control is a challenge in computer networks. The metric used to evaluate congestion control are fairness between the vehicle, the time needed for the convergence, and oscillation size [2]. Congestion control in VANETs should operate in a distributed manner without involving any infrastructure. Due to the highly dynamic nature of VANETs, the convergence time of the control mechanism must be minimal.

Several work used game theory in wireless networks [3] [4] [5] [6] [7] [8]. The authors in [9] proposed a beacon power control algorithm; every player calculates the maximum beaconing power to achieve the maximum communication power and keeps the Channel Busy Ratio (CBR) under a threshold. In [10], the authors study the performance of a multi-hop broadcast protocol in VNETs safety by designing a generic probabilistic forwarding scheme and proposing an analytical model to study the performance of the proposed model. The authors in [11] provide a mechanism to find the optimal beacon rates founded on the maximization of the utility function and show the impact of the beacon rate on the performance of the network. In [12], the author studied a dynamic congestion control mechanism as a means of broadcasting BSM, and to guarantee the reliable and timely delivery of messages to all

neighbors in a network. The authors in [13] used the tabu search algorithm with multi-channel allocation capability to reduce the time delay and jitter for improving the quality of service in VANET. In [10], the authors proposed a vehicle mobility prediction founded beacon rate adaptation approach, where each vehicle uses the prediction module to get the situation of their neighbors in real-time. The authors in [14] studied the competition among vehicles in beaconing power as a non-cooperative game. In [15] the authors used the non-cooperative game for designing a beacon rate control mechanism. The authors proved the uniqueness of the Nash equilibrium point and proposed a distributed method is used to find the equilibrium point. In this paper, we utilize a non-cooperative game and the cooperative game to study the joint control beaconing rate and beaconing power in VANETs. We propose three algorithms for learning joint beaconing rate and beaconing power at Nash equilibrium and Nash bargaining solution.

In this paper, a fair and stable joint beaconing power and beaconing rate problem in VANETs are formulated and solved based on the non-cooperative games and cooperative game. The incentive and objective of the proposed approach are finding the vehicle beaconing power and beaconing rate in a distributed manner to decrease the number of losses of beacons. The theory of supermodular games and the Nash bargaining solution are used to solve the corresponding optimization problem. We prove the existence of the Nash equilibrium point in the non-cooperative game. Furthermore, we implement three learning algorithms that find the equilibrium point in a distributed manner by adjusting beaconing rates and beaconing powers jointly in a single step. Performance evaluation shows the convergence of the proposed algorithm to the equilibrium beaconing power and the beaconing equilibrium rate, and show the impact of system parameters on vehicle strategies. Also, it is revealed that the proposed cooperative game algorithm is the best choice for the vehicle to control the beaconing rate and beaconing power.

The rest of this paper is organized as follows. In Section II, we describe the proposed model. In Section III, we present the non-cooperative game formulation and the price of anarchy. In Section IV, we present a cooperative game. Then, we present the Performance evaluation in Section V. Finally, in Section VI conclusions.

## II. SYSTEM MODEL

The utility function of each vehicle is the difference between revenue and fees. Accordingly, the payoff of the vehicle  $i$  can be written as:

$$U_i = a_i \log(r_i + p_i + 1) - c_i p_i CBR_i(p_i, r_i, p_{-i}, r_{-i}) - (C_{s_i} + C_{p_i} p_i + C_{r_i} r_i) \quad (1)$$

where  $a_i$  and  $c_i$  are two positive parameters.  $CBR_i(p_i, r_i, p_{-i}, r_{-i})$  is the channel busy ratio that vehicle  $i$  senses, and it is a function of all vehicle beaconing rates and beaconing power, where  $p_{-i} = (p_1, \dots, p_{i-1}, p_{i+1}, \dots, p_N)$ . The term  $a \log(r_i + p_i + 1)$  is the revenue of vehicle  $i$ ; it is an increasing function with respect to beaconing rate and

beaconing power. A logarithmic function has been used because it is increasing and has excellent concavity properties. Thus, the vehicle with lower beaconing power and their beaconing rate has more incentive to increase their beaconing power and their beaconing rate. The second term  $c_i p_i CBR_i(p_i, r_i, p_{-i}, r_{-i})$ , is the congestion cost. It indicates that a vehicle should pay higher costs at higher congestions, which discourages the vehicles from using a high beacon rate and high beacon power. The third term  $C_{s_i} + C_{p_i} p_i + C_{r_i} r_i$  is the energy consumed to send beacons and to switch the state of the transceiver.  $C_{s_i}$  is the energy consumed for switching the state of the transceiver,  $C_{p_i}$  is the energy consumed for sending beacons with power  $p_i$ , and  $C_{r_i}$  is the energy consumed for sending beacons with a rate  $r_i$ .

Then, we define  $CBR_i(p_i, r_i, p_{-i}, r_{-i})$  as that in [16] by

$$CBR_i(p_i, r_i, p_{-i}, r_{-i}) = \sum_{j=1}^N h_{ij} r_j \quad (2)$$

where

$$h_{ij} = T_{frame} \times \frac{\Gamma(m, m \frac{C_{Tt}}{d_{ij}^\gamma})}{\Gamma(m)} \quad (3)$$

$$\Omega_{ij} = \frac{p_j \lambda^2}{(4\pi)^2 d_{ij}^\gamma} \quad (4)$$

$\Gamma$  is the gamma function,  $\Gamma(\dots)$  is the upper incomplete gamma function,  $C_{Tt}$  is the threshold power level of carrier sense,  $p_j$  is the BSM transmit power of vehicle  $j$ ,  $d_{ij}$  is the distance between  $j$ th and  $i$ th vehicles,  $m$  is Nakagami fading parameter,  $\lambda$  is the wavelength,  $\gamma$  is the path loss exponent,  $r_j$  is the beaconing rate of vehicles  $j$ , and  $T_{frame}$  is the time needed to transmit a beacon message.

Equation (2) indicates that the channel load experienced by vehicle  $i$  is the weighted sum of the beaconing rate of all the other vehicles  $\sum_{j=1}^N h_{ij} r_j$ . The channel load also depends on various parameters such as channel fading, the time needed to transmit a beacon message, and the distance of other vehicles. The coefficients  $h_{ij}$  defined in (3), represents the action of these parameters in the channel load sensed by vehicle  $i$ .

## III. A NON-COOPERATIVE GAME FORMULATION

Let  $G = [\mathcal{N}, \{R_i, P_i\}, \{U_i(\cdot)\}]$  denote the non-cooperative beaconing rate and beaconing power game (NRPG), where  $\mathcal{N} = \{1, \dots, N\}$  is the index set identifying the vehicle,  $P_i$  is the beaconing power strategy set of vehicle  $i$ ,  $R_i$  is the beaconing rate strategy set of vehicle  $i$ , and  $U_i(\cdot)$  is the utility function of vehicle  $i$  defined in Equation (1). We assume that the strategy spaces  $R_i$  and  $P_i$  of each vehicle  $i$  are compact and convex sets with maximum and minimum constraints, for any given vehicle  $i$  we consider as strategy spaces the closed intervals  $R_i = [\underline{r}_i, \bar{r}_i]$  and  $P_i = [\underline{p}_i, \bar{p}_i]$ . Let the beaconing power vector  $\mathbf{p} = (p_1, \dots, p_N)^T \in P^N = P_1 \times P_2 \times \dots \times P_N$ , beaconing rate vector  $\mathbf{r} = (r_1, \dots, r_N)^T \in R^N = R_1 \times R_2 \times \dots \times R_N$ .

**Definition 1** The strategy vector  $(\mathbf{p}^*, \mathbf{r}^*) = (p_1^*, p_2^*, \dots, p_N^*, r_1^*, r_2^*, \dots, r_N^*)$  is a Nash equilibrium of the NRPG  $G = [\mathcal{N}, \{R_i, P_i\}, \{U_i(\cdot, \cdot)\}]$  if

$$\forall (i, r_i, p_i) \in (\mathcal{N}, R_i, P_i),$$

$$U_i(p_i^*, r_i^*, \mathbf{p}_{-i}^*, \mathbf{r}_{-i}^*) \geq U_i(p_i, r_i, \mathbf{p}_{-i}^*, \mathbf{r}_{-i}^*)$$

**Definition 2** The game  $G$  is submodular if she satisfies the following conditions:

- $S_i = P_i \times R_i$  is a compact subset of Euclidean space.
- $U_i(p_i, r_i), p_i \in P_i, r_i \in R_i$  is smooth and:
  - ✓ submodular in  $(p_i, r_i)$  for fixed  $(\mathbf{p}_{-i}, \mathbf{r}_{-i})$  i.e.,

$$\frac{\partial^2 U_i}{\partial p_i \partial r_i} \leq 0 \quad (5)$$

- ✓ Has non-increasing differences in  $\{(p_i, r_i), (\mathbf{p}_{-i}, \mathbf{r}_{-i})\}$ , i.e.,

$$\frac{\partial^2 U_i}{\partial r_i \partial r_j} \leq 0, \quad \forall j \neq i \quad (6)$$

given that

$$\frac{\partial^2 U_i}{\partial r_i \partial p_j} = 0, \quad \forall j \neq i \quad (7)$$

**Theorem 1** The utility function  $U_i(\mathbf{p}, \mathbf{r})$  is submodular in  $(p_i, r_i)$  for fixed  $(\mathbf{p}_{-i}, \mathbf{r}_{-i})$ .

**Proof:** The second-order partial derivative utility function is written as:

$$\frac{\partial^2 U_i}{\partial p_i \partial r_i} = -\frac{a_i}{(1+r_i+p_i)^2} - c_i h_{ii} \leq 0 \quad (8)$$

then the utility function  $U_i(\mathbf{p}, \mathbf{r})$  is submodular in  $(p_i, r_i)$  for each fixed  $(\mathbf{p}_{-i}, \mathbf{r}_{-i})$ .

**Theorem 2** The utility function  $U_i(\mathbf{p}, \mathbf{r})$  has non-increasing differences in  $\{(p_i, r_i), (\mathbf{p}_{-i}, \mathbf{r}_{-i})\}$ .

**Proof:** The second partial derivative of the utility function is

$$\frac{\partial^2 U_i}{\partial r_i \partial r_j} = 0 \quad (9)$$

and

$$\frac{\partial^2 U_i}{\partial r_i \partial p_j} = 0 \quad (10)$$

Then the utility function  $U_i(\mathbf{p}, \mathbf{r})$  has non-increasing differences in  $\{(p_i, r_i), (\mathbf{p}_{-i}, \mathbf{r}_{-i})\}$ .

Based on theorems 1, theorems 2, and definition 2, we conclude the following theorems.

**Theorem 3** The NRPG  $G$  is submodular in  $(p_i, r_i)$  for all  $i \in \mathcal{N}$ .

Based on theorem 3, the game  $G$  is a submodular game, and the set of its Nash equilibrium points is nonempty. Therefore, the following holds:

**Theorem 4** The NRPG game  $G = [\mathcal{N}, \{R_i, P_i\}, \{U_i(\mathbf{p}, \mathbf{r})\}]$  has at least one Nash equilibrium [6], which is defined as:

$$(p_i^*, r_i^*) = \arg \max_{p_i \in P_i, r_i \in R_i} U_i(\mathbf{p}, \mathbf{r}) \quad (11)$$

The following theorem proves the uniqueness of the Nash equilibrium point.

**Theorem 5** The unique Nash equilibrium point of the NRPG  $G$  is given by:

$$(p_i^*, r_i^*) = \arg \max_{p_i \in P_i, r_i \in R_i} U_i(\mathbf{p}, \mathbf{r}) \quad (12)$$

s.t.

$$\left. \frac{\partial U_i(\mathbf{p}, \mathbf{r})}{\partial p_i} \right|_{p_i=p_i^*} = 0 \quad \text{and} \quad \left. \frac{\partial U_i(\mathbf{p}, \mathbf{r})}{\partial r_i} \right|_{r_i=r_i^*} = 0 \quad (13)$$

and

$$(p_i, r_i) J(p_i, r_i) (p_i, r_i)^T \leq 0, \quad \forall p_i \in P_i, \quad \forall r_i \in R_i \quad (14)$$

where  $J = \begin{pmatrix} \frac{\partial^2 U_i}{\partial p_i^2} & \frac{\partial^2 U_i}{\partial p_i \partial r_i} \\ \frac{\partial^2 U_i}{\partial p_i \partial r_i} & \frac{\partial^2 U_i}{\partial r_i^2} \end{pmatrix}$  is the Hessian matrix at point  $(p_i, r_i)$ .

**Proof:** The conditions of the first-order partial derivatives (13) determine the stationary points of the utility function  $U_i(\mathbf{p}, \mathbf{r})$ , which can either be a maximum, a minimum or a saddle point. The condition (14) is necessary to find the global maximum of the utility function.

$$J = \begin{pmatrix} \frac{\partial^2 U_i}{\partial p_i^2} & \frac{\partial^2 U_i}{\partial p_i \partial r_i} \\ \frac{\partial^2 U_i}{\partial p_i \partial r_i} & \frac{\partial^2 U_i}{\partial r_i^2} \end{pmatrix} \quad (15)$$

$$= \begin{pmatrix} -\frac{a_i}{(1+r_i+p_i)^2} & -\frac{a_i}{(1+r_i+p_i)^2} - c_i h_{ii} \\ -\frac{a_i}{(1+r_i+p_i)^2} - c_i h_{ii} & -\frac{a_i}{(1+r_i+p_i)^2} \end{pmatrix} \quad (16)$$

Thus,

$$(p_i, r_i) J(p_i, r_i) (p_i, r_i)^T = -\frac{a_i p_i^2}{(1+r_i+p_i)^2} - \frac{a_i r_i^2}{(1+r_i+p_i)^2} - \frac{a_i p_i^2}{(1+r_i+p_i)^2} - c_i h_{ii} p_i^2 - \frac{a_i r_i^2}{(1+r_i+p_i)^2} - c_i h_{ii} r_i^2 \leq 0 \quad (17)$$

Then, the Hessian matrix  $J$  is negative definite.

Since it is hard to get the analytical result of the system (13), we use an iterative and distributed algorithm that finds the unique Nash equilibrium point  $(\mathbf{p}^*, \mathbf{r}^*)$ . This algorithm is defined as follows.

#### A. Iterative Nash Equilibrium Algorithm

In this section, based on our previous analysis, we introduce two distributed and iterative learning processes that convergence toward the Nash equilibrium point of NRPG. The best response algorithm is known to reach equilibria for S-modular games, by exploiting the monotonicity of the best response functions. Each player fixes its desirable strategies to maximize its profit. Then, each player can observe the policy taken by its competitors in previous rounds and input them in its decision process to update its policy. Then, it becomes natural to accept the Nash equilibrium as the attractive point of the game. Yet, the best response algorithm requires perfect rationality and complete information, which is not practical for real-world applications and may increase the signaling load as well. Therefore, we propose an adaptive distributed learning framework to discover equilibria for the activation game based on the "Nash Seeking Algorithm" with stochastic state-

dependent payoffs for continuous actions. Algorithm 1 summarizes the best response learning steps that each player has to perform to discover its Nash equilibrium strategy.

Nash seeking algorithm is one of the most Known learning schemes. It is a discrete-time learning algorithm, using sinus perturbation, for continuous action games where each vehicle has only a numerical realization of the payoff at each time. At each iteration  $t$ , the vehicle  $i$  chooses its beaconing power and beaconing rate and obtains from the environment the realization of its payoff. The improvement of the strategy is based on the current observation of the realized payoff and previously chosen strategies. Hence, we say vehicles learn to play an equilibrium, if after a given number of iterations, the strategy profile converges to an equilibrium strategy. The proposed learning framework has the following parameters:  $\phi_i$  and  $\phi'_i$  are the perturbation phase,  $z_i$  and  $z'_i$  are the growth rate,  $b_i$  and  $b'_i$  are the perturbation amplitude, and  $\Omega_i$  and  $\Omega'_i$  are the perturbation frequency. This procedure is repeated for the window  $T$ . Algorithm 2 summarizes the Nash seeking algorithm learning steps that vehicle  $i$  has to perform in order to discover its Nash equilibrium beaconing power and beaconing rate.

---

**Algorithm 1** Best Response Algorithm
 

---

- 1: Initialize vectors  $\mathbf{p}(0) = [p_1(0), \dots, p_N(0)]$  and  $\mathbf{r}(0) = [r_1(0), \dots, r_N(0)]$  randomly;
  - 2: **For** each vehicle  $i$  at round  $t$  computes:
    - $p_i(t+1) = \underset{p_i \in P_i}{\operatorname{argmax}}(U_i(\mathbf{p}, \mathbf{r}))$ .
    - $r_i(t+1) = \underset{r_i \in R_i}{\operatorname{argmax}}(U_i(\mathbf{p}, \mathbf{r}))$ .
  - 3: **If**  $|r_i(t+1) - r_i(t)| < \varepsilon$  and  $|p_i(t+1) - p_i(t)| < \varepsilon$ , then **STOP**.
  - 4: **Else** make  $t \leftarrow t + 1$  and go to step (2).
- 

---

**Algorithm 2** Nash Seeking Algorithm
 

---

- 1: **Data:**
    - $\phi_i \in [0, 2\pi]$  and  $\phi'_i \in [0, 2\pi]$  : perturbation phase;
    - $b_i > 0, b'_i > 0$  : perturbation amplitude;
    - $\Omega_i, \Omega'_i$  : perturbation phase;
    - $z_i, z'_i$  : the growth rate;
  - 2: **Result:** Equilibrium beaconing power  $p_i$  and Equilibrium beaconing rate  $r_i$
  - 3: **Initialization:**
  - 4: Assign a value for  $\tau_{i,0}^*, \zeta_{i,0}^*, p_{i,0}^*$  and  $r_{i,0}^*$  for  $i = 1, 2, \dots, N$ ;
  - 5: **Learning pattern:** For each iteration  $t$ :
  - 6: Observes the payoff  $U_{i,t}$  and estimates  $\tau_{i,t+1}^*$  and  $\zeta_{i,t+1}^*$  using
    - $\tau_{i,t+1}^* = \tau_{i,t}^* + t^* z_i b_i \sin(\Omega_i t^* + \phi_i) U_{i,t}$ ;
    - $\zeta_{i,t+1}^* = \zeta_{i,t}^* + t^* z'_i b'_i \sin(\Omega'_i t^* + \phi'_i) U_{i,t}$ ;
  - 7: Update beaconing rate  $r_i$  and beaconing power  $p_i$  using the following rules
    - $p_{i,t+1}^* = \tau_{i,t+1}^* + b_i \sin(\Omega_i t^* + \phi_i)$ ;
    - $r_{i,t+1}^* = \zeta_{i,t+1}^* + b'_i \sin(\Omega'_i t^* + \phi'_i)$ ;
- 

### B. Price of Anarchy

The price of anarchy (PoA) is defined as the ratio between the performance measures of the worst equilibrium and the optimal outcome. A PoA close to 1 indicates that the equilibrium is approximately socially optimal, and thus the consequences of selfish behavior are relatively benign.

In [17], we measure the loss of efficiency due to actors' selfishness as the quotient between the social welfare obtained at the Nash equilibrium and the maximum value of the social welfare:

$$PoA = \frac{\min_{\mathbf{p}, \mathbf{r}} W_{NE}(\mathbf{p}, \mathbf{r})}{\max_{\mathbf{p}, \mathbf{r}} W(\mathbf{p}, \mathbf{r})} \quad (29)$$

where  $W(\mathbf{p}, \mathbf{r}) = \sum_{i=1}^N U_i(\mathbf{p}, \mathbf{r})$  is the social welfare function and  $W_{NE}(\mathbf{p}^*, \mathbf{r}^*) = \sum_{i=1}^N U_i(\mathbf{p}^*, \mathbf{r}^*)$  is a sum of utilities of all players at Nash Equilibrium.

## IV. COOPERATIVE GAME

The Nash bargaining game [18] is a cooperative game in which players have a mutual agreement for cooperation in order to obtain a higher payoff compared to the non-cooperative case. Let  $\mathcal{U}$  be a closed and convex subset of  $\mathbb{R}^N$  that represents the set of feasible payoff allocations that the players can get if they all cooperate. Suppose  $\{U_i \in \mathcal{U} | U_i \geq U_i^{\min}, \forall i \in \mathcal{N}\}$  is a nonempty bounded set. Define  $\mathbf{U}^{\min} = (U_1^{\min}, U_2^{\min}, \dots, U_N^{\min})$ , then the pair of  $(\mathcal{U}, \mathbf{U}^{\min})$  constructs a  $K$ -player bargaining game. Here, we define the Pareto efficient point [19], where a player can not find another point that improves the utility of all the players at the same time.

**Definition 3** A strategy profile  $(\mathbf{p}^*, \mathbf{r}^*) = (p_1^*, p_2^*, \dots, p_N^*, r_1^*, r_2^*, \dots, r_N^*)$  is Pareto-optimal if and only if there is no other strategy profile  $(\mathbf{p}, \mathbf{r})$  such that  $U_i(\mathbf{p}, \mathbf{r}) \geq U_i(\mathbf{p}^*, \mathbf{r}^*)$ ,  $\forall i \in \mathcal{N}$ , and  $U_i(\mathbf{p}, \mathbf{r}) > U_i(\mathbf{p}^*, \mathbf{r}^*)$ ,  $\exists i \in \mathcal{N}$ , i.e., there exists no other strategies that lead to superior performance for some players without causing inferior performance for some other players [19].

There may be an infinite number of Pareto optimal points in a game of multi-players. Thus, we must address how to select a Pareto point for a cooperative bargaining game. We need a criterion to select the best Pareto point of the system. A possible criterion is the fairness of resource allocation. Notably, the fairness of bargaining games is a Nash bargaining solution, which can provide a unique and fair Pareto optimal point under the following axioms.

**Definition 4**  $\bar{r}$  is a Nash bargaining solution in  $\mathcal{U}$  for  $\mathbf{U}^{\min}$  i.e.,  $\bar{r} = \mathcal{H}(\mathcal{U}, \mathbf{U}^{\min})$ , if the following axioms are satisfied [19].

- **Individual rationality:**  $\bar{r}_i \geq U_i^{\min}$ ,  $\bar{r}_i \in \bar{r}$ ,  $i \in \mathcal{N}$ .
- **Feasibility:**  $\bar{r} \in \mathcal{U}$ .
- **Pareto Optimality:**  $\bar{r}$  is Pareto optimal.
- **Independence of Irrelevant Alternatives:** If  $\bar{r} \in \mathcal{U}' \subset \mathcal{U}$ ,  $\bar{r} = \mathcal{H}(\mathcal{U}, \mathbf{U}^{\min})$ , then  $\bar{r} = \mathcal{H}(\mathcal{U}', \mathbf{U}^{\min})$ .
- **Independence of Linear Transformations:** For any linear scale transformation  $\theta$ ,  $\theta(\mathcal{H}(\mathcal{U}, \mathbf{U}^{\min})) = \mathcal{H}(\theta(\mathcal{U}), \theta(\mathbf{U}^{\min}))$ .
- **Symmetry:** If  $\mathcal{U}$  is invariant under all exchanges of players, that is  $\mathcal{H}_i(\mathcal{U}, \mathbf{U}^{\min}) = \mathcal{H}_j(\mathcal{U}, \mathbf{U}^{\min})$ ,  $\forall i, j$ .

**Theorem 6** A unique and fair Nash bargaining solution  $\mathbf{x}^* = (\mathbf{p}^*, \mathbf{r}^*)$  that satisfies all the axioms in Definition 4 can be obtained by maximizing a product term as follows:

$$\mathbf{x}^* = \operatorname{argmax}_{p_i \in P_i, r_i \in R_i} \prod_{i=1}^N U_i(\mathbf{p}, \mathbf{r}) \quad (18)$$

**Proof:** The proof of the theorem 6 is omitted due to space limitations. A similarly detailed proof can be found in [18].

Our work aims to maximize utility functions while decreasing the number of losses beacons. Therefore, the corresponding cooperative Nash bargaining game-theoretic power and rate control problem for vehicle underlying the communication system can be formulated as:

$$\begin{aligned} \mathbf{P1}: \quad & \max_{p_i \in P_i, r_i \in R_i} \prod_{i=1}^N U_j(\mathbf{p}, \mathbf{r}) \quad (19) \\ \text{s. t.} \quad & \begin{cases} C1: 0 \leq p_i \leq p_i^{\max} \\ C2: 0 \leq r_i \leq r_i^{\max} \end{cases} \end{aligned}$$

where constraint C1 limits the beaconing power of vehicle  $i$  to be below  $p_i^{\max}$  and C2 limits the beaconing rate of vehicle  $i$  to be below  $r_i^{\max}$ .

**Lemma 1** Define  $V_i(\mathbf{p}, \mathbf{r}) \triangleq \ln(U_i(\mathbf{p}, \mathbf{r}))$ ,  $i \in \mathcal{N}$ . These objective functions are concave and injective, which satisfy all the Nash axioms in Definition 4.

**Proof:** The proof of theorem 5 shows that the Hessian matrix of the utility function  $U_i(\mathbf{p}, \mathbf{r})$  is negatively define. Then, the utility function  $U_i(\mathbf{p}, \mathbf{r})$  is strictly concave with regard to the 2-tuple  $(p_i, r_i)$ . Subsequently,  $V_i(\mathbf{p}, \mathbf{r}) = \ln(U_i(\mathbf{p}, \mathbf{r}))$  is also concave in  $(p_i, r_i)$ . Therefore,  $V_i(\mathbf{p}, \mathbf{r})$  defined above satisfies all the axioms required by Definition 4 and Theorem 6.

According to Theorem 6 and Lemma 1, the unique Nash bargaining equilibrium with fairness can be found over the strategy space. Then, taking advantage of the increasing property of the logarithmic function, the optimization problem **P1** can be rewritten as:

$$\begin{aligned} \mathbf{P2}: \quad & \max_{p_i \in P_i, r_i \in R_i} \sum_{i=1}^N V_i(\mathbf{p}, \mathbf{r}) = \max_{p_i \in P_i, r_i \in R_i} \sum_{i=1}^N U_i(\mathbf{p}, \mathbf{r}) \quad (20) \\ \text{s. t.} \quad & \begin{cases} C1: 0 \leq p_i \leq p_i^{\max} \\ C2: 0 \leq r_i \leq r_i^{\max} \end{cases} \end{aligned}$$

#### A. Solution of the Cooperative Gam

Herein, we derive the unique equilibrium by solving the constrained optimization problem in (20) utilizing the method of Lagrange multipliers [20]. Introducing Lagrange multipliers  $\{\chi_i^{ite}\}_{i=1}^N$  and  $\{\psi_i^{ite}\}_{i=1}^N$  for the multiple constraints, the Lagrangian of problem (20) can equivalently be solved by maximizing the following expression:

$$\mathcal{F}(\mathbf{p}, \mathbf{r}, \{\chi_i^{ite}\}_{i=1}^N, \{\psi_i^{ite}\}_{i=1}^N) = \sum_{i=1}^N (a_i \log(r_i + p_i + 1) - c_i p_i CBR_i(\mathbf{p}, \mathbf{r}) - (C_{s_i} + C_{p_i} p_i + C_{r_i} r_i) - \chi_i p_i - \psi_i r_i) \quad (21)$$

Based on the standard optimization methods and the Karush–Kuhn–Tucker conditions, the beaconing power of vehicle  $i$  can be obtained by taking the first derivative of (21) with respect to  $p_i$ , which is expressed as follows:

$$\frac{\partial \mathcal{F}}{\partial p_i} = \frac{a_i}{1+p_i+r_i} - c_i CBR(\mathbf{p}, \mathbf{r}) - C_{p_i} - \chi_i \quad (22)$$

Letting  $\frac{\partial \mathcal{F}}{\partial p_i} = 0$  we get,

$$p_i^* = \frac{a_i}{c_i CBR(\mathbf{p}, \mathbf{r}) + C_{p_i} + \chi_i^*} - 1 - r_i^* \quad (23)$$

Meanwhile, the beaconing rate of vehicle  $i$  can be obtained by taking the first derivative of (21) with respect to  $r_i$  as

$$\frac{\partial \mathcal{F}}{\partial r_i} = \frac{a_i}{1+p_i+r_i} - c_i h_{ii} - C_{r_i} - \psi_i \quad (24)$$

Let (24) equals to zero, then we get

$$r_i^* = \frac{a_i}{c_i h_{ii} + C_{r_i} + \psi_i^*} - 1 - p_i^* \quad (25)$$

In this work, we employ the fixed-point technique to derive an iterative procedure that updates the beaconing rate and beaconing power control decisions, which can be given as:

$$p_i^{ite+1} = \left[ \frac{a_i}{c_i CBR(\mathbf{p}, \mathbf{r}) + C_{p_i} + \chi_i^{ite}} - 1 - r_i^{ite} \right]_0^{p_i^{\max}} \quad (26)$$

$$r_i^{ite+1} = \left[ \frac{a_i}{c_i h_{ii} + C_{r_i} + \psi_i^{ite}} - 1 - p_i^{ite} \right]_0^{r_i^{\max}} \quad (27)$$

#### B. Update of the Lagrange Multipliers

The Lagrange multipliers  $\{\chi_i^{ite}\}_{i=1}^N$  and  $\{\psi_i^{ite}\}_{i=1}^N$  need to be updated to guarantee the fast convergence property. Several practical approaches can be employed in the update of Lagrange multipliers. In this paper, the sub-gradient technique is utilized to update the multipliers, as formulated as follows:

$$\begin{cases} \psi_i^{ite+1} = [\psi_i^{ite} - \alpha^{ite} p_i^{ite+1}]^+ \\ \chi_i^{ite+1} = [\chi_i^{ite} - \alpha^{ite} r_i^{ite+1}]^+ \end{cases} \quad (28)$$

where  $(x)^+ = \max(0, x)$ ,  $\beta$  denotes the step size of iteration  $ite$  ( $ite \in \{1, 2, \dots, L_{max}\}$ ) and  $L_{max}$  denotes the maximum number of iterations.

#### C. Iterative Nash Bargaining Algorithm

In this section, a distributed algorithm is proposed as an implementation of our cooperative bargaining beaconing rate and beaconing power control solution. The proposed iterative Algorithm 3 will guarantee convergence by using the subgradient method.

---

#### Algorithm 3 Cooperative Bargaining Algorithm

---

- 1: Initialize  $c_i, a_i, C_{p_i}, C_{r_i}$  and Lagrange multipliers  $\{\chi_i^{ite}\}_{i=1}^N$  and  $\{\psi_i^{ite}\}_{i=1}^N$ ; set  $ite = 1$ ;
  - 2: Initialize  $\{p_i^{ite}\}_{i=1}^N$  and  $\{r_i^{ite}\}_{i=1}^N$ ;
  - 3: **repeat**
  - 4:   **for**  $i = 1$  to  $N$  **do**
  - 5:     (i) Update  $p_i^{ite}$  according to (26);
  - 6:     (ii) Update  $r_i^{ite}$  according to (27);
  - 7:     (iii) Update  $\chi_i^{ite}$  and  $\psi_i^{ite}$  according to (28);
  - 8:   **end for**
  - 9:   Set  $ite \leftarrow ite + 1$ ;
  - 10:   Set  $ite \leftarrow ite + 1$ ;
  - 11:   **until** Convergence or  $ite = L_{max}$
  - 12:   **return**  $\{p_i^{ite}\}_{i=1}^N$  and  $\{r_i^{ite}\}_{i=1}^N$ .
-

V. PERFORMANCE EVALUATION

Extensive experiments have been conducted toward investigating the following issues: (1) what is the number of iterations required by the proposed algorithm to converge toward the equilibrium beaoning rate and equilibrium beaoning power; (2) what is the fast algorithm that converges toward the equilibrium strategies; (3) In what way could system parameters affect the beaoning equilibrium rate and the equilibrium beaoning power? In this section, we demonstrate these experimental results by considering the previous expressions of the utility function. As an illustration, we consider a scenario with two vehicles.

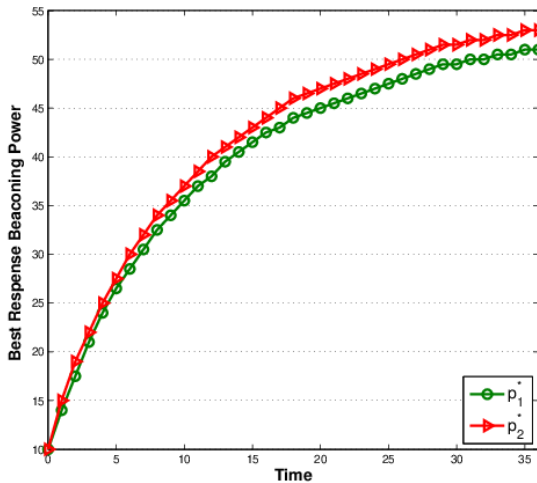


Fig. 1. Seeking the equilibrium beaoning power using the best response algorithm.

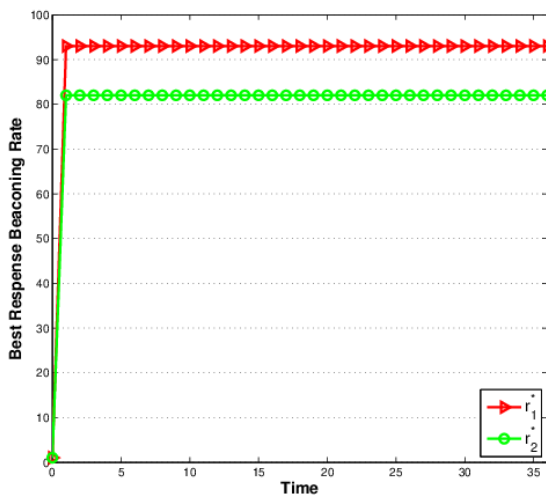


Fig. 2. Seeking the beaoning equilibrium rate using the best response algorithm.

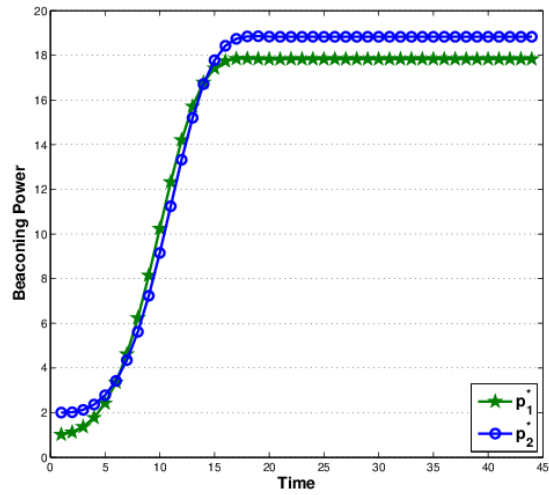


Fig. 3. Seeking the equilibrium beaoning power using the Nash seeking algorithm.

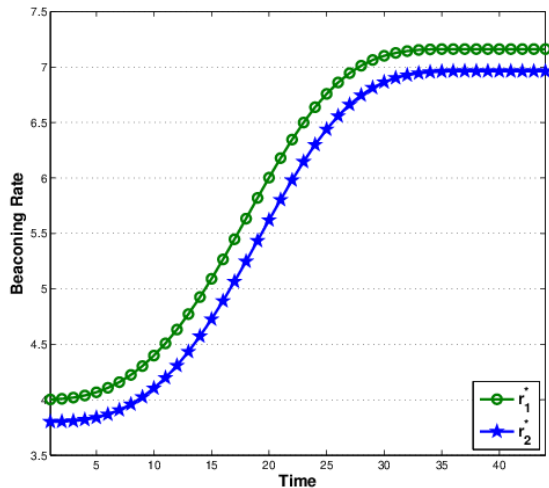


Fig. 4. Seeking the beaoning equilibrium rate using the Nash seeking algorithm.

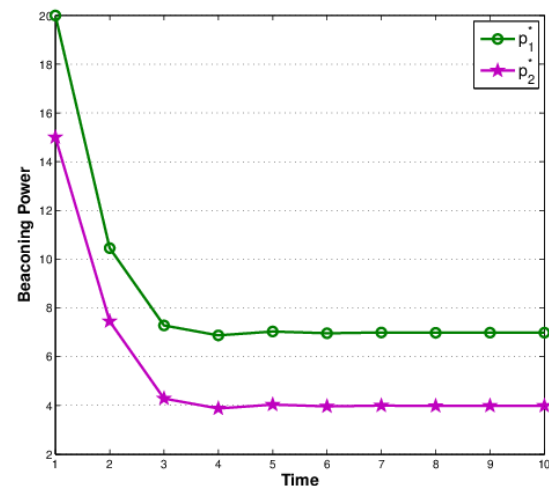


Fig. 5. Seeking the equilibrium beaoning power using a cooperative bargaining algorithm.

Joint Beacon Power and Beacon Rate Control Based on Game Theoretic Approach in Vehicular Ad Hoc Networks

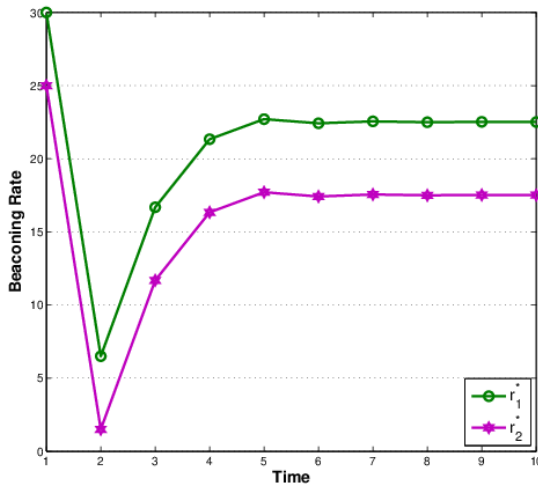


Fig. 6. Seeking the beaconing equilibrium rate using a cooperative bargaining algorithm.

The uniqueness of the joint beaconing rate and beaconing power at Nash equilibrium is demonstrated in Figures 1, 2, 3, and 4. The best response algorithm and Nash seeking algorithm converges to the values of the beaconing rate and beaconing power at Nash equilibrium. Furthermore, based on the results presented in figure 1, 2, 3, 4, 5, and 6 we observe that the convergence of the proposed algorithms is very fast, Nash seeking algorithm converges within approximately 43 iterations, the best response algorithm needs five to 35 iterations to converge, while the cooperative bargaining algorithm converges after 10 iterations to the Pareto-optimal equilibrium. Then, the cooperative bargaining algorithm is the algorithm that converges very fast to the equilibrium; thus, it can be easily adopted in a realistic scenario.

Note that for any vehicle  $i$ , its Nash equilibrium beaconing rate  $r_i$  and beaconing power  $p_i$  primarily depends on the parameter  $a_i$ ,  $c_i$ ,  $C_{p_i}$  and  $C_{r_i}$ . As such, we investigate how the Nash equilibrium points can be affected by these parameters.

Figures 7 and 8 show the beaconing rate and beaconing power of the vehicle when the parameter  $a$  increases from 1 to 20. The beaconing rate and beaconing power of the vehicle increase with the increase of the parameter  $a$ . The reason is that as the parameter  $a$  increases, the utility increase. Therefore, the vehicles are more incentive to increase their beaconing rate and beaconing power. Greater parameter  $a$  leads to the use of higher beaconing rate and beaconing power by vehicles because of the utility function increases.

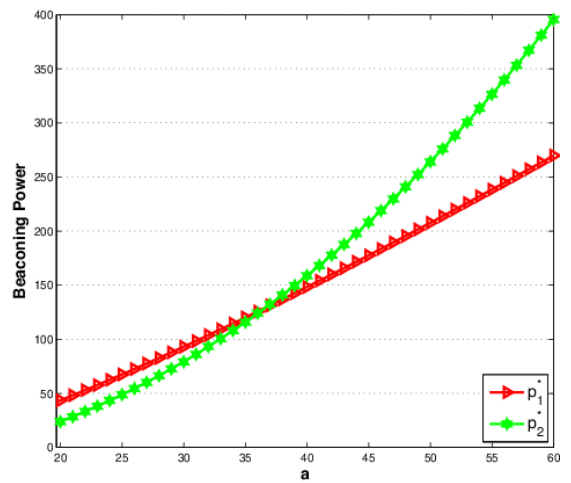


Fig. 7. Beaconing power with respect to  $a$ .

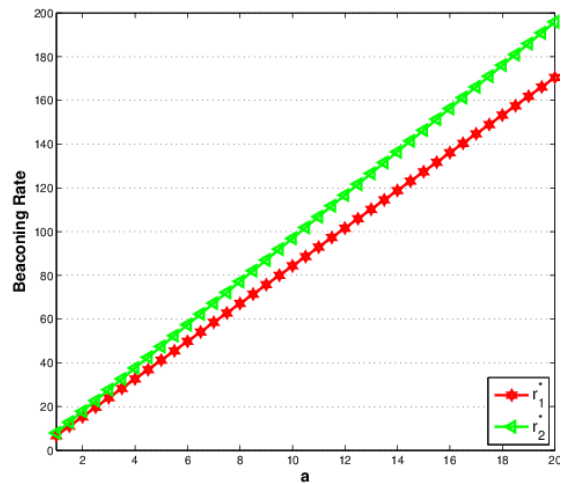


Fig. 8. Beaconing rate with respect to  $a$ .

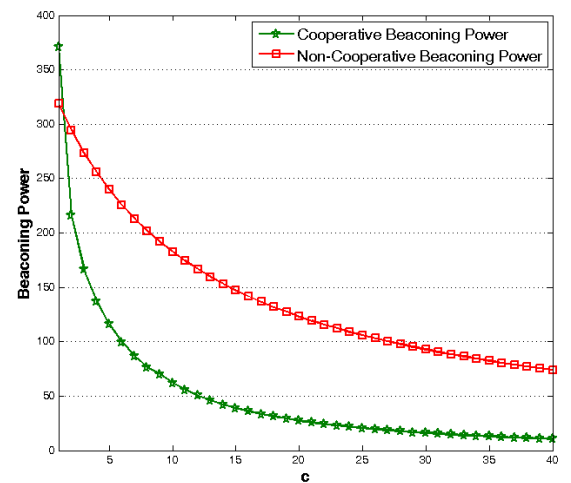


Fig. 9. Beaconing power with respect to  $c$ .

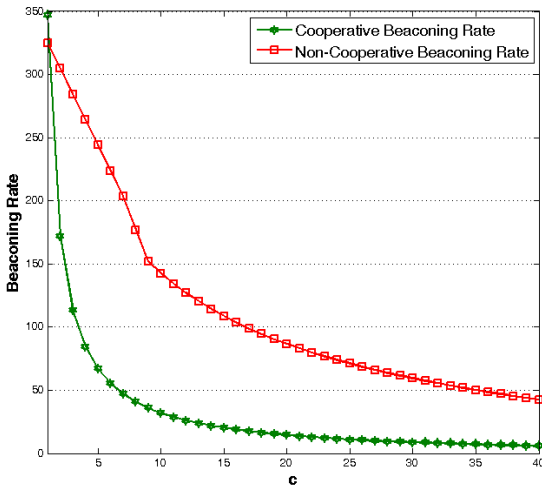


Fig. 10. Beaconing rate with respect to  $c$ .

We plot in Figures 9 and 10, respectively, the interplay of cost  $c$  the beaconing rate and beaconing power, for both vehicles that we consider in this example. On the one hand, we note that the beaconing equilibrium rate and beaconing power for both vehicles is decreasing with respect to the cost  $c$ . When the cost  $c$  increases, the vehicles pay more price at higher congestions, yielding a lower payoff. Therefore, the vehicles need to decrease their beaconing rate and beaconing power to decrease the congestion cost. In addition, the Nash bargaining solution beaconing strategy are lower than the non-cooperative beaconing strategy, which indicates that the Nash bargaining solution is more efficient in terms of congestion cost. Therefore, cooperation is the best choice for the vehicle.

Figures 11 and 12 show both the beaconing power and the beaconing for the non-cooperative games and the cooperative strategic beaconing obtained using the Nash bargaining solution. When energy cost ( $C_r$  and  $C_p$ ) increases, the beaconing power, and beaconing rate decreases, it can be seen that the Nash bargaining solution beaconing strategy exhibits low as the energy cost level increases compared to the non-cooperative beaconing strategy. A unique feature is that the strategic beaconing scheme based on the Nash bargaining solution performs better in terms of energy compared to the non-cooperative strategy for all the values of energy cost. Therefore, the Nash bargaining solution scheme guarantees a higher network lifetime compared to a non-cooperative policy.

Figure 13 shows the  $PoA$  variation curve as a function of the parameter  $c$ .  $PoA$  decreases with respect to  $c$ . When  $c$  is lower, the price of anarchy is socially efficient; moreover, when  $c$  is lower, the vehicles cooperate for optimizing the Nash equilibrium. On the other hand, when  $c$  increase the  $PoA$  is lower, then the Nash equilibrium is not socially efficient, vehicles are selfish, and each one seeks to maximize its profit individually.

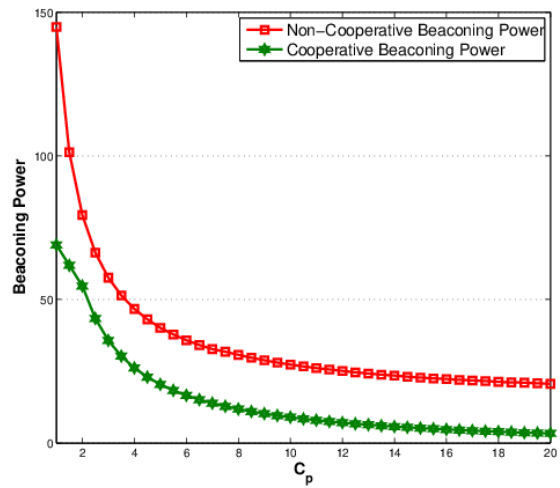


Fig. 11. Beaconing power with respect to  $C_p$ .

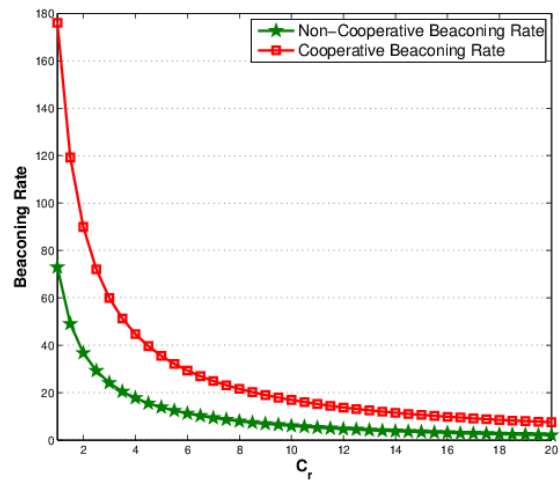


Fig. 12. Beaconing rate with respect to  $C_r$ .

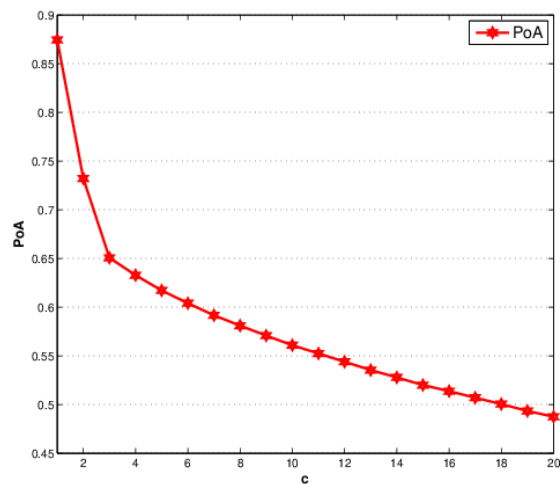


Fig. 13. Price of Anarchy as a function of parameter  $c$ .

Joint Beacon Power and Beacon Rate Control Based on Game Theoretic Approach in Vehicular Ad Hoc Networks

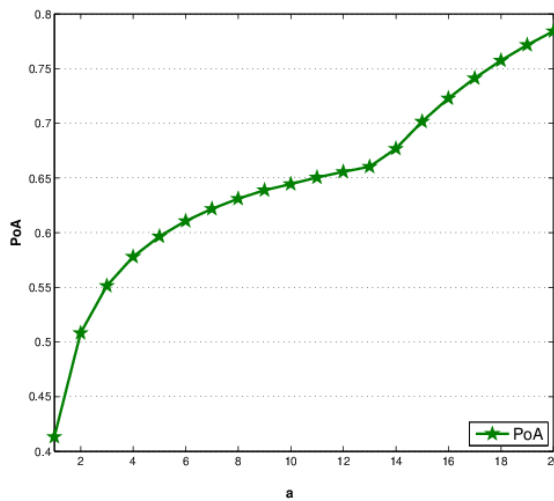


Fig. 14. Price of Anarchy as a function of parameter  $\alpha$ .

Figure 14 shows  $PoA$  variation curve as a function of parameter  $\alpha$ . In that figure,  $PoA$  increases with respect to the parameter  $\alpha$ . When the parameter  $\alpha$  is lower, the price of anarchy is lower. Then, the Nash equilibrium is not socially efficient, the vehicles are selfish, and each one seeks to maximize its profit individually. However, when the parameter  $\alpha$  increases, the equilibrium becomes more and more socially efficient, this increase finds the simple intuition that when parameter  $\alpha$  increase vehicles cooperate with each other for optimizing Nash equilibrium.

VI. CONCLUSION

In this paper, the problem of joint beaconing rate and beaconing power control in VANETs is addressed via S-modular theory. The competition between the vehicle in VNETs is formulated as a non-cooperative game and a cooperative game, where each vehicle chooses the joint beaconing rate and beaconing power. We have performed the equilibrium analysis and proposed a three distributed algorithm for computing the equilibrium point. Simulation results illustrate the impacts of the system parameters on the joint beaconing rate and beacon power and show the number of iteration required by each algorithm for the convergence to the equilibrium. The analysis and simulation results provide a better understanding of the complex interactions among vehicles under a competitive and cooperative condition, which is a benefit for the optimization of vehicle strategies.

REFERENCES

[1] J. E. Paquet, "Guidance for Intelligent Transport Systems (ITS) in Urban Areas", *No March*, 2010.  
 [2] D.-M. Chiu et R. Jain, "Analysis of the increase and decrease algorithms for congestion avoidance in computer networks", *Comput. Netw. ISDN Syst.*, vol. 17, no 1, p. 1-14, 1989.  
 [3] M. Outanoute, H. Garmani, M. Baslam, R. El Ayachi, et B. Bouikhalene, "A Non-Cooperative Game Analysis of Competition between Content Providers in the Internet Market", *Int. J. Bus. Data Commun. Netw.*, vol. 15, no 1, p. 88-104, janv. 2019, doi: 10.4018/IJBDCN.2019010106.

[4] D. A. Omar, H. Garmani, M. El Amrani, M. Baslam, et M. Fakir, "Analysis of Bargaining Game Policy in the Internet Content Distribution Chain", *Int. J. Mob. Comput. Multimed. Commun.*, vol. 10, no 3, p. 47-73, juill. 2019, doi: 10.4018/IJMCMC.2019070103.  
 [5] D. A. Omar, H. Garmani, M. El Amrani, M. Baslam, et M. Fakir, "Analyzing the Customers' Dynamic Confusion in Telecommunication Networks Share Game", *Int. J. Bus. Data Commun. Netw.*, vol. 15, no 2, p. 15-34, juill. 2019, doi: 10.4018/IJBDCN.2019070102.  
 [6] H. Garmani, M. Outanoute, M. Baslam, et M. Jourhmane, "New Competition-Based Approach for Caching Popular Content in ICN", in *Networked Systems*, vol. 11028, A. Podelski et F. Taiani, Éd. Cham: Springer International Publishing, 2019, p. 286-300.  
 [7] H. Garmani, M. Baslam, et M. Jourhmane, "Analysis of Competition between CPs Fronting Advertisers", *Int. J. Adv. Sci. Technol.*, vol. 117, p. 53-66, août 2018, doi: 10.14257/ijast.2018.117.05.  
 [8] D. Ait Omar, M. Outanoute, M. Baslam, M. Fakir, et B. Bouikhalene, "On understanding price-QoS war for competitive market and confused consumers", *Computing*, vol. 101, no 9, p. 1327-1348, sept. 2019, doi: 10.1007/s00607-018-0642-5.  
 [9] L. Le, R. Baldessari, P. Salvador, A. Festag, et W. Zhang, "Performance evaluation of beacon congestion control algorithms for VANETs", in *2011 IEEE Global Telecommunications Conference-GLOBECOM 2011*, 2011, p. 1-6.  
 [10] F. Li et C. Huang, "A Mobility Prediction Based Beacon Rate Adaptation Scheme in VANETs", in *2018 IEEE Symposium on Computers and Communications (ISCC)*, Natal, juin 2018, p. 00671-00677, doi: 10.1109/ISCC.2018.8538734.  
 [11] H. P. Luong, M. Panda, H. Le Vu, et Q. B. Vo, "Analysis of multi-hop probabilistic forwarding for vehicular safety applications on highways", *IEEE Trans. Mob. Comput.*, vol. 16, no 4, p. 918-933, 2017.  
 [12] K. N. Qureshi, A. H. Abdullah, O. Kaiwartya, S. Iqbal, R. A. Butt, et F. Bashir, "A Dynamic Congestion Control Scheme for safety applications in vehicular ad hoc networks", *Comput. Electr. Eng.*, vol. 72, p. 774- 788, nov. 2018, doi: 10.1016/j.compeleceng.2017.12.015.  
 [13] M. Ishaq, M. H. Malik, et M. E. Aydin, "Managing Congestion in Vehicular Networks Using Tabu Search", in *Engineering Applications of Neural Networks*, vol. 893, E. Pimenidis et C. Jayne, Éd. Cham: Springer International Publishing, 2018, p. 118-129.  
 [14] F. Goudarzi et H. Asgari, "Non-Cooperative Beacon Power Control for VANETs", *IEEE Trans. Intell. Transp. Syst.*, p. 1-6, 2018, doi: 10.1109/TITS.2018.2813258.  
 [15] F. Goudarzi et H. Asgari, "Non-Cooperative Beacon Rate and Awareness Control for VANETs", *IEEE Access*, vol. 5, p. 16858-16870, 2017, doi: 10.1109/ACCESS.2017.2742864.  
 [16] Q. Chen, D. Jiang, T. Tielert, et L. Delgrossi, "Mathematical Modeling of Channel Load in Vehicle Safety Communications", in *2011 IEEE Vehicular Technology Conference (VTC Fall)*, San Francisco, CA, USA, sept. 2011, p. 1-5, doi: 10.1109/VETECE.2011.6093282.  
 [17] L. Guijarro, V. Pla, J. R. Vidal, et J. Martinez-Bauset, "Analysis of price competition under peering and transit agreements in Internet Service provision to peer-to-peer users", in *2011 IEEE Consumer Communications and Networking Conference (CCNC)*, janv. 2011, p. 1145-1149, doi: 10.1109/CCNC.2011.5766356.  
 [18] J. F. Nash Jr, "The bargaining problem", *Econom. J. Econom. Soc.*, p. 155-162, 1950.  
 [19] D. Fudenberg et Tirole, J., *Game Theory*. The MIT Press, Cambridge, Massachusetts, 1993.  
 [20] C. Shi, S. Salous, F. Wang, et J. Zhou, "Power allocation for target detection in radar networks based on low probability of intercept: A cooperative game theoretical strategy", *Radio Sci.*, vol. 52, no 8, p. 1030 -1045, 2017.



**Hamid Garmani** received the Ph.D. degrees from University Sultan Moulay Slimane, Morocco, in 2020. His research interests include network economics, network security, applications of game theory in wireless networks, and radio resource management.



**Driss Ait Omar** received the Ph.D. degrees from University Sultan Moulay Slimane, Morocco, in 2019. His research interests include network economics, applications of game theory in wireless networks, network security.



**Mohamed El Amrani** is a PhD student at the Faculty of Sciences and Technology, University Sultan Moulay Slimane, Morocco. His research interests include network economics, network security, applications of game theory in wireless networks, and radio resource management.



**Mohamed Baslam** is a Professor of computer science in the Faculty of Sciences and Technology, Sultan Moulay Slimane University, Morocco. His current research interests include performance evaluation and optimization of networks based on game-theoretic and queuing models, applications in communication/transportation and social networks, such as wireless flexible networks, bio-inspired and self-organizing networks, and economic models of the Internet and yield management.



**Mostafa Jourhmane** is a professor of mathematics and computer science in the Faculty of Sciences and Technology, Sultan Moulay Slimane University, Morocco. His research interests include Numerical analysis, classification, image processing, neural networks, big data, Network Engineering Games, social networks and their control and the analysis through game theoretical models of network and neutrality issues.

Segmentation of MRI images to detect multiple sclerosis using non-parametric, non-uniform intensity normalization and support vector machine methods

# Segmentation of MRI images to detect multiple sclerosis using non-parametric, non-uniform intensity normalization and support vector machine methods

Mohammad Moghadasi<sup>1</sup> and Gabor Fazekas<sup>2</sup>

**Abstract**— Multiple sclerosis (MS) is an inflammatory, chronic, persistent, and destructive disease of the central nervous system whose cause is not yet known but can most likely be the result of a series of unknown environmental factors reacting with sensitive genes. MRI is a method of neuroimaging studies that results in better image contrast in soft tissue. Due to the unknown cause of MS and the lack of definitive treatment, early diagnosis of this disease is important. MRI image segmentation is used to identify MS plaques. MRI images have an image error that is often called non-uniform light intensity. There are several ways to correct non-uniform images. One of these methods is Nonparametric Non-uniform intensity Normalization (N3). This method sharpens the histogram. The aim of this study is to reduce the effect of bias field on the MRI image using N3 algorithm and pixels of MRI images clustered by k-means algorithm. The dimensionality of the data is reduced by Principal Component Analysis (PCA) algorithm and then the segmentation is done by Support Vector Machine (SVM) algorithm. Results show that using the proposed system could diagnose multiple sclerosis with an average accuracy of 93.28%.

**Index Terms**—Brain MRI Image; Multiple Sclerosis; Non-Uniform Image; Light Intensity; N3 Method; MR Image Segmentation; Support Vector Machines (SVM); Machine Learning Techniques; K-Means;

## I. INTRODUCTION

Multiple Sclerosis (MS) is a common, non-traumatic, and neurodegenerative disease that causes young people with disabilities to be characterized pathologically by areas of inflammation, axonal depletion, and the distribution of glycosides throughout the central nervous system. MS often causes sensory, visual, coordination, and other disorders [1]. The two main clinical phenomena of MS are recurrence and progression of the disease. Symptoms of an early recovery in the disease may be due to remodeling, inflammation resolution, and compensatory mechanisms including axonal sodium channel remodeling and membrane flexibility. After repeated attacks the effects of recovery mechanisms are lessened [2]. Early diagnosis of MS is an important step in the treatment process. One of the most important means of diagnosis and follow-up is the use of magnetic resonance imaging (MRI). But with the large volume of MR data being analyzed, it is difficult and time consuming to manually classify these lesions. Auto-

immune segmentation of MS lesions has therefore been considered in brain MR images [3]. The human brain is made up of various tissues that can be anatomically divided into sections such as the skull, cerebrospinal fluid, gray matter, white matter, muscle, fat, capillary, and cavity.

MRI is one of the most important models of medical imaging. It is virtually non-invasive and produces excellent contrast for soft tissues. MRI is a great imaging technique for studying the brain. Different MRI protocols are used for this purpose, including the following [6]:

- T1-weighted (T1-W)
- T2-weighted (T2-W)
- PD-weighted (PD-W)
- FLAIR (Fluid-Attenuated inversion recovery T2 images)

Traditional MRI techniques, such as T1-W and T2-W, are very sensitive in detecting MS plaques. Metrics derived from MRI have become a very important paraclinical tool for the diagnosis of MS. Both acute and chronic MS plaques appear as focal areas of high signal intensity in the T2-W sequence. T1-W imaging is very sensitive in detecting inflammatory activity [4]. Brain and spinal cord degeneration is an important part of the pathology of MS and is clinically a major component of disease progression. Quantitative (numerical) criteria for whole-brain atrophy can be obtained by automated and semi-automated methods that demonstrate the progress of brain tissue volume analysis in vivo in a sensitive and reproducible manner. Quantitative analysis of focal lesions in cross-sectional and longitudinal studies is used to calculate the total number of lesions and the total volume of manual and semiautomatic segmental lesions [5]. Brain MRI image segmentation is difficult due to variable imaging parameters, light intensity interference, noise, gradient, motion, echo, and so two steps are generally required before applying any method for segmenting the MS lesion, the removal of image artifacts, and any non-brain tissue should be removed from the image. MRI images suffer from image error that is often related to the bias field or the intensity of the non-uniformity. The bias field is a low-frequency, very stable signal that lowers the quality of MRI images, especially those produced by older MRI machines. In most MRI analyzes, bias field correction is a crucial component of the first steps of pre-processing that complicate the effect of automatic image analysis [6]. Bias field correction methods are [7].

<sup>1,2</sup>Department of Informatics, University of Debrecen, Debrecen, Hungary

<sup>1</sup>E-mail: Mohammad.Moghadasi@inf.unideb.hu

<sup>2</sup>E-mail: Fazekas.Gabor@inf.unideb.hu

There are various methods for bias field correction which are divided into three different model groups [9]:

- Model-based methods of production
- Exploration methods
- Combined method

The N3 algorithm is one of the hybrid methods between production-based and exploration-based methods, and the advantage is that it can be applied to any MRI image without prior knowledge of that image [8]. N3 is a non-uniform correction technique that finds a multiplication field that maximizes the frequency content of the scanned intensity distribution [9]. N3 continues with a Gaussian estimation of the actual scan intensity by deconvolution and then using this distribution and the actual scan to obtain the non-uniform field estimation. The field is then cleared by a cubic B-spline light intensity field to estimate the use of the selected distance base point. This filter estimate is then removed from the actual scan and the process restarted. Repeat continues until the uniformity estimates converge [10]. Many preprocessing and fragmentation methods have been introduced for the analysis of MRI images and the detection of MS lesions, which are described below.

In the method of Van Leemput et al., they developed an atlas-based monitoring method and presented an image light intensity-based texture classification using a model derived from the expected value maximization (EM) algorithm. However, simultaneous detection of MS lesions as outliers was not well described by the model. This method derives a prior classification of a digital cerebral atlas containing information about the expected location of White matter (WM), Gray matter (GM) and Cerebrospinal fluid (CSF). Their method also corrects for field MRI heterogeneities, light intensity models, estimating the texture specific image of the data itself, and combining contextual information within a classification using an MRF [11]. In the method of Wu et al., they presented an automatic segmentation of the MS lesion into three subtypes of KNN-based (k-nearest neighbors) lesion enhancement, black holes, and high-intensity lesions. According to the assumptions of this method, the lesion is only found within the White matter (WM) areas and all lesions are excluded from the mask [12].

The method of Zijdenbos et al., which uses Atlas probability extraction, includes tissue containing White matter (WM), Gray matter (GM) and Cerebrospinal fluid (CSF). Light intensity T1-W, T2-W and PD-W images are classified as Artificial Neural Network (ANN) class inputs that segment the lesion [13]. In the method of Shiee et al., it fragments brain tissue in a repetitive manner. They used multi-channel images to segment the main structure of the whole brain. They Used atlas-based segmentation techniques that applied statistical atlas and topological atlas together with the Fuzzy C-Means (FCM) algorithm for segmentation. As reported by them, the advantages of topological atlas are that all fragmented structures are location-bound, which allows subsequent processes to resuscitate and detect the membrane [14, 15]. Seld et al., presented a new (N3) method of correction for non-

uniformity of image light intensity, did not rely on a parametric model of tissue light intensity or lesion fragmentation within continuous areas. The former is illustrated by the ability of the N3 method to correct the non-uniformity of image light intensity in MRI data irrespective of the pulse sequence without initial training. The other is illustrated by the ability of methods to correct nonuniformity by using the structure of a random field even when nonuniformity is not clearly visible. N3 is a fully automated iterative method that operates on 3D volumetric data [16, 17]. In Borys et al. method, an approach of correcting the intensity uniformity is presented. The idea was to replace Wenn's FC-harmon method with the K-harmonic method. The algorithm was tested with MRI datasets obtained from a phantom object using a breast MRI coil to simulate real conditions during the study. The results were compared with the other five methods using two indices - integral uniformity and standard deviation of the signal within the object. For the proposed and improved method, the least integral uniformity and reasonable signal deviation were obtained [18]. With Lin et al. method, the proposed algorithm first applies N3, then follows Fuzzy C-Means (FCM), and then smooths the bias field created using the Gaussian kernel and the "B - spline" surface junctions to change the texture contrast problem. The results of segmentation based on N3 FCM-corrected images were compared with N3 and FCM-modified images alone and, alternatively, Coherent Local Intensity Clustering (CLIC), corrected images. The quality of segmentation was evaluated and rated by radiologists based on different correction methods [19, 20, 21].

In this paper, we aim to improve the existing methods by applying N3 algorithm as one of the pre-processing steps of MR images and bias field deletion in segmentation of MRI images.

## II. NON-UNIFORMITY OF IMAGE LIGHT INTENSITY

Non-uniformity of image light intensity makes the light intensity change slow and it is often seen in MR images due to some of the following factors [22]:

- Induction of radio frequency (RF).
- Non-uniform heterogeneous receiver sensitivity
- Electrodynamical interactions with the purpose described as RF diffusion
- Wave effect mode

Other less important factors involved in non-homogeneity include:

- Eddy currents caused by switching the slope of the field
- Coil disturbance
- RF data bandwidth filter
- Geometric distortion

The effect of geometric distortion on the non-uniformity of image light intensity for normal clinical scanners can be ignored. Since the grading routines often represent several millimeters of surface geometric distortion on a field of one side size, and the distortions of the squares change slowly, then one

Segmentation of MRI images to detect multiple sclerosis using non-parametric, non-uniform intensity normalization and support vector machine methods

can expect the corresponding changes in image light intensity to be one percent. This is less than the other causes of malignancy [23, 24, 25]. In MR, the spatial imaging process is encoded by resonant frequency. Hence, the frequency-dependent changes in the sensitivity of the RF reception system result in the corresponding light intensity changes in the image results along the frequency coding path. If a filter is used to limit the bandwidth of an incoming signal that is non-uniform frequency response, a similar problem arises. Since the sensitivity of an RF coil is often uniform and close to its resonance frequency and the coil resonance frequency of the inner subject, the uniformity of image light intensity is improved by adjusting the coil for MR resonance frequency before each scan. Therefore, light intensity changes can disrupt RF coils and filter the data bandwidth that can be considered a scanner defect [26].

A. Non-uniformity model

The correction problem for non-uniformity of image light intensity is greatly simplified if modeled as a fine multiplier. This model is consistent with the multiplicative non-uniformity caused by differences in the sensitivity of the coil of acceptance and the small non-uniformity amplitude due to the excitation and excitation currents. Consider the following model of image construction in MR [27, 28, 29]:

$$v(x) = u(x)f(x) + n(x) \tag{1}$$

In  $x$  location,  $v$  is the measured signal,  $u$  is the actual signal propagated from the tissue,  $f$  is a non-random variable bias field, and  $n$  is the white Gaussian noise assumed to be independent of  $u$ . The difficulty of compensating for the non-uniformity of the image light intensity is to estimate  $f$ . A combination of multipliers and additives makes this difficult. Consider a non-noise case where the true light intensity  $u$  at each axis of the  $X$ -location is independent of randomly distributed random variables. Then by taking the logarithm as  $\hat{u}(x) = \log(u(x))$  Let the model of image construction be summed up:

$$\hat{v}(x) = \hat{u}(x) + \hat{f}(x) \tag{2}$$

Now we show the probable density of  $\hat{v}$ ,  $\hat{u}$  and  $\hat{f}$  with  $V$ ,  $U$  and  $F$ , respectively. Assuming that  $\hat{f}$  and  $\hat{u}$  are independent of each other, the random variables are unrelated, their total distribution can be found by deconvolution:

$$V(\hat{v}) = F(\hat{v})U(\hat{v}) = \int F(\hat{v} - \hat{u})U(\hat{u})d\hat{u} \tag{3}$$

The non-uniform distribution of  $F$  can be seen as an opaque distribution of light intensity [17]. From the signal processing point of view, blurring results in a reduction in the high frequency component  $U$  field. The non-uniform correction of the light intensity of the image is to return the frequency of the

$U$  contents. Since the shape of the  $F$ -core is not known, it is unclear what frequency components of  $U$  can be retrieved to obtain the observed  $V$  distribution from the actual  $U$  distribution. However, since the uniformity of the field  $\hat{u}$  is limited to the soft variations, there are several possible  $U$  distributions corresponding to the given  $V$  distribution. In  $N3$ , the non-uniformity correction method is to find smooth changes in the multiplicative field so as to maximize the  $U$  frequency.

B. Non-uniformity correction methods

The methods available to correct for non-uniformity of image light intensity can be classified into three groups: analytical non-uniformity modeling, modified proprietary protocols that measure non-uniformity, and data-driven post processing. Suppose a multiplicative non-uniform field is corrected by dividing it from the image. The analytical methods described above are useful tools for understanding the mechanism of the generation of changes in image light intensity. However, the non-uniform dependence on the geometry makes these methods impractical because a new model is required for each scan. Among the techniques that include modified proprietary protocols, the fact is that inhomogeneity is largely subject-specific and is an area for excluding them that involves regular scanning of a calibration phantom. In addition, repeated scans of the calibration phantoms in the clinical setting are not practical [30]. The most common data-driven post processing methods are used for homomorphic filtering to estimate multiplicative non-uniform field and image segmentation. These methods assume that the frequency content of the non-uniform field is less than the anatomy [17, 31, 32].

III. THE PROPOSED METHOD

In the first step, the preprocessing step is performed to remove the skull, and then the  $N3$  algorithm is performed to remove the noise from the image. By executing this step, the corrected image is applied as input to the  $K$ -means algorithm. We consider the number of clusters to be equal to four, because there are four different tissue types: Gray matter (GM), White matter (WM), Cerebrospinal fluid (CSF) and background in the image after clustering the result. The vector form is given as an input to the principal component analysis (PCA) algorithm for feature recognition and limiting search space. Then the output of this step is applied to the SVM algorithm for classification and afterwards clustered by  $KNN$ . Ultimately with an unintentional distribution, 70% of the data randomly was applied to training and 30% test to determine whether a person is healthy or unhealthy.

A. Practical Implementation of Method  $N3$

Let's assume if " $d$ " =  $(d_1, d_2, \dots, d_N)^T$  the light intensity, " $a$ " the wavelength of an MRI scan, and " $b$ " =  $(b_1, b_2, \dots, b_N)^T$  the corresponding gains result in the bias field. As it has been generally done in previous articles by bias field correction [8, 24-26]. The  $N3$  method assumes that  $d$  and  $b$  are logarithmic, so that the effect of  $b$  is incremental. The  $b$  is assumed to have a shape with zero Gaussian mean and a definite variance. Histogram  $d$  is also a blurred version of the actual histogram,

and the background picture leads to a convolution with histogram  $b$ . The purpose of the algorithm will be to reverse the N3 method by deconvolution as well as by estimating the smoothed bias field model. This inversion process is repeated continuously to improve the bias field estimates [33].

*B. Deconvolution step*

The first step in the deconvolution algorithm is the histogram. By estimating the current bias field represented by  $\tilde{b}$ , a normalized histogram with  $d - \tilde{b}$  is calculated from the corrected bias field data  $d - \tilde{b}$ , and assumed to be a soft bias field in the first iteration ( $\tilde{b} = 0$ ) [34, 35]. The bin centers are given by the following formulas:

$$\begin{aligned} \tilde{\mu}_1 &= \min(d - \tilde{b}) \\ \tilde{\mu}_K &= \max(d - \tilde{b}) \\ \tilde{\mu}_k &= \tilde{\mu} + (k - 1)h \end{aligned} \tag{4}$$

Which  $h = (\tilde{\mu}_K - \tilde{\mu}_1)/(K - 1)$  is bin width. ( $v_k, k = 1, \dots, K$ ) histogram entries are filled using the interpolation model [10]:

$$v_k = \frac{1}{N} \sum_{i=1}^N \varphi \left[ \frac{d_i - \tilde{b}_i - \tilde{\mu}_k}{h} \right], \varphi[s] = \begin{cases} 1 - |s| & \text{if } |s| < 1 \\ 0 & \text{otherwise} \end{cases} \tag{5}$$

By defining  $\hat{v}$  as a 512-dimensional vector such that  $\hat{v} = (v_1, v_2, \dots, v_K)^T$ , the histogram is deconvolved by the following formula:

$$\hat{\pi} = F^{-1}DF\hat{v} \tag{6}$$

In the above formula  $F$  represents the discrete Fourier transform matrix with the following elements:

$$F_{n,k} = e^{-2\pi j(k-1)(n-1)/512}, n, k = 1, \dots, 512 \tag{7}$$

And  $D$  represents a diagonal matrix with the following elements:

$$D_k = \frac{f_k^*}{|f_k^*|^2 + \gamma}, k = 1, \dots, 512 \tag{8}$$

Where  $\gamma = 0.1$  is a constant value and  $f = (f_1, f_2, \dots, f_{512})^T = Fg$  where  $g$  is a 512 vector and contains the hidden Gaussian kernel with the following variance:

$$\sigma^2 = \frac{f^2}{8 \log 2} \tag{9}$$

*C. Bias correction step*

When the  $\hat{\pi}$  histogram is decanulated, the light intensity of the corresponding  $\tilde{d}_{\mu l}$  corrected image in the decanogram histogram at each bin center of  $\tilde{\mu}_l, l = 1, \dots, K$  is estimated by the following formula [10]:

$$\tilde{d}_{\mu l} = \sum_k w_k^l \tilde{\mu}_k, w_k^l = \frac{(\tilde{\mu}_l | \tilde{\mu}_k, \sigma_k^2) \hat{\pi}_k}{\sum_k (\tilde{\mu}_l | \tilde{\mu}_k, \sigma_k^2) \hat{\pi}_k} \tag{10}$$

And the magnitude of the DD-corrected image is found in each voxel with linear interpolation:

$$\tilde{d}_i = \sum_{l=1}^K \tilde{d}_{\mu l} \varphi \left[ \frac{d_i - \tilde{b}_i - \tilde{\mu}_k}{h} \right], \varphi[s] = \begin{cases} 1 - |s| & \text{if } |s| < 1 \\ 0 & \text{otherwise} \end{cases} \tag{11}$$

Finally, the remaining  $r = d - \tilde{d}$  is calculated and cleared to obtain the bias field estimate:

$$b_i = \Phi \tilde{c} \tag{12}$$

Calculated in the previous formula  $\tilde{c}$  by the following:

$$\tilde{c} \leftarrow (\Phi^T \Phi + N\beta\psi)^{-1} \Phi^T r \tag{13}$$

Which in this  $\Phi$  formula is an  $N \times M$  matrix of spatial smoothing basic functions, where each  $\Phi_{i,m}$  element,  $m$  th Evaluates the base function in the  $i$  voxel.  $\psi$  is a semiconductor positive matrix that fines the curvature of the bias field, and the  $\beta$  is a user-defined adjustment constant whose default value is  $\beta = 10^{-7}$ .

IV. POST-PROCESSING

The N3 method is repeated alternately between the deconvolution phase and the bias field correction step until the standard deviation of the bias estimation difference between the two iterations is less than a specified threshold. By default, the N3 method operates on a sub-volume. After convergence, the estimation of the bias field exponentially returns to the amplitude of the original image, which subsequently corresponds to Equation 13 and, for example, to  $r = \exp(\tilde{b})$ . The resultant coefficients are then used to calculate the final estimate of the bias field by evaluating from Equation 12 with  $\Phi$  full resolution. Finally, inaccurate data are segmented by estimating the bias field to obtain the corrected volume.

V. RESULTS

Two databases were used in this article, one consisting of brain MRI images of healthy individuals and the other one belonging to patients who were all infected with MS. The first database was obtained from the CASI Laboratory of Surgery at the University of North Carolina. This database identifies people who have had a mild or severe stroke or who have had any brain injury for the probability of error in the test results in

Segmentation of MRI images to detect multiple sclerosis using non-parametric, non-uniform intensity normalization and support vector machine methods

red and are recommended to be eliminated if necessary. The second database is obtained from the eHealth lab of Computer Science University of Cyprus. All images are sequenced for each individual, and we selected a specific cross-section where the highest level of the brain was visible and changed the TIFF format to JPG to run the program quickly. This database contains the date of birth of all patients, date of shooting, age and folder name of each individual.

Skull removal is one of the important steps in preprocessing because fat, skull and other non-brain tissues can be a cause of incorrect classification in some ways due to the similarity of the light intensity of the image to brain structures.

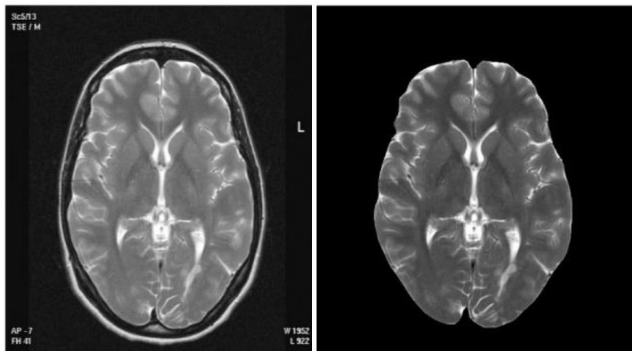


Fig. 1. Preprocessed image sample and skull removal

After executing various steps of N3 algorithm, its output is as follows:

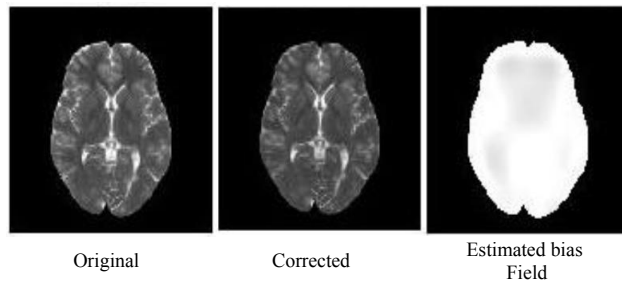


Fig. 2. Approximate images, inputs, outputs, and bias fields of N3 algorithm

The output of the previous step is considered as the input of this step. In this method, after finding the appropriate K number to find the optimal state, it is usually considered  $k = 4$  with the number of different brain tissues including GM, White matter (WM), cerebrospinal fluid, and background. In order to evaluate the accuracy of the proposed method in the appropriate area of MRI images we use:

- Method 1: Accuracy of the proposed method in correct diagnosis of MS disease using N3
- Method 2: Accuracy of the proposed method in correct diagnosis of MS without using N3

You can see the disaggregation matrix for the proposed model using Support Vector Machine (SVM) and both methods 1 and 2 in Table.

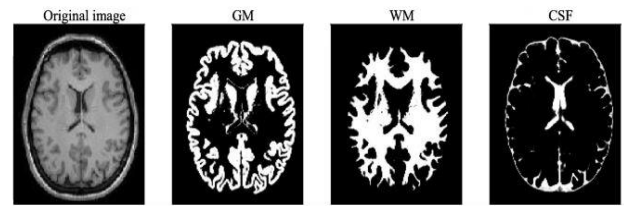


Fig. 3. Output from clustering of human brain MRI image with 4 clusters

To evaluate the N3 method, we compare our proposed method with that of the N3 algorithm, and we show that with age we have improved the algorithm by 1.5% compared to the non-N3 algorithm. By repeatedly replicating the above method and applying these algorithms to the images in the database randomly and obtain the average percentage improvement of N3 method.

TABLE I: Compare with and without N3 methods using SVM

| Algorithm                                | Average correct diagnosis |
|--|---------------------------|
| correct diagnosis of MS disease using N3 | 93.28                     |
| correct diagnosis of MS without using N3 | 89.5                      |

VI. DISCUSSION

N3 stands for Non-Parameter Normalization of Non-Parametric Image Intensity and is a new data-driven method for correcting non-uniformity of image light in MRI data. In this paper, a novel method of classifying machine learning-based MS disease using datasets is presented. The proposed method is performed in five steps:

- Calling images of healthy and unhealthy patients from the database
- Apply pre-processing step on images
- Run N3 algorithm and remove bias field error from images
- Input Implementation of the K-means algorithm for clustering the output from the previous step
- Run SVM algorithm to classify existing images

The proposed method used the database information mentioned above. By using N3 algorithm the bias field effect of the image is minimized and then clustered by k-means algorithm and then by PCA algorithm the dimensionality of the data is reduced and then the segmentation is done by Support Vector Machine (SVM) algorithm and the images are the range is normalized from 0 to 255, and finally, based on these features, images and lesions are classified using the SVM algorithm. Experimental results showed that using the proposed system, one could diagnose multiple sclerosis with an average accuracy of 93.28%.

## VII. REFERENCES

- [1] Mohammad Moghadasi and Gabor Fazekas, "Multiple sclerosis Lesion Detection via Machine Learning Algorithm based on converting 3D to 2D MRI images", *Infocommunications Journal*, Vol. XII, No 1, March 2020, pp. 38-44. doi:10.36244/ICJ.2020.1.6
- [2] Mohammad Mohammad Moghadasi and Dr. Gabor Fazekas, "An Automatic Multiple Sclerosis Lesion Segmentation Approach based on Cellular Learning Automata" *International Journal of Advanced Computer Science and Applications(IJACSA)*, 10(7), 2019. doi: 10.14569/IJACSA.2019.0100726
- [3] P. Baranyi, A. Csapo and G. Sallai: *Cognitive Infocommunications (CogInfoCom)*, Springer International Publishing, 2015, Springer International Publishing, Switzerland, p. 191 (978-3-319-19607-7), doi: 10.1007/978-3-319-19608-4
- [4] L. Kovács, Gy. Eigner: "Tensor Product Model Transformation-based Parallel Distributed Control of Tumor Growth", Volume 15, Issue Number 3, 2018. doi: 10.12700/APH.15.3.2018.3.7
- [5] Csapó, Gábor & Csernoch, Maria & Abari, Kálmán., "Sprego: case study on the effectiveness of teaching spreadsheet management with schema construction. Education and Information Technologies", *Education and Information Technologies*, 2019, doi: 10.1007/s10639-019-10024-2
- [6] M. Moghadasi and G. Fazekas, "Multiple Sclerosis Detection via Machine Learning Algorithm, Accurate Simulated Database 3D MRI to 2D Images, using value of Binary Pattern Classification - A Case Study," 2019 10th IEEE International Conference on Cognitive Infocommunications (CogInfoCom), Naples, Italy, 2019, pp. 233-240, doi: 10.1109/CogInfoCom47531.2019.9089962
- [7] Zhang, Yudong, Siyuan Lu, Xingxing Zhou, Ming Yang, Lenan Wu, Bin Liu, Preetha Phillips, and Shuihua Wang.: "Comparison of Machine Learning Methods for Stationary Wavelet Entropy-Based Multiple Sclerosis Detection: Decision Tree, k-Nearest Neighbors, and Support Vector Machine." *SIMULATION* 92, no. 9 (September 2016): 861–71. doi: 10.1177/0037549716666962
- [8] Coupland AP, Thapar A, Qureshi MI, Jenkins H, Davies AH.: "The definition of stroke" *Journal of the Royal Society of Medicine*. 2017 Jan; 110(1):9-12. doi: 10.1177/0141076816680121
- [9] C. Li, J. C. Gore, and C. Davatzikos, "Multiplicative intrinsic component optimization (MICO) for MRI bias field estimation and tissue segmentation," *Magnetic resonance imaging*, vol. 32, no. 7, pp. 913-923, 2014. doi: 10.1016/j.mri.2014.03.010
- [10] C. T. Larsen, J. E. Iglesias, and K. Van Leemput, "N3 bias field correction explained as a Bayesian modeling method," in *Bayesian and graphical models for biomedical imaging*: Springer, 2014, pp. 1-12. doi: 10.1007/978-3-319-12289-2\_1
- [11] Mohammad Moghadasi, Seyed Majid Mousavi and Gábor Fazekas, "Cloud Computing Auditing" *International Journal of Advanced Computer Science and Applications(ijacs)*, 9(12), 2018. doi: 10.14569/IJACSA.2018.091265
- [12] Boyes, R. G., Gunter, J. L., Frost, C., Janke, A. L., Yeatman, T., Hill, D. L. G., Bernstein, M. A., Thompson, P. M., Weiner, M. W., Schuff, N., Alexander, G. E., Killiany, R. J., DeCarli, C., Jack, C. R., & Fox, N. C. (2008). Intensity non-uniformity correction using N3 on 3-T scanners with multichannel phased array coils. *NeuroImage*, 39(4), 1752-1762. doi: 10.1016/j.neuroimage.2007.10.026
- [13] X. Lladó et al., "Segmentation of multiple sclerosis lesions in brain MRI: a review of automated approaches," *Information Sciences*, vol. 186, no. 1, pp. 164-185, 2012. doi: 10.1007/s00234-011-0992-6
- [14] K. Van Leemput, F. Maes, D. Vandermeulen, A. Colchester and P. Suetens, "Automated segmentation of multiple sclerosis lesions by model outlier detection," in *IEEE Transactions on Medical Imaging*, vol. 20, no. 8, pp. 677-688, Aug. 2001, doi: 10.1109/42.938237
- [15] Y. Wu et al., "Automated segmentation of multiple sclerosis lesion subtypes with multichannel MRI," *NeuroImage*, vol. 32, no. 3, pp. 1205-1215, 2006. doi: 10.1007/s00234-011-0886-7
- [16] Zhang, Yudong, Siyuan Lu, Xingxing Zhou, Ming Yang, Lenan Wu, Bin Liu, Preetha Phillips, and Shuihua Wang.: "Comparison of Machine Learning Methods for Stationary Wavelet Entropy-Based Multiple Sclerosis Detection: Decision Tree, k-Nearest Neighbors, and Support Vector Machine." *SIMULATION* 92, no. 9 (September 2016): 861–71. doi: 10.1177/0037549716666962
- [17] Coupland AP, Thapar A, Qureshi MI, Jenkins H, Davies AH.: "The definition of stroke" *Journal of the Royal Society of Medicine*. 2017 Jan; 110(1):9-12. doi: 10.1177/0141076816680121
- [18] S. M. Mousavi, M. Moghadasi and G. Fazekas, "Dynamic resource allocation using combinatorial methods in Cloud: A case study," 2017 8th IEEE International Conference on Cognitive Infocommunications (CogInfoCom), Debrecen, 2017, pp. 000073-000078, doi: 10.1109/CogInfoCom.2017.8268219
- [19] C. Confavreux, S. Vukusic, T. Moreau, and P. Adeleine, "Relapses and progression of disability in multiple sclerosis," *New England Journal of Medicine*, vol. 343, no. 20, pp. 1430-1438, 2000. doi: 10.1056/NEJM200011163432001
- [20] A. Ortiz, J. Górriz, J. Ramírez, D. Salas-Gonzalez, and J. M. Llamas-Elvira, "Two fully-unsupervised methods for MR brain image segmentation using SOM-based strategies," *Applied Soft Computing*, vol. 13, no. 5, pp. 2668-2682, 2013. doi: 10.1016/j.asoc.2012.11.020
- [21] A. Y. Sharma and Y. K. Meghrajani, "Automated segmentation of multiple sclerosis lesions using statistical approach," 2015 International Conference on Innovations in Information, Embedded and Communication Systems (ICIECS), Coimbatore, India, 2015, pp. 1-5, doi: 10.1109/ICIECS.2015.7193144
- [22] J. Bogaert, S. Dymarkowski, A. M. Taylor, and V. Muthurangu, *Clinical cardiac MRI*. Springer Science & Business Media, 2012. doi: 10.1007/978-3-642-23035-6
- [23] Failo R, Wielopolski PA, Tiddens HA, Hop WC, Mucelli RP, Lequin MH. Lung morphology assessment using MRI: a robust ultra-short TR/TE 2D steady state free precession sequence used in cystic fibrosis patients. *Magn Reson Med*. 2009 Feb;61(2):299-306. doi: 10.1002/mrm.21841. PMID: 19165879
- [24] Hickman, S J, G J Barker, P D Molyneux, and D H Miller. "Technical Note: The Comparison of Hypointense Lesions from 'Pseudo-T1' and T1-Weighted Images in Secondary Progressive Multiple Sclerosis." *Multiple Sclerosis Journal* 8, no. 5 (October 2002): 433–35. doi: 10.1191/1352458502ms824xx
- [25] M. N. Ahmed, S. M. Yamany, N. Mohamed, A. A. Farag and T. Moriarty, "A modified fuzzy c-means algorithm for bias field estimation and segmentation of MRI data," in *IEEE Transactions on Medical Imaging*, vol. 21, no. 3, pp. 193-199, March 2002, doi: 10.1109/42.996338
- [26] Lin, M., Chan, S., Chen, J. H., Chang, D., Nie, K., Chen, S. T., Lin, C. J., Shih, T. C., Nalcioglu, O., & Su, M. Y. (2011). A new bias field correction method combining N3 and FCM for improved segmentation of breast density on MRI. *Medical physics*, 38(1), 5–14. doi: 10.1118/1.3519869
- [27] A. P. Zijdenbos, R. Forghani and A. C. Evans, "Automatic "pipeline" analysis of 3-D MRI data for clinical trials: application to multiple sclerosis," in *IEEE Transactions on Medical Imaging*, vol. 21, no. 10, pp. 1280-1291, Oct. 2002, doi: 10.1109/TMI.2002.806283
- [28] Sweeney, E. M., Shinohara, R. T., Shice, N., Mateen, F. J., Chudgar, A. A., Cuzzocreo, J. L., Calabresi, P. A., Pham, D. L., Reich, D. S., & Crainiceanu, C. M. (2013). OASIS is Automated Statistical Inference for Segmentation, with applications to multiple sclerosis lesion segmentation in MRI. *NeuroImage. Clinical*, 2, 402–413. doi: 10.1016/j.nicl.2013.03.002

Segmentation of MRI images to detect multiple sclerosis using non-parametric, non-uniform intensity normalization and support vector machine methods

[29] Shiee, N., Bazin, P. L., Ozturk, A., Reich, D. S., Calabresi, P. A., & Pham, D. L. (2010). A topology-preserving approach to the segmentation of brain images with multiple sclerosis lesions. *NeuroImage*, 49(2), 1524-1535. doi: 10.1016/j.neuroimage.2009.09.005

[30] Sled JG, Zijdenbos AP, Evans AC. A nonparametric method for automatic correction of intensity nonuniformity in MRI data. *IEEE Trans Med Imaging*. 1998 Feb;17(1):87-97. doi: 10.1109/42.668698. PMID: 9617910

[31] Vrooman, H. A., Cocosco, C. A., van der Lijn, F., Stokking, R., Ikram, M. A., Vernooij, M. W., Breteler, M. M., & Niessen, W. J. (2007). Multi-spectral brain tissue segmentation using automatically trained k-Nearest-Neighbor classification. *NeuroImage*, 37(1), 71-81. doi: 10.1016/j.neuroimage.2007.05.018

[32] Kwan RK, Evans AC, Pike GB. MRI simulation-based evaluation of image-processing and classification methods. *IEEE Trans Med Imaging*. 1999 Nov;18(11):1085-97. doi: 10.1109/42.816072. PMID: 10661326.

[33] Collins DL, Zijdenbos AP, Kollokian V, Sled JG, Kabani NJ, Holmes CJ, Evans AC. Design and construction of a realistic digital brain phantom. *IEEE Trans Med Imaging*. 1998 Jun;17(3):463-8. PMID: 9735909. doi: 10.1109/42.712135

[34] J. Grande-Barreto and P. Gómez-Gil, "Unsupervised brain tissue segmentation in MRI images," 2018 IEEE International Autumn Meeting on Power, Electronics and Computing (ROPEC), Ixtapa, Mexico, 2018, pp. 1-6, doi: 10.1109/ROPEC.2018.8661425

[35] Lötsch, J., Schiffmann, S., Schmitz, K. et al. "Machine-learning based lipid mediator serum concentration patterns allow identification of multiple sclerosis patients with high accuracy", *Sci Rep* 8, 14884 (2018). doi: 10.1038/s41598-018-33077-8



**Mohammad Moghadasi** is a PhD student at University of Debrecen, Faculty of Informatics, with a background of Software Information Technology. He is currently working in digital image processing on multiple sclerosis lesion detection. He is interested and has experience in database, networking and cloud computing as well. He is also a lecturer.



**Dr. Gabor Fazekas** is an Associate Professor at University of Debrecen, Faculty of Informatics, Department of Information Technology. He has extensive experience in supervising PhD dissertations. He is very well knowledgeable in research and teaching. He recently was retired but still supervising PhD students in the fields of computer systems, databases, image processing, combinatorial coding, didactic and many more.

DECLARATIONS

Funding

This research did not receive any specific grant from funding agencies in the public, commercial, or not-for-profit sectors. This work was not financially supported by any organization.



**17<sup>th</sup> International Conference on Network and Service Management**  
*Smart Management for Future Networks and Services*  
 25-29 October 2021, Izmir, Turkey

**CALL FOR PAPERS**

The 17th International Conference on Network and Service Management (CNSM) is inviting authors to submit original contributions in network and service management research. CNSM 2021 is a selective single-track conference, covering all aspects of the management of networks and services, pervasive systems, enterprises, and cloud computing environments. The core track will be accompanied by a series of workshops and poster sessions.

Papers accepted and presented at CNSM 2021 will be published as open access on the conference website and will be submitted to IEEE Xplore and IFIP Digital Libraries. Authors of selected papers, accepted for publication in the CNSM 2021 proceedings, will be invited to submit an extended version of their papers to the IEEE Transactions on Network and Service Management journal.

**Topics of Interest** (but not limited to)

**Network Management**

- Software-defined networks
- Virtual networks
- Overlay networks
- Wireless and cellular networks
- Sensor networks
- Internet of Things
- Information-centric networks
- Enterprise and campus networks
- Data center networks
- Optical networks
- Home networks
- Access networks
- Smart cities and Smart grids

**Management Technologies**

- Network function virtualization
- Software-defined networking
- Orchestration
- Network slicing
- Service function chaining
- Cloud computing and cloud storage
- Edge/Fog computing
- Middleware
- Data models and semantic models
- Operations support systems and business support systems

**Service Management**

- Cloud computing services
- Content delivery services
- Multimedia services
- Internet connectivity and Internet access
- Internet of Things services
- Security services
- Context-aware services
- Information technology services

**Methods**

- Mathematical optimization
- Control theory
- Probability theory, stochastic processes, queuing theory
- Machine learning, deep learning, artificial intelligence
- Federated learning
- Evolutionary computing
- Economic theory and game theory
- Mathematical logic and reasoning
- Data mining and (big) data analysis
- Monitoring and measurements
- Computer simulation experiments
- Prototype implementation and testbed experimentation
- Field trials

**Management Paradigms**

- Centralized management
- Distributed management
- Hierarchical management
- Federated management
- Autonomic and cognitive management
- Policy-based management
- Intent-Based management
- Pro-active management
- Energy-aware management
- Quality of experience-centric management

**Business Management**

- Economic/financial aspects
- Multi-stakeholder aspects
- Service level agreements
- Lifecycle aspects
- Process & workflow aspects
- Privacy aspects

**Functional Areas**

- Fault management
- Configuration management
- Performance management
- Security management
- Accounting Management

Authors are invited to submit original contributions that have not been published or submitted for publication elsewhere. Papers should be prepared using the IEEE 2-column conference style and are limited to 9 pages including references (full papers) or 5 pages including references (short papers). They have to be submitted electronically in PDF format through EDAS at <https://www.edas.info/newPaper.php?c=28015>

For more information please check <http://www.cnsm-conf.org/2021/>

**Important Dates**

- Paper Submission: **28 May 2021**  
 Acceptance Notification: **15 July 2021**  
 Camera Ready due: **1 Aug 2021**

<http://www.cnsm-conf.org/2021/>

**Technical Program Co-Chairs:**

Müge Sayıt, Ege University, Turkey  
 Stuart Clayman, University College London, UK

**General Co-Chairs:**

Prosper Chemouil, Cnam, France  
 Mehmet Ulema, Manhattan College, USA



## Guidelines for our Authors

### Format of the manuscripts

Original manuscripts and final versions of papers should be submitted in IEEE format according to the formatting instructions available on

<https://journals.ieeeauthorcenter.ieee.org/>  
Then click: "IEEE Author Tools for Journals"  
- "Article Templates"  
- "Templates for Transactions".

### Length of the manuscripts

The length of papers in the aforementioned format should be 6-8 journal pages.

Wherever appropriate, include 1-2 figures or tables per journal page.

### Paper structure

Papers should follow the standard structure, consisting of *Introduction* (the part of paper numbered by "1"), and *Conclusion* (the last numbered part) and several *Sections* in between.

The Introduction should introduce the topic, tell why the subject of the paper is important, summarize the state of the art with references to existing works and underline the main innovative results of the paper. The Introduction should conclude with outlining the structure of the paper.

### Accompanying parts

Papers should be accompanied by an *Abstract* and a few *Index Terms (Keywords)*. For the final version of accepted papers, please send the short cvs and *photos* of the authors as well.

### Authors

In the title of the paper, authors are listed in the order given in the submitted manuscript. Their full affiliations and e-mail addresses will be given in a footnote on the first page as shown in the template. No degrees or other titles of the authors are given. Memberships of IEEE, HTE and other professional societies will be indicated so please supply this information. When submitting the manuscript, one of the authors should be indicated as corresponding author providing his/her postal address, fax number and telephone number for eventual correspondence and communication with the Editorial Board.

### References

References should be listed at the end of the paper in the IEEE format, see below:

- a) Last name of author or authors and first name or initials, or name of organization
- b) Title of article in quotation marks
- c) Title of periodical in full and set in italics
- d) Volume, number, and, if available, part
- e) First and last pages of article
- f) Date of issue
- g) Document Object Identifier (DOI)

[11] Boggs, S.A. and Fujimoto, N., "Techniques and instrumentation for measurement of transients in gas-insulated switchgear," *IEEE Transactions on Electrical Installation*, vol. ET-19, no. 2, pp.87–92, April 1984. DOI: 10.1109/TEI.1984.298778

Format of a book reference:

[26] Peck, R.B., Hanson, W.E., and Thornburn, T.H., *Foundation Engineering*, 2nd ed. New York: McGraw-Hill, 1972, pp.230–292.

All references should be referred by the corresponding numbers in the text.

### Figures

Figures should be black-and-white, clear, and drawn by the authors. Do not use figures or pictures downloaded from the Internet. Figures and pictures should be submitted also as separate files. Captions are obligatory. Within the text, references should be made by figure numbers, e.g. "see Fig. 2."

When using figures from other printed materials, exact references and note on copyright should be included. Obtaining the copyright is the responsibility of authors.

### Contact address

Authors are requested to submit their papers electronically via the following portal address:

[https://www.ojs.hte.hu/infocommunications\\_journal/about/submissions](https://www.ojs.hte.hu/infocommunications_journal/about/submissions)

If you have any question about the journal or the submission process, please do not hesitate to contact us via e-mail:

Editor-in-Chief: Pál Varga – [pvarga@tmit.bme.hu](mailto:pvarga@tmit.bme.hu)

Associate Editor-in-Chief:

Rolland Vida – [vida@tmit.bme.hu](mailto:vida@tmit.bme.hu)

László Bacsárdi – [bacsardi@hit.bme.hu](mailto:bacsardi@hit.bme.hu)



# IEEE Global Communications Conference

7-11 December 2021 • Madrid, Spain  
*Connecting Cultures around the Globe*

## CALL FOR PAPERS AND PROPOSALS

The 2021 IEEE Global Communications Conference (GLOBECOM) will be held in Madrid, Spain, from 7 -11 December 2021. Themed “*Connecting Cultures around the Globe,*” this flagship conference of the IEEE Communications Society will feature a comprehensive high-quality technical program including 13 symposia and a variety of tutorials and workshops. IEEE GLOBECOM 2021 will also include an attractive Industry program aimed at practitioners, with keynotes and panels from prominent research, industry and government leaders, business and industry panels, and vendor exhibits.

### TECHNICAL SYMPOSIA

- Cognitive Radio and AI-Enabled Networks
- Communication and Information System Security
- Communication QoS, Reliability and Modeling
- Communication Software and Multimedia
- Communication Theory
- Green Communication Systems and Networks
- IoT and Sensor Networks
- Mobile & Wireless Networks
- Next-Generation Networking and Internet
- Optical Networks & Systems
- Signal Processing for Communications
- Wireless Communications
- Selected Areas in Communications
  - *Aerial Communications*
  - *Big Data*
  - *Cloud Computing, Networking and Storage*
  - *E-Health*
  - *Full-Duplex Communications*
  - *Machine Learning for Communications*
  - *Molecular, Biological and Multi-Scale Communications*
  - *Quantum Communications*
  - *Satellite and Space Communications*
  - *Smart Grid Communications*
  - *Social Networks*

### INDUSTRY FORUMS AND EXHIBITION PROGRAM

Proposals are sought for forums, panels, demos, seminars and presentations specifically related to issues facing the broader communications and networking industries.

### TUTORIALS

Proposals are sought for half- or full-day tutorials in all communication and networking topics.

### WORKSHOPS

Proposals are sought for half- or full-day workshops in all communication and networking topics.

### IMPORTANT DATES

#### Paper Submission

15 April 2021 (23:59)

#### Tutorial Proposals

15 April 2021

#### Acceptance Notification

25 July 2021

#### Workshop Proposals

15 March 2021

#### Camera-Ready

1 September 2021

#### Technical Panel Proposals

1 June 2021

*Full details of submission procedures are available at [globecom2021.ieee-globecom.org](http://globecom2021.ieee-globecom.org)*

### ORGANIZING COMMITTEE

#### General Chairs

Juan Manuel Corchado, University of Salamanca, Spain  
Ana García Armada, Universidad Carlos III de Madrid, Spain

#### Executive Chair

Joel Rodrigues, INATEL, Brazil

#### Executive Vice-Chair

Víctor Gil, Universidad Carlos III de Madrid, Spain

#### Technical Program Chair

Sennur Ulukus, University of Maryland, USA

#### Technical Program Vice Chairs

Rui Dinis, FCT-UNL, Portugal  
Santiago Mazuelas, BCAM, Spain

#### Tutorials Chairs

Octavia Dobre, Memorial University, Canada  
Pascal Lorenz, University of Haute-Alsace, France

#### Workshops Chairs

Mohsen Guizani, University of Idaho, USA  
Guangjie Han, Hohai University, China

#### Publications Chairs

Sofiene Affes, INRS, Canada  
Mutlu Koca, Boğaziçi University, Turkey

#### Industry Forums & Exhibition Chairs

Enrique Díaz-Plaza, IBM, Spain  
Jaime Lloret, Universitat Politècnica de València, Spain

#### Operations Chair

Javier Prieto, University of Salamanca, Spain

[globecom2021.ieee-globecom.org](http://globecom2021.ieee-globecom.org)

# SCIENTIFIC ASSOCIATION FOR INFOCOMMUNICATIONS



---

## Who we are

Founded in 1949, the Scientific Association for Infocommunications (formerly known as Scientific Society for Telecommunications) is a voluntary and autonomous professional society of engineers and economists, researchers and businessmen, managers and educational, regulatory and other professionals working in the fields of telecommunications, broadcasting, electronics, information and media technologies in Hungary.

Besides its 1000 individual members, the Scientific Association for Infocommunications (in Hungarian: HÍRKÖZLÉSI ÉS INFORMATIKAI TUDOMÁNYOS EGYESÜLET, HTE) has more than 60 corporate members as well. Among them there are large companies and small-and-medium enterprises with industrial, trade, service-providing, research and development activities, as well as educational institutions and research centers.

HTE is a Sister Society of the Institute of Electrical and Electronics Engineers, Inc. (IEEE) and the IEEE Communications Society.

## What we do

HTE has a broad range of activities that aim to promote the convergence of information and communication technologies and the deployment of synergic applications and services, to broaden the knowledge and skills of our members, to facilitate the exchange of ideas and experiences, as well as to integrate and

harmonize the professional opinions and standpoints derived from various group interests and market dynamics.

To achieve these goals, we...

- contribute to the analysis of technical, economic, and social questions related to our field of competence, and forward the synthesized opinion of our experts to scientific, legislative, industrial and educational organizations and institutions;
- follow the national and international trends and results related to our field of competence, foster the professional and business relations between foreign and Hungarian companies and institutes;
- organize an extensive range of lectures, seminars, debates, conferences, exhibitions, company presentations, and club events in order to transfer and deploy scientific, technical and economic knowledge and skills;
- promote professional secondary and higher education and take active part in the development of professional education, teaching and training;
- establish and maintain relations with other domestic and foreign fellow associations, IEEE sister societies;
- award prizes for outstanding scientific, educational, managerial, commercial and/or societal activities and achievements in the fields of infocommunication.

---

## Contact information

President: **FERENC VÁGUJHELYI** • [elnok@hte.hu](mailto:elnok@hte.hu)

Secretary-General: **ISTVÁN MARADI** • [istvan.maradi@gmail.com](mailto:istvan.maradi@gmail.com)

Operations Director: **PÉTER NAGY** • [nagy.peter@hte.hu](mailto:nagy.peter@hte.hu)

International Affairs: **ROLLAND VIDA, PhD** • [vida@tmit.bme.hu](mailto:vida@tmit.bme.hu)

Address: H-1051 Budapest, Bajcsy-Zsilinszky str. 12, HUNGARY, Room: 502

Phone: +36 1 353 1027

E-mail: [info@hte.hu](mailto:info@hte.hu), Web: [www.hte.hu](http://www.hte.hu)